



Computational Biomechanics in the Remodelling Rat Heart Post Myocardial Infarction

Department of Surgery
Chris Barnard Division of Cardiothoracic Surgery
Cardiovascular Research Unit

Thesis presented for the degree of
Doctor of Philosophy in Cardiovascular Biomechanics

Author: Fulufhelo James Masithulela
(Student No: MSTFUL001)

Supervisor: Assoc. Prof. Thomas Franz
Co-Supervisor: Assoc. Prof. Neil Davies
Co-Supervisor: Dr. Laura Dubuis

Cardiovascular Research Unit, University of Cape Town

2016

The copyright of this thesis vests in the author. No quotation from it or information derived from it is to be published without full acknowledgement of the source. The thesis is to be used for private study or non-commercial research purposes only.

Published by the University of Cape Town (UCT) in terms of the non-exclusive license granted to UCT by the author.

Declaration

I, **Fulufhelo James Masithulela**, hereby declare that the work on which this thesis is based is my original work (except where acknowledgements indicate otherwise) and that neither the whole work nor any part of it has been, is being, or is to be submitted for another degree in this or any other university. I empower the university to reproduce for the purpose of research either the whole or any portion of the contents in any manner whatsoever.

Signature:

Signed

Date: 8th of February 2016

Curriculum Vitae

Fulufhelo James Masithulela (“Fulu”) was born on 16 May 1981 in Phadzima-Dzumbathoho Village, Nzhelele, Venda, Limpopo Province, South Africa, to his parents Vho-Ailwei Joseph and Alinah Pinkie Tserengoa-Masithulela. Fulu's earliest and favourite memories are of harvesting crops with his family during the summer and fall seasons and this led him to pursue biomedical engineering.

He completed his grade 12 at Humbelani Senior Secondary School with full matric exemption. In December 2006, Fulu received his Bachelor of Science degree in Mechanical Engineering from the Department of Mechanical, Industrial and Aeronautical Engineering, Faculty of Engineering at the University of the Witwatersrand, Johannesburg. In the following year, Fulu enrolled as a Master's student in the same department. He soon began his Master's research with Dr. Ionel Botef, which culminated in a dissertation on the use of finite element methods for the design and modelling of a friction stir welding machine. Fulu's interest in academic research then steered him to pursue a doctorate from the Department of Cardiothoracic Surgery of the University of Cape Town in December 2010. Fulufhelo is currently a senior lecturer in the college of science, engineering and technology, school of engineering, department of mechanical and industrial engineering at the University of South Africa, in South Africa.

Fulufhelo has presented this work at national and international conferences:

[1] Masithulela F, Davies NH, Sharp S-K, Saleh MG, Spottiswoode BS, Meintjes EM, Zilla P, Franz T. *Rat Heart Left and Right Ventricle 3D Geometrical Reconstruction and Validation using 3T Magnetic Resonance Imaging*. CHPC National Meeting 2011: Better HPC and Data-curation Adoption, Better Research and Industrial Development, Dec 7-9, 2011, Pretoria, South Africa.

[2] Masithulela F, Davies NH, Sharp S-K, Saleh MG, Spottiswoode BS, Meintjes EM, Zilla P, Franz T. *Rat Heart Ventricle 3D Geometrical Reconstruction - Towards Understanding of Cardiac Mechanics in Myocardial Infarction*. ICMB 2012 - International Conference on Medical Information and Bioengineering, Mar 24-25, 2012, Shenzhen, China.

[3] Masithulela F, L Dubuis, Davies NH, Franz T. *Finite element analysis of the infarcted remodelling rat heart during diastolic filling*. South African Biomedical Engineering and Technology Conference, April 1-4, 2014, Stellenbosch, South Africa.

[4] Masithulela F, Dubuis L, Davies NH, Franz T. *Finite element analysis of the infarcted remodelling rat heart at end-systole*. CHPC National Meeting 2014: CHPC National meeting,

Towards an Energy Efficient HPC System, Dec 1-5, 2014, Kruger National Park, Mpumalanga, South Africa.

[5] Masithulela F, Dubuis L, Davies NH, Franz T. *Finite element analysis of Passive filling in a Rat Heart with Fibrotic Myocardial Infarction*. ASME 2015 International Mechanical Engineering Congress & Exposition, Nov 13-9, 2015, Houston, USA

[6] Masithulela F, Dubuis L, Davies NH, Franz T. *The effect of over-loaded right ventricle during passive filling in rat heart - a biventricular finite element model*. ASME 2015 International Mechanical Engineering Congress & Exposition, Nov 13-9, 2015, Houston, USA

Furthermore, Fulufhelo is looking forward to additionally publishing the remainder of the work in accredited international journals.

Dedication

To my wife, son, daughter, my parents, my brothers and my sisters who offered me unconditional love and support throughout the course of this thesis.

“Na vheiwe vha matongoni, fola khelo ni dahisane nothe, hu songo vha na ano dzima munwe”

“Dzulani zwavhudi mutwanamba wa ha-tshivhula tsha matshokotika tsha gumbo lo fhelaho nga mipfa, ndi ene wa ha tshinoni tsha pinda vhusiku vha sala vha tshi vhona ngwala lo fhira”

“I rema nga lunwe mbevhana, mulindi u do vhuya wa dala” – Venda proverb

Acknowledgements

My deepest thanks go to Professor Thomas Franz for giving me the opportunity to work with him and introducing me to the fascinating field of computational biomechanics. I thank him for his guidance while working in the computational biomechanics lab. His expertise and enthusiasm regarding nonlinear finite elements and continuum mechanics were inspirational. It has been a great joy to study under his direction and to help extend our understanding of cardiac mechanics. I would like to mention that through Professor Neil Davies's continuing work and experiments in myocardial infarction, this work draws many insights for his work. I also thank Dr Laura Dubuis for her support. It has been a tremendous honour to work with her. I found her to be highly knowledgeable in this area of study. I greatly admire Dr Laura Dubuis's insights and experience and her devotion to helping me with the work presented in this thesis.

I would like to further thank Mazin Sirry, Hugo Krynauw, Renee Miller and Dr. Jeroen Kortsmid who were the fellow PhD, Masters Students and Postdoctoral fellow at Biomechanics and Mechanobiology Lab at the University of Cape Town for their insights and input during my studies. Prof Ernesta M. Meintjes, Dr. Bruce Spottiswoode and Mr. Muhammed Saleh helped in providing the MRI data used in this research work. Thanks goes to Yunfei Shi who is the PhD student at Taber Labs (Mechanics of Morphogenesis) for his encouraging views in the area of constitutive modelling in Abaqus®.

I thank Dr. Greg Mitchell at Finite Element Analysis Services (FEAS (Pty) Ltd). His expertise and attentiveness in modelling and computational methods is beyond compare. Greg's direction and guidance have been essential for my work and I am grateful for his help.

My research was possible through the support of grants from the National Research Foundation of South Africa and the Centre for High Performance Computing. The Central University of Technology also contributed immensely through the SOAR fellowship.

To my wife, son and late daughter, Muthumuni, Mukhethwa and Muneiwa. I thank you all for the support you have given me throughout this study. Without your support this would have been much more difficult to prioritise and complete. To my parents Mr. Joseph Masithulela and Ms. Pinkie Tserengoa, I thank you for everything you have done. Notwithstanding that you are both illiterate, you have instilled a culture of learning and perseverance in me.

To my friends and colleagues at the University of South Africa (UNISA), I am forever grateful for our friendship and support. Special thanks goes to Professor Moses Strydom for his willingness to assist. The greatest thing one can hope to do with his friends is change and be changed. You have definitely impressed upon me a unique enjoyment of life that I will never forget.

Abstract

Cardiovascular diseases account for one third of all deaths worldwide, more than 33% of which are related to ischemic heart disease, including myocardial infarction (MI). This thesis seeks to provide insight and understanding of mechanisms during different stages of MI by utilizing finite element (FE) modelling.

Three-dimensional biventricular rat heart geometries were developed from cardiac magnetic resonance images of a healthy heart and a heart with left ventricular (LV) infarction two weeks and four weeks after infarct induction. From these geometries, FE models were established. To represent the myocardium, a structure-based constitutive model and a rule-based myofibre distribution were developed to simulate both passive mechanics and active contraction.

The ejection fraction for the healthy, two-week infarct and four-week infarct models was found to be 64.9%, 54.6% and 49.5%, respectively. The infarcted region was mainly in the LV and represented 16.2% and 30.3% of the LV wall two-weeks and four-weeks after the infarct induction, respectively. The end-diastolic volume of the infarcted heart at two-week and four-week time point increased by 26.1% and 78.2%, respectively, compared to the healthy heart. Similarly, the end-systolic volume increased by 62.9% and 155.1% for two-week infarct and four-week infarct, respectively.

The stress and strain in the LV free wall infarct region and the non-infarcted septal wall region were assessed in the healthy and infarct cases. In the LV free wall, the end-diastolic (ED) circumferential strain in the two-week infarct and four-week infarct model was 69.5% and 67.7% lower than in the healthy model, respectively, whereas this strain was 62.5% and 100.0% higher, respectively, in two-week infarct and four-week infarct case compared to the healthy case in the septal wall. At end-systole (ES), the circumferential strain of the two-week and four-week infarct model was 97.1% and 93.3% lower, respectively, in the free wall, and 24.3% and 30.7% lower, respectively, in the septal wall, when compared to the healthy control. In the LV free wall infarct region, circumferential stress in the two-week infarct and four-week infarct was 74.2% and 91.1% higher, respectively, than in the healthy control at ED but 83.9% and 54.3% lower, respectively, than in the healthy control at ES. In the septal wall, ED circumferential stress in the two-week infarct and four-week infarct model exceeded the stress in the healthy heart by 94.5% and 188.6%, respectively, but was 63.9% and 68.1% lower, respectively, at ES.

This study assisted in the development of computational tools for the assessment of cardiac mechanics involved in the progression of MI. The outcomes will be beneficial in the advancement of therapy concepts for MI and their translation into clinical application.

Table of Contents

Declaration.....	i
Curriculum Vitae	ii
Dedication.....	iv
Acknowledgements.....	v
Abstract	vii
Table of Contents.....	x
List of Figures	xiii
Abbreviations	xxii
Nomenclature	xxiv
1 Introduction.....	1
1.1 Background and Significance.....	1
1.2 Problem Identification	2
1.3 Aim and Objectives	3
1.4 Thesis Outline.....	5
2 Theory and Literature Review	7
2.1 Anatomy and Physiology of the Heart	7
2.1.1 Anatomy of the heart.....	7
2.1.2 Physiology of the heart	11
2.1.3 Cardiac functional parameters	13
2.1.4 Physiology of rat heart	15
2.2 Myocardial Infarction of the Heart.....	18
2.3 Myocardial Mechanics of the Heart.....	20
2.4 Basic Continuum Mechanics.....	21
2.4.1 General formation	21
2.4.2 Kinetics	23
2.4.3 Strain	25
2.4.4 Distortional change	26
2.4.5 Cauchy stress tensor	27
2.4.6 Principle of virtual work	28
2.4.7 Alternative stress representations	29
2.4.8 Finite element implementation Fung model.....	31
2.4.9 Finite element modelling	34
2.5 Computational Cardiac Biomechanics Modelling of Healthy Heart	35
2.5.1 Cardiac modelling software.....	39

2.5.2	Reconstruction of cardiac geometries	39
2.5.3	Modelling myofibre orientation	40
2.5.4	Mathematical representation of fibre orientation.....	45
2.5.5	Cardiac constitutive models	46
2.6	Modelling the Infarct.....	47
3	Simulation of Passive Filling in Healthy and Infarcted Hearts	50
3.1	Introduction	50
3.2	Materials and Methods.....	50
3.2.1	MRI datasets.....	50
3.2.2	Geometrical reconstruction	51
3.2.3	Geometry verification	53
3.2.4	Tissue structure definition	53
3.2.5	Finite element modelling	56
3.2.6	Data analysis and capturing.....	59
3.3	Results.....	62
3.3.1	Reconstructed biventricular geometries	62
3.3.2	Comparison of models and MRI measurements	67
3.3.3	End-diastolic myocardial mechanics for healthy and infarcted ventricles.....	70
3.3.4	End-diastolic myocardial mechanics in the left-ventricular infarct region and the septal wall.....	87
4	Simulation of Active Contraction in Healthy and Infarcted Hearts.....	106
4.1	Introduction	106
4.2	Materials and Methods.....	106
4.2.1	MRI Dataset.....	106
4.2.2	Geometrical reconstruction	107
4.2.3	Tissue structure definition and implementation of fibre orientation	107
4.2.4	Geometry verification	107
4.2.5	Modelling of infarcted myocardium.....	107
4.2.6	Constitutive model of active myocardium	107
4.2.7	Implementation of the active contraction	109
4.2.8	Boundary conditions	110
4.3	Results.....	112
4.3.1	Reconstructed geometry	112
4.3.2	Comparison of numerical models and MRI measurements	114
4.3.3	Validation of the active contraction code.....	116
4.3.4	Ventricular function	124
4.3.5	End-systolic myocardial mechanics in left and right ventricle	126

4.3.6	End-systolic myocardial mechanics in the LV infarct region and the non-infarcted septal wall.....	135
5	Discussion	154
5.1	Overall Discussion	154
5.2	Development of FEM	156
5.2.1	Geometrical reconstruction of healthy and infarct models	156
5.2.2	Boundary and loading conditions	157
5.2.3	Constitutive law and the active stress model.....	159
5.2.4	Developing the infarct models.....	160
5.3	Validation of the Models.....	161
5.3.1	Implementation of active contraction code	161
5.3.2	Validation of the developed passive and active models	162
5.4	Comparison of Healthy and Infarcted Cases.....	162
5.4.1	Cardiac functional parameters	162
5.4.2	Myocardial stress and strain	164
5.4.3	Review of strains and stress in the septal wall in conjunction with LV dimensions of healthy and infarcted cases.....	176
6	Conclusions and Recommendations.....	179
6.1	Review of Aims and Outcomes of the Research	179
6.2	Novel Aspects of the Presented Study	180
6.3	Recommendations for Further Work	182
6.3.1	Determination of contribution of the infarct in the septal strain and stress	182
6.3.2	Residual stress in reconstructed geometric configuration.....	183
6.3.3	Fibre orientation in the infarcted region.....	183
6.3.4	The effect of blood perfusion.....	183
6.3.5	Development of specific fibre structure	184
6.3.6	Modelling of functional border zone	184
6.3.7	Boundary conditions	184
6.3.8	Structure and Fluid interaction	184
6.3.9	Possible dyssynchrony of the ventricles due to the infarct.....	185
References	186
Appendix A – UMAT subroutine	205
Appendix B – ORIENT Subroutine	206

List of Figures

Figure 2-1: The anterior view of the heart (Katz, 2010).	8
Figure 2-2: The heart frontal section (Katz, 2010)	8
Figure 2-3: The frontal section of the heart (Opie, 2004)	9
Figure 2-4: Microscopic anatomy of cardiac muscle (Opie, 2004)	10
Figure 2-5: The action potential of contractile cardiac muscle cells (Little, 1981).....	11
Figure 2-6: An electrocardiogram (ECG) tracing (Katz, 2010)	11
Figure 2-7: Summary of events during the cardiac cycle (Katz, 2010).....	12
Figure 2-8: EDPVR and ESPVR of the left ventricle of a rat (top –young rats, bottom- aging rats) (Pacher et al., 2004)	15
Figure 2-9: LV Pressure-volume loop (Pacher et al., 2004).	16
Figure 2-10: Schematic diagram of rat (Pacher et al., 2004).	17
Figure 2-11: Dying muscle and sectional view of the human heart. (a) Occluded coronary artery causing a myocardial infarction. Heart sections showing (b) healthy myocardium (c) infarcted myocardium and (d) dilated myocardium (Zhang et al., 2013).	20
Figure 2-12: Temporal course of the phases of healing for various animal model (Holmes et al., 2005).....	20
Figure 2-13: The myocardial motion of the normal heart and conversion used in the study. (a) Myocardial movement in systolic and diastolic phases. (b) Legends of a cardiac cycle. (c) Stress and strain directions.....	21
Figure 2-14: Kinematics of axial truss member in three-dimensional (Bonet, 1997)	22
Figure 2-15: Deformable body in general motion (Bonet, 1997)	23
Figure 2-16: General motion in the neighbourhood of a particle (Bonet, 1997).....	25
Figure 2-17: Distortional component of F (Bonet, 1997)	27
Figure 2-18: Traction vector (Bonet, 1997).....	28
Figure 2-19: Stress components (Bonet, 1997).....	28
Figure 2-20: Principle of virtual work (Bonet, 1997).....	29
Figure 2-21: First Piola-Kirchoff stress tensor (Bonet, 1997)	31
Figure 2-22: Fibre directions generated using Poisson interpolation. (a) Shows fibre directions at three location along the long axis. (b) Showing normal directions at the corresponding slices. Blue colour represents the -70° and red colour represents $+80^\circ$ (Wong and Kuhl, 2014).	40
Figure 2-23: Myofibre orientation and fibre angle definition. (a) Schematic representation of fibre pathways in the left ventricular wall (b) Illustration of the helix fibre angle α_h and	

transverse fibre angle α_t use to quantify muscle fibre orientation (Bovendeerd et al., 2002).	41
Figure 2-24: Schematic of the arrangement of muscle and collagen fibres and the surrounding matrix. (a) structure without loadings; (b) tensile load applied in the muscle fibre direction, showing decreased inter-fibre separation so that the collagen network bears load primarily in the muscle fibre direction; (c) compressive load applied in the muscle fibre direction, showing the muscle fibres buckled and lateral extension of the collagen network (Holzapfel and Ogden, 2009b).....	42
Figure 2-25: Schematic diagram of LV fibre orientation. (a) The left ventricle and a cut-out from equator. (b) The structure through the thickness from the epicardium to the endocardium. (c) Five longitudinal circumferential sections. (d) myocytes and collagen fibres. (e) a cube of layered tissue (Holzapfel and Ogden, 2009a).	43
Figure 2-26: Helix angle of healthy heart. (a) Myofibre orientation of rat heart during systolic phase (Chen et al., 2003b). (b) LV angle variation of rat heart. Helix angle of healthy human heart (c) Myofibre orientation of human heart during diastolic phase. (d) LV angle variation of human heart (Streeter et al., 1969).	44
Figure 2-27: Longitudinal and circumferential stresses during various time points infarction (Holmes et al., 2005).....	49
Figure 3-1: Procedure of creating biomechanical model of the rat heart.....	52
Figure 3-2: Set of short-axis MR images from base to apex of a rat heart at four-week after myocardial infarction. The contours of epicardium and endocardium of both left and right ventricle are highlighted.	52
Figure 3-3: Fibre orientation in the biventricular rat heart model. (b) 3D healthy rat heart model showing nodes, (b) Fibre orientation in the LV of healthy rat heart model (showing how fibre angles are distributed from the endocardium to the epicardium) (c) 3D healthy rat heart model showing fibre angles distribution from the base to the apex and (d) Fibre orientation in the RV of healthy rat heart model.	54
Figure 3-4: Fibre orientation of across the myocardial wall.....	55
Figure 3-5: Boundary conditions at end-diastole. (a) Pressure boundary conditions and displacement constraints using the cylindrical coordinates. (b) Basal surface and (c) Endocardial pressure in LV and RV.	59
Figure 3-6: Paths utilised in further processing of results for (a) two-week infarct and (b) four-week infarct models.	60
Figure 3-7: 3D healthy heart model. (a) Healthy rat heart with both LV and RV (b) Cavity measured volume of healthy LV;.....	61

Figure 3-8: Short axis view taken at the middle of the long axis. (a) Healthy 3D rat heart model (b) Isometric view and Side view (c) Short axis healthy rat heart model. (d) Long axis healthy rat heart model.	63
Figure 3-9: Reconstructed ventricular geometry and heart structure. (a) Pre mesh. (b) Post meshing. (c) The bi-ventricular healthy heart model (d) Basal surface slice cut parallel to the short axis.	64
Figure 3-10: Endocardial view of LV and RV. (a) Healthy rat heart model (b) two-week infarcted and (c) four-week infarct models.....	65
Figure 3-11: Short-axis slice at the mid-ventricle of 3D models. (a) Healthy rat heart model (b) Infarcted after two-week model (c) Infarcted after four-week model. Long-axis slice through the healthy and infarct region of 3D models. 3D models reconstructed models. (d) Healthy rat heart (e) Infarcted after two-week (f) Infarcted after four-week.....	66
Figure 3-12: Undeformed and deformed state of the FE rat heart models. Short-axis slice at the mid-ventricle and long-axis slices through healthy and infarcted myocardium of (a) Healthy long-axis slice, (b) Healthy short-axis slice, (c) two-week infarcted long-axis slice, (d) two-week infarcted short-axis slice, (e) four-week infarcted long-axis slice and (f) four-week infarcted short-axis slice.....	67
Figure 3-13: Contour plots of end-diastolic stress in in the healthy, two-week and four-week infarct models. (a)-(c): Radial stress, (d)-(f):Circumferential stress, and (g)-(i): Longitudinal stress.....	73
Figure 3-14: Contour plots of end-diastolic stress in short axis cross section equidistant between the base and the apex for the healthy, two-week and four-week infarct models. (a)-(c): Radial stress, (d)-(f):Circumferential stress, and (g)-(i): Longitudinal stress.....	74
Figure 3-15: Contour plots of end-diastolic stress in central long axis cross section for the healthy, two-week and four-week infarct models. (a)-(c): Radial stress, (d)-(f):Circumferential stress, and (g)-(i): Longitudinal stress.....	75
Figure 3-16: Contour plots of end-diastolic strain in central long axis cross section and endocardium for the healthy, two-week and four-week infarct models. (a)-(c): Radial strain, (d)-(f):Circumferential strain, and (g)-(i): Longitudinal strain	78
Figure 3-17: Contour plots of end-diastolic strain in short axis cross section equidistant between the base and the apex for the healthy, two-week and four-week infarct models. (a)-(c): Radial strain, (d)-(f): Circumferential strain, and (g)-(i): Longitudinal strain.....	79
Figure 3-18: Contour plots of end-diastolic strain in central long axis cross section for the healthy, two-week and four-week infarct models. (a)-(c): Radial strain, (d)-(f): Circumferential strain, and (g)-(i): Longitudinal strain.....	80
Figure 3-19: Transmural distribution of end-diastolic stress versus normalised myocardial thickness of LV free wall and septal wall for of healthy, two-week and four-week infarct	

models. (a)-(c): Radial stresses, (d)-(f): Circumferential stresses, and (g)-(i): Longitudinal stresses.	84
Figure 3-20: Transmural distribution of end-diastolic strain versus normalised myocardial thickness of LV free wall and septal wall for of healthy, two-week and four-week infarct models. (a)-(c): Radial strain, (d)-(f): Circumferential strain, and (g)-(i): Longitudinal strain.	86
Figure 3-21: Comparison of average end-diastolic stress at paths C, D, E and F at endocardium, mid-wall and epicardium of the healthy, two-week and four-week infarct models. (a)-(c): Radial stress, (d)-(f): Circumferential stress, and (g)-(i) Longitudinal stress.	88
Figure 3-22: Comparison of average end-diastolic strain at paths C, D, E and F at endocardium, mid-wall and epicardium of the healthy, two-week and four-week infarct models. (a)-(c): Radial strain, (d)-(f): Circumferential strain, and (g)-(i) Longitudinal strain	90
Figure 3-23: Comparison of average end-diastolic stress at paths I, J, K and L at endocardium, mid-wall and epicardium of the healthy, two-week and four-week infarct models. (a)-(c): Radial stress, (d)-(f): Circumferential stress, and (g)-(i) Longitudinal stress.	93
Figure 3-24: Comparison of average end-diastolic strain at paths I, J, K and L at endocardium, mid-wall and epicardium of the healthy, two-week and four-week infarct models. (a)-(c): Radial strain, (d)-(f): Circumferential strain, and (g)-(i) Longitudinal strain	96
Figure 3-25: End-diastolic stress for healthy, two-week and four-week infarct models. Average radial (a), circumferential (b) and longitudinal (c) stress at paths C, D, E and F. Average radial (d), circumferential (e) and longitudinal (f) stress at paths I, J, K and L.	101
Figure 3-26: End-diastolic strain for healthy, two-week and four-week infarct models. Average radial (a), circumferential (b) and longitudinal (c) strain at paths C, D, E and F. Average radial (d), circumferential (e) and longitudinal (f) strain at paths I, J, K and L.	105
Figure 4-1: Boundary conditions at ES. (a) Basal surface and (b) Endocardial pressure applied on LV and RV.	111
Figure 4-2: The pressure wave form of the left and right ventricle against time (Guccione et al., 1993b).....	111
Figure 4-3: (a) Sectional view and (b) 3D model of the two-week infarct model. (c) Sectional view and (d) 3D reconstructed bi-ventricular model of a four-week infarct rat heart	

model. Green and white colours represent healthy and infarcted tissues, respectively.	113
Figure 4-4: Meshed smoothed and calibrated end-systolic 3D rat heart geometries. (a) Healthy model, (b) two-week infarct model, and (c) four-week infarct model. Green and white colours represent healthy and infarcted tissues, respectively.....	114
Figure 4-5: Finite element models at end-systole. (a) Healthy model, (b) two-week infarct model, and (c) four-week infarct model.	114
Figure 4-6: Uniaxial test loading and boundary conditions	117
Figure 4-7: Stress vs. strain of uniaxial test in Z, Y and X directions. (a) along Z-direction and (b) along Y – direction and (c) uniaxial test along X– direction	118
Figure 4-8: Eqi-biaxial test loading and boundary conditions.....	119
Figure 4-9: Stress vs. strain of uniaxial test along X and Y directions.....	120
Figure 4-10: Shear test loading and boundary conditions.....	120
Figure 4-11: Stress vs. strain in the S11 and S12 directions	121
Figure 4-12: Active contraction of one element (a): $T_{max} = 0.3714$ kPa, (b): $T_{max} = 0.2714$ kPa, (c): $T_{max} = 0.1357$ kPa	122
Figure 4-13: Active contraction of one element strain contours (a): $T_{max} = 0.3714$ kPa, (b): $T_{max} = 0.2714$ kPa, (c): $T_{max} = 0.1357$ kPa.....	123
Figure 4-14: EDV and ESV for healthy, two-week infarct and four-week infarct models.	125
Figure 4-15: Stroke volume for each model.....	125
Figure 4-16: Ejection fraction for healthy, two-week and four-week infarct models.....	125
Figure 4-17: The effects of large infarcts on diastolic and systolic (EDPVR and ESPVR) pressure-volume relationship.	126
Figure 4-18: Contractility of healthy, two-week and four-week infarct models.....	126
Figure 4-19: Contour plots of end-systolic strains in a central long axis cross-section and endocardium of healthy, two-week and four-week infarct models. (a)-(c): Radial strains. (d)-(f): Circumferential strains. (g)-(i): Longitudinal strains.....	128
Figure 4-20: Contour plots of end-systolic strains on the short-axis cross-section equidistant between the base and the apex of the healthy, two-week and four-week infarct models. (a)-(c): Radial strains. (d)-(f): Circumferential strains. (g)-(i): Longitudinal strains.....	129
Figure 4-21: Contour plots of end-systolic strains in the central long axis cross section of the healthy, two-week and four-week infarct models. (a)-(c): Radial strains. (d)-(f): Circumferential strains. (g)-(i): Longitudinal strains.	130
Figure 4-22: Transmural distribution of end-systolic stresses as function of normalised myocardial thickness of LV free wall and septal wall for of healthy, two-week and four-week infarct models. (a)-(c): Radial stresses, (d)-(f): Circumferential stresses, and (g)-(i): Longitudinal stresses. (Paths C, D, E and F: red; paths I, J, K and L: blue.)	132

Figure 4-23: Transmural distribution of end-systolic strains as function of normalised myocardial thickness in LV free wall and septal wall for healthy, two-week and four-week infarct models. (a)-(c): Radial stresses, (d)-(f): Circumferential stresses, and (g)-(i): Longitudinal stresses. (Paths C, D, E and F: red; paths I, J, K and L: blue.)	134
Figure 4-24: Comparison of end-systolic stresses at endocardium, mid-wall and epicardium in regions C, D, E and F of the healthy, two-week and four-week infarct models. (a)-(c): Radial stresses, (d)-(f): Circumferential stresses, and (g)-(i) Longitudinal stresses. ..	137
Figure 4-25: Comparison of end-systolic strains at endocardium, mid-wall and epicardium in regions C, D, E and F of the healthy, two-week and four-week infarct models: (a)-(c): Radial strains, (d)-(f): Circumferential strains, and (g)-(i): Longitudinal strains.....	139
Figure 4-26: Comparison of stresses in Epicardium, Mid-wall and Endocardium at ES in IJKL region. (a), (b) and (c) represents the radial stresses of the healthy, two-week and four-week infarct models, respectively; (d)-(f) represents the circumferential stresses of the healthy, two-week and four-week infarct models, respectively and (g)-(i) represents the longitudinal stresses of the healthy, two-week and four-week infarct models, respectively.....	142
Figure 4-27: Comparison of strains in Epicardium, Mid-wall and Endocardium at ES in IJKL region. (a), (b) and (c) represents the radial stresses of the healthy, two-week and four-week infarct models respectively; (d)-(f) represents the circumferential stresses of the healthy, two-week and four-week, infarct models, respectively and (g)-(i) represents the longitudinal stresses of the healthy, two-week and four-week infarct models, respectively.....	145
Figure 4-28: End-systolic stress for healthy, two-week and four-week infarct models. Average radial (a), circumferential (b) and longitudinal (c) stress at paths C, D, E and F. Average radial (d), circumferential (e) and longitudinal (f) stress at paths I, J, K and L.	149
Figure 4-29: End-systolic strain for healthy, two-week and four-week infarct models. Average radial (a), circumferential (b) and longitudinal (c) strain at paths C, D, E and F. Average radial (d), circumferential (e) and longitudinal (f) strain at paths I, J, K and L.	153
<i>Figure 5-1: Average radial, circumferential and longitudinal strains during passive filling simulation in (a) free wall paths C, D, E and F and (b) septal wall paths I, J, K and L.</i>	168
<i>Figure 5-2: Average radial, circumferential and longitudinal stresses at end-diastole along (a) paths C, D, E and F in the free wall infarct region and (b) paths I, J, K and L in the septal wall.</i>	171

Figure 5-3: Average radial, circumferential and longitudinal strains during active contraction simulation along (a) paths C, D, E and F in the free wall and (b) paths I, J, K and L in the septal wall. 173

Figure 5-4: Average stresses during active contraction along (a) paths at C, D, E and F in the free wall and (b) paths I, J, K and L in the septal wall. 175

Figure 5-5: Strain range in the septal wall in (a) radial, (b) circumferential and (c) longitudinal direction. 178

Figure 5-6: Stress range in the septal wall in (a) radial, (b) circumferential and (c) longitudinal direction. 178

List of Tables

Table 2-1: Comparison of Biological Parameters in the Human and Rat (Brau et al., 2004).	17
Table 2-2: Quantitative assessment of the GHM fits for rat heart DT-MRI datasets (Savadjiev et al., 2012a).....	46
Table 3-1: Constitutive model parameters for passive LV and RV heart model (Omens et al., 1993).	57
Table 3-2: Stress scaling coefficients for healthy and infarcted (two-week and four-week after) rat heart models.....	58
Table 3-3: Geometrical physical dimensions at end-diastole	63
Table 3-4: Comparison of reconstructed heart geometries - cavity and wall volumes and cavity area of LV for healthy, two-week and four-week infarct models.....	69
Table 3-5: Comparison of MRI heart geometries - cavity and wall volumes and cavity area of LV for healthy, two-week and four-week infarct models.....	69
Table 3-6: Comparison of error for MRI data and 3D reconstructed heart geometries.....	69
Table 3-7: Model verification of healthy, two-week and four-week infarct models.....	70
Table 3-8: Comparison of cavity volumes for healthy, two-week and four-week infarct models at ED.....	70
Table 3-9: ESV and EDV of left and right ventricle predicted for healthy model.....	70
Table 4-1: Parameters used in the active contraction model (Guccione et al., 1963b).....	109
Table 4-2: Geometrical dimensions at ES	112
Table 4-3: Comparison of LV cavity volumes obtained from reconstructed models and MRI	115
Table 4-4: Comparison of epicardial volume during ES of RV	115
Table 4-5: Comparison of wall volume of the heart during ES	116
Table 4-6: Comparison of wall area of the heart during ES	116
Table 4-7: Comparison of endocardial area of LV and RV during ES	116
Table 4-8: Constitutive model parameters for validation of active contraction code (Omens et al., 1993).....	117
Table 4-9: Boundary conditions of uniaxial test in single hex element (along x-direction)..	117
Table 4-10: Boundary conditions of biaxial test in single hex element (along x-direction)..	119
Table 4-11: Boundary conditions of shear test in single hex element (along x-direction)...	121
Table 4-12: Validation of active stress model.....	122
Table 4-13: Validation of active maximum strain model.....	123
Table 4-14: Validation of active minimum strain model.....	123

<i>Table 5-1: Difference of average strain in the LV free wall (infarct region) for different models at end-diastole</i>	169
<i>Table 5-2: Difference of average strain in the septal wall for different models at end-diastole</i>	169
<i>Table 5-3: Difference of average stress in the free wall (Infarct region) for different models at end-diastole</i>	171
<i>Table 5-4: Difference of average stress in the septal wall for different models at end-diastole</i>	171
<i>Table 5-5: Difference of average strain in the LV free wall (infarct region) for different models at end-systole</i>	174
<i>Table 5-6: Difference of average strain in the septal wall for different models at end-systole</i>	174
<i>Table 5-7: Difference of average stress in the LV free wall (infarct region) for different models at end-systole</i>	176
<i>Table 5-8: Difference of average stress in the LV septal wall for different models at end-systole</i>	176
Table 5-9. Infarct sizes, LV volumes and functional parameters, as well as ED and ES values and ranges of strains and stresses in septal wall for healthy, 2-week infarct and 4-week infarct cases and comparison between cases.....	177

Abbreviations

2D	Two dimensional
3D	Three dimensional
AI	Acute infarct
API	Application programming interface
CMRI	Cardiac magnetic resonance imaging CO Cardiac output
CUBIC	Cape Universities Brain Imaging Centre
CVD	Cardiovascular disease
DED	End-diastolic diameter
DES	End-systolic diameters
ED	End-diastolic
EDP	End-diastolic pressure
EDPVR	End-diastolic pressure volume relationship
EDV	End diastolic volume
EF	Ejection fraction
Endo	Endocardium
Epi	Epicardium
ES	End systolic
ESP	End systolic pressure
ESPVR	End-systolic pressure volume relationship
ESV	End systolic volume
FE	Finite element
FEA	Finite element analysis
FEM	Finite element method
FI	Fibrotic infarct
FS	Fractional shortening
GE	Gradient Echo
GHH	Generalised helicoid model
HA	Heart attack
HF	Heart failure
HIV/AIDS	Acquired immunodeficiency syndrome
HR	Heart rate
IGES	Initial graphics exchange specification
LV	Left ventricle
LVM	Left ventricular mass
MI	Myocardial infarction

MRI	Magnetic resonance imaging
ORIENT	Material orientation user subroutine
SED	End-systolic diameter
SV	Stroke volume
UMAT	User material subroutine
WHO	World Health Organisation

Nomenclature

λ	Stretch ratio
A, a	Cross-sectional area
b	Time intercept of linear relaxation duration-sarcomere length relation
B	Governs the shape of peak isometric tension-sarcomere length relation
\mathbf{B}	Left Cauchy-Green deformation tensor
Ca_o	Peak intracellular calcium concentration
$(Ca_o)_{\max}$	Maximum peak intracellular calcium concentration
$C1, D1$	Material constants on Fung model
\mathbf{C}	Right Cauchy-Green deformation tensor, spatial tensor of elasticity
C_t	Internal variable
C_v	Force-velocity function
dev	Deviator
ε	Engineering strain
$\varepsilon_{11}, \varepsilon_{22}, \varepsilon_{33}$	Principal engineering v
\mathbf{E}	Green's material tensor
$E_{Ca_{50}}$	The length-dependent calcium sensitivity
\mathbf{F}	Deformation gradient
g	Distance from the endocardium
h_o	Left ventricle wall thickness
\mathbf{I}	Fourth and second order identity tensor
l_o	Sarcomere length at which no activation tension develops
l_R	The stress free sarcomere length
J	Jacobian, elastic volume ratio
L, l	Length
m	Slope of linear relaxation duration-sarcomere length relation
n	Unit vector
σ	Cauchy (true) stress
$\sigma_{11}, \sigma_{22}, \sigma_{33}$	Principal stress
ρ	Density
\mathbf{P}	First Piola-Kirchhoff tensor
R	Maximum fibre angle
\mathbf{S}	Second Piola-Kirchhoff tensor
τ, τ^o	Kirchhoff stress
T	Internal force
T_o	Isometric tension development

t	Time after onset of contraction
t	Time
t_0	Time-to-peak tension
T_{\max}	Isometric tension under maximal activation
t_r	A linear function of sarcomere length
V, v	Volume
W	Virtual work, Strain energy function
δW_{int}	Virtual work, Strain energy function
X	Initial undeformed position
x_a, x_b	Deformed position

1 Introduction

1.1 Background and Significance

The heart is regarded as an electro-mechanical pump with complex mechanical behaviour. Its primary function is to pump blood throughout the body, delivering nutrients and oxygen, and removing wastes from organs. The mechanical behaviour plays an important role in the heart function (Nash and Hunter, 2000). One of the important goals of cardiac mechanics research is to gain an understanding of tissue properties and how changes in tissue structure and properties affect the pumping function of the heart. The integration of structural constitutive laws, specimen-specific geometry and physiological boundary conditions can be achieved by computational modelling (Vetter and McCulloch, 2000). Magnetic resonance imaging (MRI) measured *in-vivo* data of the heart can be used to reconstruct the 3D models of healthy and infarcted hearts. Understanding of the regional mechanics of the heart plays an important role in understanding and improving the heart function after myocardial infarction. Once the understanding is achieved several therapies can be pursued. The most pursued therapy of myocardial infarction is cellular transplantation into the damaged tissue with the aim of improving the regional and global heart function (Nguyen et al., 2010, Wang et al., 2010a, Yoon et al., 2009). Generally, the injection of biomaterials (hydrogel) into the infarct region can potentially lead to change in geometry of the ventricle and can ultimately change the cardiac mechanics by reducing elevated wall stresses (Jiang *et al.*, 2009; Kortsmitt *et al.*, 2012; Kortsmitt *et al.*, 2013; Miller *et al.*, 2013; Wang *et al.*, 2009). Cardiovascular magnetic resonance (CMR) and finite element methods (FEM) (Kerckhoffs et al., 2006, Usyk et al., 2002) can be used to assess the short-term mechanical effects of non-treated tissue and treated tissue by injecting biomaterial hydrogel into the infarct zone after myocardial infarction (Fieno *et al.*, 2000; Gerber *et al.*, 2002; Leor *et al.*, 2009; Munroe *et al.*, 1961; Wagner et al., 2003).

In attempting to understand the mechanical effects of extracellular matrix injection into an infarct area, the following hypotheses may be tested; (i) cardiac mechanics can be altered significantly by the change in left ventricular volume; (ii) stiffness and location of extracellular matrix can influence both the regional and global function of the heart after myocardial infarction; (iii) the timing of extracellular matrix injection into the infarct can influence and improve cardiac function.

The transmural stress and strain distributions in the healthy and infarcted myocardium play an important role in the global and local functioning of the heart. The remodelling of the

myocardium is greatly influenced by the ventricular wall stresses and strains. Various experiments were conducted in measuring the strains of the healthy myocardium based on arrested hearts of several species. These experiments were done mainly by measuring the displacements of the heart wall by spaced markers that are implanted in the myocardium. The direct measurement of local strains using spaced markers is not reliable. The mathematical modelling based on the conservation laws of continuum mechanics becomes an alternative method of measuring the wall stress (Monroe and French, 1961).

MRI has been used in clinical applications for more than 25 years and has played a major role in the field of cardiovascular imaging (Heatlie and Pointon, 2004). Among many other modalities, cardiovascular magnetic resonance has not only become a robust modality but has also attracted many students and researchers to improve in coil technology, pulse sequence design and scanner hardware. Additionally, MRI has become the common tool to assess physiology and function in congenital heart disease (Fogel, 2000). When compared with other modalities, MRI has a unique characteristic because tissue characteristics of the selected organ can be investigated by selecting different pulse sequences.

1.2 Problem Identification

Cardiovascular disease (CVD) is the leading cause of death in low income and middle income countries. In Sub-Saharan Africa CVD is the highest cause of death due to the high prevalence of HIV/AIDS and hypertension. This exists in areas where the healthcare resources are already overburdened. In South Africa more than a third of deaths of people who are over 65 years are attributed to CVD (Bradshaw et al., 2003, Steyn et al., 1992, Steyn et al., 1997, Steyn et al., 2005, Sliwa et al., 2008). In America approximately 565,000 of the population experience a new myocardial infarction every year and 75 % of men and 65 % of women survive only one year. Similarly, according to the world health organisation (WHO), cardiovascular disease is estimated to kill 17.3 million people worldwide every year. 80 % of the deaths are said to be occurring in low and middle income countries. It is estimated that in 2030, 23.3 million people will die of cardiovascular disease. In addition, this heart disease contributes to nearly one third of deaths globally (Holmes et al., 2005). Moreover, about 50 % of Americans experience repeated myocardial infarction every year. Furthermore, the clinical cardiology tends to focus on the management of healing or healed infarcts. Therefore, much progress has been achieved by pharmacological therapies to prevent or limit left ventricle remodelling which can prevent progression to dilated heart failure (Holmes et al., 2005). While this has been achieved by mainly *ex-vivo* experiments,

there is a need to further develop the computational models which will assist in further understanding the mechanisms of the infarcted tissue.

At the present time, more dramatic therapies are in further development phase, namely the direct injection of stem cell into the healing infarct and tissue-engineered replacement patches of myocardium. However, most of these therapies are not developed from an understanding of the mechanical properties of the healing infarct, but rather from a trial and error type method. While there have been some dramatic successes, poor understanding of mechanical properties of the infarct, due to the trial and error methods of some of these therapies, has resulted in some catastrophic failures. An example of these failures was a dramatic increase in infarct size following administration of high dose steroid during the trial of postinfarction steroid therapy. This therapy was based on the preliminary evidence that the steroid administration limits postinfarction necrosis (Holmes et al., 2005, McCulloch and Mazhari, 2001).

Cardiac biomechanics depends on various cardiac phases and may be distorted by a variety of cardiac disorders. Even though the strain distribution can be measured experimentally and clinically by MRI, computational models can be used to measure the regional wall stress. By combining both the computational methods (Finite Element Modelling (FEM)) and experimental methods (MRI) a clear understanding of cardiac mechanic under conditions such as myocardial infarction may be achieved (McCulloch and Mazhari, 2001).

This research project, therefore, has two primary goals. The first goal of the project is to utilise the MRI experimental data to create 3D heart models to assist in providing further insights by study of cardiac mechanics after treated and non-treated myocardial infarction. The second goal is to use the MRI experimental data and/or outcome to validate and verify the developed computational models of non-treated and treated myocardial infarction (MI) of rats.

1.3 Aim and Objectives

Remodelling is one of the main important features and determinants of cardiac heart failure. Remodelling takes place after the heart undergoes or is subjected to myocardial infarction. Remodelling can manifest itself in two ways, first, the thickening of the ventricular wall due to an overloading of pressure, and second, the dilation of the ventricles due to the overloading of volume. The main aim of this research is to study the cardiac mechanics of rat heart post myocardial infarction. This will assist in providing a clearer understanding of the

biomechanical mechanisms associated with myocardial infarction. Therefore, the study of myocardial deformations is important in order to understand the mechanisms underlying cardiac dysfunction. Biomechanical computational models are created to study and provide insight into the cardiac mechanics of the infarcted or failing heart. This thesis seeks to provide insight and understanding of biomechanical mechanisms during different stages of heart failure by utilising FE modelling. The contribution of this work is in theoretical and practical aspects of healthy and infarcted tissue modelling.

The aim of this research project is to study the effects of myocardial infarction (MI) on myocardial stresses, strains and cardiac function of an infarcted left ventricle (LV) during different stages. This study includes determining the relationship between the infarct size and the corresponding wall/myocardial mechanics and ventricular mechanics. The ventricular mechanics of remodelling rat heart is achieved by studying the effect of cardiac function after myocardial infarction. The global functioning of the remodelling rat heart is achieved by studying the following parameters: contractility; stroke volume (SV); and ejection fraction (EF). Furthermore, the wall mechanics during remodelling of rat heart is achieved by studying myocardial transmural stresses and strains.

The main aim is achieved by developing computational models using commercial software Abaqus® to simulate passive filling and active contraction of the rat heart based on specific MRI data. The project will draw mainly on the disciplines of mechanical and biomedical engineering, but will employ a multi-disciplinary research approach which will include a polymer/materials science, human biology collaboration.

In this study, the focus will be drawn to the study of wall/myocardial and ventricular mechanics during remodelling rat heart.

The specific objectives of the project are to:

- 1) Use the *in vivo* experimental results to create 3D computational models of non-treated myocardial infarction in order to study the mechanisms of myocardial infarction;
- 2) Perform *in vivo* studies on non-treated myocardial infarction using MRI for rats;
- 3) Utilise computational models to study structural cardiac parameters;
- 4) Study the myocardial and cardiac mechanics of rats with myocardial infarct at selected time points after infarction (e.g. 0, two-week, four-week) at end-diastole;
- 5) Study the myocardial and cardiac mechanics of rats with myocardial infarct at selected time points after infarction (e.g. 0, two-week, four-week) at end-systole;

- 6) Implement the active contraction model in Abaqus® to be used for simulating the systolic phases of the healthy and infarct models;
- 7) Study the mechanisms of healthy and infarcted myocardium by analysing the resulting stresses and strains during systolic and diastolic phases.

1.4 Thesis Outline

In this thesis special emphasis is given to the stresses and strains distribution in three directions, namely, radial, circumferential and longitudinal at end-diastole and active contraction phases. This is done to gain an understanding of the mechanisms of non-treated myocardial infarction in three time points, zero, two and four-week after infarction of the rat heart.

Chapter 2 includes physiological, anatomical and material characteristics of the soft tissue. The cardiac mechanics play an important role in understanding the performance of the heart. Various researchers presented their thoughts on how MI can be modelled. Several ideas have been gathered from different sources on how the MI can best be modelled. It is understood that MI affects heart functions. In this chapter, the global functions of the heart are also discussed. There is a brief discussion on how MRI is applied in heart modelling. The application of a conventional MRI machine into small animals is deliberated. Various ways of modelling the myofibre orientation are also discussed. This is to ensure that the correct methodology is implemented in analysing stresses and strains in the heart walls. Lastly, the methodologies on how the 3D models of healthy and infarcted hearts are reconstructed are discussed in detail.

In Chapter 3, the basic continuum mechanics foundation needed in implementing the correct constitutive models in Abaqus® are covered. This has been achieved by firstly defining the deformation gradient, distortional change and strain. The Cauchy stress model is useful in continuum mechanics of the soft tissue and its application has been discussed in detail. Chapter 3 shows the methodology and results of simulation on healthy and infarcted hearts after two and four-week at end-diastole phase. The results are shown in terms of contour plots of stresses and strains in different directions. Stresses and strains at different regions of the LV were extracted and tabulated for comparison purposes. In this chapter, the 3D models validation and verification is performed. The validation was achieved by measuring the LV volume and area of the MRI data and the 3D constructed model.

Chapter 4 deals with the simulation at end-systole in healthy and infarcted hearts. Active contraction depends heavily on the myofibre orientation on the heart wall. The mathematical representation of fibre orientation was also investigated and tabulated. The implementation of myofibre orientation was achieved with the ORIENT subroutine. In addition, Chapter 4 deals with the implementation of the active myocardium. The Fung model was used to define the behaviour of soft tissue at end-diastole phase. In this chapter the validation and verification of the UMAT subroutine is discussed by using a single element using three tests: uniaxial, biaxial and shear. *This chapter also deals with the validation and verification of active contraction models implemented in Abaqus® using a UMAT subroutine.* Validation of results of the active model are presented in this chapter. All constants used in simulating both passive filling and active contraction of the healthy and infarcted hearts are tabulated.

Chapter 5 addresses the general discussions based on the methodology used in the generation of the geometry of the 3D heart models. The constitutive law and its applicability in the use of soft tissue at end-systole and passive filling phases are discussed. In this chapter, the development and limitations of the infarct models are discussed in detail. At the end, the limitations and recommendations, and the significance of this work, are discussed.

Chapter 6, summarises the contribution of this work, together with proposed further development for the future.

2 Theory and Literature Review

2.1 Anatomy and Physiology of the Heart

2.1.1 Anatomy of the heart

The human heart is described as being the size of the fist, hollow and cone shaped and having a mass of between 250 and 350 grams. By contrast the rat heart is viewed as the size of a thumb and it weighs between 0.130 and 0.250 grams. The average base length of the rat heart is 21 mm (most are between 20 and 23 mm), average external width of the heart is 13 mm (most between 13 and 15 mm), average thickness of the external wall of left ventricle is 3 mm (most between 2.5 and 3 mm), average width of the left ventricle is 3.85 mm (most between 3 and 4 mm) and the average body length is 223 mm.[p

The heart is covered and protected by a double-walled sac called the pericardium. The function of the fibrous pericardium (the tough and dense connective tissue layer) is to protect the heart, isolate the heart from surrounding structures, and ultimately prevent the heart from over-filling with blood. As shown in Figure 2-1, the second layer of pericardium is called serous pericardium. This is a thin and two-layered membrane whose overall function is to strengthen the protection of the heart. The parietal layer of the serous pericardium lines the internal surface of the fibrous membrane. The most integral part of the heart wall is called the visceral layer (epicardium). The heart wall is defined as the combination of epicardium, myocardium and the endocardium. The film of serous fluid between the parietal and visceral layers is called the pericardial cavity. The serous membranes are lubricated by fluid and have the ability to slide smoothly against each other during the movement of the heart. This allows the healthy heart to work in a frictionless environment.

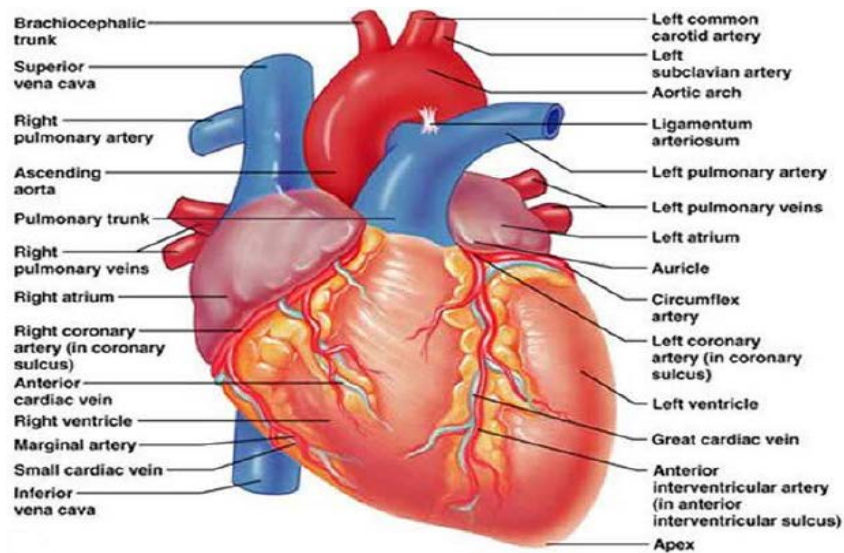


Figure 2-1: The anterior view of the heart (Katz, 2010).

The heart is composed mostly of myocardium (see Figure 2-2). This middle layer called myocardium has the ability to contract and expand and is mainly composed of cardiac muscle. The layers in myocardium are tethered to each other by crisscrossing connective tissue fibres. As shown in Figure 2-2, the muscle (myocardium) is arranged in circular bundles linking all parts of the heart together. The muscle fibres are reinforced and anchored by the fibrous skeleton of the heart. The dense network of collagen and elastic fibres' thicknesses vary from one area to the other. The connective tissue fibres are essential in a heart because they provide additional support around the tissue valves. The support is needed because without it the vessels and valves might be over stretched by the continuous pressure of blood flowing through.

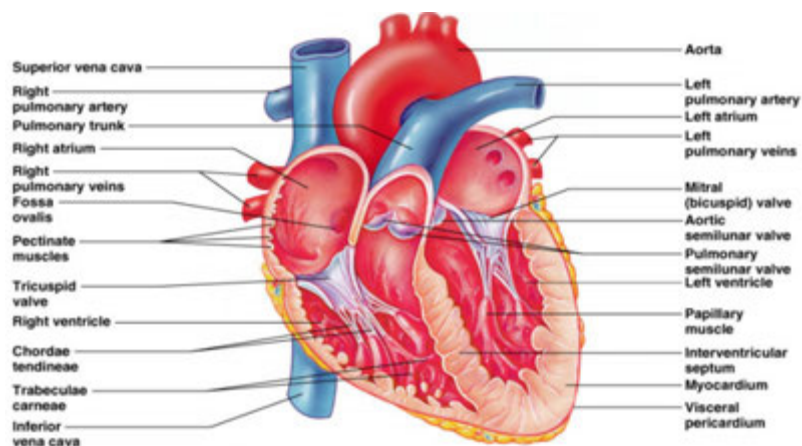


Figure 2-2: The heart frontal section (Katz, 2010)

The heart consists of four chambers, namely: two superior atria and two inferior ventricles. The heart is longitudinally portioned by the inter-atrial septum. In addition, the ventricles are

separated by the inter-ventricular septum. The left ventricle controls the inferoposterior aspect of the heart and forms the heart apex. The heart consists of grooves that function as a carrier for supplying blood vessels to the myocardium.

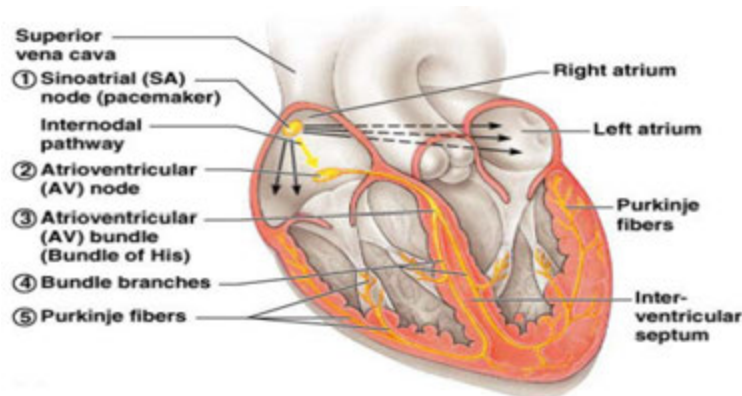


Figure 2-3: The frontal section of the heart (Opie, 2004)

Artioventricle are wrinkled, protruding appendages. Their function is to increase the atrial volume. The right atrium consists of two basic parts, namely; a smoothed-wall posterior part and an anterior portion. The main function of atria is to act as receiving chambers for blood circulation in the heart. The atria only push blood to ventricles and as such contract little. Furthermore, unlike ventricles, atria are known to contribute minimally to the pumping function of the heart. The blood enters the right atrium through three veins: namely: (i) superior vena cava; (ii) the inferior vena cava; and (iii) the coronary sinus. The coronary sinus collects blood draining from the myocardium. Most of the heart base is made out of four pulmonary veins. The main function of the pulmonary veins is to transport blood from the lungs to the heart. Figure 2-3 shows the frontal section of the human heart.

Ventricles are understood to make up most of the heart. Trabeculate carneae are irregular ridges of muscles that are found in the interior of ventricular chambers. The papillary muscles are cone shaped and bundled and play a role in valve function. It is understood that ventricles form part of the heart pumping function. The blood is pushed out from the heart when the ventricles contract. The function of the pulmonary trunk is to direct the blood to the lungs where the blood receives a gas exchange. The right ventricle pumps blood in the pulmonary trunk while the left ventricle ejects blood into the largest artery in the body called the aorta.

The heart is known to have side-by-side pumps, each serving a separate blood circuit. The pulmonary circuit is formed by blood vessels that carry blood to and from the lungs for gas

exchange. The systemic circuit is responsible for carrying blood from and to all body tissues. The blood returning from the body suffers oxygen depletion. This indicates that the returning blood has more carbon dioxide. For the purpose of cleaning, this blood then enters the right atrium and passes into the right ventricle, which pumps it to the lungs through the pulmonary trunk. Through this process the blood then absorbs oxygen and unloads carbon dioxide (See Figure 2-4).

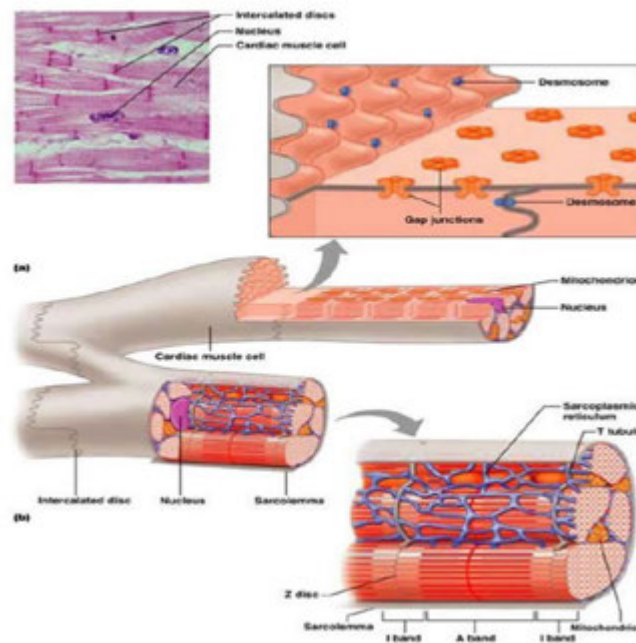


Figure 2-4: Microscopic anatomy of cardiac muscle (Opie, 2004)

The uniqueness of the blood pumping role of the heart is governed by the cardiac muscle. The contraction of the cardiac muscle happens by the sliding filament mechanism. The most distinguishing factors of cardiac muscles are that they are short, fat, branched and interconnected. The endomysium is a loose connective tissue matrix which contains various capillaries. The contraction of the cardiac muscles is initiated by action potentials that sweep across cell membranes (see Figure 2-4). The special ability of cardiac muscles is to depolarise spontaneously and eventually pace the heart. Only about 1% of cardiac fibres are auto rhythmic. The heart pumping work is done by contractile muscle fibres that constitute most of the heart muscle. The depolarisation allows a few voltage-gated fast Na^+ channels in the sarcolemma so that extracellular Na^+ enters the channel. Once Ca^{2+} provides the signal via troponin binding the excitation-contraction occurs. This allows bridge activation and couples the depolarisation wave to the sliding of myofilaments as shown in Figure 2-5.

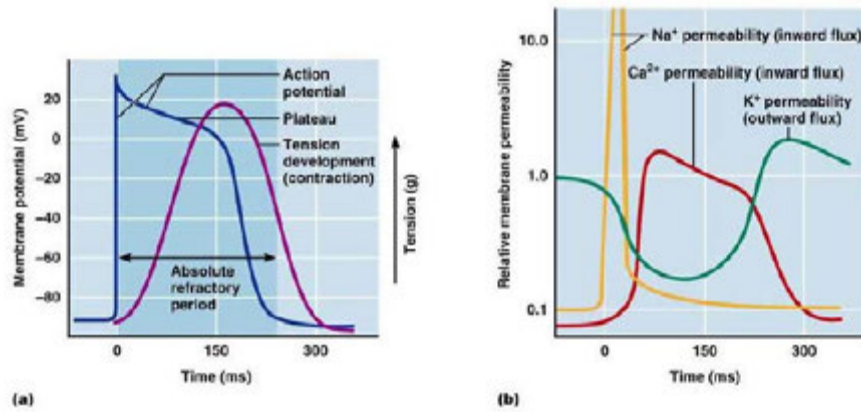


Figure 2-5: The action potential of contractile cardiac muscle cells (Little, 1981)

2.1.2 Physiology of the heart

The properties of heart muscle do not depend on the nervous system, hence the fundamental ability of the cardiac muscle is to depolarise and contract. The intrinsic cardiac conduction system consists of non-contractile cardiac cells that are specialised to initiate and distribute impulses throughout the heart, so that it depolarises and contracts in an orderly and sequential manner.

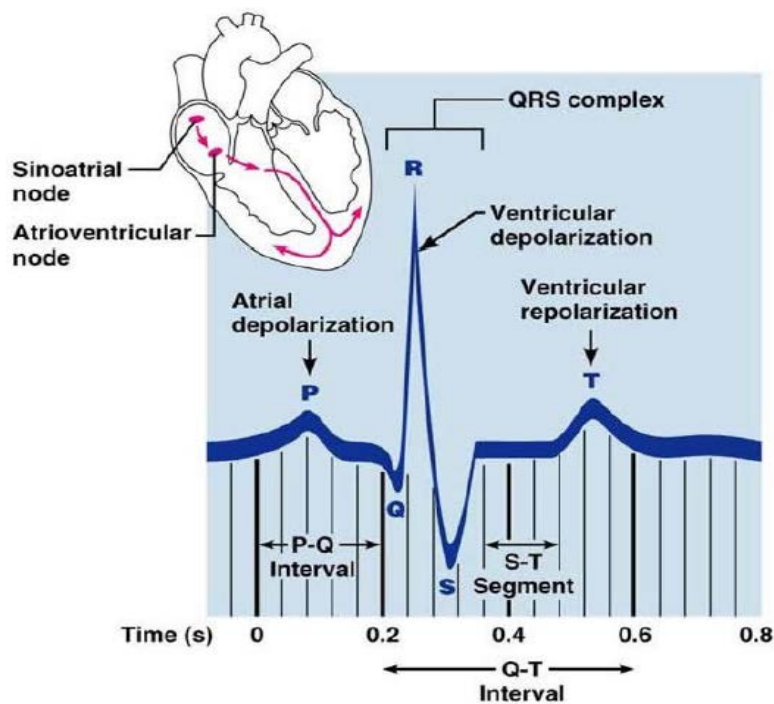


Figure 2-6: An electrocardiogram (ECG) tracing (Katz, 2010)

The electrocardiograph is a device used to detect the electrical currents generated in and transmitted through the heart and spread through the body. This device uses a graphic record of the heart activity. Three waves are typical in an ECG: the P wave, the complex

QRS wave, and the T wave. In a human being the small P wave lasts about 0.08s and results from movement of the depolarisation wave from the SA node through the atria. The ventricular depolarisation and ventricular contraction are shown in the complex QRS wave. The complex QRS wave is due to the continuous change of the paths of the depolarisation waves via the ventricular walls that produces current in all directions. The QRS wave duration is also 0.08s. The ventricular repolarisation is a result of the P wave and is lower than the depolarisation which lasts about 0.16s. P and T waves have a lower amplitude compared to the complex QRS wave. This is mainly because the atrial repolarisation takes places during the period of ventricular excitation (See Figure 2-6).

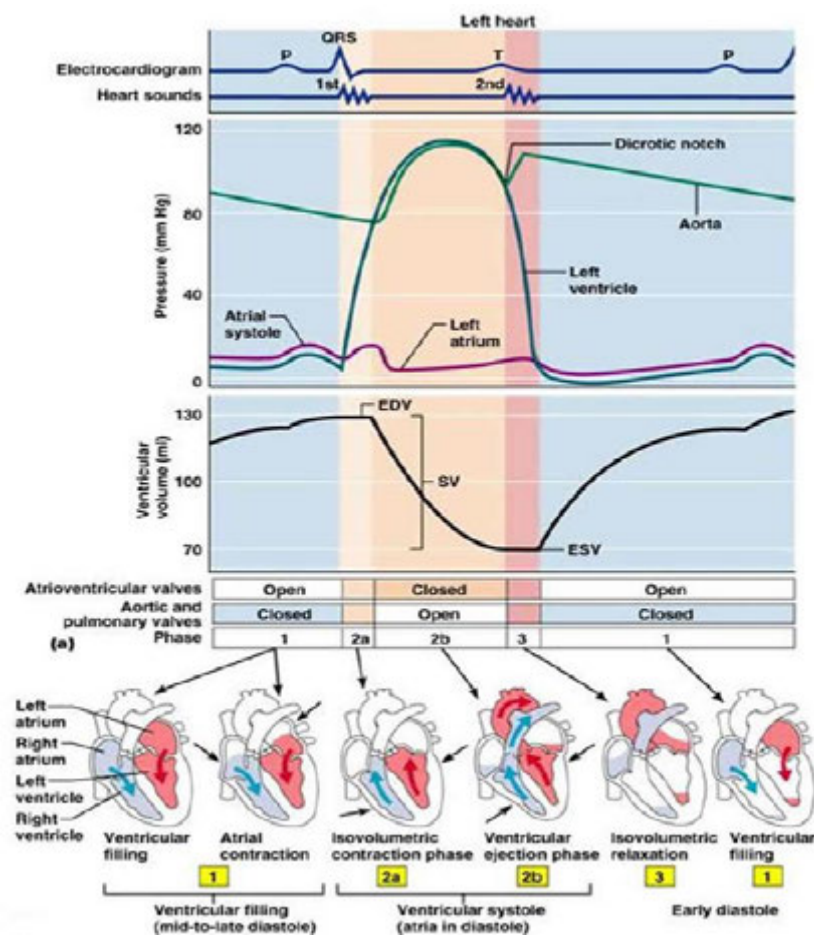


Figure 2-7: Summary of events during the cardiac cycle (Katz, 2010)

The healthy heart has the ability to move twistingly as it contracts to eject blood back to the body and relaxes as it allows the filling of chambers. The terms systole and diastole refer to the period of contraction and relaxation respectively. The cardiac cycle may be defined as the blood flow from the heart during one heartbeat which is composed of arterial systole and diastole and ventricular systole and diastole. The cardiac cycle is also associated with the pressure and blood volume in the heart. Electrical events shown in Figure 2-7 dictate the

mechanical movements and events of the heart. According to Figure 2-7, (1) is the ventricular filling: mid to late diastole. At this stage the pressure in the heart is low and the blood flowing from the circulation is flowing passively through the atria and the open AV valves into the ventricles, and the aortic and pulmonary valves are closed. Stage (2) is called ventricular systole (atria in diastole). This is when the ventricles start to contract while atria relax. At this stage the ventricular pressure increases rapidly and sharply while closing the AV valves. Stage (3) is the isovolumetric relaxation: early diastole. At this stage the ventricles relax mainly because the blood remaining in the region is low. This is also called the end-systolic volume (ESV). This is the time when the ventricular pressure drops rapidly. During this period the blood in the aorta and pulmonary trunk flows back toward the heart.

2.1.3 Cardiac functional parameters

Cardiac output is defined as the amount of blood pumped from the heart in one minute. The stroke volume is defined as the amount of blood pumped out by one ventricle in one heartbeat. The cardiac output (CO) is the product of heart rate (HR) and stroke volume (SV). Cardiac reserve is defined as the difference between resting and maximal CO. The stroke volume is defined as the difference between the end-diastolic volume (EDV) and the end-systolic volume (ESV). ESV is the amount of blood left in the ventricle after the contraction of the heart and EDV is the amount of blood that collects in the ventricle during relaxation.

There are several cardiac parameters that are normally used in clinical and research settings. The commonly utilised functional cardiac parameters include the blood pressure, blood volume and flow rate in four cardiac chambers. On a global scale, the end-systolic volume (ESV), end-diastolic volume (EDV), myocardial mass and the ejection fraction (EF) of both the LV and RV are utilised in assessing the normality of the heart. The dilation of LV after myocardial infarction (MI) can be indicated by the increase in the EDV of LV. The LV hypertrophy and increased systolic stress can be as a result of a depressed EF (Holmes, 2004; Holmes *et al.*, 1994; Holmes *et al.*, 2004; Holmes *et al.*, 2006. Non-invasive imaging techniques could be used in measuring the LV pump function using the following formulae:

$$EF = \frac{EDV - ESV}{EDV} = \frac{SV}{EDV} \quad (1)$$

where $SV = EDV - ESV$ is the stroke volume. (2)

$E_a = \frac{ESP}{SV}$ is defined as the effective arterial elastance. The impact on LV and assessment of arterial load is conducted by the effective arterial elastance.

The local scale information about the ability of contractile myocardium is measured by fractional shortening (FS). The fractional shortening measures the change in LV diameters between the relaxed and contracted states. The FS is defined as follows:

$$FS = \frac{DED-DES}{DED} \quad (3)$$

DED and DES represent the end-diastolic and end-systolic diameters, respectively. In various areas of the heart, a more detailed image of cardiac function can be measured by calculating the local FS. The dynamic system of the heart could be measured by considering the wall/myocardial mechanics which include the wall movement, thickening and strain.

As shown in Figure 2-8, the end-diastolic and end-systolic pressure volume relationships (EDPVR and ESPVR, respectively) are envisaged by plotting the left ventricular pressure versus the volume for the diastolic and systolic phases. The EDPVR describes the passive properties of the LV at the end-diastole phase. The slope of the EDPVR at any point provides ventricular compliance. The ESPVR describes the maximum pressure that can be developed in the LV for any given LV volume (See Figure 2-8).

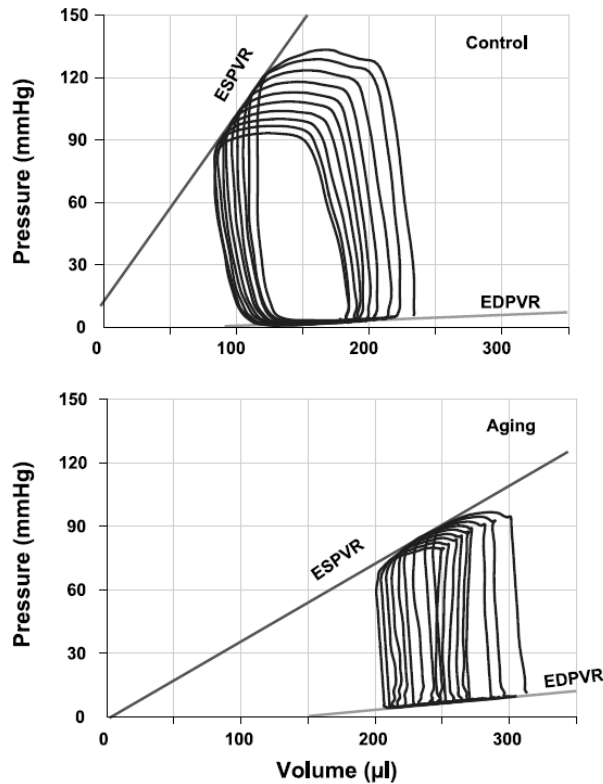


Figure 2-8: EDPVR and ESPVR of the left ventricle of a rat (top –young rats, bottom- aging rats) (Pacher et al., 2004)

2.1.4 Physiology of rat heart

The LV accomplished the mechanical work in all four chambers of the heart during cycle (See Figure 2-9) The LV consist of muscles that have undergone large deformations and high stresses. The pressure and volume are important determinants in assessing the cardiac performance of the heart during heart cycles. During a single cardiac cycle, four steps are manifested sequentially, namely: (1) the diastolic phase; (2) iso-volumetric contraction; (3) the systolic phase; and (4) iso-volumetric relation. Figure 2.8 shows the typical P-V loop for the left ventricle. At point 1, the EDV and EDP are read. It is at this point when the mitral valve closes. The contraction of the muscle also begins at this point to raise the blood pressure. At point 2, the systolic phase begins where the aortic valve opens. At this point the blood is now ejected outside the LV. The pressure and volume increases and decreases respectively to further eject the blood out of the LV. The end of systolic phase happens at point 3. Point 3 is categorised by the ESV and ESP. The muscles relax for the intake of blood to the ventricle. The LV undergoes an iso-volumetric relaxation until reaching point 4. During filling, the mitral valve opens and the muscle relaxes further to ensure that the volume increases so that more blood is filled in the ventricle (Nardinocchi et al., 2010).

Figure 2-10 shows the schematic diagram of a rat. The overall biological parameters of a rat are summarised in Table 2-1. The general structure of the circulatory system of the rat is almost identical to that of humans. Pulmonary circulation carries blood through the lungs for oxygenation and then back to the heart. Systemic circulation moves blood through the body after it has left the heart. Comparing the rat heart to that of an average human being, the average rat heart rate is found to be higher.

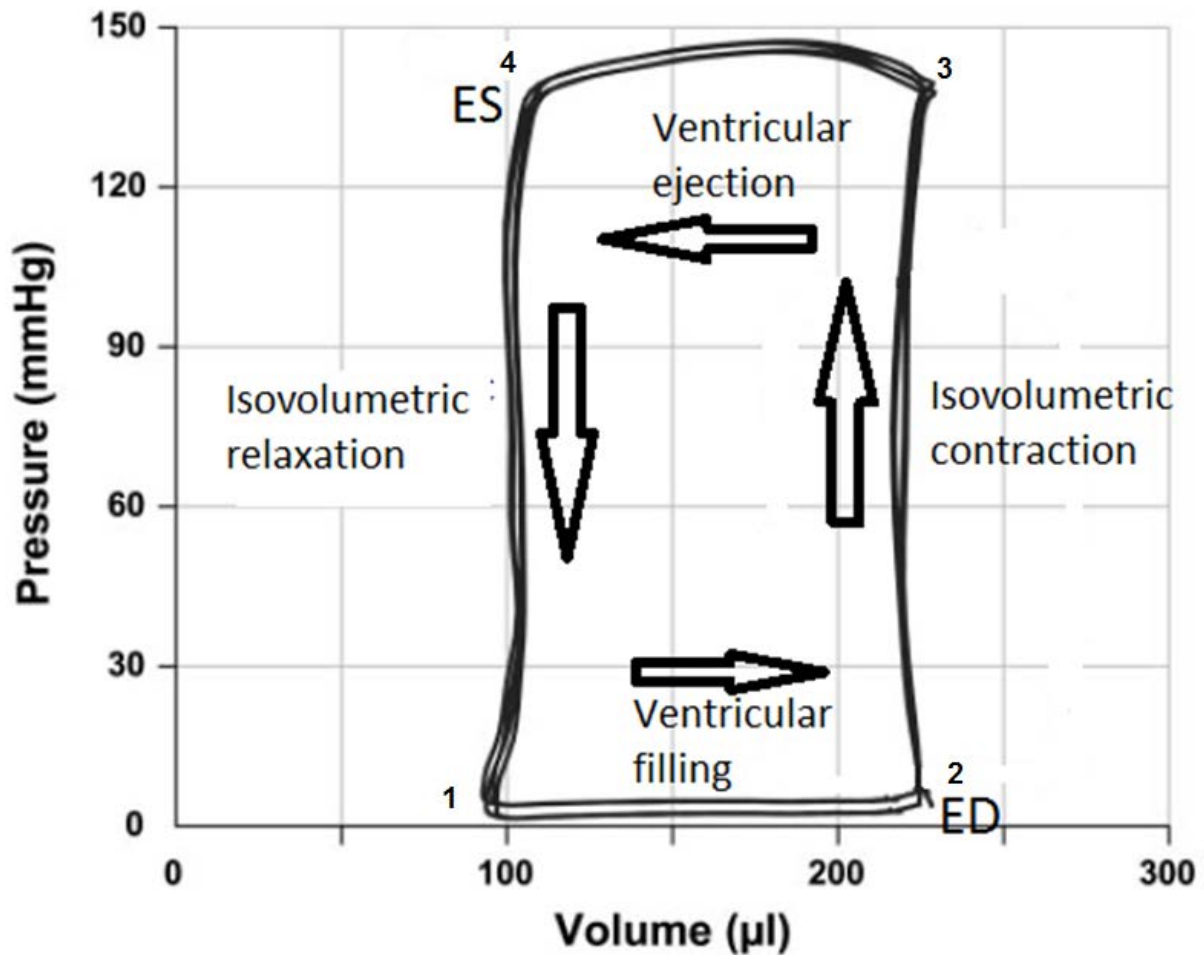


Figure 2-9: LV Pressure-volume loop (Pacher et al., 2004).

Table 2-1: Comparison of Biological Parameters in the Human and Rat (Brau et al., 2004).

	Human	Rat
Body weight (g)	70000	250
Heart weight (g)	330	1
Heart diameter (mm)	100	15
Heart excursion (mm)	30	5
Heart rate (bpm)	60	300
R-R interval (ms)	1000	200
Blood volume (mL)	5200	13.5
Cardiac output (mL/minute)	5600	74
Aortic flow (cm/second)	23.2	16.6
Breathing rate (breaths/minute)	12	60
Tidal volume (mL)	500	3
Minute volume (L/minute)	6	0.18

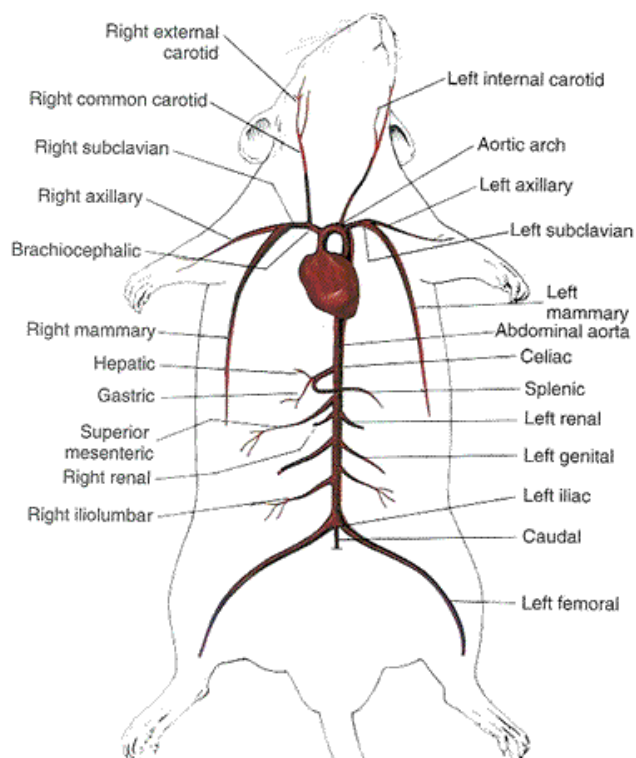


Figure 2-10: Schematic diagram of rat (Pacher et al., 2004).

2.2 Myocardial Infarction of the Heart

Myocardial infarction (MI) is caused by blocking of blood and oxygen in the arteries. This condition is normally known as heart attack (HA). It is a result of damaged tissue of the heart wall due to decreased blood flow. The MI is caused by the blockage of blood by blood clot that obstructs an artery. The thrombus formation is caused by cholesterol build up over a period of time. The development of atherosclerotic plaque occurs over a period of years to decades. The two primary characteristics of the clinically symptomatic atherosclerotic plaque are a fibromuscular cap and an underlying lipid-rich core. Plaque erosion can occur because of the actions of matrix metalloproteases and the release of other collagenases and proteases in the plaque, which result in thinning of the overlying fibromuscular cap. The second non-atherogenic cause of MI is the use of drugs that can lead to coronary vasospasm, including methamphetamines and cocaine.

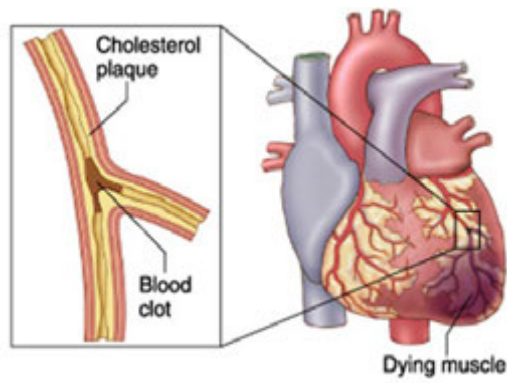
MI has four main phases, namely: 1) acute ischemia, 2) necrosis, 3) fibrosis and 4) remodelling. Acute ischemia happens from the first few minutes to hours after the infarction. During this time the infarct sizes will depend on a number of factors including the loading. It is reported that for a few hours after the infarction, the material properties of the infarct do not change considerably. However, after six hours of the infarction, the infarcts begin to stiffen. The structural changes during the acute ischemia are less predictable. In general, most changes during the first few hours appear to affect the infarct at end-systole where forces are generated within the myocardium. During acute ischemia, the myocardium is reported to have no ability to generate systolic forces. This implies that the myocardium now behaves like the passive material throughout the cardiac cycle. Many experiments reported that the diastolic pressure-length curves move rightward. It can be concluded that the infarct during acute ischemia behaves as a passive nonlinear viscoelastic material.

The fibrotic phase appears to happen two-week after the infarction in a rat animal model as shown in Figure 2-11. During this time, the collagen content increases quickly. There are several definitions of fibrotic phase, but (Holmes et al., 2005) define the phase as the time where the number of fibroblasts and amount of new collagen start to increase quickly. In a rat the collagen content starts increasing from day 7 up to three weeks. At this phase, the myofibre orientation in the scar is the same as that of the healthy myocardium but the transmural mean angle becomes small to the order value of 30° . It was reported that during this phase, the stiffness of the infarct increases and a distinctive anisotropy is acquired. In various animal experiments, the stiffness increases from six to ten times that of the healthy myocardium. Strains in the circumferential direction were found to be greater than the

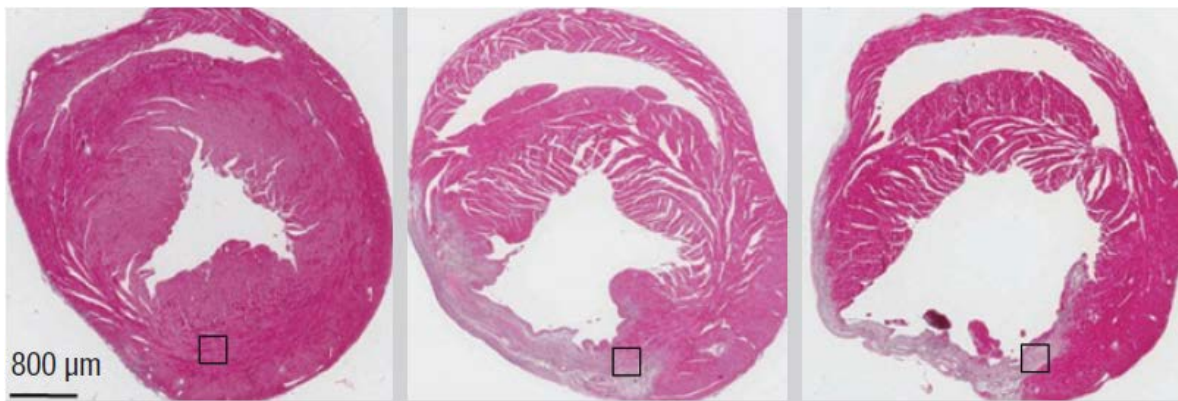
longitudinal strains at end-diastole of two-week infarcted rat hearts. The important determinants in the fibrotic phase are the three dimensional structure of the collagen fibres and the amount of collagen (Zhang et al., 2013).

The remodelling phase happens between two and four-week in the rat, as shown in Figure 2-12. During this period the mechanical properties of the infarcted region decouple from collagen content. It is reported that, while collagen may continue to increase, the stiffness of the infarct is observed to decrease. The effect of the remodelling phase can be seen at both the microscopic and global levels. At the global level, the scar tissue is seen to begin shrinking. The shrinkage is a result of decoupling of collagen content and will also result in the reduction of volume of the ventricle. If the infarct is situated in the LV, the LV volume will decrease. The stiffness of the infarct during the remodelling phase is still unknown. However, some researchers suggested that the stiffness during this phase becomes twofold compared to non-infarcted myocardium.

At the beginning of the remodelling phase, the stiffness in the infarcted region decreases. This happens irrespective of the collagen content increase in the scar tissue. During this phase, the collagen content and myofibre orientation are not the only determinants of the mechanical properties. The large infarct size in the heart model, led to the increase in wall stress and this may lead to poor functioning of the heart. This is mainly because cavity dilation and scar shrinkage lead to unpredicted performance of the heart.



(a)



(b)

(c)

(d)

Figure 2-11: Dying muscle and sectional view of the human heart. (a) Occluded coronary artery causing a myocardial infarction. Heart sections showing (b) healthy myocardium (c) infarcted myocardium and (d) dilated myocardium (Zhang et al., 2013).

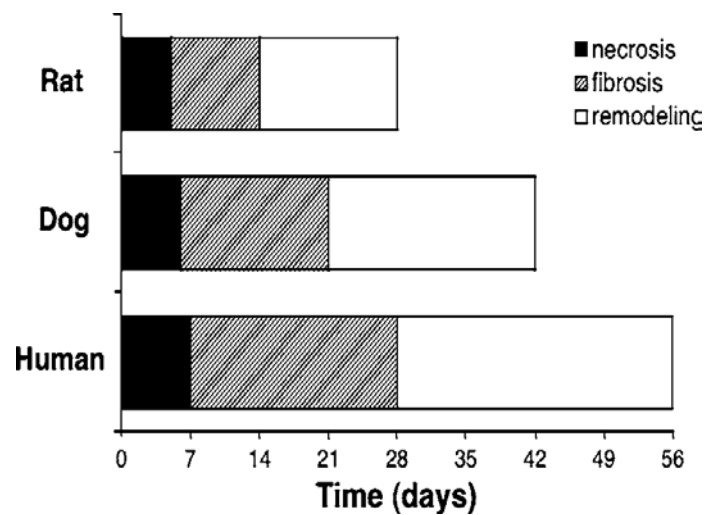


Figure 2-12: Temporal course of the phases of healing for various animal model (Holmes et al., 2005)

2.3 Myocardial Mechanics of the Heart

Figure 2-13 (a) shows the myocardial motion of the models during cardiac cycle. In the analysis, only two phases were simulated, namely: systolic and diastolic phases. Figure 2-13

(b) shows the legends used during systolic or diastolic phase. Figure 2-13 (a) and (c) show how the radial, circumferential and longitudinal directions are defined.

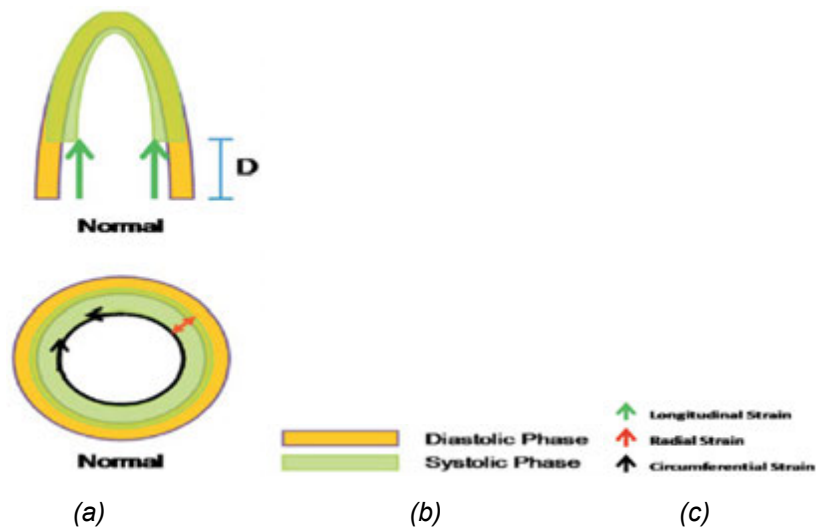


Figure 2-13: The myocardial motion of the normal heart and conversion used in the study.
 (a) Myocardial movement in systolic and diastolic phases. (b) Legends of a cardiac cycle.
 (c) Stress and strain directions.

2.4 Basic Continuum Mechanics

To understand the basic mechanics, basic continuum mechanics are presented in this section. In the analysis of solid continua, material and geometric nonlinearity are the bases of nonlinearity. Material becomes nonlinear when the stress-strain behaviour as given by the constitutive relation is nonlinear. The majority of this work is achieved by using these sources (Bonet, 1997, Crisfield, 1997, Marsden et al., 1993).

2.4.1 General formation

The stretch λ is the measure of the deformation in the rod subjected to axial load. The stretch is the ratio of the deformed length to the undeformed length. The deformation ratio is shown in 4. The true (or Cauchy) stress in the truss member is determined by considering the member subjected to the internal force \mathbf{T} , divided by the cross-sectional area A . It is argued that any member subjected to high strain is best represented by the alternative stress known as Kirchhoff stress which is defined as follows:

$$\tau = \sigma v/V . \tag{4}$$

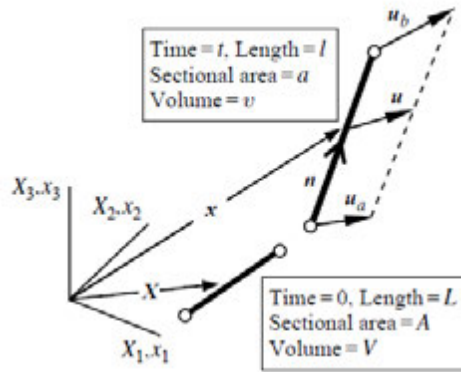


Figure 2-14: Kinematics of axial truss member in three-dimensional (Bonet, 1997)

To correspond to later developments upper case letters are used to describe the initial undeformed position, \mathbf{X} , length L , cross-sectional area A and volume V at time $t = 0$. Lower case letters are used to describe the current deformed position, \mathbf{x} , length l , cross-sectional area a and volume v at time t . The deformed length of the member rod and the unit vector \mathbf{n} associated with it can be expressed as follows (See Figure 2-14):

$$\ell = \{(x_b - x_a) \cdot (x_b - x_a)\}^{1/2} \quad (5)$$

Unit vector is also represented as follows:

$$\mathbf{n} = \frac{1}{\ell} (x_b - x_a) \quad (6)$$

The above equation is built on the assumption that the rod subjected top axial load will go under the uniform large strain measured by stretch. The Jacobian or volume change ratio and the stretch can be represented as follows:

$$\lambda = \frac{\ell}{L}; J = \frac{v}{V} \quad (7)$$

The engineering strain and logarithmic strains are defined as follows:

$$d\varepsilon = \frac{dl}{l}; \quad (8)$$

$$\varepsilon = \ln \lambda = \int_L^l \frac{dl}{l} \quad (9)$$

2.4.2 Kinetics

The description of motion is vital in finite deformation analysis. Kinematics is defined as the study of deformation and motion without considering and referring to the cause of the deformation (See Figure 2-15).

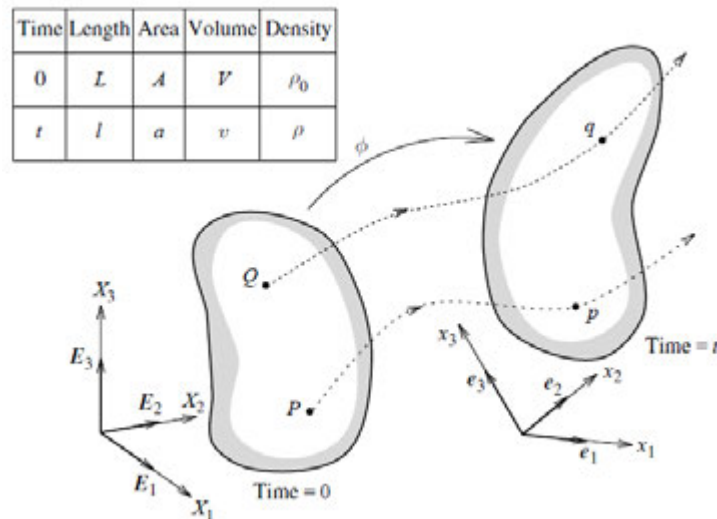


Figure 2-15: Deformable body in general motion (Bonet, 1997)

The general motion of a deformable body is shown in Figure 2-15. The body shown in Figure 2-15 is the material particles labelled by the coordinates with respect to Cartesian basis E_i . By mapping between the position at the beginning and the final status of the particle, the motion can be mathematically represented as follows:

$$x = \phi(X, t) \quad (10)$$

The understanding between material and spatial description is further explored by introducing the density of the material:

(a) Material description: the variation of ρ over the body is described with respect to the

original (or initial) coordinate \mathbf{X} used to label a material particle in the continuum at time $t = 0$ as

$$\rho = \rho(\mathbf{X}, t) \quad (11)$$

(b) Spatial description: ρ is described with respect to the position in space, \mathbf{x} , currently occupied by a material particle in the continuum at time t as

$$\rho = \rho(\mathbf{x}, t) \quad (12)$$

In Equation (11) a change in time t implies that the same material particle \mathbf{X} has a different density ρ . Consequently, interest is focused on the material particle \mathbf{X} . In Equation (12), however, a change in the time t implies that a different density is observed at the same spatial position \mathbf{x} , now probably occupied by a different particle. Consequently, interest is focused on a spatial position \mathbf{x} .

2.4.2.1 Deformation gradient

The deformation gradient \mathbf{F} is the key quantity in finite element analysis because the two neighbouring particles after deformation can be described in terms of their relative material position before deformation. Hence, the deformation is critical in defining deformation which leads to strain definition. As shown in Figure 2-16, the two material particles Q_1 and Q_2 are in the neighbourhood of the material particle P . The elemental vectors $d\mathbf{X}_1$ and $d\mathbf{X}_2$ are used to define the position of material particles Q_1 and Q_2 as follows:

$$d\mathbf{X}_1 = \mathbf{X}_{Q_1} - \mathbf{X}_P; \quad d\mathbf{X}_2 = \mathbf{X}_{Q_2} - \mathbf{X}_P \quad (13)$$

After the deformation of material particles P , Q_1 and Q_2 , the current partial positions can be mathematically expressed as follows:

$$x_p = \phi(\mathbf{X}_P, t); \quad x_{q_1} = \phi(\mathbf{X}_{Q_1}, t); \quad x_{q_2} = \phi(\mathbf{X}_{Q_2}, t) \quad (14)$$

The corresponding elemental vectors become:

$$dx_1 = x_{q_1} - x_p = \phi(\mathbf{X}_P + d\mathbf{X}_1, t) - \phi(\mathbf{X}_P, t) \quad (15)$$

$$dx_2 = x_{q_2} - x_p = \phi(\mathbf{X}_P + d\mathbf{X}_2, t) - \phi(\mathbf{X}_P, t) \quad (16)$$

Therefore, the deformation gradient tensor F is defined as follows:

$$F = \frac{\partial \phi}{\partial X} = \nabla_0 \phi \quad (17)$$

∇_0 represents the gradient with respect to the material configuration. The elemental vectors dx_1 and dx_2 can be obtained in terms of dX_1 and dX_2 as (See Figure 2-16):

$$dx_1 = FdX_1; \quad dx_2 = FdX_2 \quad (18)$$

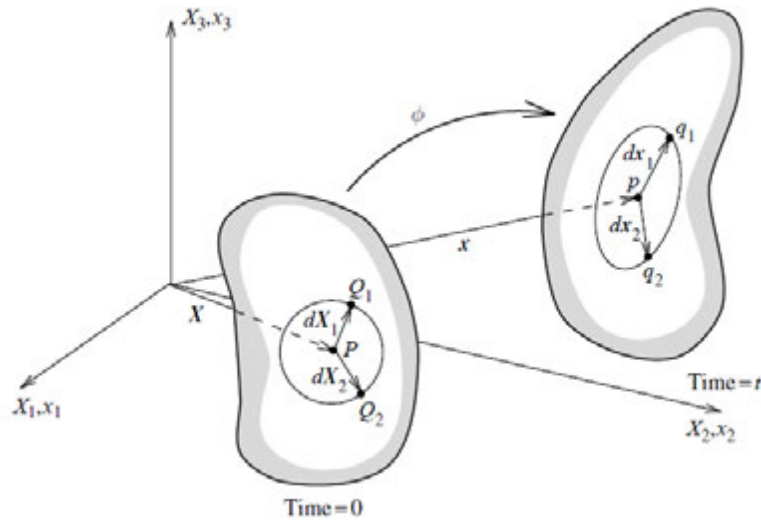


Figure 2-16: General motion in the neighbourhood of a particle (Bonet, 1997)

2.4.3 Strain

The strain is regarded as the general measure of deformation in a material subjected to applied force. As shown in Figure 2-16, the scalar product of the two elemental vectors dX_1 and dX_2 after deformation dx_1 and dx_2 . The change in scalar product of the two elemental vectors involves the change in length and angle between the two vectors. The material vectors of spatial scalar product $dx_1 \cdot dx_2$ can be found as follows:

$$dx_1 \cdot dx_2 = dX_1 \cdot C dX_2 \quad (19)$$

Where C represents the right Cauchy-Green deformation tensor. The right Cauchy-Green deformation tensor is given in terms of the deformation gradient F as:

$$C = F^T F \quad (20)$$

Alternatively, left Cauchy-Green or Finger tensor is expressed as follows:

$$\mathbf{B} = \mathbf{F}\mathbf{F}^T \quad (21)$$

The change in scalar product can now be found in terms of the material vectors $d\mathbf{X}_1$ and $d\mathbf{X}_2$ and the Lagrangian or Green strain tensor \mathbf{E} as:

$$\frac{1}{2}(dx_1 \cdot dx_2 - d\mathbf{X}_1 \cdot d\mathbf{X}_2) = d\mathbf{X}_1 \cdot \mathbf{E}d\mathbf{X}_2 \quad (22)$$

Where \mathbf{E} is defined as the material tensor

$$\mathbf{E} = \frac{1}{2}(\mathbf{C} - \mathbf{I}) \quad (23)$$

2.4.4 Distortional change

The separation of compressible and nearly incompressible materials necessitates the separation of volumetric from the distortional components of deformation (See Figure 2-17). This means that the separation of distortional components does not have any implication on the volume change. If the determinant of the deformation gradient results to the ratio of the volume, then the determinant of deformation gradient must satisfy the following:

$$\det \hat{\mathbf{F}} = 1 \quad (24)$$

The above condition could be satisfied by choosing \mathbf{F} such that the following relationship holds:

$$\hat{\mathbf{F}} = J^{-1/3}\mathbf{F} \quad (25)$$

Therefore, based on equation x and equation y, the following holds true:

$$\begin{aligned} \det \hat{\mathbf{F}} &= \det (J^{-1/3}\mathbf{F}) \\ &= (J^{-1/3}) \det \mathbf{F} = J^{-1}J = 1 \end{aligned} \quad (26)$$

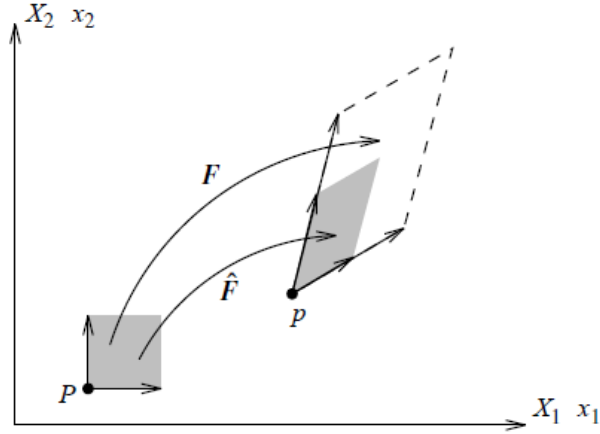


Figure 2-17: Distortional component of \hat{F} (Bonet, 1997)

2.4.5 Cauchy stress tensor

The Cauchy stress tensor in linear analysis is defined as force per unit area. Figure 2-18 shows the deformable body at its current state (See Figure 2-18). The concept of stress is developed by studying the action of the forces applied by one region R1 of the body on the remaining part R2 of the body with which it is in contact (See Figure 2-19). The element of the area Δa is normal to n in the neighbourhood of spatial point p as shown in Figure 2.18. Therefore, the traction vector t , is defined as follows:

$$t(n) = \lim_{\Delta a \rightarrow 0} \frac{\Delta p}{\Delta a} \quad (27)$$

The relationship between n and t must satisfy the Newton third law. Therefore, in applying the Newton's third law, the following agrees:

$$t(-n) = -t(n) \quad (28)$$

The stress tensor is developed by associating the tree traction vectors in the Cartesian directions e_1, e_2, e_3

$$t(e_1) = \sigma_{11}e_1 + \sigma_{21}e_2 + \sigma_{31}e_3 \quad (29)$$

$$t(e_2) = \sigma_{12}e_1 + \sigma_{22}e_2 + \sigma_{32}e_3 \quad (30)$$

$$t(e_3) = \sigma_{13}e_1 + \sigma_{23}e_2 + \sigma_{33}e_3 \quad (31)$$

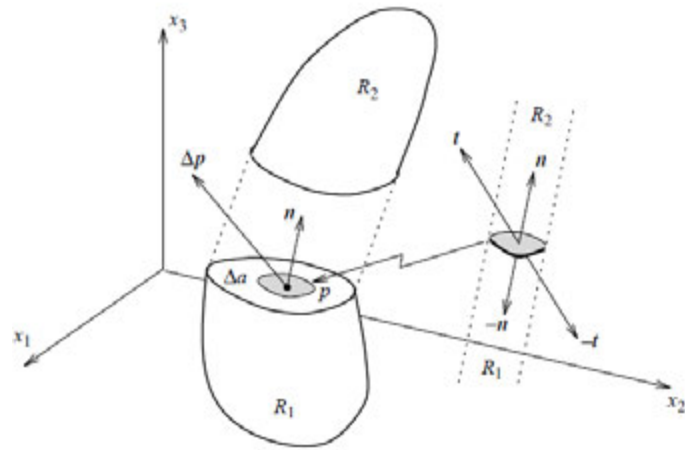


Figure 2-18: Traction vector (Bonet, 1997)

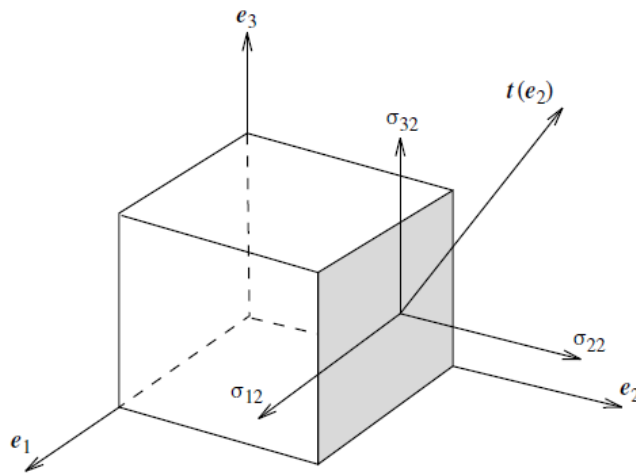


Figure 2-19: Stress components (Bonet, 1997)

2.4.6 Principle of virtual work

In establishing the finite element formulation, the weak form of the differential equation is used. Therefore in solid mechanics the use of virtual work equation is used in establishing the differential equation. In order to prove this, assume an arbitrary velocity from the current position of the body as shown in Figure 2-20. The arbitrary virtual velocity is denoted by δv . Similarly the virtual work δw per unit volume and time done by the residual force r during the virtual motion is represented by: $r \cdot \delta v$. The equilibrium implies the following:

$$\delta w = r \cdot \delta v = 0 \tag{32}$$

The weak statement of the static equilibrium of the body is given by the following relationship:

$$\delta W = \int_v^0 (\text{div } \sigma + f) \cdot \delta v \, dv = 0 \quad (33)$$

Finally, the spatial virtual equation can be expressed in terms of virtual velocity gradient and anti-symmetric virtual spin tensor.

$$\delta W = \int_v \sigma : \delta \mathbf{d} \, dv - \int_v \mathbf{f} \cdot \delta \mathbf{v} \, dv - \int_{\partial v} \mathbf{t} \cdot \delta \mathbf{v} \, da = 0 \quad (34)$$

The scar equation above states that the equilibrium of a deformable body will become the basis for the finite element discretization.

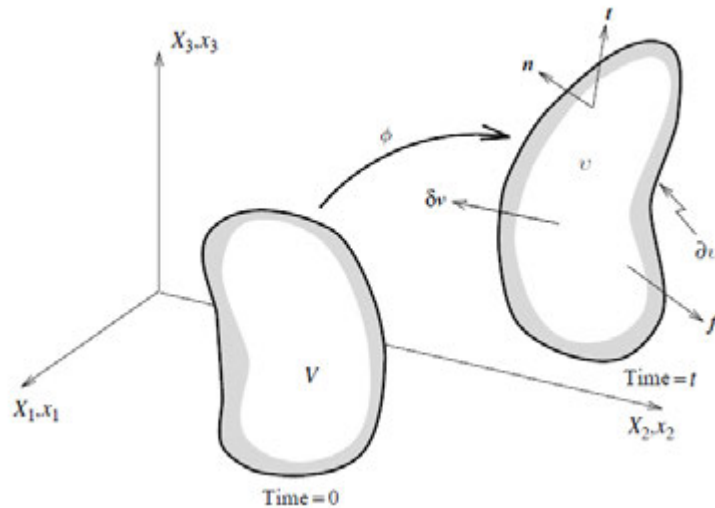


Figure 2-20: Principle of virtual work (Bonet, 1997)

2.4.7 Alternative stress representations

2.4.7.1 The Kirchhoff stress tensor

The virtual work done by the stress may be expressed by the following terms:

$$\delta W_{int} = \int_v \sigma : \delta \mathbf{d} \, dv \quad (35)$$

Pairs such as σ and \mathbf{d} in this equation are said to be *work conjugate* with respect to the current deformed volume in the sense that their product gives work per unit current volume. The virtual work equation expressed in terms of the material coordinate system encourages

the pairs of stresses and strain rates to materialise. This materialisation can be achieved by initially expressing the initial volume and the area by transforming the integrals using the following relationship:

$$\int_V J \boldsymbol{\sigma} : \delta \mathbf{d} dV = \int_V \mathbf{f}_0 \cdot \delta \mathbf{v} dV + \int_{\partial V} \mathbf{t}_0 \cdot \delta \mathbf{v} dA \quad (36)$$

\mathbf{f}_0 represents the body force per unit undeformed volume which is the same as $J\mathbf{f}$. The \mathbf{t}_0 is the traction vector per unit initial area which is equal to $t(da/dA)$. The area ratio can then be expressed as:

$$\frac{da}{dA} = \frac{J}{\sqrt{\mathbf{n} \cdot \mathbf{b}\mathbf{n}}} = J \sqrt{\mathbf{N} \cdot \mathbf{C}^{-1} \mathbf{N}} \quad (37)$$

Given the above equation, the internal virtual work can then be expressed in terms of the Kirchhoff stress tensor $\boldsymbol{\tau}$

$$\delta W_{int} = \int_V^0 \boldsymbol{\tau} : \delta \mathbf{d} dV \quad (38)$$

$$\text{Therefore, } \boldsymbol{\tau} = J \boldsymbol{\sigma} \quad (39)$$

This equation reveals that the Kirchhoff stress tensor $\boldsymbol{\tau}$ is work conjugate to the rate of deformation tensor with respect to the initial volume. Note that the work per unit current volume is not equal to the work per unit initial volume. However, Equation (40) and the relationship $\rho = \rho_0/J$ ensure that the work per unit mass is invariant and can be equally written in the current or initial configuration as:

$$\frac{1}{\rho} \boldsymbol{\sigma} : \mathbf{d} = \frac{1}{\rho_0} \boldsymbol{\tau} : d \quad (40)$$

2.4.7.2 The second Piola-Kirchhoff stress tensor

The first Piola-Kirchhoff tensor \mathbf{P} is an asymmetrical two-point tensor and as such is not completely related to the material configuration (See Figure 2-21). It is possible to contrive a totally material symmetric stress tensor, known as the *second Piola-Kirchhoff stress* \mathbf{S} ,

$$dP = \phi_*^{-1}[dp] = F^{-1} dp \quad (41)$$

$$dP = S dA; S = J F^{-1} \sigma F^{-T} \quad (42)$$

$$\delta d = F^{-T} \delta \dot{E} F^{-1} \quad (43)$$

Combining and substituting the above equation, the internal virtual work becomes:

$$\begin{aligned} \delta W_{int} &= \int_V \sigma : \delta d \, dv = \int_V J \sigma : (F^{-T} \delta \dot{E} F^{-1}) \, dV \\ &= \int_V \text{tr}(F^{-1} J \sigma F^{-T} \delta \dot{F}) \, dV = \int_V S : \delta E \, dV \end{aligned} \quad (44)$$

The material virtual work equation is now expressed in terms of second Piola-Kirchhoff tensor as follows:

$$\sigma = J^{-1} P F^T; \quad \sigma = J^{-1} F S F^T \quad (45)$$

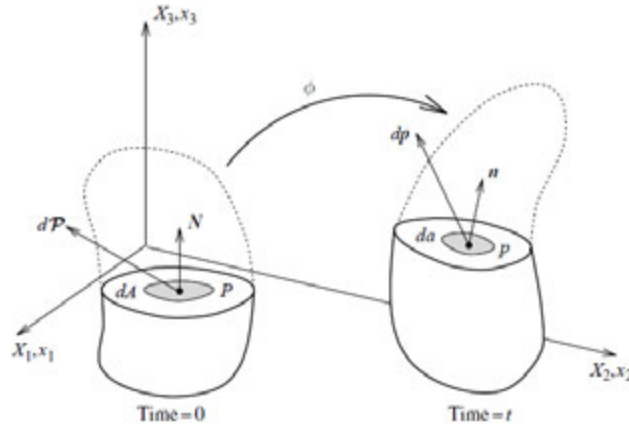


Figure 2-21: First Piola-Kirchhoff stress tensor (Bonet, 1997)

2.4.8 Finite element implementation Fung model

Formulation of specialised pseudoelastic constitutive relations is a prerequisite in modelling of soft tissue. In Abaqus®, this can be achieved by coding a user subroutine called UMAT (Abaqus, 2010).

The elastic deviatoric Green-Lagrange strain is defined as:

$$\bar{E} = \frac{1}{2} (\bar{K}^T \cdot \bar{K} - I) \quad (46)$$

The Cauchy stresses are calculated by using the equation 10.4.17 Simo *et al.* (1998) The expression for the Kirchhoff stress tensor is denoted by τ^o

$$\tau^o = JU^{o'}(\Theta)\mathbf{1} + dev[2F\overline{\partial_{\bar{C}}W^o}(\bar{C})\bar{F}^T] \quad (47)$$

where

$$dev[\cdot] = (\cdot) - \frac{1}{3}[(\cdot):I]I . \quad (48)$$

Therefore Cauchy stresses can be represented as follows:

$$\sigma = J^{-1}dev\left[\bar{K} \cdot \frac{\partial \bar{W}}{\partial \bar{E}} \cdot \bar{K}^T\right] + \frac{dU}{dJ}I . \quad (49)$$

The DDSDE is calculated by calculating the spatial tensor of elasticity C. This is achieved by using the following equation from Holzapfel *et al.* (2000).

$$C^o = J^2U^{o''}(\Theta)I \otimes I + JU^{o'}(\Theta)(\mathbf{1} \otimes \mathbf{1} - 2I) + \bar{c}^o . \quad (50)$$

This equation defines the tangent elastic moduli of the material in the spatial representation.

Therefore DDSDE

$$\begin{aligned} JC = & \bar{C} + \frac{1}{9}\left(\bar{C} : \frac{\partial^2 \bar{W}}{\partial \bar{E} \otimes \partial \bar{E}} : \bar{C}\right)I \otimes I - \frac{1}{3}I \otimes \left[\bar{K} \cdot \left(\frac{\partial^2 \bar{W}}{\partial \bar{E} \otimes \partial \bar{E}} : \bar{C}\right) \cdot \bar{K}^T\right] - \frac{1}{3}\left[\bar{K} \cdot \left(\frac{\partial^2 \bar{W}}{\partial \bar{E} \otimes \partial \bar{E}} : \bar{C}\right) \cdot \bar{K}^T\right] \otimes I - \\ & \frac{2}{3}[dev(\tau) \otimes I + I \otimes dev(\tau)] + \frac{2}{3}tr\left(\bar{K} \cdot \frac{\partial \bar{W}}{\partial \bar{E}} \cdot \bar{K}^T\right)\left(\mathbb{S} - \frac{1}{3}I \otimes I\right) + J\frac{dU}{dJ}(I \otimes I - 2S) + J^2\frac{d^2U}{dJ^2}I \otimes \\ & I \end{aligned} \quad (51)$$

\mathbb{C} represents the spatial deviatoric elasticity, whose components are defined by:

$$\mathbb{C}_{ijkl} = \bar{K}_{iI}\bar{K}_{jJ}\bar{K}_{kK}\bar{K}_{lL}\frac{\partial \bar{W}}{\partial \bar{E}_{IJ}\partial \bar{E}_{KL}} . \quad (52)$$

The deviatoric right Cauchy-Green deformation tensor \bar{C} is represented by:

$$\bar{C} = \bar{K}^T \cdot \bar{K} \quad (53)$$

and, the deviatoric left Cauchy-Green deformation tensor \bar{B} is represented by:

$$\bar{B} = \bar{K} \cdot \bar{K}^T \quad (54)$$

$\bar{\mathbf{I}}$ represents the fourth order identity tensor

The Kirchhoff stress tensor is represented by:

$$\boldsymbol{\tau} = J\boldsymbol{\sigma} \quad (55)$$

The components of the fourth-order symmetry tensor are represented by:

$$\mathbb{S}_{ijkl} = \frac{1}{6}(\delta_{il}\delta_{jk} + \delta_{ik}\delta_{jl}) \quad (56)$$

An objective stress-rate constitutive relationship is written as:

$$\boldsymbol{\tau}^\Delta = J\boldsymbol{\zeta} : \mathbf{d} \quad (57)$$

where $\boldsymbol{\zeta}$ represents the corotational tensor of elasticity, and $\boldsymbol{\sigma}$ is the current Cauchy stress tensor.

$$J\mathbb{C}_{ijkl} + \frac{1}{2}(\tau_{il}\delta_{jk} + \tau_{jk}\delta_{il} + \tau_{ik}\delta_{jl} + \tau_{jl}\delta_{ik}) \quad (58)$$

The distortional deformation gradient is given by:

$$\bar{\mathbf{F}} = \mathbf{F} \left(\frac{\bar{J}}{J} \right)^{\frac{1}{n}} \quad (59)$$

where: $\bar{J} = 1$ and $n = 3$

The strain energy function is given by Fung model:

$$W = \frac{c_1}{2}(e^Q - 1) + \frac{1}{D_1} \left(\frac{I^2 - 1}{2} - \ln J \right) . \quad (60)$$

U is defined as:

$$U = \frac{1}{D_1} \left(\frac{I^2 - 1}{2} - \ln J \right) \quad (61)$$

W is the strain energy per unit of reference volume, C1 and D1 are temperature dependent material parameters, J is the elastic volume ration, and Q is defined as follows:

$$\bar{Q} = \bar{e}^G : \mathbf{b} : \bar{e}^G = \bar{e}_{ij}^G \mathbf{b}_{ijkl} \bar{e}_{kl}^G \quad (62)$$

Mathematica® is used to take the derivatives of both equations A and B. The resulting matrices are computed numerically, creating a generalised Fung model (Young et al., 2010).

$$\frac{d\bar{W}}{d\bar{E}}, \frac{d^2\bar{W}}{d\bar{E} \otimes d\bar{E}}, \frac{dU}{dJ} \text{ and } \frac{d^2U}{dJ^2} \quad (63)$$

2.4.9 Finite element modelling

Finite element method (FEM) is widely defined as a numerical technique for finding approximate solutions to boundary value problems. This method is mostly used in areas where there is a need to solve complex elasticity and structural analysis problems. FEM has been used in understanding and designing real life structures like aircraft, vehicles, etc. There are four main advantages of FEM, namely: (i) the ability to achieve accurate representation of complex geometry; (ii) solving stress analysis of different materials; (iii) the ability to represent the total solution of the system; and (iv) ability to capture and represent local effects.

In structural mechanics FEM is regarded as the dominant discretization technique. In FEM the physical and mathematical model is divided into the subdivision disjoint (non-overlapping) components of simple geometry called finite elements. The reactions of all elements are expressed in terms of a finite number of degrees of freedom characterised as the value of an unknown function at a set of nodal points.

While FEM has been used extensively for many years in the motor, aviation and civil industries, its application in understanding the structural behaviour of the soft tissues is limited and began only a few years ago.

To achieve the desired unknown parameters (e.g. temperatures, stresses and strains) in finite element analysis, the energy function is minimised. This allows the finite element model to receive the correct solution. The finite element model is set to consist of functional energy.

To achieve the solution in FEM, the following procedures must be followed:

- 1) Divide structure elements with nodes. This process is called discretization or meshing;
- 2) Assemble the elements at the nodes to create an approximate system of equations for the whole structure. This will create the element matrices;
- 3) The approximate system of equations is solved involving unknown quantities such as displacements at the nodes;
- 4) The desired quantities such as strains and stresses are calculated at certain elements.

In any finite element analysis software, the following steps are required to achieve the desired solution:

- 1) The geometry is required. The geometry could be anything from 1D, 2D and 3D models;
- 2) Elements must be created which connect the nodal points;
- 3) Physical properties must be defined;
- 4) Boundary conditions or restraints. This must be as close as possible to the real situation;
- 5) Loading must be defined in detail. This is an important aspect because if the incorrect force or loading is applied the results obtained will be wrong;
- 6) The analysis can then begin.

2.5 Computational Cardiac Biomechanics Modelling of Healthy Heart

Stress, strain and material are the most fundamental parameters in the study of ventricular wall mechanics after myocardial infarction. According to Omens, *et al.* (1993), the understanding of myocardial stress and strain distribution is vital for four reasons:

- 1) Wall stress is affected by the blood flow and coronary vascular resistance. As a result, the coronary pressure and volume can affect the myocardial mechanics;
- 2) Knowledge of ventricular stress and strain is vital in understanding the interactions between healthy and non-healthy muscle tissue;
- 3) Damage and structural failure, healing and recovery, hypertrophy and remodelling of ischemia myocardium are all thought to depend on wall stress or strain or both;
- 4) Left ventricular wall stress is a major determinant of myocardial oxygen demand and hence the risk and degree of ischemic injury.

The mechanics of the heart are complex and inherently multi-dimensional (Costa et al., 2001). Computational models of healthy heart have been investigated rigorously over four decades. Among many other things, the myocardial stress and strain are the most important determinants of various aspects of cardiac physiology, pathophysiology and clinical factors. The computational cardiac biomechanics models have the ability to qualitatively provide the description of heart ventricular mechanics for the evaluation of cardiac performance (Bogen *et al.*, 1984; Hu *et al.*, 2005; Klepach *et al.*, 2012; Lee *et al.*, 2013; Lee *et al.*, 2014c; Wenk *et al.*, 2011a; Wenk *et al.*, 2011b; Wenk *et al.*, 2013b). Furthermore, computational studies of heart function using MRI and FE methods have been developed (Beg *et al.*, 2004; Hu *et al.*, 2005; Lee *et al.*, 2014d; Watanabe *et al.*, 2004).

The stresses and strains in the myocardial wall play a central role in cardiac mechanics as they affect many physiological factors such as pumping performance, myocardial oxygen demand, and coronary blood flow. The main determinants of myocardial stresses and strains are: 1) cardiac geometry, most importantly the ventricular geometry; 2) structure of myocardial tissue; 3) loading conditions (e.g. filling pressure, arterial pressure, and ventricular volume); 4) constraints (e.g. pericardial and thoracic environment); 5) material properties of the myocardium (passive properties, active properties).

In connection with biomechanics, the mammalian cardiac geometry has been studied most extensively in dogs (Streeter and Hanna, 1973a, Streeter and Hanna, 1973b, Nielsen et al., 2009, McPherson et al., 1987, Pao and Ritman, 1998) but has also been described for other animal species such as sheep (Guccione et al., 2001, Moustakidis et al., 2002), rabbit (Vetter and McCulloch, 2000, Vetter and McCulloch, 1998), and rat (Wise et al., 1999, Crowley, 1997), and for man (Bettendorff-Bakman et al., 2008, Bettendorff-Bakman et al., 2006, Schmid, 2006, Schmid et al., 2009). Three-dimensional geometrical information has been reconstructed from histological measurements, e.g. cross-sectional morphometric analysis of explanted hearts (Vetter *et al.*, 1998; Vetter *et al.*, 2000b), and in-vivo imaging modalities such as magnetic resonance imaging (MRI) (Crowley, 1997, Wise et al., 1999, Bettendorff-Bakman et al., 2006, Schmid, 2006, Schmid et al., 2009, Delhaas et al., 2008, Kroon et al., 2008). Data on myocardial tissue structure, most importantly myofibre orientation has been reconstructed from histological analyses (Nielsen et al., 2009, Vetter and McCulloch, 1998, Stevens and Hunter, 2003), diffusion-weighted MRI (Reese et al., 2010, Scollan et al., 1998) and calculation (Rijcken et al., 1999).

Loading conditions of the heart, and most importantly the left ventricle, have been defined with circulatory models of varying complexity. The basic parameters in cardiac mechanics

are blood pressure, volume and flow rate, in particular in the major cardiac chambers. From the point of myocardial wall stress and strain, ventricular pressure is most relevant. Typically, the pressure in the left ventricle throughout a cardiac cycle is presented either in association with the aortic pressure (constituting the LV afterload) or as ventricular pressure-volume relationship. Afterload models have often been considered in cardiac mechanics computations (Usyk et al., 2002, Watanabe et al., 2004, Usyk et al., 2001, Kerckhoffs, 2003). The best-known models for LV afterload are two- and three-element Windkessel models (Frank, 1899, Stergiopoulos et al., 1999). The LV preload, i.e. the ventricular filling pressure, has received less attention, at least with regard to model representations (Kerckhoffs et al., 2006) and the incorporation in computational models of cardiac mechanics is rare (Watanabe et al., 2004).

Unlike metals and other engineering materials, living tissues exhibit complex microstructure and material behaviour. The mechanical behaviour of the living tissue is thought to change with time (i.e. the tissue can grow or thicken) (Lee et al., 2014b). The computational study of the short-term mechanisms responsible for LV and RV post-infarct with precise geometry of the infarcted and myocardium remodelling has not been presented. Most researchers including Bettendorff-Bakman *et al.* (2006); Bettendorff-Bakman *et al.* (2008); (Kortsmit et al., 2013, Kortsmit et al., 2012, Miller et al., 2013, Wall et al., 2006, Wise et al., 1999, Bettendorff-Bakman et al., 2006, Bettendorff-Bakman et al., 2008) model the mechanisms of the infarcted region assuming that the wall of the infarcted area is the same as that of the healthy myocardium. In reality this cannot be accurate because once the heart wall is infarcted the wall has a tendency to begin thinning until the heart reaches failure (HF). In addition, even though the left ventricle is believed to contribute intensively in the failure of heart due to MI, the lack of FE biventricular models is clear (Kortsmit et al., 2012, Miller et al., 2013, Kortsmit et al., 2013). In this study, the FE models to be utilised are biventricular i.e. they include both LV and RV. The biventricular FE models are to be validated and verified providing information which is useful in understanding the cardiac mechanics of both healthy and infarcted hearts. The uniqueness of the blood pumping role of the heart is governed by the cardiac muscle. The contraction of cardiac muscle happens by the sliding filament mechanism. The most distinguishing factors of cardiac muscles are that they are short, fat, branched and interconnected (Granzier and Irving, 1995). Fibre orientation plays a critical role in understanding the cardiac mechanics of healthy and infarcted hearts.

There have been numerous studies on the structure of fibre in various experiments that were conducted on different species (Strijkers et al., 2009, Chen, 2005, Chen et al., 2005b, Mekkaoui et al., 2012, Chen et al., 2003b). Ayache *et al.* (2009) and (Rabben et al., 1999,

Ayache et al., 2009) proposed the fibre orientation of the LV of human heart. In their article they have used rule-based fibre orientation generation. In trying to assign the fibre direction, they have used a rule-based myocardial fibre generation algorithm. In these studies the sudden discontinuities between nodes was eliminated by averaging the distance between each node. The algorithm developed in the study was proposed for human heart but may be used in rat heart.

The model to accurately predict the myofibre orientation of the rat heart (both LV and RV) was developed (Savadjiev et al., 2012a). This model was developed such that the fibrous composite of the heart wall is predicted. Inaccurate orientation of the fibres can lead to a non-realistic simulation of the heart functionality and false local myocardial wall deformation. Simulation of cardiac biomechanics requires the definition of a vector representing the orientation of cardiac fibres inside a mesh of the geometry of the heart anatomy. This is achieved by defining the vector at each integration point of the element via an ORIENT subroutine. Fibre orientation across the heart wall is critical, since an alteration of its distribution or orientation may lead to non-realistic incomplete models. Therefore, this research addresses the question of modelling fibre structure of rat heart in a precise manner, thereby providing accurate understanding of stress and strain distribution across the myocardium. The active contraction is critically important in understanding the cardiac mechanics of beating heart; most researchers and work presented in the literature concentrated on FE models of passive filling of the heart in the LV (Chen et al., 2005b, Guccione et al., 1995a).

Passive and active myocardium properties play roles in the diastolic and systolic performance of the heart, respectively. Studies that attempted to simulate active contraction of the LV have done so by assuming that the fibre orientations of both the active and passive states are constant in longitudinal direction and for both LV and RV (Aikawa et al., 2001, Bovendeerd et al., 2009, Dorri et al., 2006, Göktepe et al., 2011). The active contraction simulation of rat heart has not yet been presented in the literature. The effects of mechanical properties of the infarct zone on the ventricular performance are different during systole and diastole. Furthermore, this study addresses the challenge of modelling active contraction of the heart in both LV and RV using available commercial FE modelling software called Abaqus®. This was achieved by implementing the constitutive Fung model suitable for simulating the active contraction in Abaqus®. The effects of MI on the LV mechanics during various MI stages are to be assessed by means of accurate assessment of myocardial fibre stress and cardiac performance metrics such as end-systolic and end-diastolic pressure volume relationships (ESPVR, EDPVR), ejection fraction (EF), stroke volume (SV) end-

diastolic pressure (EDP) relationship, and stroke volume (SV) end-diastolic volume (EDV) relationship. All these factors were found to be useful in providing further understanding of the importance of infarcted hearts.

2.5.1 Cardiac modelling software

There are various finite element software packages available to perform the FE analysis. In this study, the FEM software used is called *Abaqus® FEA* (Dassault Systemes, Providence, USA, 2007). Abaqus® has four core uses: computer fluid dynamics; computer aided engineering; and structural analysis. Abaqus® is a general purpose FE software programme, however, it has been used in various research studies in the area of cardiac mechanics (Ahn and Kim, 2010, Bilston, 2002, Hu and Desai, 2004, Liu et al., 2004, Suh et al., 1991).

Solid Edge® (Siemens PLM Software) is a commercial and mechanical design system software with exceptional tools for creating 3D models. This is mainly used in creating mechanical engineering drawings and as a design tool. The selection of this software was based on its ability to create 3D models based on exported Excel plots and its ability to develop the smoothing technique. The license used during this study is the student license which is freely provided by Siemens® PLM Software.

Segment® software is mainly used for segmentation of medical images. The software is freely available for research purposes. This software was developed mainly for use with cardiovascular MRI in mind. In addition, the software is written in Matlab and the source code is available which makes it easier for researchers to make modifications. The specific version used during this study is *Segment version 1.9 R9* (<http://segment.heiberg.se>).

2.5.2 Reconstruction of cardiac geometries

MRI has been used as a tool for the assessment of physiology and function in congenital heart disease in both postoperative and preoperative state (Belle et al., 1998, Carr et al., 2008, Chen et al., 2003a, Higuchi et al., 2009, Hu et al., 2005, Rudin et al., 1991, Shao et al., 1997, Stuckey et al., 2008, Williams et al., 1993, Zimmermann et al., 2006, Cao et al., 2008). It is generally accepted that MRI can accurately measure the blood flow parameters using phase-encoded velocity mapping, structural cardiac parameters and local and global deformation of the myocardial wall.

In various studies of ventricular mechanics and myocardial mechanics using computational modelling, the MRI data has been used for cardiac reconstruction of 3D geometries of the heart in different species (Lee et al., 2014d, Lee et al., 2013, Lee et al., 2014c, Lee et al., 2014a, Wenk et al., Wenk et al., 2013b, Wenk et al., 2011a, Klepach et al., 2012, Wang et al., 2014). There are several advantages of MRI: (i) there is no exposure to radiation, (ii) it is useful in showing soft tissues and (iii) it provides useful information on how blood flows and circulates.

2.5.3 Modelling myofibre orientation

Cardiac modelling helps one to understand the mechanisms of heart diseases and the understanding of these mechanisms leads researchers to come up with ways to cure and prevent these diseases and ultimately save lives. Therefore, when modelling cardiac electro-mechanics, the fibre orientations of the wall ventricles must be considered. Fibre orientation of the heart is critical for a heart during myocardial contraction and excitation. Mechanical function and electrical propagation of the heart significantly depend on the fibre orientation of ventricular myocardium. The fibre orientation of the myocardium has been found to affect current distribution during defibrillation shocks and is responsible for the stability of 3D reentrant activity. For a dog and pig the total rotation angle of the fibres is from 120° to 180° , respectively. The most distinguishing feature of ventricular fibre of myocardium is the gradual counter clockwise rotation throughout the heart wall.

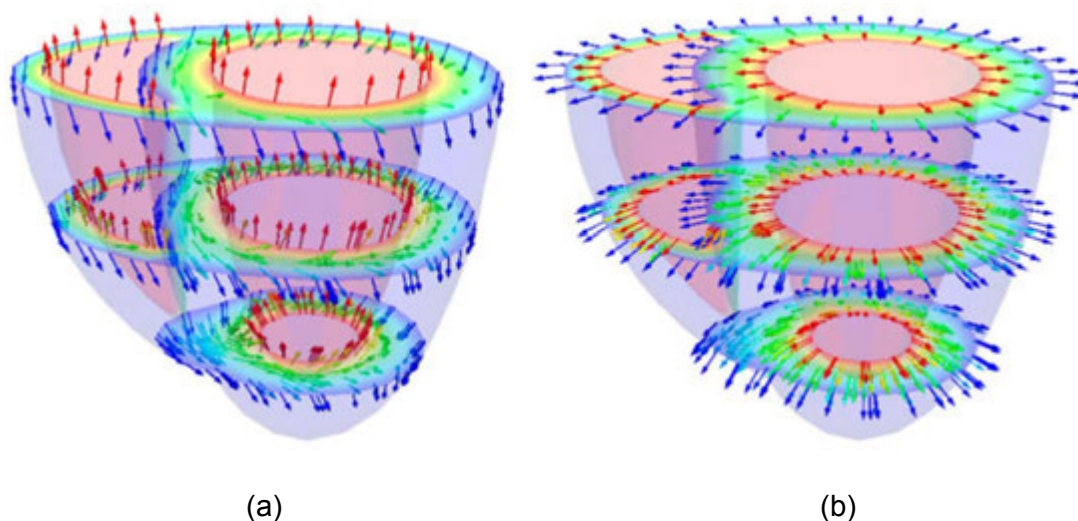


Figure 2-22: Fibre directions generated using Poisson interpolation. (a) Shows fibre directions at three locations along the long axis. (b) Showing normal directions at the corresponding slices. Blue colour represents the -70° and red colour represents $+80^{\circ}$ (Wong and Kuhl, 2014).

Muscle fibres (cells) of the heart are thought to be highly complex but they are found to have a highly organised pattern. It has been proven that the majority of the muscle fibres contribute to the reliability and global performance of the heart. As shown in Figure 2-22 (a) the ventricle walls are composed of a single helically folded muscular structure.

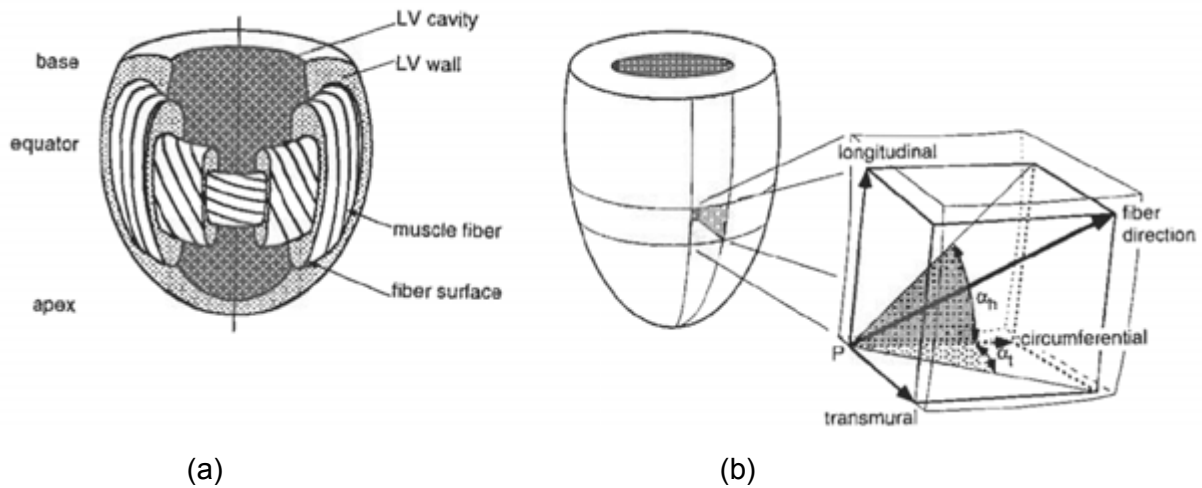


Figure 2-23: Myofibre orientation and fibre angle definition. (a) Schematic representation of fibre pathways in the left ventricular wall (b) Illustration of the helix fibre angle α_h and transverse fibre angle α_t use to quantify muscle fibre orientation (Bovendeerd et al., 2002).

It is evident that knowledge of cardiac and cardiovascular physiology was generally obtained and gathered through the use of animals (Rehwald et al., 1997, Berr et al., 2005, Bucholz et al., 2008, Chen et al., 2005a, Driehuys et al., 2008, Ma \bar{A} et al., 2005, Montet-Abou et al., 2006, Ohnishi et al., 2007, Slawson et al., 1998). The use of large animals like dogs for cardiovascular research has declined recently due to the cost associated with a large animal model. Therefore, in performing the cardiac modelling of rat heart it is critical that the fibre orientation of the ventricular wall be modelled precisely (See Figure 2-23). Most literature has reported on fibre orientation of the left ventricular wall of rat heart. Since this study is also including the right ventricular wall of the rat heart, it is vital that the fibre orientation of rat heart be used.

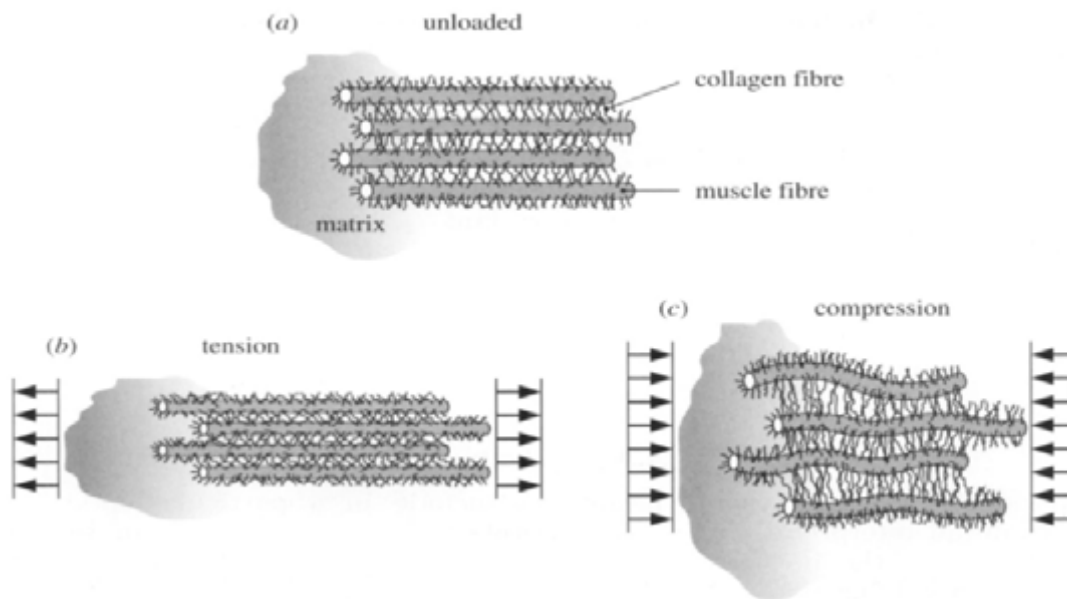


Figure 2-24: Schematic of the arrangement of muscle and collagen fibres and the surrounding matrix. (a) structure without loadings; (b) tensile load applied in the muscle fibre direction, showing decreased inter-fibre separation so that the collagen network bears load primarily in the muscle fibre direction; (c) compressive load applied in the muscle fibre direction, showing the muscle fibres buckled and lateral extension of the collagen network (Holzapfel and Ogden, 2009b)

Figure 2-24 shows the schematic structure of the embedded collagen muscle fibre subjected to compression and tension loadings. The loadings are subjected to loadings which are applied in the fibre direction. In Figure 2-24, it is evident that the muscle fibres are extended and the length of the inter-fibres decreased. There is a significant difference between the fibre orientation of different species (Healy et al., 2011, Chen et al., 2003a). The fibre structure of rabbit, sheep, and mouse was studied and compared. The studies concluded that the fibre orientation of the heart differs with species and the size of the heart. Therefore to study the cardiac mechanics of the rat heart, there is a need to look at the accurate fibre orientation of the rat heart because this has an influence on the mechanics.

In cardiac modelling of rat heart, both the fibre orientation of healthy heart tissue and infarcted heart needs to be explored. Simultaneously, the fibre orientation in normal (healthy heart of human, sheep, and rat) and remodelled myocardium in sheep was studied (Mekkaoui et al., 2012). This study found that in healthy heart, the sub-endocardial and sub--epicardial myofibres had both positive and negative helix angle (HA). The infarcted heart was found to have a significant positive shift in HA. The helix angle (HA) is defined by the inclination of the fibre out of the short axis plane. In the lateral wall of the left ventricle (LV), fibres with a positive HA course towards the antero-apex and those with a negative HA course towards the postero-apex. The fibre arrangement on the infarcted regions is different

from the healthy tissue. Many studies concluded that the fibre orientation in the infarcted region is at zero degrees (Bogaert et al., 1999, Chen et al., 2003a, De Bakker et al., 1988, de Baker et al., 1990, Gardner et al., 1985, Luke and Saffitz, 1991, Olivetti et al., 1990, Reese et al., 1995, Sosnovik et al., 2009, Ursell et al., 1985, Walker et al., 2005a, Wickline et al., 1992, Wu et al., 2006).

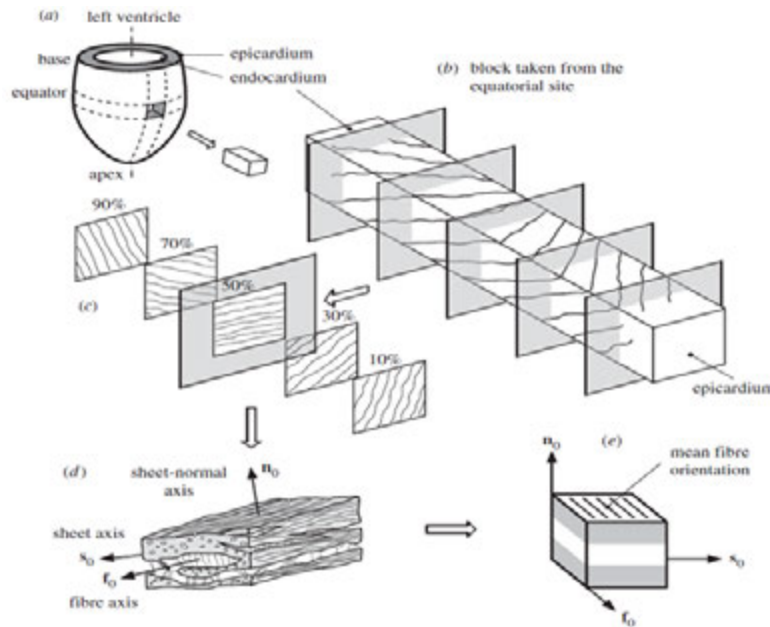


Figure 2-25: Schematic diagram of LV fibre orientation. (a) The left ventricle and a cut-out from equator. (b) The structure through the thickness from the epicardium to the endocardium. (c) Five longitudinal circumferential sections. (d) myocytes and collagen fibres. (e) a cube of layered tissue (Holzapfel and Ogden, 2009a).

The sketch shown in Figure 2-25 is the illustration of three-dimensional layered organisation of myocytes from the epicardium to the endocardium. Figure 2-25 shows and confirms that the muscle fibre orientations varies with location from side to side of the wall in the equatorial region, the principal muscle fibre direction rotates from $+53^{\circ}$ to $+70^{\circ}$ (sub-epicardial region) to approximately 0° in the mid-wall region to -53° to -70° (sub-endocardial region) with respect to the circumferential direction of the left and right ventricle. The understanding of myofibre direction in various animals models were studied using MRI (Healy et al., 2011, Chen, 2005, Chen et al., 2005b, LeGrice et al., 1995a). In this way, the accurate fibre orientation has been achieved.

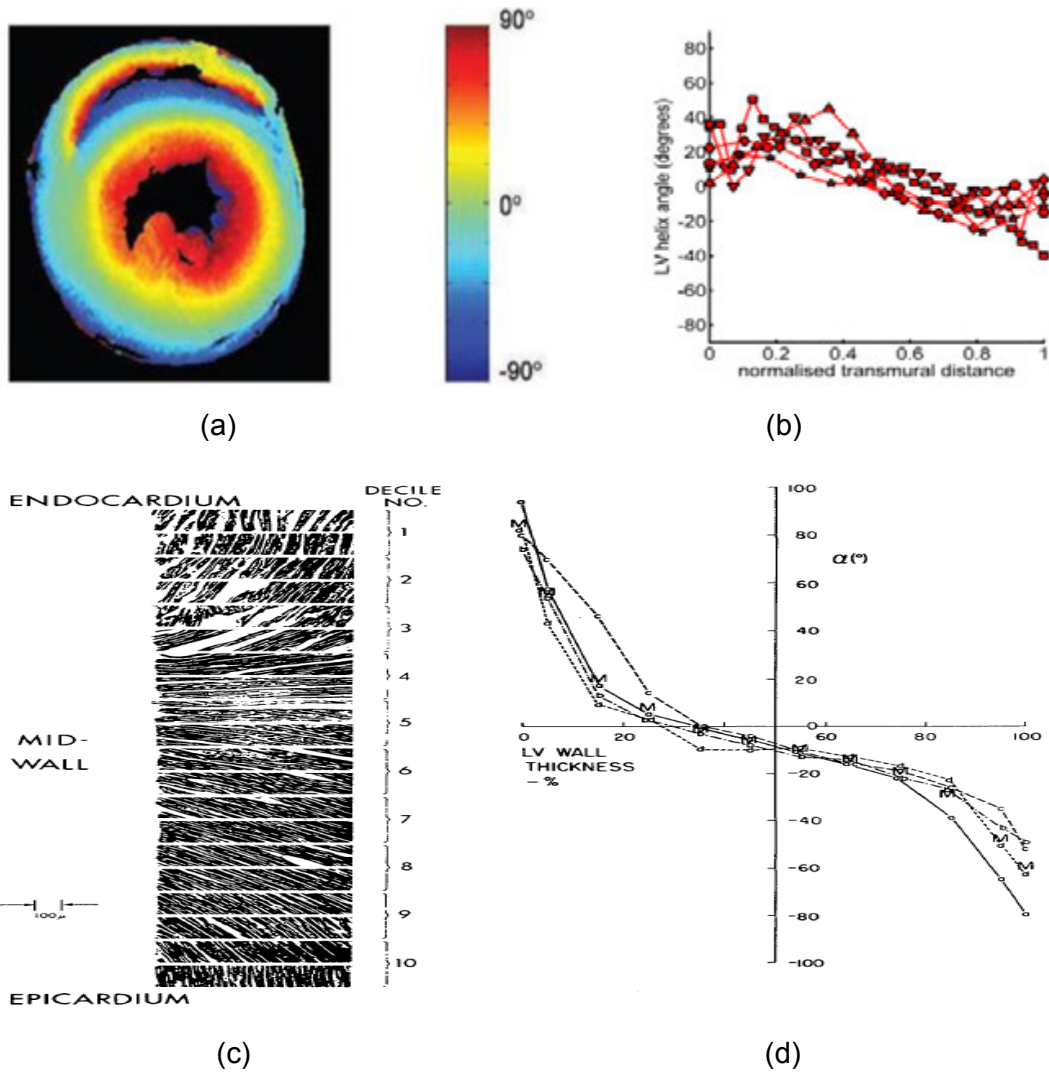


Figure 2-26: Helix angle of healthy heart. (a) Myofibre orientation of rat heart during systolic phase (Chen et al., 2003b). (b) LV angle variation of rat heart. Helix angle of healthy human heart (c) Myofibre orientation of human heart during diastolic phase. (d) LV angle variation of human heart (Streeter et al., 1969).

Figure 2-26 (a) shows the myofibre orientation on the rat heart from the endocardium to the epicardium. It can be deduced from Figure 2-26 (a) that the myofibre orientation at the endocardium is negative degree while on the epicardium the orientation is more positive degree. The helix angle on the LV of the rat hearts varies from -53° to $+54^{\circ}$ from endocardium to the epicardium on the short axis. While it is not clear on the myofibre orientation on the RV, it is safe to assume that the orientation is similar to that in the LV.

2.5.4 Mathematical representation of fibre orientation

There are various models available for the implementation of fibre orientation. The accuracy and the reliability of the present models need to be assessed so that they may be applied in the current study. In this study, two models will be discussed and assessed.

2.5.4.1 The Vavadjiev model

The main function of myofibres is to reinforce and strengthen the heart wall during passive and active contraction. (Savadjiev et al., 2012a, Savadjiev et al., 2007)) developed a model to accurately model the bundle of myofibre orientation of the heart. It was shown that the myofibre orientation takes the form of the generalised helicoid. The model created was based on smooth variation of curvature parameters across the myocardium walls of different species including the dog, the rat and the human. The study had addressed the challenge of analysing fibrous composite of the heart wall (Savadjiev et al., 2007, Savadjiev et al., 2012b). In this study the fibre orientation of the heart used the generalised helicoid model (GHM) to accurately model the fibre direction across the heart wall. This model insists on the use of accurate local coordinate frame.

Accordingly, the GHM expresses the fibre orientation across the heart wall in terms of the curvatures. The orientation theta (Θ) is a function of (x,y,z). The $\Theta(x,y,z)$ denotes the alignment in the x-y plane with respect to the x axis, which is aligned with the local fibre direction and with the z axis taken to be the component of the heart wall orthogonal to it. In order to ensure that the frame rotates smoothly and consistently, the reference frame must be chosen as detailed in (Savadjiev et al., 2012a) (See Table 2-2).

$$\theta(x, y, z) = \arctan\left(\frac{K_T x + K_N y}{K_N x + K_T y + 1}\right) + K_B z \quad (64)$$

where K_T , K_N and K_B are parameters of GHM.

Table 2-2: Quantitative assessment of the GHM fits for rat heart DT-MRI datasets (Savadjiev et al., 2012a)

*	K_B (rad/mm)	K_N (rad/mm)	K_T (rad/mm)	μ (rad)	k(-)
Rat 1	-0.19±0.14	0.008±0.053	0.003±0.053	0.109±0.003	128±9
Rat 2	-0.21±0.12	0.008±0.045	0.005±0.043	0.090±0.002	132±7
Rat 3	-0.22±0.11	0.008±0.043	0.006±0.049	0.107±0.003	121±9
Rat 4	-0.20±0.14	0.008±0.053	0.000±0.053	0.101±0.001	144±6
Average	-0.205±0.128	0.008±0.0495	0.0035±0.0495	0.1018±0.002	131±8

*All values reported as mean standard deviation. A neighbourhood of $5 \times 5 \times 5$ about the central voxel v is used for each fit. Errors are measured only for the voxels closest to v . K_B , K_N , and K_T are species-normalised values.

2.5.4.2 The Streeter model

The Streeter Model (Streeter et al., 1969) seems to go well with the way the ORIENT subroutine has been built in Abaqus®. The Vavadjie Model cannot be easily implemented in Abaqus® because it works mainly on the local coordinates systems. The local coordinates system in ORIENT currently cannot be accessed and this makes it difficult or impossible to implement the Vavadjie Model in Abaqus®.

During the contraction phase of the heart, the myocardium thickens significantly (Wenk et al., 2011a). It has been shown that as the heart contracts, the total change in fibre orientation from epicardium to endocardium remains quantitatively the same (McCulloch and Mazhari, 2001). This implies that the myofibre orientation at end-diastole and active filling remains the same (Ohnishi et al., 2007). Therefore, the fibre orientation data range used at end-diastole may also be used at end-systole simulation.

2.5.5 Cardiac constitutive models

The structure of soft tissues is related to its mechanical properties. Constitutive modelling is used to predict the mechanical behaviour subjected to generalised loadings. The cardiac behaviour of soft tissue myocardium can be expressed in various constitutive laws. The famous constitutive law is the Fung model. The Fung constitutive law is extensively used in modelling soft tissues. In understanding the mechanisms of ventricular mechanics, there are four important fundamentals:

- 1) Accurate 3D geometry representation;
- 2) Accurate myofibre orientation representation;
- 3) Realistic description of boundary conditions and continuum balance laws;

- 4) Accurate constitutive equations describing the material properties of the myocardium.

Hyperelastic, transversely isotropic strain energy W is given. The Fung model (Fung, 1984) is represented by the following function:

$$W = \frac{1}{2}C(e^Q - 1) \quad (65)$$

Q is a quadratic function of three principal strain components. In this case, the Q represents the special three dimensional isotropy with respect to fibre coordinate system.

$$Q = [b_f E_{11}^2 + b_t(E_{22}^2 + E_{33}^2 + E_{23}^2 + E_{32}^2) + b_{fs}(E_{12}^2 + E_{21}^2 + E_{13}^2 + E_{31}^2)] \quad (66)$$

where C , b_f , b_t and b_{fs} , are absolute constants which are independent of deformation and position in the body. In essence the main function C is to scale stresses. Where E_{11} , E_{22} and E_{33} are the fibre strain, cross-fibre strain and radial strain, respectively. E_{23} is the shear strain in the transverse plane and E_{12} and E_{13} are the shear strains in the fibre-cross-fibre and fibre-radial planes, respectively. The subscripts R, C and F represent the radial, cross-fibre and fibre directions, respectively.

2.6 Modelling the Infarct

Ventricular remodelling and tissue healing after myocardial infarction are dynamic and simultaneous processes (Zimmerman et al., 2004). With the aim of providing a basis to systematic development of MI therapies based on the understanding of the mechanical mechanisms involved, Holmes and colleagues presented a description of the mechanics of healing myocardial infarcts (Holmes et al., 2005) and distinguished four stages of myocardial infarction:

- (i) Acute ischemia (first minutes to hours after infarction),
- (ii) Necrotic phase (hours to 1 week after infarction),
- (iii) Fibrotic phase (1 week to 2-4 weeks after infarction), and
- (iv) Remodelling phase (2-4 weeks to 4-8 days after infarction).

The time points of these stages vary between species; lower numbers refer to small animals (e.g. rat), upper numbers refer to man (Abdessalem et al., 2010a, Abdessalem et al., 2010b). The myocardial infarction stages are also shown in Figure 2-12.

The computational biomechanics studies of damaged heart have been conducted by several authors (Bovendeerd *et al.*, 2009; Guccione *et al.*, 1995b; Klepach *et al.*, 2012; Lee *et al.*, 2014b; Usyk *et al.*, 2002; Wenk *et al.*, 2011a; Wenk *et al.*, 2011b; Wenk *et al.*, 2013b). One particular study by (Walker *et al.*, 2005b) considered the MRI based finite element analysis on the left ventricular aneurysm in sheep with myocardial infarction. In order to validate their FE models of left ventricular aneurysm, they have used the tagged MRI to determine systolic material parameters in three dimensional stress-strain relationships (Walker *et al.*, 2008, Walker *et al.*, 2005b). Moreover, they have also concentrated on bi-axial material testing in each heart. Even though they have used the precise geometry from the MRI data, it is unclear how they have modelled the infarct in heart. Increased left ventricular wall stress after myocardial infarction is associated with remodelling (Aikawa *et al.*, 2001).

A computational model that predicts reverse remodelling in human LV heart has been developed. In this study, the strain driven growth model was introduced (Lee *et al.*, 2014a). For heart to adequately pump blood, it must be able to contract. Therefore, the study of contractility using the antero-apically infarcted sheep heart was developed. In this study, the main limitation was that the interaction with the RV was neglected. By neglecting the interaction of LV with RV, the model provides results that are not comparable with the experiment due to overstretching in the infarct (Wenk *et al.*, 2011b). Furthermore, the contractility in the border zone of a human heart post myocardial infarction is studied by the finite element model. This model shows that there is substantially less contractility (25%-33%) in the border zone of the MI (Wenk *et al.*, 2011a). Furthermore, a coupled biventricular finite element and lumped-parameter circulatory system model of heart failure is presented. In this study, the modelling of the interaction between the heart and the circulatory system is presented by creating an animal-specific (canine) finite element biventricular model (Wenk *et al.*, 2013b). The growth and remodelling of the human heart LV after myocardial infarction was studied. The two computational models were developed in this study; one model was before operation where MI is present, and the other model is after operation where MI is surgically excluded (Klepach *et al.*, 2012).

Various researchers presented the computational models of non-treated myocardial infarction (Lee *et al.*, 2013, Wenk *et al.*, Wenk *et al.*, 2013b, Wenk *et al.*, 2011a, Klepach *et al.*, 2012, Wenk *et al.*, 2011b, Lee *et al.*, 2014a). For example, studies by Lee *et al.* (2014d) and (Wall *et al.*, 2006, Lee *et al.*, 2014c) produced the FE model of treated myocardial infarction. They have modified the model's mesh and regional material properties to simulate the expected change in the myocardium but the model is still oversimplified. The

assessment of left ventricular (LV) and right ventricle (RV) diastolic function usually relies on non-invasive measures of left ventricular relaxation and stiffness (Nucifora et al., 2010).

Figure 2-27 shows the data over a period of time on the advancement of anisotropy in the healing of ovine infarcts. It can be seen that in the control species, the longitudinal stresses are higher than the circumferential stresses. This observation changes from two-week after infarction to six weeks where the increase of circumferential stresses changes and presents higher magnitude as compared to the control when comparing with the longitudinal stresses.

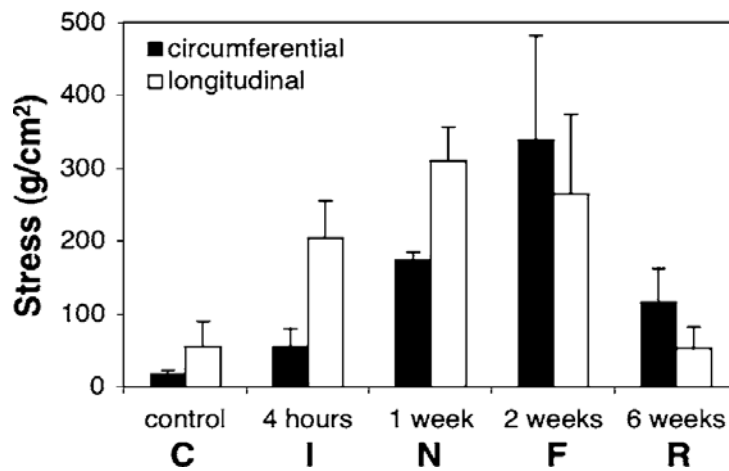


Figure 2-27: Longitudinal and circumferential stresses during various time points infarction (Holmes et al., 2005)

3 Simulation of Passive Filling in Healthy and Infarcted Hearts

3.1 Introduction

Development of a computational model for the simulation of local myocardial mechanics in the presence of MI is critical in the understanding of its mechanisms. The comparison of transmural stress and strain with the healthy and non-treated infarcted case is necessary in understanding the effect of infarcts on the local measures and global functioning of the heart.

Methods and models based on computational solid mechanics were developed utilising existing approaches established for the healthy and the non-treated infarcted heart. The developed methods and models were verified and validated to an extent feasible within the framework of this project. The Finite Element Method (FEM) was used to simulate solid mechanics of the myocardium i.e. strains and stresses in the myocardial wall. 3D geometrical models of the heart were developed from volumetric imaging information MRI data using solid modeller Solid Edge®. The 3D reconstructed geometries of the healthy and infarcted hearts are presented in section 3.2.2.

Validation of computational methods and models developed were performed using experimental data (collected in *in vivo* studies of related research not conducted by the applicant) and by comparison with data reported in literature. Simulation of myocardial biomechanics was conducted with emphasis on mechanics in infarct zone, wall stresses and strains including local restriction of deformation. Section 3.2.2 shows how the reconstruction of geometries were conducted using the Segment® segmentation software. The methodology used for the validation and verification of the heart models is presented in section 3.2.3. Section 3.2.5 further discusses the boundary conditions applied in modelling both the infarcted and non-infarct models. Section 3.3.3 shows and discusses the contours plots results of the healthy and infarct models. Validation of average stress and strain was done by comparing the study results with similar published works as presented in section 3.3.3.

3.2 Materials and Methods

3.2.1 MRI datasets

The data acquisition and details of the animal models have been described previously by (Saleh et al., 2012)). Cardiac magnetic resonance imaging (CMRI) was performed on both

healthy and infarct rat heart at the Cape Universities Brain Imaging Centre (CUBIC). CUBIC is a joint initiative between Stellenbosch University, the South African Medical Research Council, Siemens and the University of Cape Town. The scans were performed on a MAGNOM Allegra 3T MRI scanner (Siemens, Erlangen, Germany). The advantage of this brain-only scan is that it has a small bore, maximum gradient strength of $40 \text{ mT}\cdot\text{m}^{-1}$ and slew rate of $40 \text{ mT}\cdot\text{m}^{-1}$. In order to achieve the scanning of small animal like a rat, a circularly polarized 70 mm inner diameter birdcage radiofrequency (RF) coil was designed and built to receive and transmit the signal (Saleh et al., 2012).

The sequence used in this project was Gradient Echo (GE) sequence (fast low angle shot – FLASH – sequence). This sequence enables one to obtain and achieve cardiac images for both the functional and structural assessment of rat heart. To achieve high temporal resolution, the minimum number of segments of 1 k-space line per cardiac frame per cardiac cycle was attained. The slice thickness of 1 mm was achieved by reducing the time bandwidth product. The following parameters were used in acquiring short-axis images:

- field of view (FOV) = 60 mm;
- matrix size = 256 x 256;
- in-plane resolution 234 μm ;
- slice thickness 1.0 mm;
- TR 7.6-8.0 ms;
- TE 3.44-3.50 ms;
- flip angle 25° and 40° ;
- bandwidth 282 +/- 3 Hz/pixel;
- 3 signal averages.

The FLASH sequence was triggered by both ECG and respiration (Saleh et al., 2012).

3.2.2 Geometrical reconstruction

The left and right ventricle were segmented in short-axis MRI image stacks at end-systolic time points (Heiberg et al., 2010). From data of the segmented ventricular contours, 3D geometries were reconstructed using Solid Edge®. The stages of reconstruction of the bi-ventricular cardiac geometry are illustrated in Figure 3-1 (a), (b) and (c), whereas the fully reconstructed rat heart in end-diastolic configuration is displayed in Figure 3-3 (a) and (b). Figure 3-2 shows a set of cardiac short-axis MR images from base to apex of a rat heart after myocardial infarction with epicardial and endocardial segmented contours of left and right ventricle. Figure 3-2 shows segmentation in IGES file format of both left and right

ventricles using Solid Edge® software. Figure 3-3 (a) and (b) shows the meshed 3D geometry of the rat heart at end diastole ready for Finite Element Analysis (FEA). The FE mesh comprises 18569 tetrahedral elements.

The reconstruction of rat heart geometries was completed using Solid Edge ST5 version software (3D modelling). The MRI images were segmented using Segment® (<http://segment.heiberg.se>). Segment® provides an input file with both x and y coordinates of the endocardium and epicardium. These coordinates were used to create 3D heart models in Solid Edge®. Figure 3-1 shows the procedure followed to create the 3D rat heart models from MRI data.

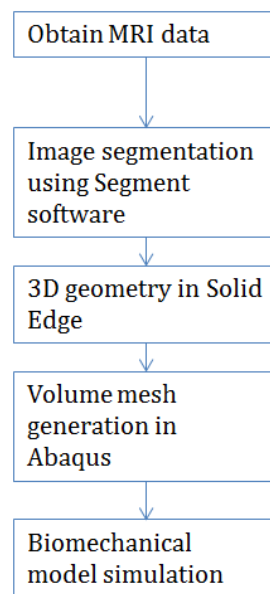


Figure 3-1: Procedure of creating biomechanical model of the rat heart

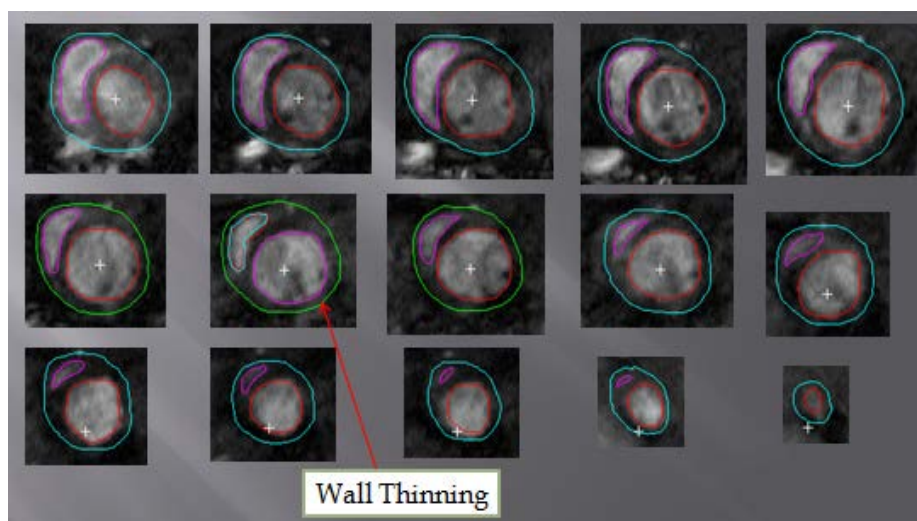


Figure 3-2: Set of short-axis MR images from base to apex of a rat heart at four-week after myocardial infarction. The contours of epicardium and endocardium of both left and right ventricle are highlighted.

3.2.3 Geometry verification

There was a need to validate the reconstructed models by using MRI data (experimental data). The aim of validating the constructed model was to ensure that the difference between the experimental data and the reconstructed 3D models is minimised. The ESV was constructed from MRI data. The segmented MRI data were used to create 3D rat heart models. In the current study, both the healthy and infarct models to simulate passive filling were validated by adjusting material constant C such that the LV and RV EDVs correspond with the MRI data. The wall volume of the reconstructed 3D model at end-diastole time point was then compared with the MRI data.

3.2.4 Tissue structure definition

3.2.4.1 Myofibre orientation

The fibre orientation adopted in this study was first reported by (Streeter et al., 1969) and used by (Beyar and Sideman, 1984b, Dang et al., 2005, Wenk et al.). In studying the stress and strains in the healthy myocardium of dog heart. Following the description given by (Streeter et al., 1969) of the fibres' orientation along the equator, the fibre angle at the reference state is postulated to vary from $+53^\circ$ at the endocardium to -53° at the epicardium relative to circumferential direction of the LV and RV for the healthy rat heart as reported by (Beyar and Sideman, 1984a). Figure 2-13 in section 2.3 defined clearly how circumferential direction is defined in the LV heart model. Several authors reported the transmural distribution of myofibre orientation during systolic and diastolic phases (LeGrice et al., 1995b, Usyk et al., 2002, Mekkaoui et al., 2012, Napadow et al., 2001). The fibre angle varies linearly from epicardium to endocardium. The fibre angle orientation was used in both the LV and RV including the septum. Equation (67) was used to define the fibre angles in both LV and RV. The fibre angle on the LV and RV of the rat hearts varies from -53° to $+53^\circ$ from endocardium to the epicardium on the short axis relative to circumferential direction (See Figure 3-3).

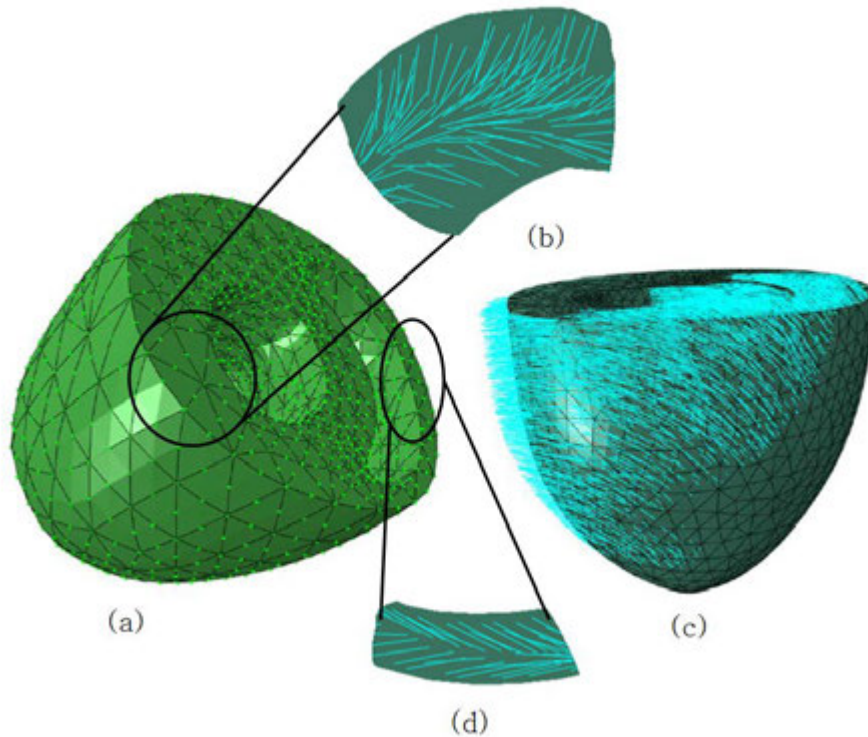


Figure 3-3: Fibre orientation in the biventricular rat heart model.

- (a) 3D healthy rat heart model showing nodes,
- (b) Fibre orientation in the LV of healthy rat heart model (showing how fibre angles are distributed from the endocardium to the epicardium)
- (c) 3D healthy rat heart model showing fibre angles distribution from the base to the apex and
- (d) Fibre orientation in the RV of healthy rat heart model.

The angle variation α as developed by (Beyar and Sideman, 1984a) is given by the following relationship;

$$\alpha = R \left(1 - \frac{2g}{h_0} \right) \quad (67)$$

Where g is the distance from the origin to the endocardium, h_0 is the left ventricle wall thickness and R is the maximum fibre angle at the endocardial surface (Beyar and Sideman, 1984a).

3.2.4.2 Resultant fibre orientation in Abaqus®

Figure 3-4 shows the fibre angles in the LV. The distribution of fibre plays a vital role in the accuracy of cardiac mechanics. As shown in Figure 3-3 the myofibre orientation on the LV are distributed such that the fibre angle distribution varies from -53° and the endocardium and

-53° on the epicardium relative to circumferential direction (Figure 2-13) in section 2.3 defined clearly how circumferential direction is defined in the LV heart model. As predicted by various studies in the literature the fibre alignment at the mid-wall is 0° . The ORIENT

subroutine written in Fortran 77 language was developed and implemented in an Abaqus® environment so that myofibre orientation is as accurate as required. This is critically important especially during systolic phase where the deformation of the myocardium depends mostly on the direction of the fibre (Guccione et al., 1993a).

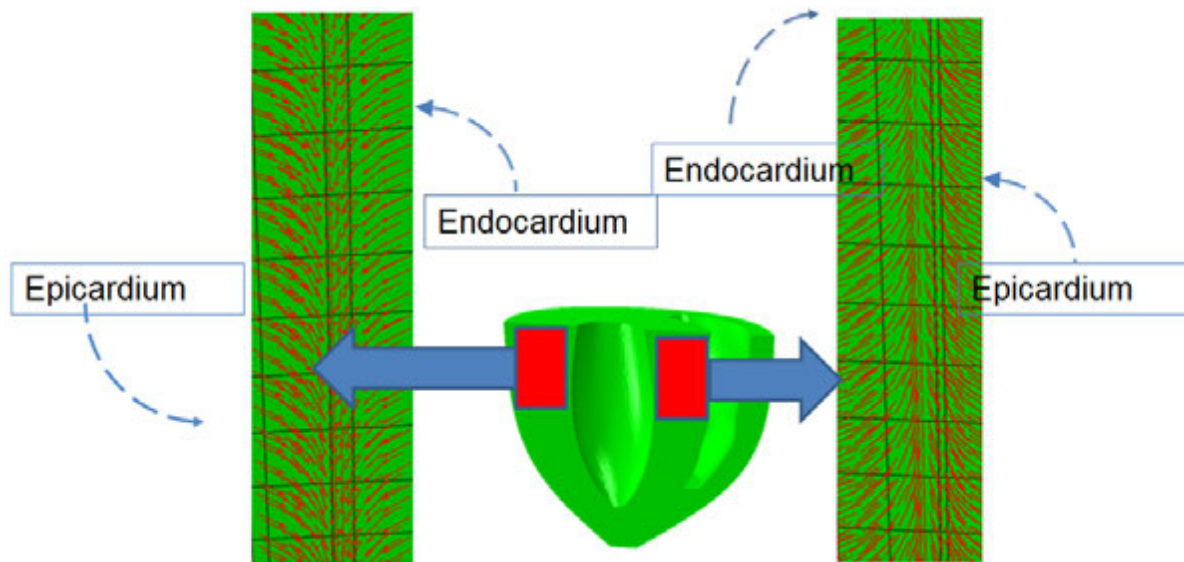


Figure 3-4: Fibre orientation of across the myocardial wall

3.2.4.3 Implementation of fibre orientation in Abaqus®

Implementation of fibre orientation in Abaqus® is done using the ORIENT subroutine. This subroutine is called at the start of the analysis at each location (material point, special-purpose element). An array T containing the direction cosines of the preferred orientation in terms of the default basis directions. T(1,1), T(2,1), T(3,1) give the (1, 2, 3) components of the first direction; T(1,2), T(2,2), T(3,2) give the second direction and T(1,3), T(2,3), T(3,3) represent the third directional cosine. The ORIENT subroutine in Abaqus® does not need the directions to be normalised. If the second direction is not orthogonal to the first direction, Abaqus®/Standard will orthogonalize and normalise the second direction with respect to the first. The third direction is then determined by taking the cross product of the first and second directions. For planar elements the first two directions must lie in the plane of the element. The ORIENT subroutine presented in Appendix B was used to generate the myofibre orientation shown in Figure 3-4.

The direction cosines can be represented as follows:

(1) The first direction of cosine can be represented by:

$$T(1,1) = \cos\phi\cos\theta$$

$$T(2,1) = \cos\phi\sin\theta$$

$$T(3,1) = \sin\phi$$

(2) The second direction of cosine is represented by:

$$T(1,2) = -\sin\theta$$

$$T(2,2) = \cos\theta$$

$$T(3,2) = 0$$

(3) The third direction of cosine is represented by:

$$T(1,3) = -\sin\phi\cos\theta$$

$$T(2,3) = -\sin\phi\sin\theta$$

Figure 3-3 (a) shows the tetrahedral elements applied on the healthy model in Abaqus®. Furthermore, Figure 3-3 (b) and (c) shows the myofibre orientation applied on the healthy model (LV and RV) using ORIENT subroutine in Abaqus®. The myofibre direction is applied at each integration point of the element as defined in the ORIENT subroutine.

3.2.5 Finite element modelling

3.2.5.1 Constitutive model of passive myocardium

Biventricular FE models were created for the healthy, two-week and four-week infarcted rat heart using a particular animal for healthy rat heart and another animal for both the infarcted hearts. These models were created by reconstructing MRI data. The ventricular walls of each rat heart model were meshed with approximately 18569 8-node tetrahedral elements. Each region, the healthy and infarct, was assigned different material properties. The quadratic node tetrahedron element has the ability to show the exact analytic solution for pure bending dominated problems even with a coarse mesh with only one element in depth.

Nearly incompressible, transversely isotropic hyperelastic constitutive law for passive myocardium used in this study was used by researchers (Guccione et al., 1995a, McCulloch et al., 1992, Guccione and McCulloch, 1993). The constitutive law was modelled with a predefined Fung model in Abaqus®. The passive material properties were represented by the strain energy function:

$$W = \frac{1}{2}C(e^Q - 1) \tag{68}$$

Q is a quadratic function of three principal strain components. In this case, the **Q** represent the special three dimensional isotropy with respect to fibre coordinate system.

$$Q = [b_f E_{11}^2 + b_t(E_{22}^2 + E_{33}^2 + E_{23}^2 + E_{32}^2) + b_{fs}(E_{12}^2 + E_{21}^2 + E_{13}^2 + E_{31}^2)] \quad (69)$$

where C, b_f , b_t and b_{fs} , are absolute parameters which are independent of deformation. In simplicity the main parameter C is to scale stresses. Where E_{11} , E_{22} and E_{33} are the fibre strain, cross-fibre strain and radial strain, respectively. E_{23} is the shear strain in the transverse plane and E_{12} and E_{13} are the shear strains in the fibre-cross-fibre and fibre-radial planes, respectively. The subscripts 1, 2 and 3 represent the radial, cross-fibre and fibre directions, respectively. Table 3-1 shows the constitutive model parameters used at end-diastole simulation.

The segmented MRI data were utilized to produce 3D rat heart models. In the present study, both the normal and infarct heart models to simulate passive (inactive) filling were validated by changing material parameter C such that the LV and RV EDVs comparable with the MRI data. The wall volume of the reconstructed 3D heart model at end-diastole time point was then contrasted and the MRI information. It was found that the stress scaling factor C to be used in this simulation was 0.002 MPa (See Table 3-1). The stress scaling factor was increased from 1.1 kPa to 2kPa such that the difference between the EDV of the model and EDV of the MRI is minimised.

Table 3-1: Constitutive model parameters for passive LV and RV heart model (Omens et al., 1993).

Parameter	Constants	Value	Units
Fibre strain coefficient	b_f	9.2	-
Cross-fibre strain coefficient	b_t	3	-
Shear strain coefficient	B_{fs}	3.7	-
Stress scaling factor	$C^\#$	0.002	MPa

[#] C value given based on the validated models. This value is different from (Omens et al., 1993)

Table 3-2: Stress scaling coefficients for healthy and infarcted (two-week and four-week after) rat heart models

	Healthy model	Two-week infarct model	Four-week infarct model
C - Stress scaling coefficient (Healthy myocardium/tissue)	0.002 MPa	0.002 MPa	0.002 MPa
C - Stress scaling coefficient (Infarcted myocardium/tissue)	n/a	0.02 MPa	0.02 MPa

Note: Two-week and four-week infarct models contain both the healthy and infarcted myocardium. The healthy heart model contains only healthy myocardium.

The full description of the strain function used for modelling the passive myocardium is found in section 2.4.5. Table 3-1 shows the constitutive modelling parameters used in healthy and infarcted rat heart models. Furthermore, Table 3-2 shows the stress scaling coefficient used in healthy, two-week and four-week infarct models. These parameters are applied such that the EDV of the model is close to that of the MRI data.

3.2.5.2 Boundary conditions

In order to simulate the diastolic phase of rat heart, the endocardial pressure was applied to the systolic phase model on both the left and right ventricles. A pressure of 4.8 kPa and 0.96 kPa was applied in left and right ventricles, respectively. The applied endocardial pressure was linearly increased from 0-4.8 kPa and 0-0.96 kPa for left and right ventricles, respectively. The MRI dataset was used to optimize the stress scaling coefficient of the strain energy function C. The calibration was achieved by increasing or decreasing the stress scaling coefficient of the strain energy function until the ESV volume is equal to the EDV measured by the MRI.

Figure 3-5 (a) shows how boundary conditions were applied on the basal surface of the heart model. All the nodes at the base were allowed to move in the radial direction. Furthermore, the nodes at the base were restrained from moving in the circumferential and longitudinal directions. Using the Abaqus® convention, the nodes at the basal surface were set such that $U_2 = U_3 = 0$. This convention was applied in both the LV and RV. Similarly, Figure 3-5 (b) shows the surfaces where the pressure was applied. It is important to note that the boundary conditions did not change. The same boundary conditions were applied in both the non-infarct model and the infarcted heart models.

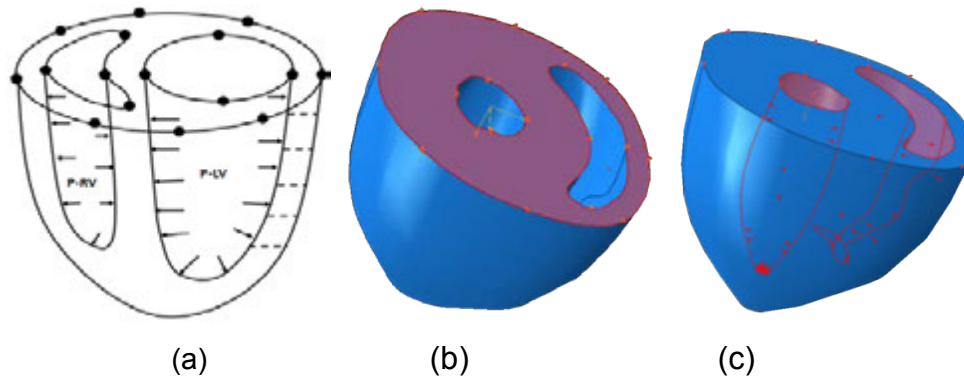


Figure 3-5: Boundary conditions at end-diastole. (a) Pressure boundary conditions and displacement constraints using the cylindrical coordinates. (b) Basal surface and (c) Endocardial pressure in LV and RV.

3.2.6 Data analysis and capturing

Since the infarct is on the LV, the LV was used to study the effect of infarct on heart performance. This was achieved by capturing the stresses and strains in radial, circumferential and longitudinal directions. This was achieved by creating paths so that the stresses and strains from the endocardium to the epicardium are recorded and plotted as a function of normalised myocardial length. The paths used in capturing stresses and strains are created from the base to the apex excluding the RV. The stresses and strains are recorded along the longitudinal direction of the heart at the centre. In other order the heart was divided into two halves along the longitudinal direction. Figure 3-6 shows the arrangement of paths to be used in further processing of results. Figure 3-6 (a) shows the paths in the two-week infarct model. In this model the paths E and F are in the infarcted region. Furthermore, Figure 3-6 (b) shows the model after four-week infarcts. In this model the paths C, D, E and F are in the infarcted regions. From Figure 3-6 (a) regions E and F are located on the infarcted tissue of the two-week infarct model. On the other side, Figure 3-6 (b) shows regions C, D, E and F of the infarcted tissue on the four-week infarcted tissue.

This section shows the results of the healthy, two-week and four-week infarcted 3D models of the rat heart. The stress and strains of healthy and infarcted regions will be compared. Figure 3-6 shows the arrangement of paths to be used in further processing of results. Figure 3-6 (a) and (b) shows the paths used in plotting the stresses and strains on the LV and RV for two and four-week infarcted 3D rat heart models.

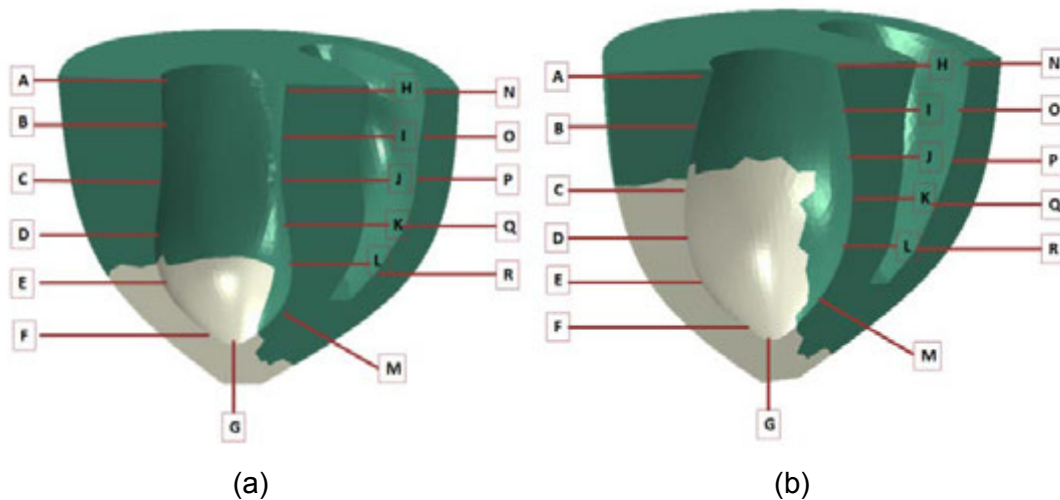


Figure 3-6: Paths utilized in further processing of results for
(a) two-week infarct and (b) four-week infarct models.

The endocardial volumes were obtained from Abaqus®. In Abaqus® endocardial volumetric readings cannot be obtained in a straightforward process. In order to achieve the volumetric readings (ESV and EDV) the following has been done:

- (a) Import the model as ... mesh;
- (b) The mesh is then converted from solid to shell model;
- (c) Delete the unwanted shell membranes;
- (d) Copy (mirror) the desired volume;
- (e) Convert mesh from tri to tet;
- (f) Measure the volume of both the mirrored and the original volumes;
- (g) Divide the volumetric reading by two to get a final volumetric reading.

Measurement of myocardial mass and wall volumes were obtained by using Solid Edge software. The reason for using Solid Edge is that Abaqus® does not offer the opportunity to measure epicardial areas and volumes.

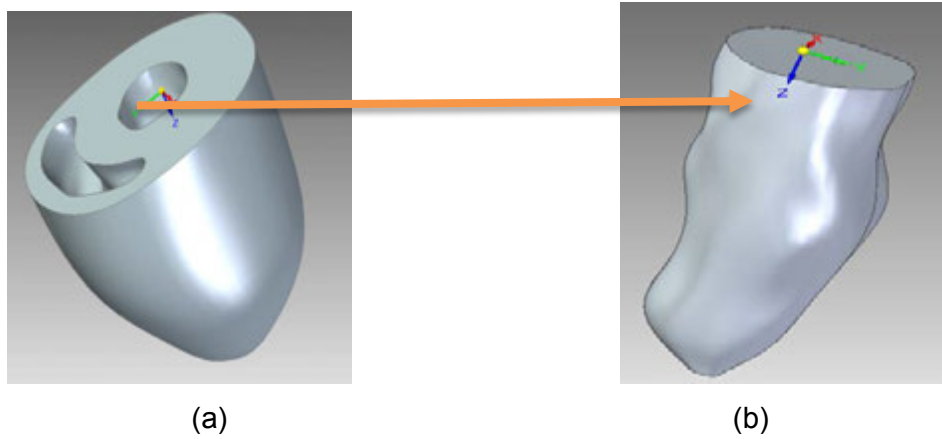


Figure 3-7: 3D healthy heart model. (a) Healthy rat heart with both LV and RV (b) Cavity measured volume of healthy LV;

3.3 Results

3.3.1 Reconstructed biventricular geometries

3.3.1.1 3D reconstructed model of healthy heart

Figure 3-8 (a) and (b) shows the 3D model for the healthy rat heart used as a control. The control model is constructed from the healthy heart MRI data. This is when the heart is assumed to be working normally and without myocardial infarction. The LV volume was measured to 79.8 μL . The myocardial volume seems to match the MRI. As shown in Figure 3-8 (d), the thickness of the free wall (LV) (myocardium) of the healthy rat heart model appears to be constant from the base to the apex. As expected, the thickness of the RV free wall is double the size of the LV free wall on the healthy model. The size of the septal wall is seen to be less than the free wall of the LV but also larger than the free wall of the RV on the healthy model (See Figure 3-8 (c)).

3.3.1.2 Dimensions of reconstructed healthy model

The geometrical reconstruction of the 3D model during end-systolic phase was conducted the same way as that which were reported in section 3.2.2. Table 3-3 shows the overall dimensions of the healthy heart model during ESV. The number of elements used before and after meshing is equal. The objective of Table 3-3 is to show how the dimensions of a healthy model were constructed from the MRI data. The overall dimension during end-systolic phase was validated by comparing it with the MRI data of the same model. The overall radius of the LV of the healthy model is labelled as g and has a magnitude of 2.784 mm. The distance from the centre of the LV to the epicardium is recorded to be 5.14 mm and is labelled as f . the thickness d of the RV has the magnitude of 1.136 mm (See Table 3-3).

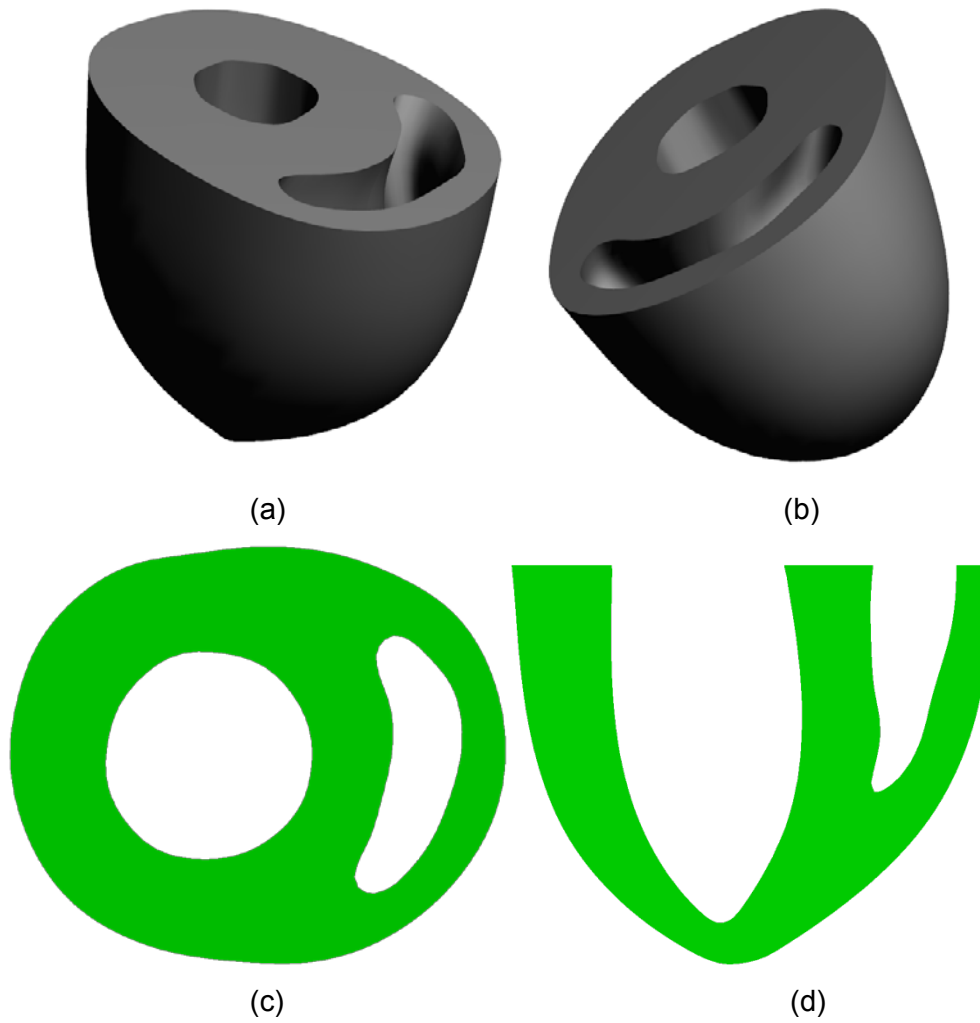


Figure 3-8: Short axis view taken at the middle of the long axis.
 (a) Healthy 3D rat heart model (b) Isometric view and Side view
 (c) Short axis healthy rat heart model. (d) Long axis healthy rat heart model.

Table 3-3: Geometrical physical dimensions at end-diastole

Parameters	After Mesh (mm)	Before Mesh (mm)
a	12.500	12.520
b	11.254	11.300
c	12.963	12.950
d	1.1362	1.1500
e	5.5835	5.6300
f	5.1440	5.1500
g	2.7838	2.7500
h	3.4585	3.4600
i	2.7675	2.7700
No. of elements	18569	18569

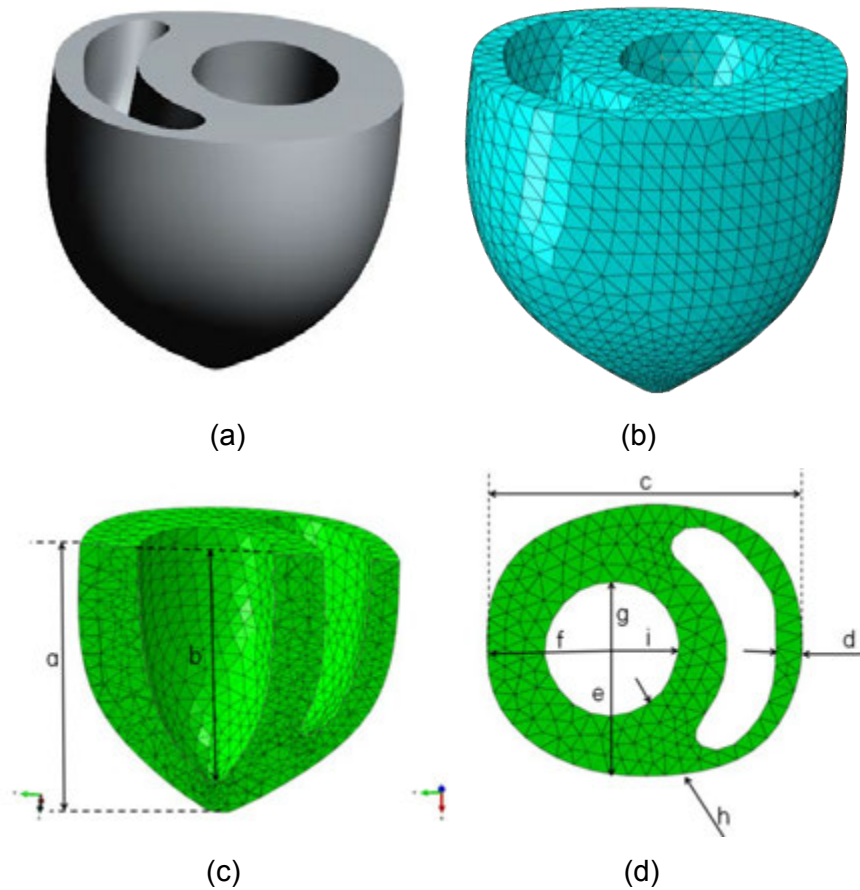


Figure 3-9: Reconstructed ventricular geometry and heart structure. (a) Pre mesh. (b) Post meshing. (c) The bi-ventricular healthy heart model (d) Basal surface slice cut parallel to the short axis.

3.3.1.3 MI model geometries

The cavity and wall volume of the infarcted rat heart models are different from the healthy models since the reconstructed geometries used underwent wall thinning and volume dilation. The same animal was used to reconstruct the infarcted heart models after two and four-week using the MRI data. However, the healthy rat heart model was reconstructed from a different animal. Due to the accuracy and non-automation of the segmentation process the cavity and wall volume may change. The wall, cavity and epicardial volumes of each model are shown in Table 3-4 and Table 3-5. Figure 3-10 shows the cross-sectional view of the healthy and infarct models considered in the current study. As shown in Figure 3-10 (b) and (c) the wall thinning and dilation occurs in both the infarcted hearts after two and four-week. The endocardial volume of the healthy model is small compared to the infarct models. In the infarct models, the wall thinning in the four-week infarct model is evident (See Figure 3-10(a) and (b)).

Figure 3-10 (a)-(c) shows the ESV of the healthy, two and four-week infarct models, respectively. The ESV was measured for each model at the end of the simulation. The ESV is calculated by Abaqus® software. Since the ESV is in two folds, the final ESV is divided into two to get the accurate volume. In Figure 3-11 (a)-(c), the healthy, two and four-week models are shown to elaborate the progression of myocardial wall thinning during the MI. Figure 3-11 (a) shows the healthy model reconstructed from the MRI data at the end of systole time point. Similarly, Figure 3-11 (a) and (b) show the 3D reconstructed two and four-week infarct models from MRI data. It can be seen that there is wall thinning in both the two and four-week infarct models. However, there is further thinning of the myocardial wall on the four-week infarct model as shown in Figure 3-11 (c).

Figure 3-12 shows the deformed and undeformed state of the FE rat models (healthy and infarct models). The long axis at the mid-ventricle through healthy and infarct models is shown by Figure 3-12 (a), (c) and (e). Similarly, the short axis at the mid-ventricle through healthy and infarct models is shown by Figure 3-12 (b), (d) and (f). What is important to note here are that the displacements in the infarcted regions of the two and four-week models are limited as compared to the healthy region.

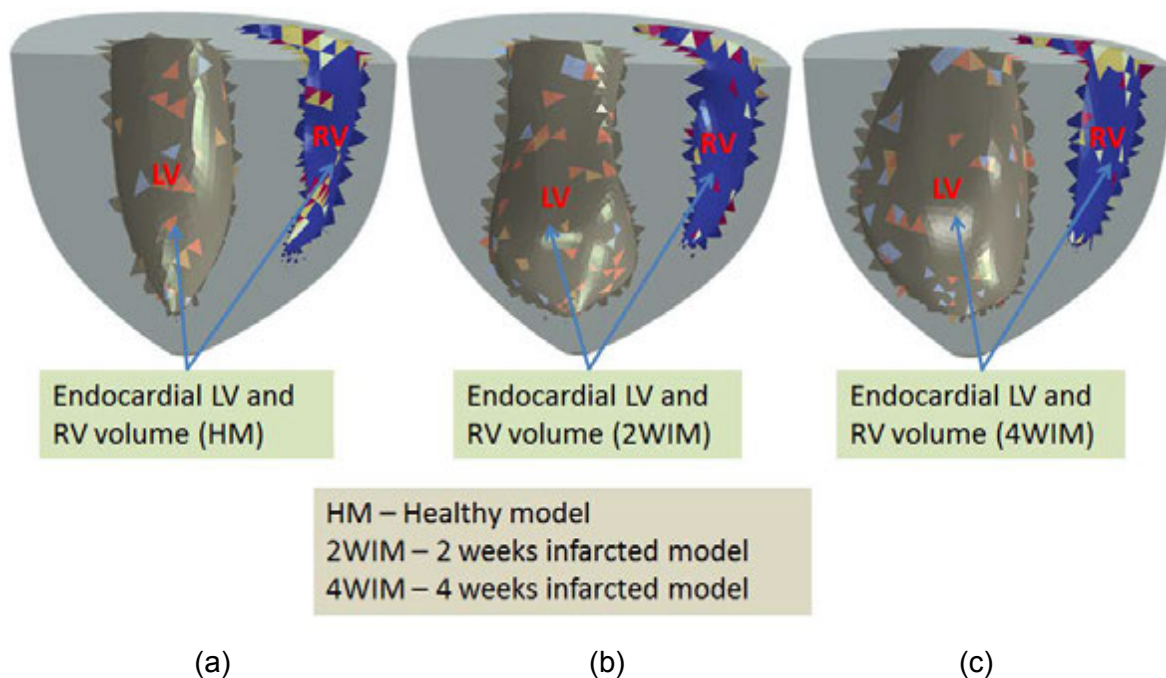


Figure 3-10: Endocardial view of LV and RV. (a) Healthy rat heart model (b) two-week infarcted and (c) four-week infarct models.

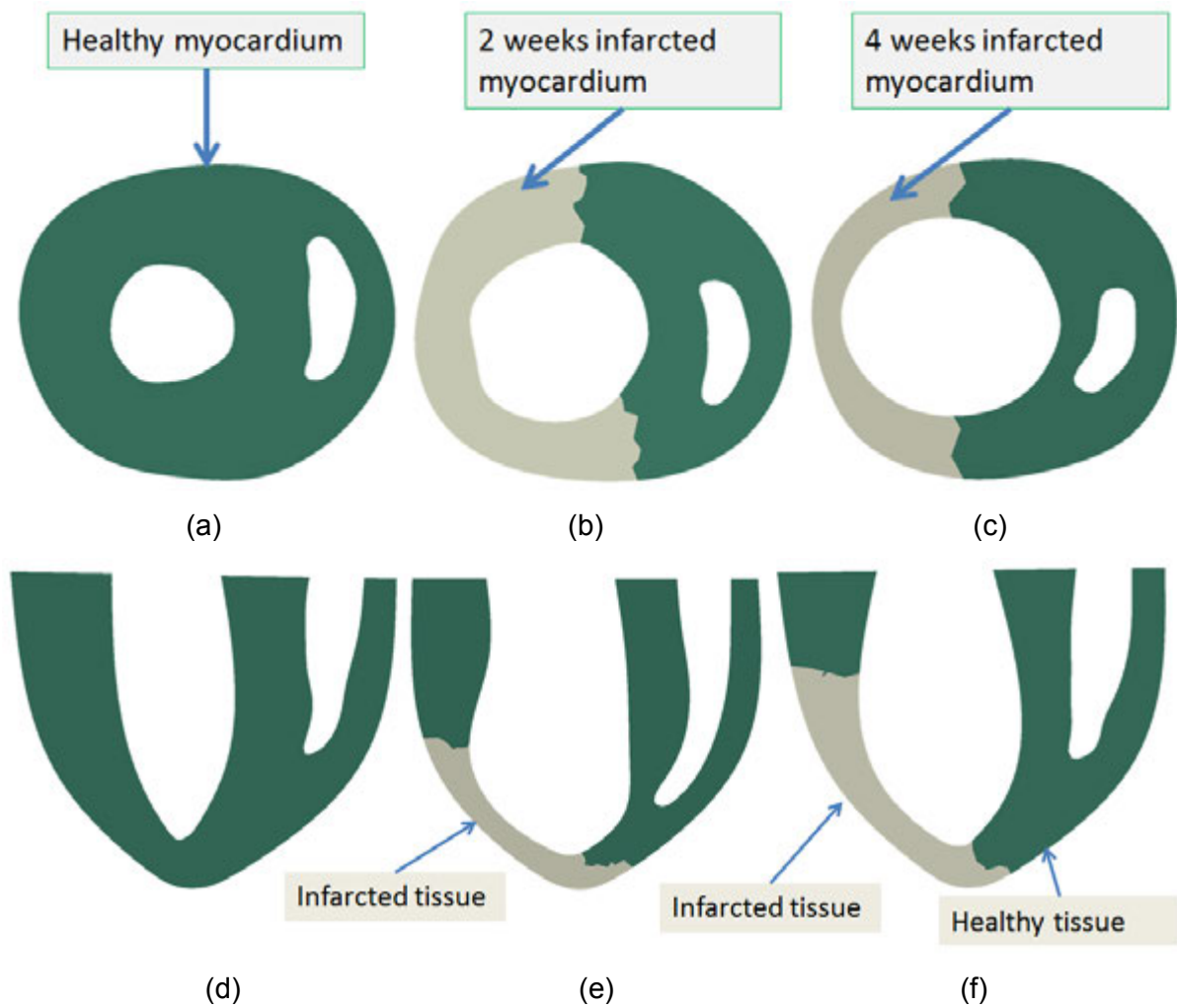


Figure 3-11: Short-axis slice at the mid-ventricle of 3D models. (a) Healthy rat heart model (b) Infarcted after two-week model (c) Infarcted after four-week model. Long-axis slice through the healthy and infarct region of 3D models. 3D models reconstructed models. (d) Healthy rat heart (e) Infarcted after two-week (f) Infarcted after four-week.

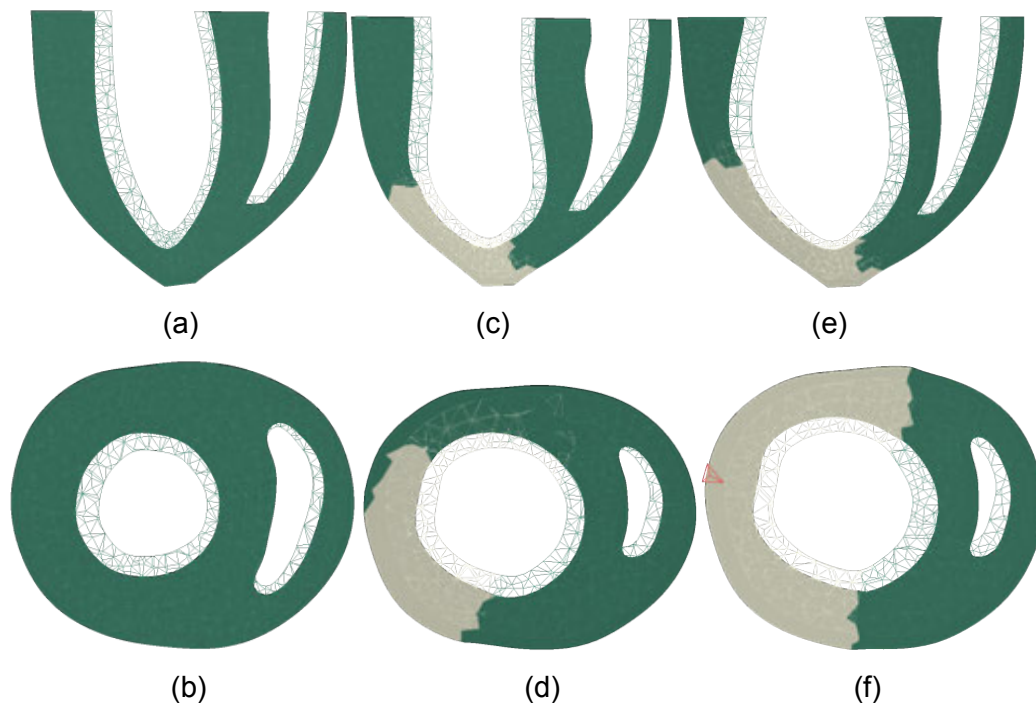


Figure 3-12: Undeformed and deformed state of the FE rat heart models. Short-axis slice at the mid-ventricle and long-axis slices through healthy and infarcted myocardium of (a) Healthy long-axis slice, (b) Healthy short-axis slice, (c) two-week infarcted long-axis slice, (d) two-week infarcted short-axis slice, (e) four-week infarcted long-axis slice and (f) four-week infarcted short-axis slice.

3.3.2 Comparison of models and MRI measurements

This section provides understanding of how the MRI data of 3D heart models were compared with reconstructed data. The results of verified and validated 3D models are presented in this section. Table 3-4 shows the epicardial reconstructed volume of the healthy and infarct models at two and four-week at end-diastole time point. There is an increase of both the epicardial volume and area in the infarct models. This is due to cavity dilation and the shrinkage of the infarcted region due to loading conditions including diastolic pressure loading on the rat heart. The errors between the mesh and segmented MRI data are 0.46 %, 0.41 % and 0.41 % for the non-infarcted and the infarct models, respectively. The errors were calculated by comparing the reconstructed volume and area with the MRI volume and area. The epicardial volume of the reconstructed two-week model is less than that of the healthy model by 3.13 %. Furthermore, the epicardial volume of the reconstructed four-week model is greater than that of the healthy model by 68.04 %. As shown in Table 3-4, the similar trends are shown when comparing the epicardial area of the two-week and four-week infarct model with the healthy model.

Table 3-5 shows the MRI data of the cavity and wall volumes and cavity area of healthy and infarct models. Table 3-5 shows the cavity and wall volumes and cavity area of healthy and infarct models considered in the current study. The object of Table 3-5 is to show how MI affects the cavity volume and area of the LV due to wall thinning of the myocardium. The wall volume is defined as the combination of the RV and LV (biventricular model) volumes. As shown in Table 3-5, the cavity volume of the healthy, two-week and four-week infarct models are 72.97 μL , 118.94 μL and 18616 μL , respectively. Similarly, as shown in Table 3-5 the cavity volume of the healthy, two-week and four-week infarct models are 108.74 mm^2 , 143.30 mm^2 and 166.48 mm^2 , respectively. The cavity volume of the healthy model is lower by 38.65 % and 99.61 % when compared to the two-week and four-week infarct models, respectively. Additionally, the cavity area of the healthy model is lower by 24.12 % and 34.98 % when compared to two-week and four-week infarct models, respectively.

The experimental error as shown in Table 3-6 for cavity and wall volumes and cavity area are well within error of 3 %. The error was obtained by comparing the cavity volume on the 3D constructed geometry and the MRI data using Solid Edge® and Segment® software. As shown in Table 3-7, the epicardial surface volume of bi-ventricular healthy and infarct models is presented. The aim of Table 3-7 is to show the difference between the epicardial surface volumes of different models. However, the surface epicardial area of all models is also considered for comparison purpose. The surface epicardial volume of the reconstructed healthy model has higher volume of 992.55 mm^3 when compared with the two-week infarct model. However, the surface epicardial volume of the reconstructed four-week infarct model has the highest volume of 1667.53 mm^3 . As a result, the analyses of the surface area for both models follow the same trend as the epicardial volume. The reason why the two-week infarct model has lower surface epicardial volume is that at two-week after infarction the rat heart tends to shrink due to structural changes including low collagen content in the infarcted region. When comparing the MRI epicardial volume, it was found that it has similar epicardial volume to the reconstructed 3D models of 0.46 %, 0.41 % and 0.41 % of healthy, two-week and four-week models, respectively. Table 3-8 shows the EDV of healthy and infarct models. When comparing the simulation cavity volume of the healthy and infarct models after simulation with MRI data, it was found that the errors of healthy, two-week and four-week heart models are 0.34 %, 1.36 % and 0.78 %, respectively. Table 3-9 shows the comparison of the ESV and EDV for the control (healthy) model with the average from the literature for rats. The 3D model of the healthy heart contracted from the MRI data shows the ESV and EDV of 207.5 μL and 72.97 μL , respectively. The average ESV and EDV from the literature

are 220.5 μL and 88.5 μL . The error of the ESV and EDV when comparing the MRI data and the literature is found to be 5.91 % and 17.55 %, respectively. Similarly as shown in Table 3-9, the reconstructed 3D model from the MRI data shows the ESV and EDV of 41.5 μL and 14.6 μL , respectively on the RV of the healthy heart.

Table 3-4: Comparison of reconstructed heart geometries - cavity and wall volumes and cavity area of LV for healthy, two-week and four-week infarct models.

	Cavity Volume (μL) (LV only)	Cavity Area (mm^2) (LV only)	Wall Volume (μL) (LV plus RV)
Healthy	72.965	108.740	763.870
Two-week infarct	118.940	143.300	707.147
Four-week infarct	186.160	166.480	656.515

Table 3-5: Comparison of MRI heart geometries - cavity and wall volumes and cavity area of LV for healthy, two-week and four-week infarct models.

	Cavity Volume (μL) (LV only)	Cavity Area (mm^2) (LV only)	Wall Volume (μL) (LV plus RV)
Healthy	73.56	106.23	765.67
Two-week infarct	117.20	141.45	710.78
Four-week infarct	188.62	168.54	650.52

Table 3-6: Comparison of error for MRI data and 3D reconstructed heart geometries.

	Cavity Volume (μL) (LV only)	Cavity Area (mm^2) (LV only)	Wall Volume (μL) (LV plus RV)
Healthy	0.808 %	2.363 %	0.235 %
Two-week infarct	1.485 %	1.308 %	0.511 %
Four-week infarct	1.304 %	1.222 %	0.922 %

Table 3-7: Model verification of healthy, two-week and four-week infarct models

	Healthy	Two-week Infarcted	Four-week Infarcted
Reconstructed model Epicardial Volume (mm ³)	992.55	961.32	1667.53
Reconstructed model Epicardial Area (mm ²)	532.64	517.99	735.62
MRI segmented volume (mm ³)	990.55	965.26	1660.65
Error (%)	-0.46	0.41	-0.41

Table 3-8: Comparison of cavity volumes for healthy, two-week and four-week infarct models at ED.

	(After simulation) Cavity Volume (μL)	(MRI data) Cavity Volume (μL)	Error (%)
Healthy	207.50	208.20	0.336%
Two-week infarct	261.72	265.32	1.357%
Four-week infarct	369.70	372.62	0.784%

Table 3-9: ESV and EDV of left and right ventricle predicted for healthy model

	Model (LV)	Average (LV) (Saleh et al., 2012)	Model (RV)
ESV (μL)	207.5	220.5	41.5
EDV (μL)	72.97	88.5	14.6

3.3.3 End-diastolic myocardial mechanics for healthy and infarcted ventricles

This section shows the results for passive filling of the healthy, two-week and four-week infarcted 3D models of the rat heart (i.e. at end-diastole time point). The stresses and strains of healthy and infarcted regions will be compared. As shown in Figure 3-6 (a), the paths that are in the infarcted region for the two-week infarct models are indicated by transmural paths E and F. Similarly, Figure 3-6 (b), the paths in the infarcted region for four-week infarct model are indicated by transmural paths C, D, E and F.

3.3.3.1 Distribution of end-diastolic stress and strain in left and right ventricle

This section shows the contour plots of stress and strain in the short and long axis of the healthy and infarct models. Figure 3-13 shows contour plots of the radial, circumferential and longitudinal stresses in the healthy, two-week and four-week infarcted 3D rat heart. The

radial stress values shown in Figure 3-13 agree with the pressure boundary conditions applied on the models. The pressure of 4.8 kPa was applied normal to the endocardial wall and there was no pressure applied on the epicardial wall. Figure 3-13 (a)-(c) shows that there is nearly -0.5 kPa radial stress on the epicardium and -4.83 kPa on the LV endocardium. The endocardium of the RV at the septal wall for the healthy model (see Figure 3-13 (a)) shows higher stress of -2.66 kPa as compared to the free wall which is showing -0.5 kPa on the endocardium.

Figure 3-13 (a) shows that the circumferential stresses are higher than the radial stresses in healthy and infarct models. The circumferential stress of the healthy model at the endocardium is shown to be 19.2kPa. This observer station is similar to two and four-week infarct models. When comparing the healthy model with the infarct models, the reduction of circumferential stresses in the infarcted region as compared to that of the healthy model was observed. The circumferential stresses increase from the endocardium (19.2 kPa) to the epicardium (-3.7 kPa) (see Figure 3-14 (d)-(f)). This is due to the fact that the pressure was applied normal to the endocardial wall. The circumferential stress in the RV remains stable for all models.

The longitudinal stresses of all models are shown in Figure 3-13 (i)-(h). The stresses in longitudinal direction are low compared to radial and circumferential directions. The longitudinal stress of the healthy model at the endocardium is shown to be 1.667 kPa at the free wall. However, on the same model, the longitudinal stress of the septal wall at the endocardium is shown to be -4.583 kPa. Additionally, the longitudinal stress of the septal wall at the epicardium is shown to be -2.500 kPa. This observation is similar to the two and four-week infarct models.

In the apex region, there is a numerical error due to the collapse of mesh. Therefore this region will not be focussed on during the results discussion. The septal wall, between the left ventricle and the right ventricle, shows a variation radial stress from -4.8 kPa on the endocardium of LV to -0.5 kPa on endocardium of the RV. This is because a pressure of 4.8 kPa and 0.96 kPa were applied on the LV and RV cavities, respectively.

Figure 3-14 and Figure 3-15 show the contour stress plots for passive filling simulation in the short-axis and long-axis, respectively. Figure 3-14 shows the contour plots of radial, circumferential and longitudinal stress in the mid-ventricle position (between apex and base). In Figure 3-15 the distribution of stresses in radial, circumferential and longitudinal directions

can be seen. The advantage of presenting contours in this manner is that the effect of infarct on the stress due to MI can be clearly visualised. For example, in Figure 3-14 (e), the distribution of radial stress at the endocardium is different from the radial stress for the four-week model as shown in Figure 3-14 (c). At the infarcted region (four-week rat heart model), the radial stress at the endocardium is shown to be -2.667 kPa. Similarly, at the infarcted region (four-week rat heart model), the radial stress at the endocardium is shown to be -4.833 kPa. This trend is observed in circumferential and longitudinal stresses of two and four-week models as shown in Figure 3-14 (e), (f), (g) and (h).

Figure 3-15 shows the contour plots of radial, circumferential and longitudinal stresses of healthy and infarct models. In Figure 3-15 the contours are only shown in the long-axis view. In Figure 3-15 it is not possible to view the stress distribution on the endocardial volume (cavity) of the rat heart models as shown in Figure 3-13. The emphasis of Figure 3-6 is to view the details of stress distribution (on healthy and infarcted regions) in long-axis. Figure 3-15 (a) shows that the radial stresses of the healthy model at the apex are low compared to the radial stresses at the free wall (LV) and septal wall. However, the septal wall of the healthy model is still showing that it has high radial, circumferential and longitudinal stresses at the endocardium when compared with free wall (LV).

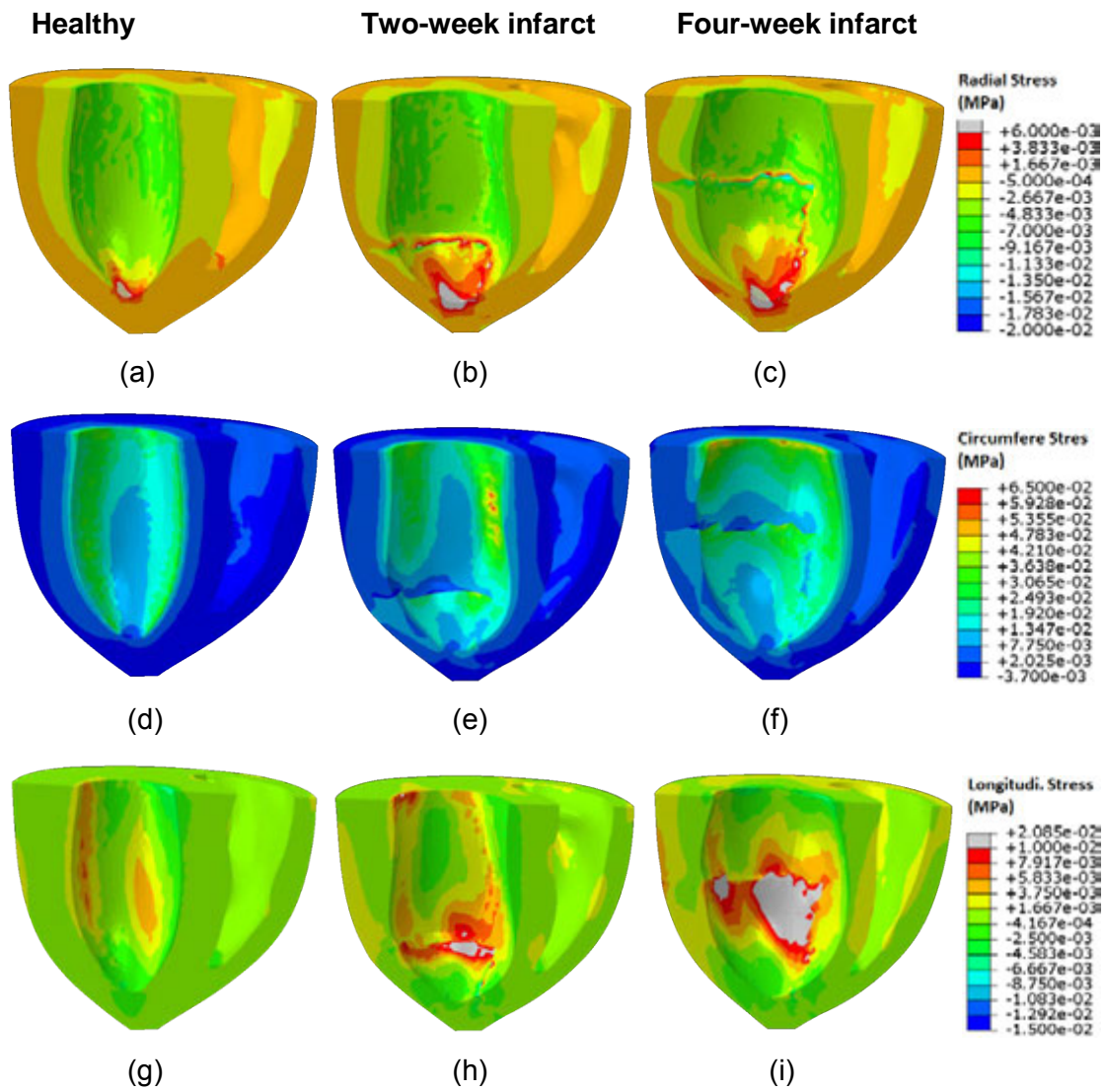


Figure 3-13: Contour plots of end-diastolic stress in in the healthy, two-week and four-week infarct models. (a)-(c): Radial stress, (d)-(f):Circumferential stress, and (g)-(i): Longitudinal stress.

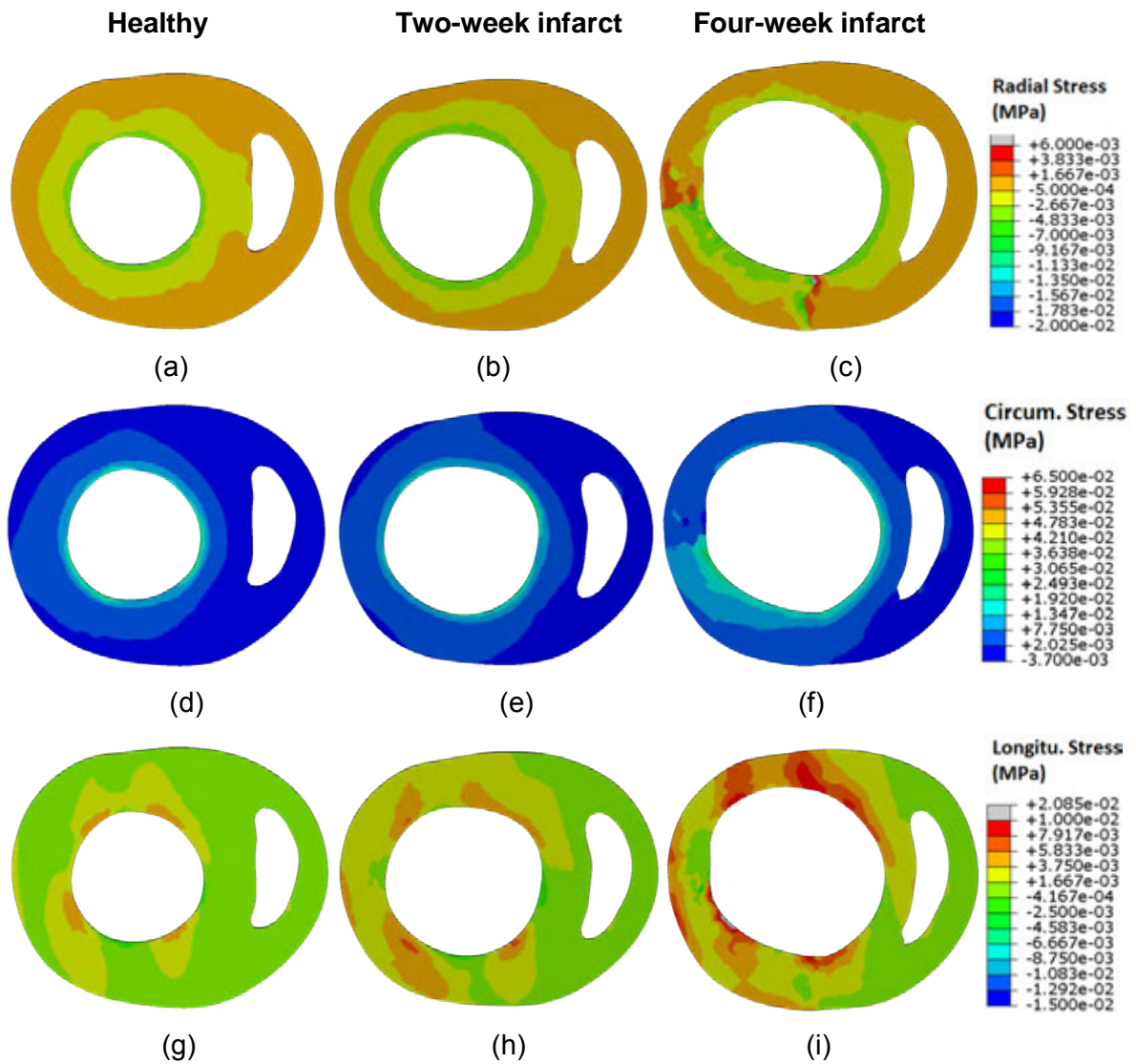


Figure 3-14: Contour plots of end-diastolic stress in short axis cross section equidistant between the base and the apex for the healthy, two-week and four-week infarct models. (a)-(c): Radial stress, (d)-(f): Circumferential stress, and (g)-(i): Longitudinal stress.

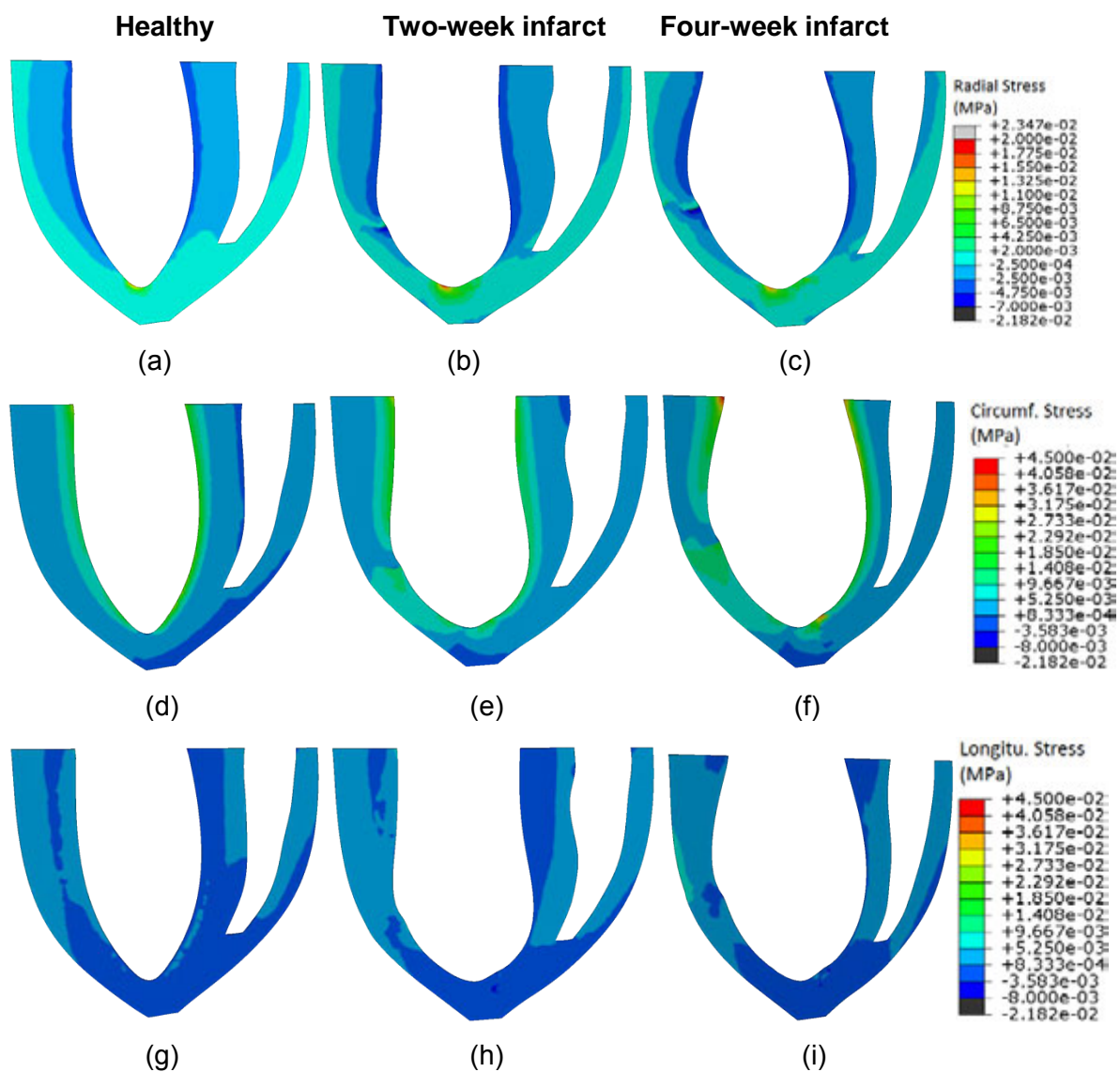


Figure 3-15: Contour plots of end-diastolic stress in central long axis cross section for the healthy, two-week and four-week infarct models. (a)-(c): Radial stress, (d)-(f): Circumferential stress, and (g)-(i): Longitudinal stress.

Figure 3-16 (a)-(i) shows the radial, circumferential and longitudinal strain contour line on healthy, two-week and four-week infarcted heart models, respectively. As shown in Figure 3-16 (a), the radial strain on the free wall (LV) was found to be -0.45 and -0.05667 on the endocardium and epicardium, respectively. In addition, as shown in Figure 3-16 (a), the radial strain on the septal wall was found to be -0.3517 and -0.1058 on the endocardium and epicardium, respectively. When comparing the radial strain of the healthy model, it is concluded that at the free wall on the endocardium, the radial strain is higher than the radial strain at the septal wall at the endocardium by 21.84%. In addition, when comparing the radial strain of the healthy model, it is concluded that at the free wall on the endocardium, the radial strain is lower than the radial strain at the septal wall at the endocardium by 45.28 %. When studying the radial strain at the infarcted region of the free wall (LV) of two-week and four-week models, it was found that the strain of -0.0075 was recorded (See Figure 3-16 (b) and (c)). The radial strain at the free wall (LV) at the healthy myocardium is higher than the infarcted region by 98.33 %.

The circumferential strain in the free wall (LV) of the healthy model (Figure 3-16 (d)) at the endocardium was found to be 0.2887 and 0.00625, respectively. Furthermore, the circumferential strain in the septal wall of the healthy model (Figure 3-16 (d)) at the endocardium was found to be -0.3025 and -0.05667, respectively. Also, when comparing the circumferential strain on the infarcted region of two and four-week models with the healthy model, it was found that there is a circumferential strain of -0.0075 and -0.45 at the free wall of the healthy and infarcted myocardium, respectively. When comparing the circumferential strain at the endocardium of the healthy model at the free wall (LV), it was found that the circumferential strain at the free wall was lower by 4.56 % when compared to the septal wall at the endocardium. Moreover, when comparing the circumferential strain at the endocardium of the healthy model at the free wall (LV), it was found that the circumferential strain at the free wall is lower by 88.97 % when compared to the septal wall at the endocardium. The radial strain at the free wall on the endocardium of the healthy model is higher than the radial strain at the septal wall. This is contrary to the circumferential strain, as the circumferential strain at the free wall on the endocardium of the healthy model is lower than the circumferential strain at the septal wall.

There is a reduction of strain in both infarct models at the infarcted region. The radial, circumferential and longitudinal strains of the healthy model were reduced from -0.45 to -0.05667 on the infarcted heart models. This is due to the fact that the material properties at these regions are modified and the scaling stress factor was increased compared to healthy

tissue by 10 times from 0.02 kPa to 0.2 kPa. In addition, the left ventricle of the healthy model deforms symmetrically in the healthy myocardium from the pericardium to the endocardium. The two-week infarcted heart, Figure 3-18 (b), (e) and (h), has a smaller infarct region of about 16% of LV wall volume whereas the infarcted at four-week (as shown in Figure 3-18 (c), (f) and (i)) is about 26 % of LV wall volume. The strain distribution in the RV is similar in all models as the RV wall was not infarcted.

Figure 3-16 (g)-(i) shows the longitudinal strain of the healthy, two and four-week infarct models. The contours of the longitudinal strain are not uniform in the same way as the radial and circumferential strain as shown in Figure 3-16 (a)-(f). What is important to note in Figure 3-16 (g)-(i), is that all models have the longitudinal strain of 0.1900 at the mid-ventricular position (between apex and base) on both the free wall (LV) and septal walls. This behaviour is different from what was observed in the radial and circumferential strain. When compared with the healthy model, the infarct models have a lower longitudinal strain of 0.0025.

The aim of Figure 3-17 is to view the strain contour of healthy and infarct models in the short-axis view. This view provides the strain distribution differentiation in the healthy and infarct models. In Figure 3-17 (a), it can be seen that the radial strain of the healthy model at the endocardium is higher than the radial strain at the epicardium position. When looking at Figure 3-17 (b and (c), it can be seen that the radial strain at the endocardium for two and four-week models is lower than the radial strain in the healthy model. Similarly, it can be seen that the circumferential strain is higher at the healthy model and lower for the two and four-week models, as shown in Figure 3-17 (d)-(f). In Figure 3-17 (g)-(i), it was found that the longitudinal strain of the free wall (LV) on the endocardium is higher than the infarct models. The longitudinal strain of the free wall (LV) on the endocardium of healthy, two and four-week models are found to be 0.1400, 0.06667 and 0.03, respectively. However, on the septal wall (endocardium of LV), it was found that the longitudinal strain of the healthy model is lower than the longitudinal strain of the two and four-week infarct models. The longitudinal strain of the septal wall (endocardium of LV) on the endocardium of healthy, two and four-week models are found to be, 0.06667 and 0.140 and 0.140, respectively.

All three hearts have greater strain in the radial direction (Figure 3-18 (a)-(c)) than in the circumferential direction (Figure 3-18 (d)-(f)) and longitudinal directions (Figure 3-19 (g)-(i)). However, the circumferential strains in the infarcted regions for both two-week and four-week infarcted hearts show a reduction of strain compared to the healthy heart. This is due

to the change of material properties on the region. It is important to note that even if there is a reduction of circumferential strains in the infarcted regions, the radial strains in the infarcted regions remain small as compared to the circumferential. Figure 3-18 (g)-(i) indicates that the strain in the longitudinal direction is minimal compared to the radial and circumferential strain. This means that the infarcted regions on the heart models have lower strain in the longitudinal direction when compared with the radial and circumferential strains. This clearly conforms to what was expected. Figure 3-17 and Figure 3-18 show the contour strain plots for passive filling simulation in the short-axis and long-axis, respectively.

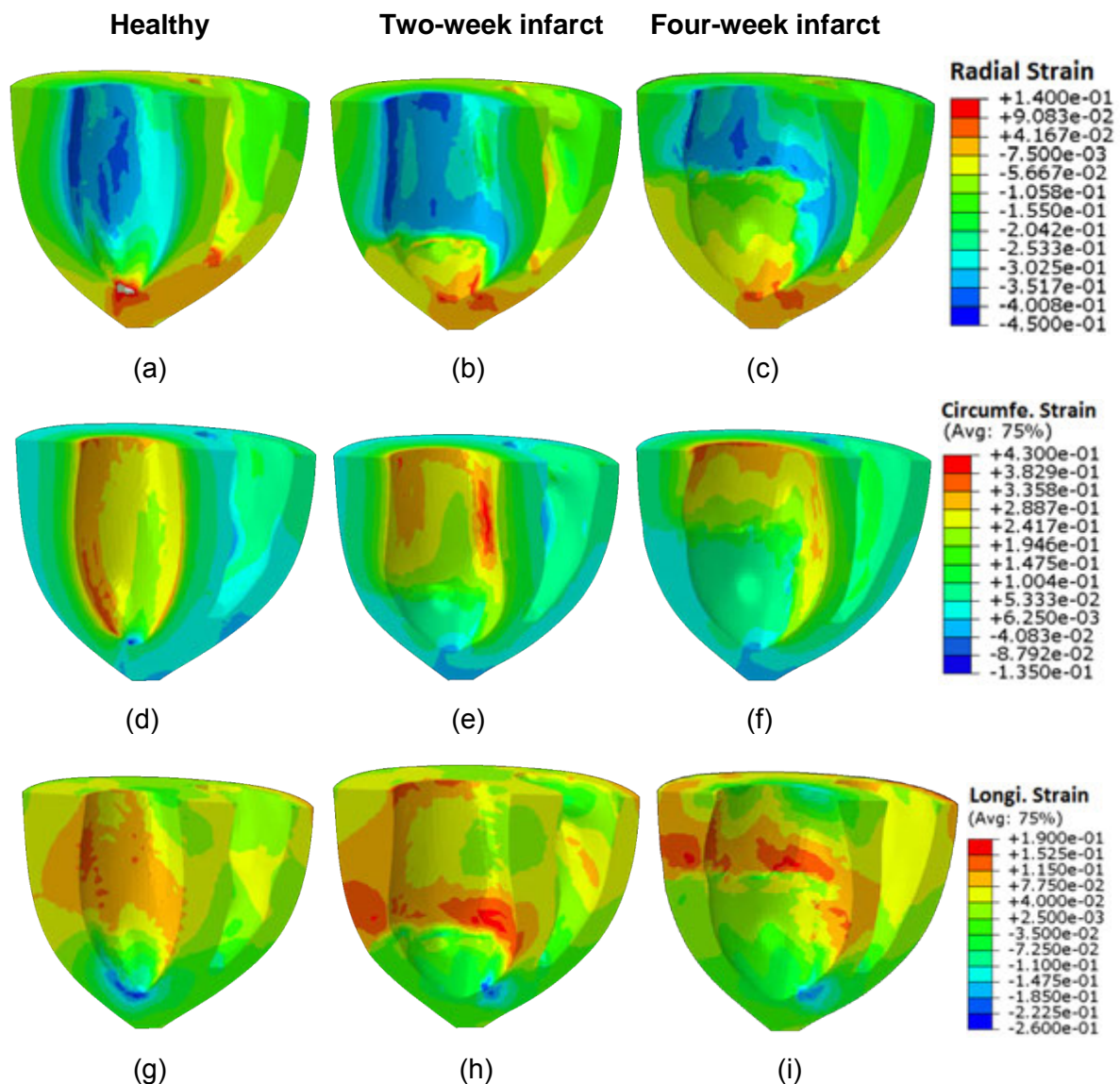


Figure 3-16: Contour plots of end-diastolic strain in central long axis cross section and endocardium for the healthy, two-week and four-week infarct models. (a)-(c): Radial strain, (d)-(f):Circumferential strain, and (g)-(i): Longitudinal strain .

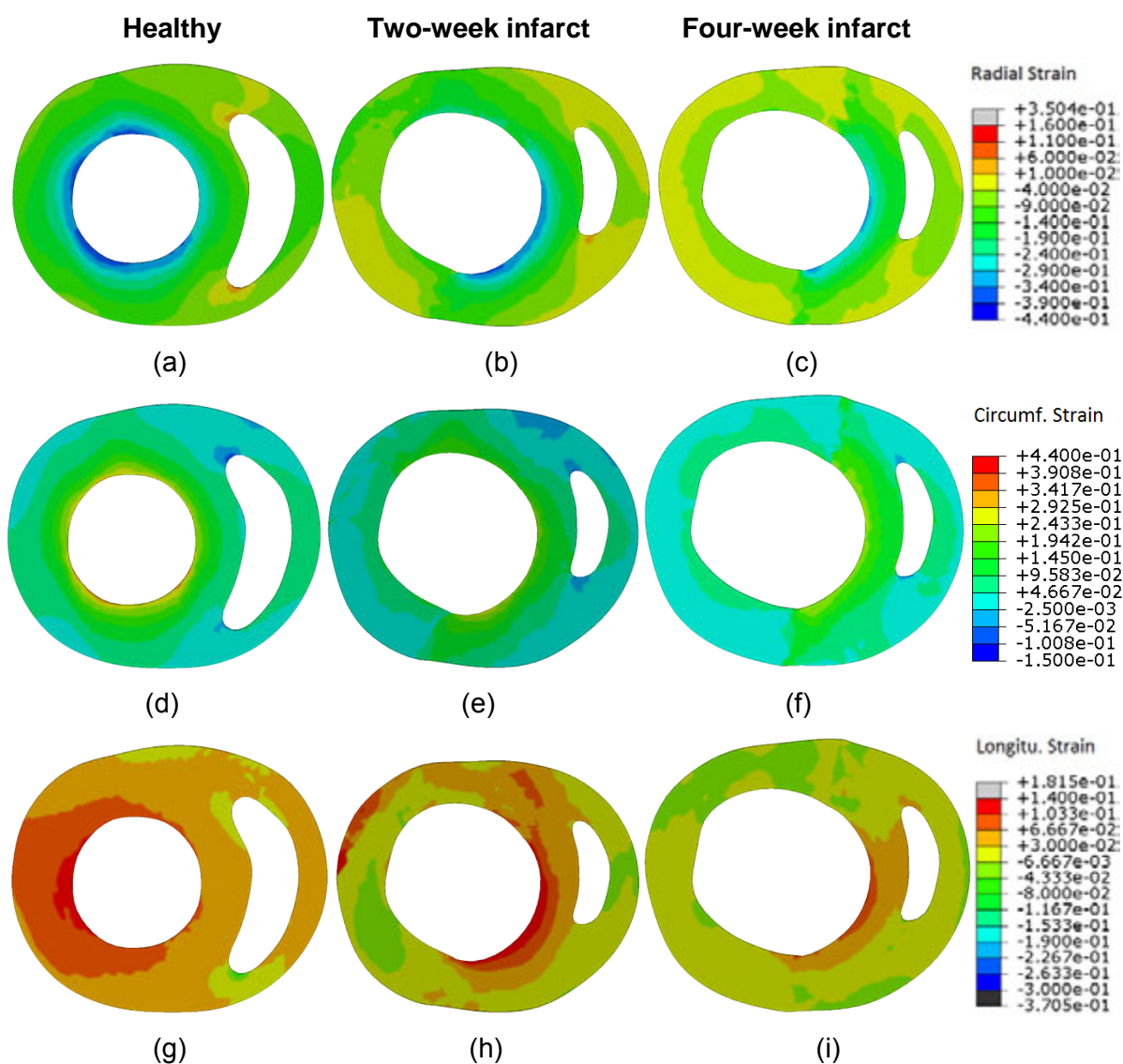


Figure 3-17: Contour plots of end-diastolic strain in short axis cross section equidistant between the base and the apex for the healthy, two-week and four-week infarct models. (a)-(c): Radial strain, (d)-(f): Circumferential strain, and (g)-(i): Longitudinal strain.

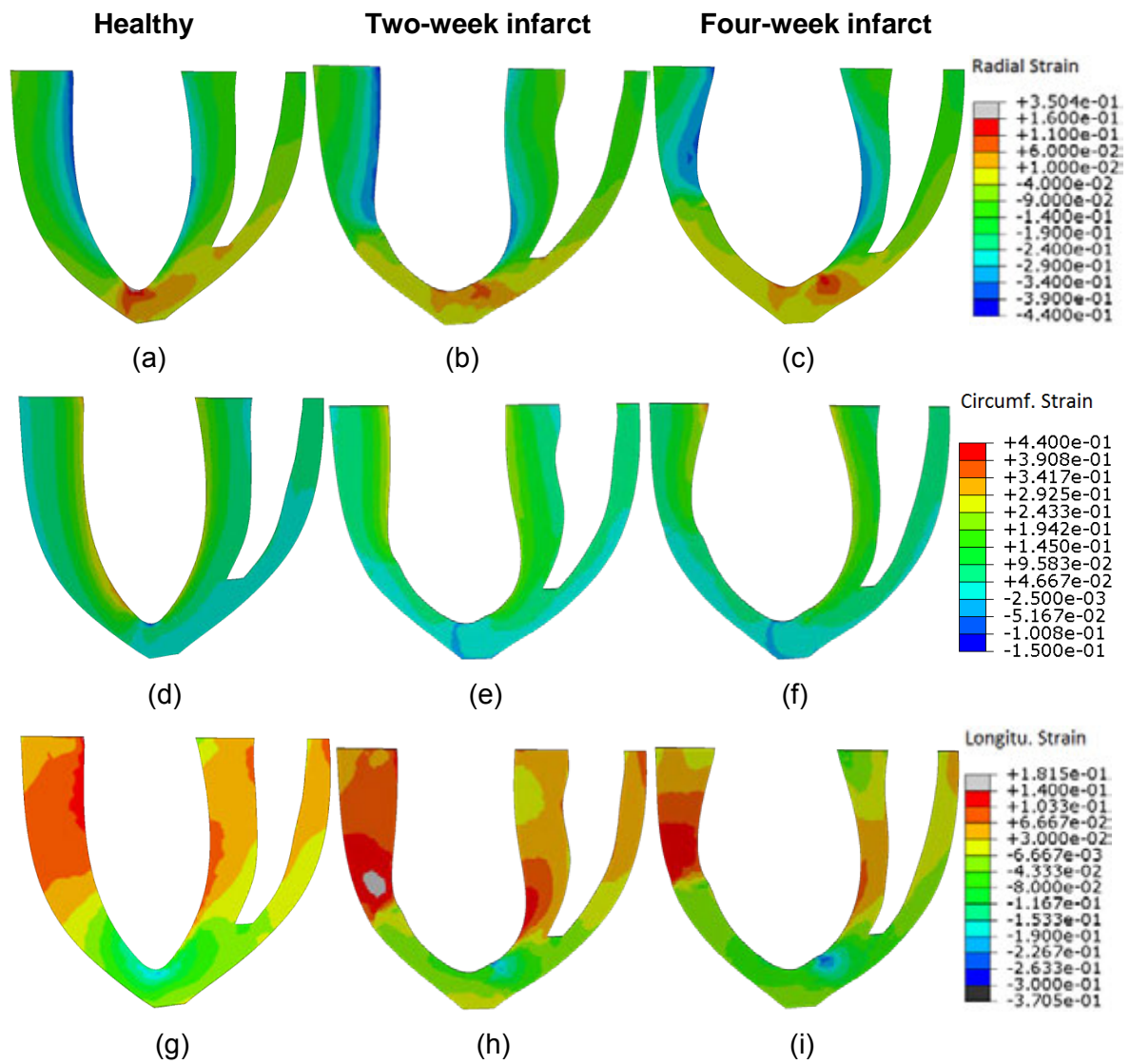


Figure 3-18: Contour plots of end-diastolic strain in central long axis cross section for the healthy, two-week and four-week infarct models. (a)-(c): Radial strain, (d)-(f): Circumferential strain, and (g)-(i): Longitudinal strain.

3.3.3.2 End-diastolic stress along intramural paths in the left ventricle

Figure 3-6 shows the arrangement of intramural paths along which stress and strain results will be assessed and illustrated. Depending on the cardiac region, the transmural position is expressed by the normalised myocardial thickness ranging between 0 and 1 as follows:

- LV free wall: 0 = epicardium, 0.5 = mid-wall and 1 = endocardium,
- Septal wall: 0 = RV endocardium, 0.5 = mid-wall and 1 = LV endocardium.

Figure 3-19 (a-c) shows the transmural radial stress. The myocardium is in compression state in the radial direction. Generally, on the free wall, the radial stresses increase from 0.6 kPa to 4.8 kPa on epicardium and endocardium, respectively. However, on the septal wall, the radial stress has a high value of -0.9 kPa at the epicardium of the RV. This is because the load pressure is applied to the endocardium. The epicardial wall is left to be free with no external load applied on it. The radial stress near the boundary condition at the base that was fixed in both radial and longitudinal directions is not predictable and remains negligible compared to other regions or paths.

Figure 3-19 (c) shows the radial stresses of the four-week infarcted rat model. The radial stresses on the septal wall of the four-week infarct model show that the stress begins at an average of -4.75 kPa. The path F shows higher radial stress value at the epicardial wall. This is contrary to others regions as the stress value starts lower than the value attributed in path F.

This is attributed to the change of stress scaling factor C to 0.2 kPa from 0.02kPa. The infarcted regions as shown in Figure 3-19 (a) are paths E and F. The rest of the paths are on the healthy myocardium and are expected to behave like the healthy model. Again, the infarcted regions on the four-week heart models are represented by regions C, D, E and F (See Figure 3-19 (b)).

As shown in Figure 3-19 (d-f), the circumferential stress remains high to the value of 5.6 kPa as compared to the radial stresses. Again, the circumferential stresses increase as a function of normalised myocardial thickness. The stress is high at the epicardium and low at the endocardium. The highest circumferential stress is approximately 19 kPa whereas the radial stress is 4.8 kPa. In both the healthy and infarcted rat heart models, the circumferential stresses were observed to be higher than both radial and longitudinal stress at the infarcted and healthy regions.

Figure 3-19 (g)-(i) shows the longitudinal stresses of the healthy and infarcted rat heart models. Paths A to F indicate low longitudinal stresses in all rat heart models when compared to both the radial and circumferential stresses. The paths I, K and L in the septal region show lower longitudinal stresses compared to the values reported along paths A to F. As shown in Figure 3-19 (g) the healthy model shows the lower longitudinal stresses in paths A, B, C, D, E and F. This behaviour is also observed in both the two and four-week infarct models. In Figure 3-19 (h) and (i), the longitudinal stresses in paths C, D, E and F increase. The longitudinal stresses increase from average of 1.5 kPa to 3.2 kPa on C, D, E and F paths is attributed to the wall thinning on the model due to infarcted tissue.

The circumferential stresses values at the infarcted regions for two and four-week models in path E and F are generally lower than those in the healthy regions. (Please note that the healthy region is found in both the healthy and infarct models). As shown in Figure 3-19 (d-f), the circumferential stresses for the four-week infarct model are higher than both healthy and the two-week infarct models due to the stretching effect. This may be attributed to the further thinning of the wall in the four-week infarct model. The paths A, B, C, D, E and F circumferential stress start with low value at the epicardium and increases as it approaches the endocardium. It is important to note that the circumferential stresses of the septal wall exhibit different behaviour than those of the wall on LV. The circumferential stresses begin at the epicardial wall of LV at a value of approximately zero.

The longitudinal stresses as shown in Figure 3-19 (g)-(i) show that the myocardium is under tension longitudinally. In the infarcted heart models considered, the longitudinal direction has the lowest average stress value of 1.5 kPa as compared to 4.8 kPa of both the radial stresses. It is important to note that the longitudinal stresses vary as a function of normalised myocardial thickness. However, for all three models, the longitudinal stress has different behaviour when compared to radial and circumferential stress. In addition, the radial stress varies from endocardium to epicardium with nearly 0.2 kPa and 4.8 kPa at the epicardium and endocardium, respectively.

Comparing the healthy and two-week infarct model, the longitudinal stresses remain the lowest when compared with both radial and circumferential stresses. At the infarcted regions E and F, the longitudinal stresses have decreased by an average of 65% when compared to radial and circumferential stresses. This exhibits a similar trend with that of the healthy model. The longitudinal stresses show that the myocardium is under tensile state. The radial and circumferential stresses path shows a steady increase from the epicardium to the

endocardium for all heart models. In this case, the stress values are high at both end i.e. endocardium and epicardium. In the majority of paths the longitudinal stresses have lower value at the mid-wall.

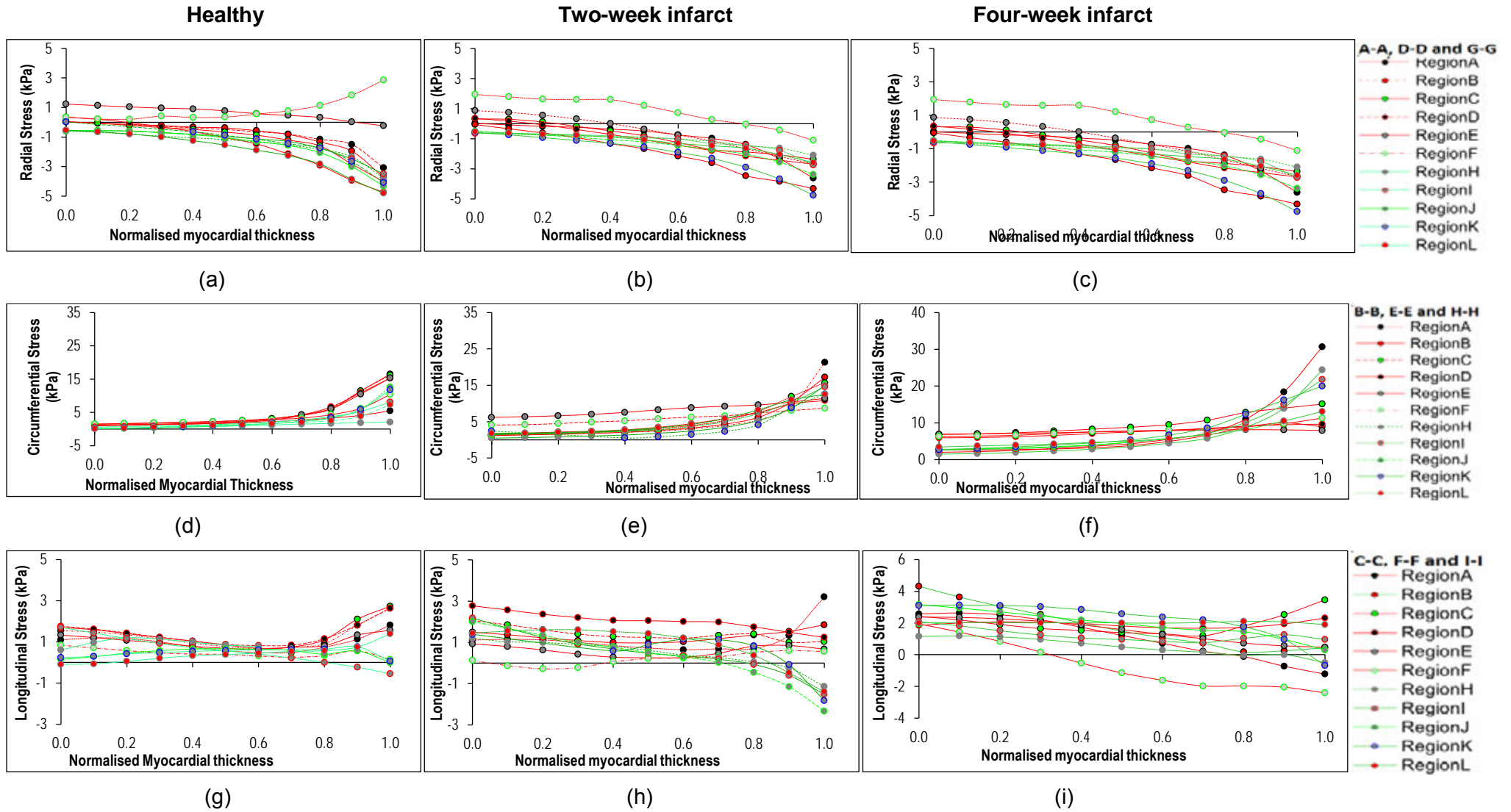


Figure 3-19: Transmural distribution of end-diastolic stress versus normalised myocardial thickness of LV free wall and septal wall for of healthy, two-week and four-week infarct models. (a)-(c): Radial stresses, (d)-(f): Circumferential stresses, and (g)-(i): Longitudinal stresses.

3.3.3.3 End-diastolic strain along intramural paths in the left ventricle

It is important to note that all paths as shown in Figure 3-20 (a), (b) and (c) have radial strain values which vary from the epicardium to the endocardium. This is attributed to the boundary conditions applied in the model. In addition, paths labelled B, C, D, E and F have the highest radial strain of -0.35. This is because the wall in this region is free to move and it is not restricted as compared to other walls, like the wall between the LV and RV. On the other side, the wall between the RV and LV is restricted because the pressure of 3.8 kPa and 1.2 kPa is applied on wall cavity. To note here is that both the strains and stresses in radial direction are negative and this simply means that the wall might be in compression. The radial strains increase from the epicardium to the endocardium. Similar to the radial stresses, the radial strains show that the myocardium is in radial compression. The radial strain at the infarcted regions is shown to be lower than in the healthy regions.

As shown in Figure 3-20 (d)-(f), the circumferential strains vary from the epicardial wall to the endocardial wall. The values increase exponentially from the epicardium to the endocardium. The values of circumferential strains are positive, indicating that the wall in this direction is under tension. Again, the paths B, C, D, E and F move more than the other regions. The circumferential strains values are higher than those of the radial and longitudinal strains. This concludes that the heart model moves more in the circumferential direction.

The circumferential strains are generally higher than those of the healthy model including the infarcted paths E and F. Similarly, the circumferential strains increase from the epicardial to the endocardial wall. In this case, the majority of strains values are positive. This means that the myocardium is in tension in the circumferential direction. This behaviour includes the infarcted regions.

As shown in Figure 3-20 (g)-(i), the longitudinal strains behave slightly differently to the longitudinal stresses. The longitudinal stresses show higher stress value at both the endocardium and the epicardium wall. Furthermore, the longitudinal strains behaviour is similar to that of the radial and circumferential strains. This means that the longitudinal strains are nearly zero at the epicardium wall and increase as they approach the endocardium. The longitudinal strains are at the highest at the endocardium wall. Figure 3-21 (g)-(i) shows the behaviour of longitudinal strains in eight paths on LV. The values show that the two-week infarct model has low movement in the longitudinal direction.

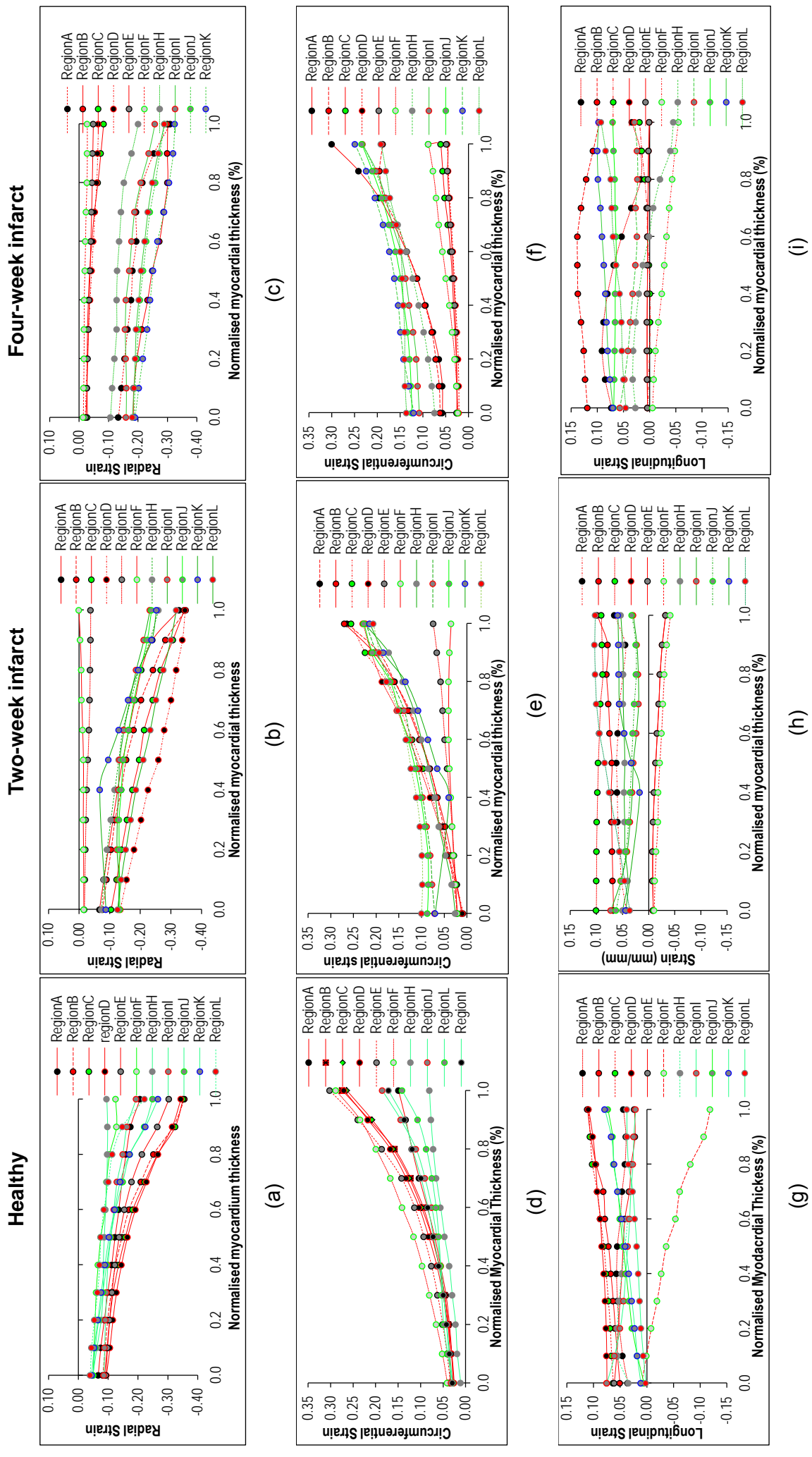


Figure 3-20: Transmural distribution of end-diastolic strain versus normalised myocardial thickness of LV free wall and septal wall for of healthy, two-week and four-week infarct models. (a)-(c): Radial strain, (d)-(f): Circumferential strain, and (g)-(i): Longitudinal strain. . .

3.3.4 End-diastolic myocardial mechanics in the left-ventricular infarct region and the septal wall

This section shows the stresses and strains in radial, circumferential and longitudinal directions for healthy, two-week and four-week infarct models. The radial, circumferential and longitudinal stresses at epicardial, mid-wall and endocardium at regions C, D, E and F are plotted for comparison purposes. This section allows for comparing how stresses and strains behave in different regions of both the healthy and infarct models. In a later section, the average stresses and strains are computed in order to compare the average values of stresses and strains in healthy and infarcted regions. This allows one to gain an understanding of the mechanisms of myocardial infarction in rat heart. This understanding is critical in the adoption of MI treatment during these stages.

3.3.4.1 End-diastolic stress and strain in the left-ventricular infarct region

Figure 3-21 (a)-(c) shows the radial stresses of healthy and infarct models in endocardium, mid-wall and epicardium of the region of the infarct defined by the paths C, D, E and F. The radial stress at the endocardial wall seems to be higher than stress in the mid-wall and epicardial wall. The highest stress recorded is in the region C and D in healthy and two-week infarct models. The regions C and D in the infarct model do not cover or include the infarcted area. Furthermore, the radial stress at endocardium in regions E and F shows to have decreased due to infarction.

Figure 3-21 (d)-(f) shows the circumferential stresses in healthy and infarct models. The circumferential stresses are reported to be high in both the healthy and infarcted myocardium. The high circumferential stresses are recorded on the infarcted regions. Similar to the radial stresses, the circumferential stresses are high at the endocardial wall and lower at the epicardial wall.

Figure 3-21 (g)-(i) shows the longitudinal stresses at the paths C, D, E and F at endocardium, mid-wall and epicardium. The longitudinal stresses are high at both the epicardium and endocardium and low at the mid-wall. This is different from the radial and circumferential stresses at these regions. The majority of high longitudinal stresses are presented in the healthy model at regions D, E and F. The longitudinal stresses at four-week infarct model are high in regions C, D, E and F.

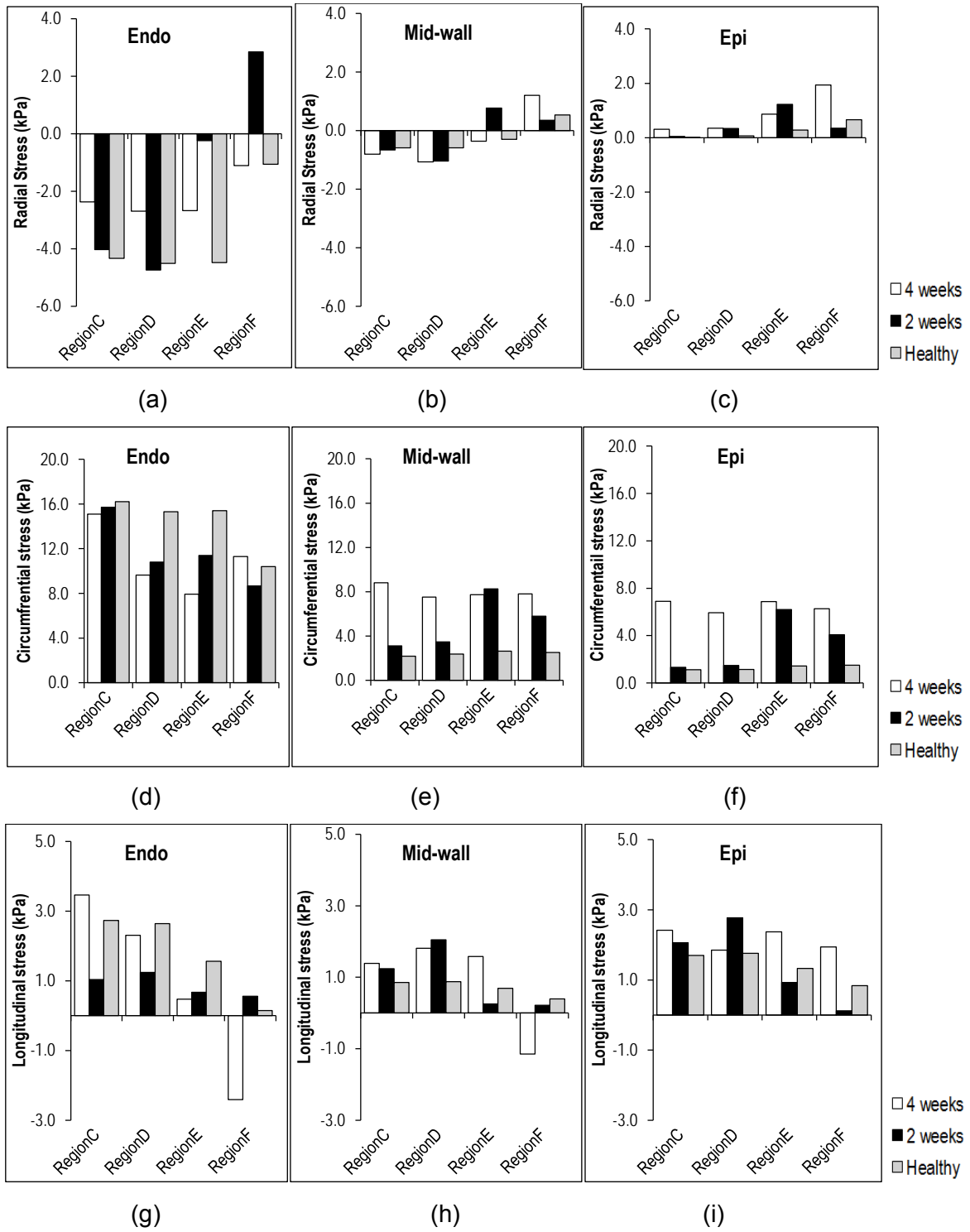


Figure 3-21: Comparison of average end-diastolic stress at paths C, D, E and F at endocardium, mid-wall and epicardium of the healthy, two-week and four-week infarct models. (a)-(c): Radial stress, (d)-(f): Circumferential stress, and (g)-(i) Longitudinal stress.

Figure 3-22 (a)-(c) shows that the radial strains for the four-week infarct model are high at the healthy regions (C and D) and lower at the infarcted regions (E and F). This is a similar trend with the two-week infarct model because at this model, the radial strains at the endocardium are high at regions C and D and low at regions E and F. In this model, the radial strains at E and F are longer than those of the four-week infarct model. At the epicardium wall the radial strains seem to have flattened for the four-week infarct model at the regions C, D, E and F. The radial strains at the mid-wall are greater than those of the epicardial wall but less than those of the endocardial wall.

In Figure 3-22 (d)-(f), it is interesting to note that the circumferential strains for healthy, two-week and four-week infarct models are generally lower than the radial strains. Again, it is vital to note that the radial stress is lower than the circumferential stress but the circumferential stress is higher than the radial stress. In this case the circumferential strain is much lower than the strains at the endocardial wall. This is in contrast to the radial strains, because the radial strains at the epicardium are lower than those of the endocardium wall, but not as great as those of the circumferential strains. At regions C, D, E and F the circumferential strains of the four-week infarct model are much lower than those of the healthy model in regions C, D, E and F. The healthy model at regions C, D, E and F exhibit highest strains value when comparing with the two-week infarct model. It is interesting to note that the circumferential strains in healthy, two-week and four-week infarct models remain flat. This means that the value of circumferential strains are independent of whether the tissue is infarcted or not infarcted at the epicardial wall.

Figure 3-22 (g)-(i) shows the longitudinal strains at regions C, D, E and F for healthy, two-week and four-week infarct models. On average, the majority of the longitudinal strains have been shown to remain constant in the endocardial wall, mid-wall and epicardial wall. The difference between the radial and circumferential strains is that at the infarcted region F, the strains at endocardium and mid-wall are under compression as opposed to the other regions where the myocardial wall remains under tension. The healthy model at region F in the endocardium has the highest longitudinal strains of -0.14. At the mid-wall the healthy model has the highest longitudinal strains of -0.05.

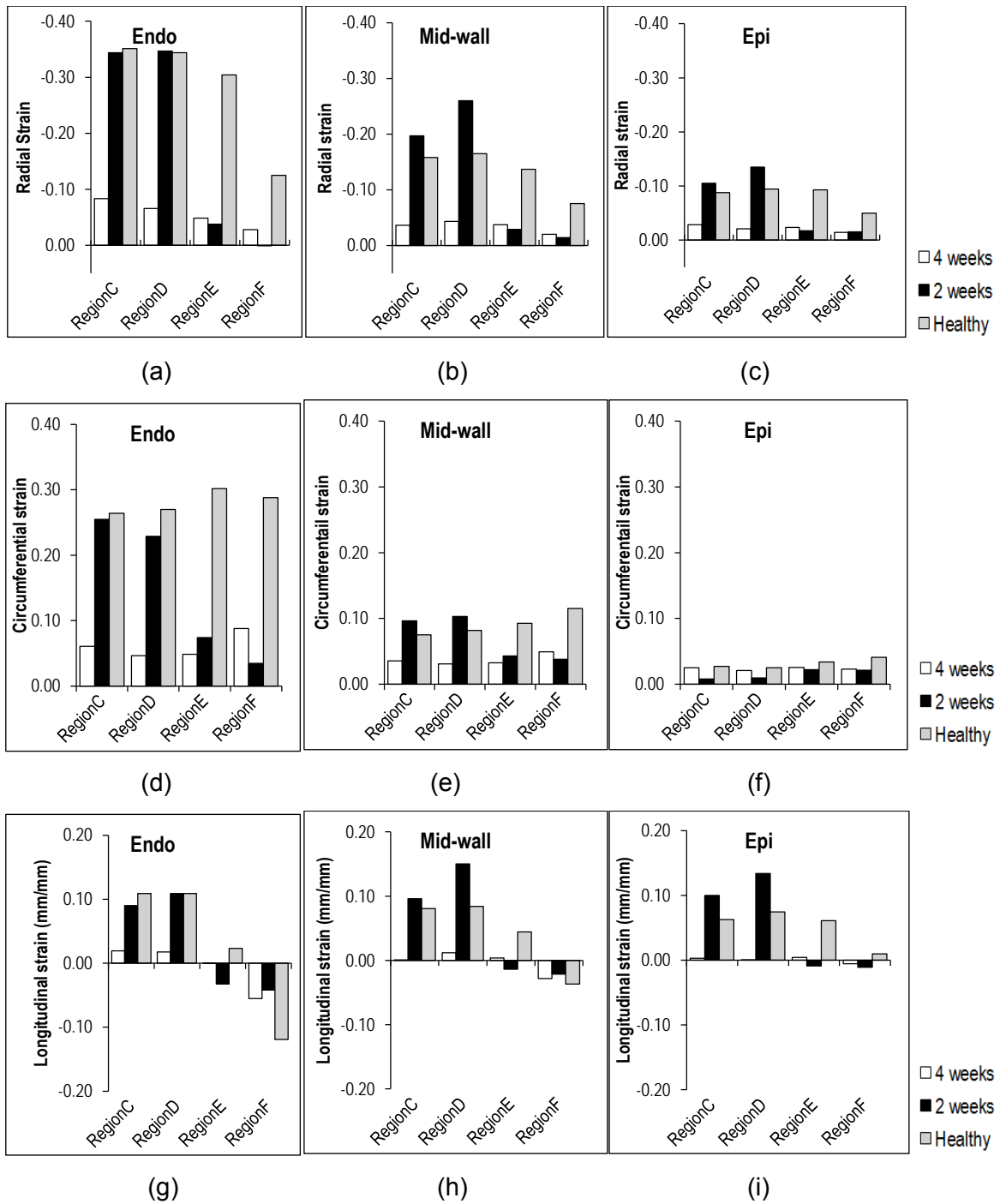


Figure 3-22: Comparison of average end-diastolic strain at paths C, D, E and F at endocardium, mid-wall and epicardium of the healthy, two-week and four-week infarct models. (a)-(c): Radial strain, (d)-(f): Circumferential strain, and (g)-(i) Longitudinal strain .

3.3.4.2 End-diastolic stress and strain in the septal wall

Figure 3-23 (a)-(c) shows the radial stresses at LV endocardium, mid-wall and LV epicardium in the septal wall of healthy, two-week and four-week infarct models. The septal region of interest was defined by the paths I, J, K and L. The radial stresses at I, J, K and L regions have the average value of 3.8 kPa in the endocardium wall. The healthy model shows the radial stress as lower than the applied pressure of 4.8 kPa in the endocardium wall. Region K shows the lowest radial stress for the healthy model at 1.1 kPa at the endocardial wall. This is similar in the mid-wall, because the radial stress at the mid-wall in the healthy model is the lowest at less than 1 kPa. Furthermore, the radial stresses in regions I, J, K and L are shown to be equal in the epicardium for healthy, two-week and four-week infarct models. The four-week infarct model has the highest value of radial stress at region K at both the endocardium and the epicardium. For the two-week infarct model, the highest radial stress is located at region L with the value of 4.7 kPa. At the same position and model, the radial stress at the mid-wall is the highest at region L with the value of approximately 2 kPa. At the epicardium in region I, the radial stress is 0.8 kPa for both the healthy and four-week infarct models. The radial stress in region I for the two-week infarct model is lower than both the healthy and four-week infarct models at a value of 0.67 kPa.

Figure 3-23 (a)-(i) shows the stress in the radial, circumferential and longitudinal directions for healthy, two and four-week infarct models in the I, J, K, L regions/paths. These stresses are measured by the defined paths in the endocardium, mid-wall and epicardium positions at end-diastole phase. It can be seen from Figure 3-23 (a), (d) and (g) that the radial, circumferential and longitudinal stresses are high at the endocardium. This is because the applied pressure mimicking the end-diastolic pressure of 4.5 kPa and 0.92 kPa was applied on the endocardial wall of LV and RV, respectively. The circumferential stresses as shown in Figure 3-24 (d), (e) and (f) are high at all positions from endocardium to the epicardium. It is vital to note that the stresses in radial, circumferential and longitudinal directions are high at the four-week infarct model followed by the two-week infarct model. The healthy model is showing low stress in all directions when compared to the four and two-week infarct models.

The highest radial stress is 4.5 kPa shown in region K followed by region J at the endocardium on the four-week infarct model. All models, including the healthy and infarcted, have no pressure applied on the epicardium. However, their radial stress at the epicardium is the lowest in all regions when compared to endocardium and mid-wall positions. In general, the radial stresses at the epicardium in regions I, J, K and L for healthy, two and four-week infarct models show stress which is flat. In other words, the radial stress remains

the same in regions I, J, K and L irrespective of the models as shown in Figure 3-23 (c). This observation could be attributed to the fact that all surfaces at the epicardial position experience the same pressure irrespective of whether the model is healthy or infarcted. The regions I, J, K and L are positioned between the LV and the RV. In fact this wall divides the RV and the LV. However, this wall is subjected to the applied pressures on both sides of the wall.

Figure 3-23 (d)-(f) shows the circumferential stress in the epicardial position in the regions I, J, K and L for healthy and infarct models. Contrary to the radial stress shown in Figure 3-24 (d), the circumferential stress for healthy and infarct models is higher than the radial stress. Furthermore, the circumferential stresses in all regions are approximately equal in magnitude for the four-week infarct model. The healthy model shows the minimum circumferential stress as compared to infarct models at end-diastole at the epicardial position. The average stress for the four-week infarct model in regions I, J, K and L is estimated to be 3.0 kPa. At the endocardium, the highest circumferential stress is 22 kPa at region I followed by 20.0 kPa at region K for the four-week infarct model. Again, the circumferential stress for the healthy model at the endocardium is lower compared to the infarct models. The general trend observed in Figure 3-23 (d) is that at each region, the highest circumferential stress is linked to the four-week infarct model followed by the two-week infarct model and lastly the healthy model. When comparing the circumferential stress at the mid-wall and epicardium for all models, it can be seen that the average circumferential stress is 6 kPa at the mid-wall, while the average circumferential stress is 3.0 kPa at the epicardium. To note here is that the circumferential stresses are all positive which indicates that the model is under tension in endocardial, mid-wall and epicardial positions at the end-diastole phase as shown in Figure 3-23 (d)-(f).

Figure 3-23 (g)-(i) shows the longitudinal stresses in regions I, J, K and L at endocardial, mid-wall and epicardial positions for healthy and infarct models. Generally, the longitudinal stresses at endocardium, mid-wall and epicardium in the regions I, J, K and L are approximately equal for healthy and infarct models. This behaviour is expected because the movement in the longitudinal direction is the same in all models since the pressure applied on the endocardial wall is the same. The longitudinal stresses in mid-wall and epicardial positions are positive and this indicates that the models are under tension. In other words, the heart models expand in the longitudinal direction. At regions K and L the longitudinal stress at the epicardium for the four-week infarct model are higher when compared to region

I and L.

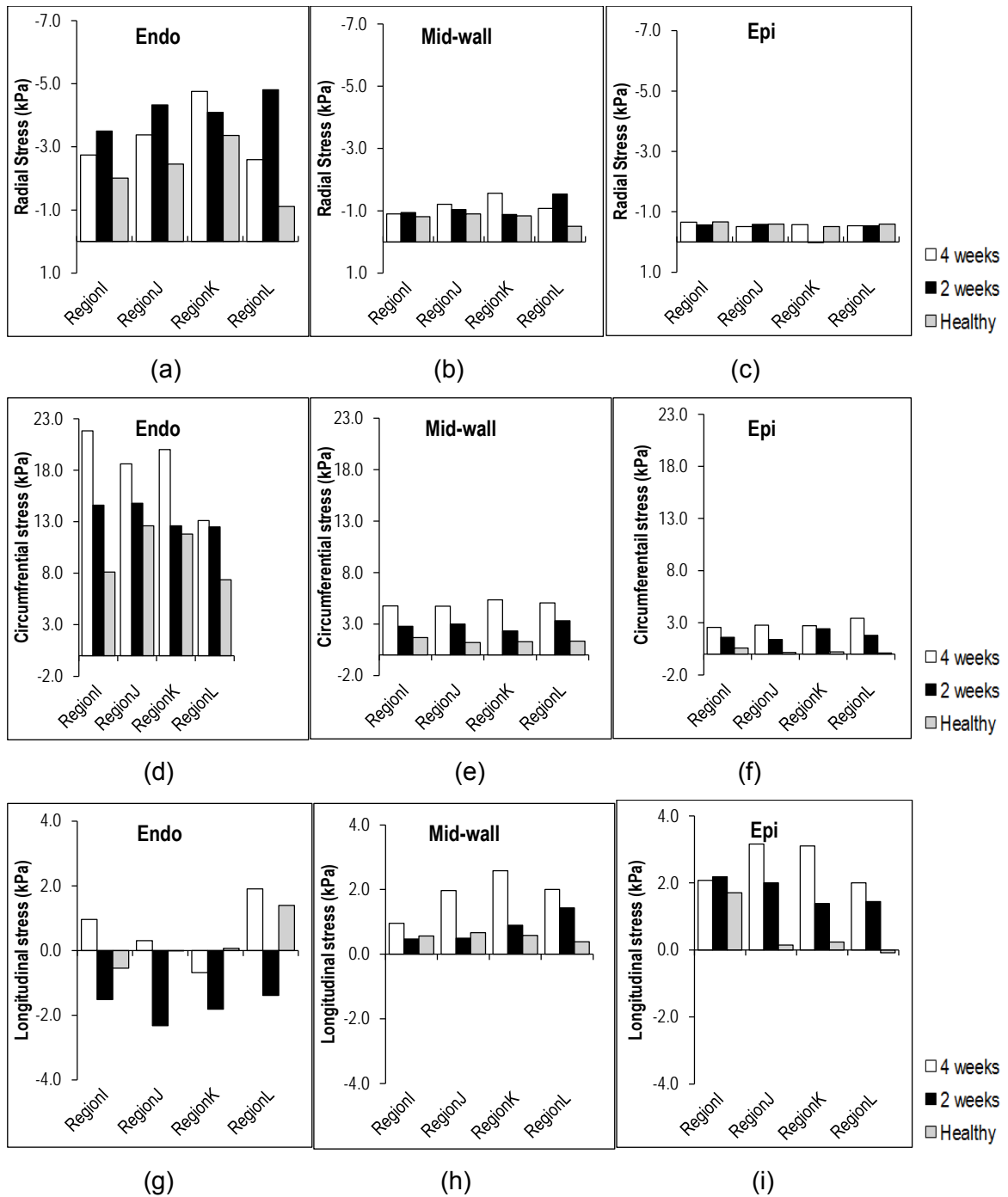


Figure 3-23: Comparison of average end-diastolic stress at paths I, J, K and L at endocardium, mid-wall and epicardium of the healthy, two-week and four-week infarct models. (a)-(c): Radial stress, (d)-(f): Circumferential stress, and (g)-(i) Longitudinal stress.

Figure 3-24 (a)-(i) shows the strains in the radial, circumferential and longitudinal directions for healthy, two and four-week infarct models in the I, J, K, and L regions/paths. As shown in Figure 3-24 (a-c), the radial strain is higher than the circumferential and longitudinal strains. In regions I, J and K the radial strains are high in the four-week infarct model. The radial strains in all regions are low in the healthy model. At the endocardial position, the radial strains are high followed by the strain at the mid-wall. The radial strain at the epicardium is seen to be the lowest when comparing it to the endocardium and mid-wall. Furthermore, the radial strain at epicardium is found to be -0.16, -0.19, -0.19 and -0.18 for regions I, J, K and L in the four-week infarct model. Furthermore, the radial strains at the mid-wall are -0.18, -0.22, -0.25 and -0.21 in region I, J, K and L in the four-week infarct models, respectively.

As shown in Figure 3-24 (a), the radial strain at the endocardial position is observed to be the highest when compared to the circumferential and longitudinal strains. The radial strains at the endocardium are -0.27, -0.30, -0.34, -0.31 for the four-week infarct model. In addition, the radial strains on the two-week infarct model are -0.22, -0.23, -0.25, -0.31 in the regions I, J, K and L, respectively. When looking at Figure 3-24 (a), it can be seen that the healthy model has lower radial strains. The radial strains in the healthy model are -0.19, -0.24, -0.25, -0.22 in regions I, J, K and L, respectively. It is important to note that the radial strains are positive at the endocardium, mid-wall and epicardium in regions I, J, K and L are in compression state. This observation is false when looking at the circumferential and longitudinal strains because they are both in tension.

Figure 3-24 (d)-(f) shows the strains in the circumferential direction for all models and regions. Generally, the strains in the circumferential direction are lower than the radial direction. However, the trend observed is that the circumferential strains are higher in the four-week infarct models and lowest in the healthy model. At the endocardium as shown in Figure 3-24 (d), the circumferential strains are 0.23, 0.23, 0.26 and 0.2 in regions I, J, K and L, respectively on the four-week infarct model. Moreover, at the mid-wall as shown in Figure 3-25 (d), the circumferential strains are 0.14, 0.15, 0.16 and 0.15 in regions I, J, K and L, respectively on the four-week infarct model. In addition, at the epicardium as shown in Figure 3-25 (d), the circumferential strains are 0.11, 0.13, 0.12 and 0.14 in regions I, J, K and L, respectively on the four-week infarct model. When looking in Figure 3-24 (d)-(f) it is clear that the circumferential strain on the endocardium, mid-wall and epicardium is high for the infarct model. The trend observed in Figure 3-24 (d)-(f) is in line with what is expected in reality because of the models physical properties.

In regions I, J, K and L, the circumferential strains in the healthy model are 0.17, 0.185, 0.19, and 0.14 at the endocardium. Additionally, in regions I, J, K and L, the circumferential strains in the healthy model are 0.075, 0.074, 0.074, and 0.074 at the mid-wall. Furthermore, in regions I, J, K and L, the circumferential strains in the healthy model are 0.025, 0.027, 0.026, and 0.025 at the epicardium. At the mid-wall and epicardial position, the circumferential strains in the healthy model are observed to be equal in the regions I, J, K and L. The observation was also found to be similar to the circumferential strains in the two-week infarct model.

Figure 3-24 (g)-(i) shows the longitudinal strains in endocardial, mid-wall and epicardial positions for healthy and infarct models in the regions I, J, K and L. When compared to the radial and circumferential strains, the longitudinal strains are low. This means that at end-diastole, there is little movement in the longitudinal direction when compared to radial and circumferential directions. This is true because the applied pressure was mainly in the radial direction and therefore there is little expectation that the model will move greatly in the longitudinal direction. Figure 3-24 (a) and (d) shows that the radial and circumferential strains in the endocardium are uniform across the regions. However, as shown in Figure 3-24 (g), the longitudinal strain in the endocardium is not uniform across the regions (I, J, K and L). The non-uniformity of longitudinal strain in the endocardium continues to the mid-wall and epicardium across regions I, J, K and L in all models. The longitudinal strains in region I at the endocardium and mid-wall are lower than the longitudinal strains in the epicardium. Longitudinal strains at regions I, J, K and L are 0.03, 0.076, 0.12, and 0.09 in the endocardium on the four-week infarct model, respectively. Furthermore, the longitudinal strains at regions I, J, K and L are 0.025, 0.064, 0.092, and 0.065 in the mid-wall on the four-week infarct model, respectively. Moreover, the longitudinal strains at regions I, J, K and L are 0.068, 0.078, 0.078, and 0.05 in the epicardium on the four-week infarct model, respectively. The pattern is similar to the longitudinal strains in the endocardium, mid-wall and epicardium in regions I, J, K and L on the healthy and two-week infarct models. The general observation is that the longitudinal strains are high at the endocardium and epicardium but lower at the mid-wall in all regions for healthy and infarct models.

The strain in the circumferential direction is lower than the strains in the radial direction as shown in Figure 3-24 (a) and (d). However the stress in the circumferential direction is higher than the stress in the radial direction for all regions in healthy and infarct models. This means that even though the strain in the circumferential direction is lower than the strain in the radial direction, the magnitude of the stress in the circumferential and radial directions

does not depend entirely on the strains. This clearly means that the stress magnitudes depend not only on the magnitude of strains but also on the constitutive parameters provided.

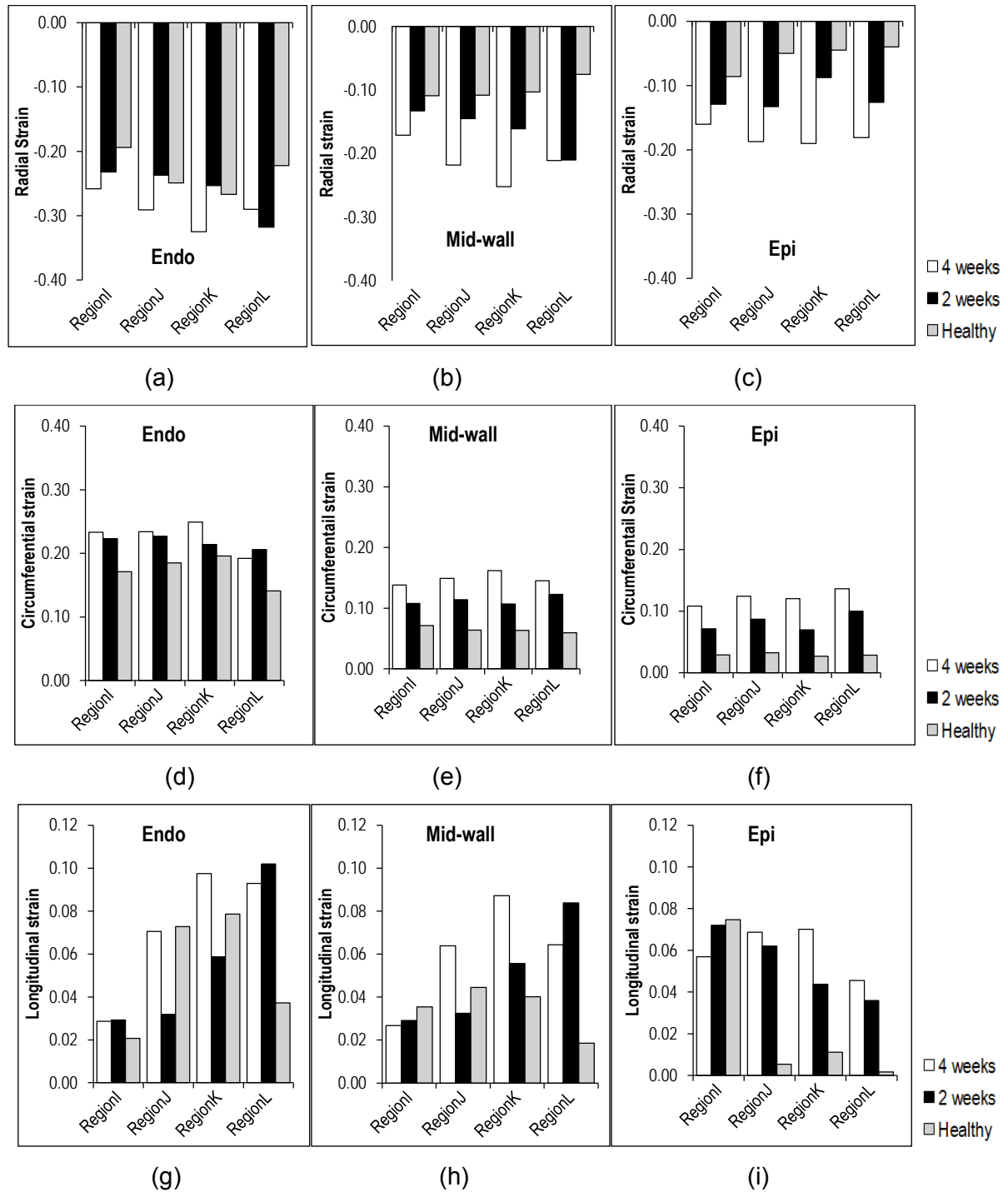


Figure 3-24: Comparison of average end-diastolic strain at paths I, J, K and L at endocardium, mid-wall and epicardium of the healthy, two-week and four-week infarct models. (a)-(c): Radial strain, (d)-(f): Circumferential strain, and (g)-(i) Longitudinal strain .

3.3.4.3 Comparison of end-diastolic stress and strain in infarct region and septal region

Transmural stress remains one of the important factors in determining and understanding the underlying mechanisms in healthy and infarcted heart. The measurement of stress across the myocardium from endocardium to the epicardium provides more information as the stress could be measured at any point across the myocardial wall. In this study, the transmural stresses across the wall were recorded in healthy and infarct models. This approach has shown great success and was utilised by various authors in heart mechanics including (Carapella *et al.*, 2014; Omens *et al.*, 1993; Wenk *et al.*, 2011b; Wenk *et al.*, 2013b). In this study, this was achieved by recording the stresses on the predefined paths from the epicardium to the endocardium. In order to ensure consistency and comparability, the paths were defined such that the stresses are compared exactly at the same path for all models. In addition, the radial, circumferential and longitudinal stresses are then recorded and compared with healthy and infarct models. The stresses at paths A, B, C, D, E, F, G, H, I, J, K and L are shown in Figure 3-6.

It was observed that the defined material properties have an influence on the value of stresses in the defined path. If stress scaling factor C escalates, the average radial, circumferential and longitudinal stresses also increase. In the infarcted regions of both two and four-week infarct models, the stress scaling factor C was increased by tenfold as compared to the healthy myocardium. This has resulted in the increase of stresses in these regions i.e., paths E and F in the two-week model and paths C, D, E and F in the four-week model.

Figure 3-25 (a)-(f) shows the average radial stresses of paths C, D, E and F for healthy, two-week and four-week infarct models. The radial average stresses in these regions are shown to be minimal. This is in agreement with the physical constraint of the model because the uniform pressure was applied only on the endocardial wall of the model. Furthermore, the average radial stresses at the endocardial wall are shown to be greater than at the epicardial wall. The pressure of 4.8 kPa (36 mmHg) was applied at the endocardial wall, so the expectation is that the average radial stresses must be equal to 4.8kPa. The healthy model is the only model in agreement with this since it has an average radial stress of 4.4 kPa. The two-week model shows that there is an average stress of 3.0 kPa. This is a low value since it is lower than the expected value of 4.8 kPa. In addition, the average radial stress of the four-week model is less than the expected value of 4.8 kPa. This model records the value of radial stress as 2.6 kPa. The lowering of average radial stresses could be due to the wall

thinning in the infarcted area. It is concluded that the wall thinning due to the infarcts has impact on the value of the radial stresses. Recently, (Wenk *et al.*, 2013b) developed a biventricular FE model of swine heart and reported on the average myofibre stress during ED and ES phases (passive filling and active contraction phases). In this regard, it was concluded that myofibre stress during ES phase is higher than in ED phase.

The radial stress on the healthy model in regions B, C and D at the epicardium is 3.2 kPa, 4.0 kPa and 3.0 kPa. While the circumferential stress in regions B, C and D at the epicardium are 15.8 kPa, 14.4 kPa and 3.0 kPa. The stresses on regions B, C, D are 2.25 kPa, 2.25 kPa and 1.35 kPa. The high circumferential stresses in this region could be attributed to the high stress scaling factor in the infarcted tissue. This shows that for healthy diastolic model simulation the highest stress recorded is on the circumferential direction. For region B the radial stress is higher by 79% than radial stress at the epicardium. At regions C, D, E and F the radial stress at the endocardium is lower than at the epicardium. The mid-wall stresses at these regions seem to be lower than those in the epicardial region.

The radial stresses on paths I, J, K and L show the linear increase from the pericardium to the endocardium. The epicardium has the lowest average radial stress and the mid-wall has recorded the mid value between the epicardial and the endocardium. Furthermore, the average radial stresses in paths I, J, K and L show the highest values. Again, this is attributed to the physical nature and the boundary conditions applied on healthy, two-week and four-week infarct models. To note here is that the average radial stress in paths C, D, E and F is greater than the average radial stress in regions I, J, K and L. The paths I, J, K and L are located in the wall between the LV and the RV. This means that this wall is subjected to both the pressures applied on the LV and the RV. The radial stresses on paths I, J, K and L have a high value of stress at the epicardium. This is contrary to what was recorded in the regions C, D, E and F. These results are different to the single ventricular model (Mojsejenko *et al.*, 2014; Omens *et al.*, 1993; Wenk *et al.*, 2011a; Wenk *et al.* 2011b) because in the biventricular model, there is no additional pressure applied on the septum.

The circumferential stresses of both paths I, J, K and L and C, D, E and F are higher than the average radial stresses in the same regions. This means that all models have the movement in the circumferential direction. Paths C, D, E and F show high circumferential stresses on the healthy model at the endocardial wall surface. The mid-wall has the circumferential stresses greater than at the epicardial wall. This is the expected behaviour since the model was constrained in such a way that the pressure is applied at the

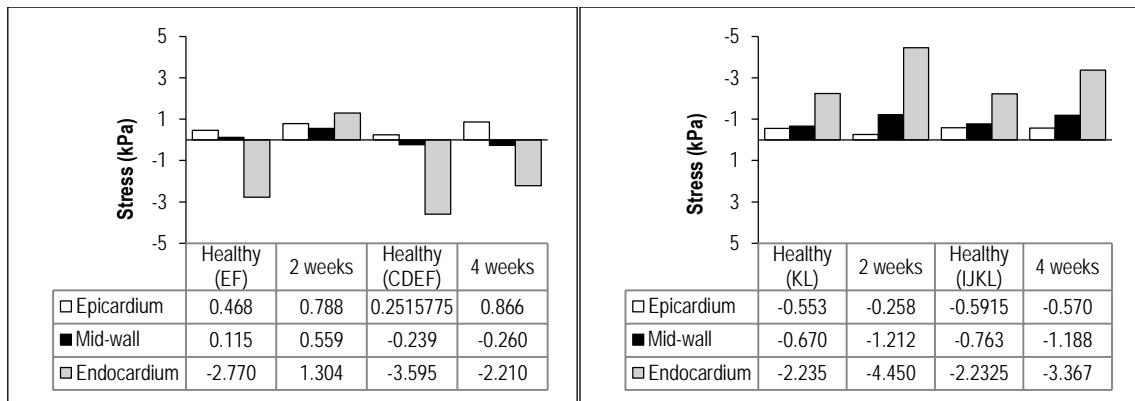
endocardial wall. Furthermore, the circumferential stress increases from 1.3 kPa on the epicardial wall to the value of 6.5 kPa on the endocardial wall from healthy to four-week infarcted, respectively. The average circumferential stress at the mid-wall increased from 2.4 kPa, 5.2 kPa and 8 kPa in healthy, two-week and four-week infarct models. The average circumferential stresses show a decrease from the healthy model with 14.3 kPa and 11.7 kPa in the mid-wall and 10.9 kPa at the four-week infarct model. This means that the healthy model has greater movement in the paths C, D, E and F as compared to the infarcted region. This happens so because the infarct models have a thinned wall and this wall becomes stiffer as compared to the healthy model.

Contrary to what was observed in the paths C, D, E and F, the paths I, J, K and L show different circumferential stresses value. The healthy model seems to move little compared to the other infarct models. The average circumferential stress in the epicardial wall on the healthy model is 0.3 kPa while two-week and four weeks infarct models have the average circumferential stresses at the epicardium of 1.8 kPa and 2.9 kPa, respectively. Furthermore, the circumferential stress for the healthy model at the mid-wall is 1.4 kPa while the circumferential stress at the mid-wall at two-week and four-week infarct models are 2.9 kPa and 5.0 kPa, respectively. The paths I, J, K and L show that there is greater movement in these regions at the endocardium from 10 kPa to 18.3 kPa in healthy and four-week infarct models.

The paths labelled I, J, K and L is the myocardium wall that is shared by the LV and RV (septal wall). The reason that the paths C, D, E and F show far less circumferential values in the epicardium, mid-wall and endocardium in all models is that the wall does not constitute the infarcted regions and it will move more than others because the material properties are not changed. The other reason affecting the movement of region C, D, E and F is that the path I, J, K and L region experience pressure in both the epicardial wall and the endocardial wall. This has the tendency to greatly increase the circumferential stress. The longitudinal direction in this model shows how the heart moves. As shown in Figure 3-25 in the healthy model, the longitudinal stress is high at both the epicardial and endocardial walls. The longitudinal stress at the mid-wall region is required to have the lowest value. The explanation for this is that the wall at the epicardium moves relative to the endocardial wall. This could be again attributed to the fibre orientation at that region.

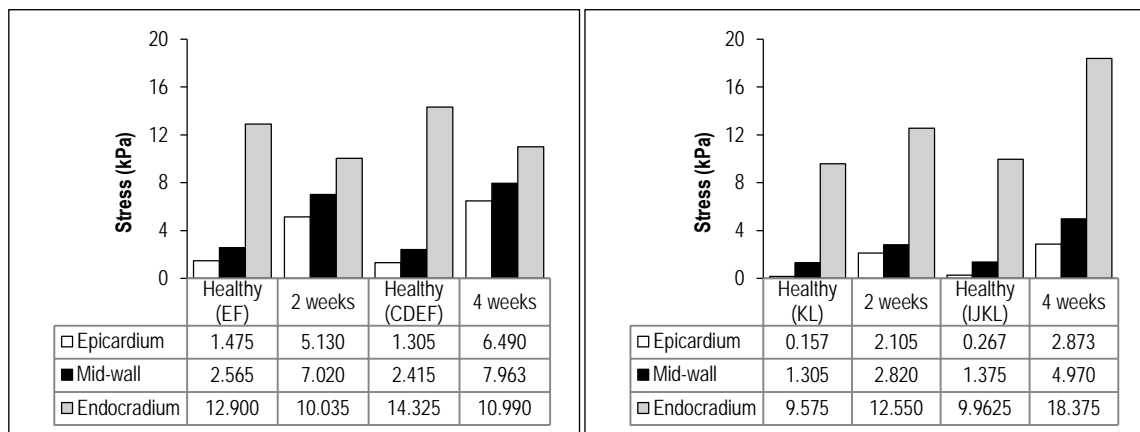
The longitudinal stresses on the paths I, J, K and L for the healthy model shows that the stresses values are high at the mid-wall for the healthy model. On the two-week infarct

model the longitudinal stresses at the mid wall show a decrease and the value is lower than the stress at the epicardial and endocardial walls. As shown in Figure 3-25, the important aspect to note is that the longitudinal stress at the epicardial wall for healthy, two-week and four-week infarct models are 0.5 kPa, 1.8 kPa and 2.6 kPa, respectively. Similarly, the longitudinal stress at mid-wall for healthy, two-week and four-week infarct models are 0.55 kPa, 0.8kPa and 1.9 kPa, respectively.



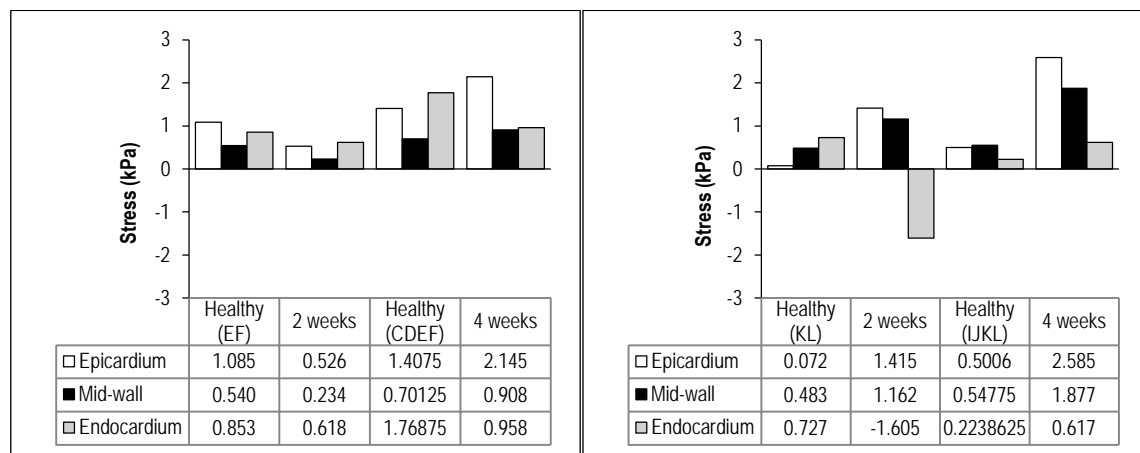
(a)

(d)



(b)

(e)



(c)

(f)

Figure 3-25: End-diastolic stress for healthy, two-week and four-week infarct models. Average radial (a), circumferential (b) and longitudinal (c) stress at paths C, D, E and F. Average radial (d), circumferential (e) and longitudinal (f) stress at paths I, J, K and L.

Strain has been used greatly in trying to understand the mechanisms associated with myocardial infarction in heart. Unlike stress, strain has been documented in various animal experiments to study the myocardial mechanics of healthy and infarcted heart tissues.

Figure 3-26 (a)-(f) shows the comparison of average radial, circumferential and longitudinal strains in LV paths C-F and septal paths I-L for healthy, two-week and four-week infarct models. The septal wall shows that it is in compression from the epicardial to endocardial wall. The healthy model shows average radial strains of -0.163, -0.268 and -0.562 at epicardial, mid-wall and endocardial position, respectively. Furthermore, the two-week infarct model shows average radial strains of -0.137, -0.250 and -0.364 in epicardial, mid-wall and endocardial wall, respectively. Moreover, the four-week model shows average radial strains of -0.04, -0.07 and -0.11 in epicardial, mid-wall and endocardial wall, respectively (see Figure 3-26 (a)).

When comparing the radial strain to the circumferential strain in all models, it was found that the average circumferential strains in the regions C-F are lower than the average radial strains (see Figure 3-26 (a) and (b)). The average circumferential strain of the healthy model at the endocardium is found to be 0.281. This strain is 50% lower than the average radial strain of the healthy model at the endocardium. The healthy model shows average circumferential strains of 0.032, 0.043 and 0.281 at epicardial, mid-wall and endocardial position, respectively. Furthermore, the two-week infarct model shows average circumferential strains of 0.015, 0.070 and 0.148 in epicardial, mid-wall and endocardial wall, respectively. Moreover, the four-week model shows average circumferential strains of 0.024, 0.037 and 0.061 in epicardial, mid-wall and endocardial wall, respectively (see Figure 3-26 (b)).

When comparing the average radial and circumferential strains of the two-week infarct model at the mid-wall (free wall), it was found that the average radial strain is 72% higher than the average circumferential strain. Similarly, when comparing the average radial and circumferential strains of the four-week infarct model at the mid-wall (free wall), it was found that the average radial strain is 45.6% higher than the average circumferential strain. The healthy model shows average longitudinal strains of 0.052, 0.043 and 0.031 at epicardial, mid-wall and endocardial position, respectively. Additionally, the two-week infarct model shows average longitudinal strains of 0.054, 0.053 and 0.031 in epicardial, mid-wall and endocardial wall, respectively. Also, the four-week model shows average longitudinal strains of 0.0001, -0.003 and -0.004 in epicardial, mid-wall and endocardial wall, respectively (see Figure 3-26 (c)).

Generally, the average longitudinal strains are found to be the lowest when compared with average radial and circumferential strains in all heart models in the free wall C-F region. The

average longitudinal strain of the healthy model at the endocardium position is found to be less by 94.50 % and 88.97% as compared to average radial and circumferential strains.

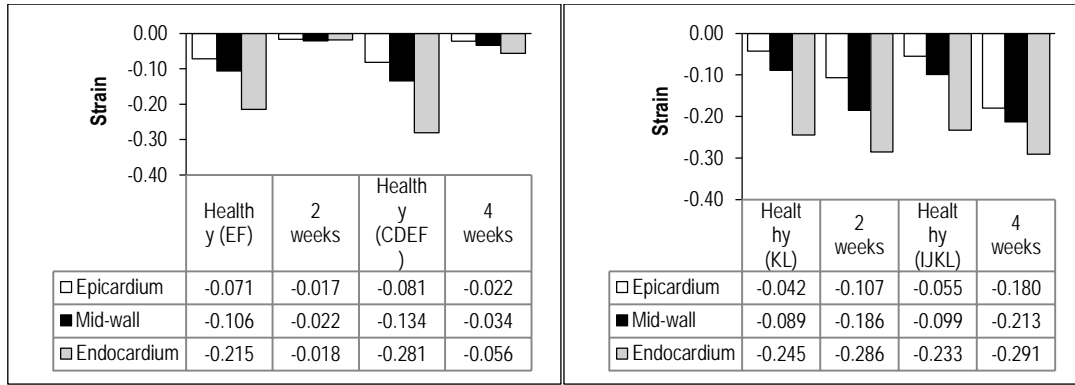
When comparing the average radial, circumferential and longitudinal strains of the free wall and septal walls, it was observed that the strains on the septal wall are higher than the strains in the free wall for all models. As shown in Figure 3-26 (d), the average radial strain in the healthy model was found to be -0.110, -0.198 and -0.466 on epicardium, mid-wall and endocardium, respectively. Additionally, as shown in Figure 3-26 (e), the average circumferential strain in the healthy model was found to be 0.029, 0.065 and 0.173 on epicardium, mid-wall and endocardium, respectively. Furthermore, as shown in Figure 3-26 (f), the average longitudinal strain in the healthy model was found to be 0.023, 0.035 and 0.052 on epicardium, mid-wall and endocardium, respectively. As shown in Figure 3-27 (d), the average radial strain in the two-week model was found to be -0.238, -0.325 and -0.520 on epicardium, mid-wall and endocardium, respectively. Additionally, as shown in Figure 3-27 (e), the average circumferential strain in the two-week model was found to be 0.082, 0.113 and 0.218 on epicardium, mid-wall and endocardium, respectively. Furthermore, as shown in Figure 3-26 (f), the average longitudinal strain in the two-week model was found to be 0.053, 0.050 and 0.055 on epicardium, mid-wall and endocardium, respectively. As shown in Figure 3-27 (d), the average radial strain in the four-week model was found to be -0.359, -0.426 and -0.582 on epicardium, mid-wall and endocardium, respectively. Additionally, as shown in Figure 3-26 (e), the average circumferential strain in the four-week model was found to be 0.122, 0.149 and 0.227 on epicardium, mid-wall and endocardium, respectively. Furthermore, as shown in Figure 3-26 (f), the average longitudinal strain in the four-week model was found to be 0.060, 0.061 and 0.072 on epicardium, mid-wall and endocardium, respectively. The average radial strain at the endocardium for the healthy model in the free wall is 17.08% higher than the average radial strain in the septal wall for the healthy model. Similarly, the average circumferential strain at the endocardium for the healthy model in the free wall is 38.43% higher than the average radial strain in the septal wall for the healthy model. In addition and in contrast, the average longitudinal strain at the endocardium for the healthy model in the free wall is 67.74% lower than the average radial strain in the septal wall for the healthy model.

The average radial strain at the mid-wall for the healthy model in the free wall is 26.12% higher than the average radial strain in the septal wall for the healthy model. Similarly, the average circumferential strain at the mid-wall for the healthy model in the free wall is 28.57% higher than the average radial strain in the septal wall for the healthy model. In addition, the

average longitudinal strain at the mid-wall for the healthy model in the free wall is 18.60% higher than the average radial strain in the septal wall for the healthy model.

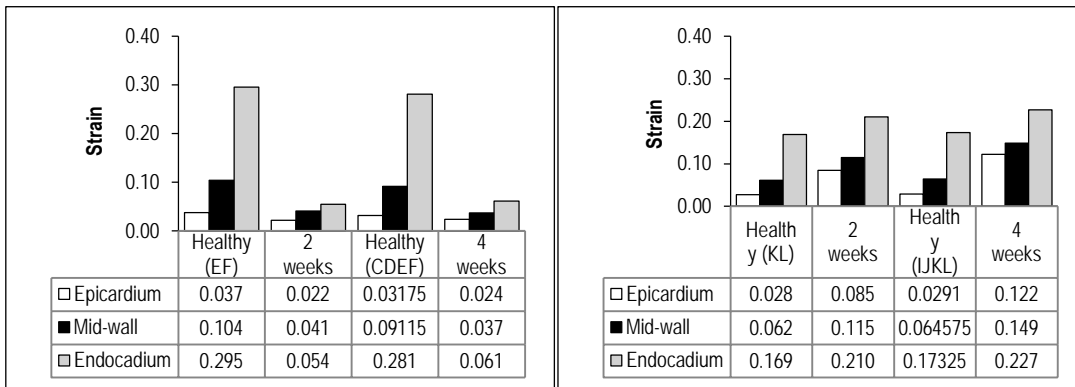
When considering the two-week infarct model, the average radial strain on the endocardium of the septal wall is 30 % higher than the average radial strain on the free wall. Similarly, the average circumferential strain on the endocardium of the septal wall is 32.11 % higher than the average circumferential strain on the free wall. Additionally, the average longitudinal strain on the endocardium of the septal wall is 43.36 % higher than the average longitudinal strain on the free wall. When considering the four-week heart model, the average radial strain on the endocardium of the septal wall is 80.58 % higher than the average radial strain on the free wall. Similarly, the average circumferential strain on the endocardium of the septal wall is 73.13 % higher than the average circumferential strain on the free wall. Additionally, the average longitudinal strain on the endocardium of the septal wall is 94.44% higher than the average longitudinal strain on the free wall.

When considering the two-week infarct model, the average radial strain on the mid-wall of the septal wall is 23.10 % higher than the average radial strain on the free wall. Similarly, the average circumferential strain on the mid-wall of the septal wall is 38.05% higher than the average circumferential strain on the free wall. Additionally, the average longitudinal strain on the mid-wall of the septal wall is 6.00 % lower than the average longitudinal strain on the free wall. When considering the four-week heart model, the average radial strain on the mid-wall of the septal wall is 84.04% higher than the average radial strain on the free wall (see Figure 3-26 (a) and (d)). Similarly, the average circumferential strain on the mid-wall of the septal wall is 75.17 % higher than the average circumferential strain on the free wall (see Figure 3-26 (b) and (e)). Additionally, the average longitudinal strain on the mid-wall of the septal wall is 95.08 % higher than the average longitudinal strain on the free wall (see Figure 3-27 (c) and (f)). Generally, it was observed that the average radial, circumferential and longitudinal strains at four-week (on the free wall) model are lower than the average radial, circumferential and longitudinal strains in both healthy and two-week infarct models on the septal wall. However, when comparing the average radial, circumferential and radial strains on the septal wall, it was observed that the strains in healthy, two and four-week models are uniformly distributed (see Figure 3-26 (d), (e) and (f)).



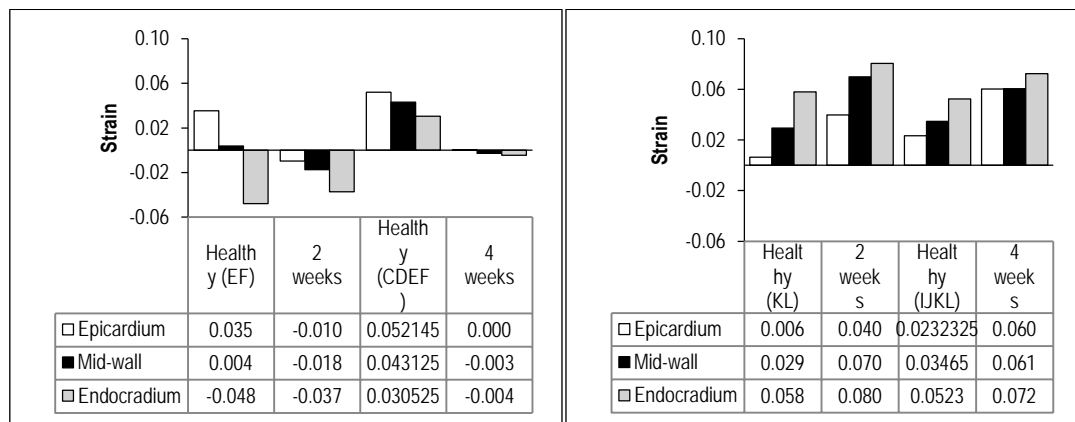
(a)

(d)



(b)

(e)



(c)

(f)

Figure 3-26: End-diastolic strain for healthy, two-week and four-week infarct models. Average radial (a), circumferential (b) and longitudinal (c) strain at paths C, D, E and F. Average radial (d), circumferential (e) and longitudinal (f) strain at paths I, J, K and L.

4 Simulation of Active Contraction in Healthy and Infarcted Hearts

4.1 Introduction

Soon after myocardial infarction, the infarcted region ceases to contract, and after 72 hours the infarcted region begins stretching and thinning; this process is commonly known as remodelling or infarct extension. The wall thinning and ventricular expansion agitate uniform strain/stress distribution in normal myocardium which affects the cardiac function. The myocardial contractility plays an important role in efficient blood pumping into the body. FE is a non-invasive method that could be helpful in assessing healthy and infarcted tissues. The goal of this chapter is to examine the effect of myocardial infarction on the rat heart during the end-systolic state. In this chapter, nearly incompressible, transversely isotropic, hyperelastic constitutive laws for active myocardial were modelled with user-defined material subroutine ORIENT in the standard FE solver, Abaqus® version 6-12. The aim of this chapter is to use the passive filling model presented in chapter 3 to perform an active contraction of the rat heart. This was achieved by adding the active stress component. In this chapter the same passive models developed in the chapter 3 were used. The transmural stress and strain in the same paths as presented in chapter 3 were used. Additionally, the functional parameters including EDV, ESV, CO and EF were determined using the presented FE results. The methodology used for simulating the healthy and infarcted heart models is given in chapter 3. In the previous chapter, the models were subjected to a static endocardial pressure of 4.8 kPa and 0.96 kPa in LV and RV, respectively. To simulate end-systolic state at ES, the endocardial pressures as a function of time of 14.6 kPa and 3.2 kPa were applied. The boundary conditions applied during end-diastolic state simulation were also used during end-systolic state. In addition, the passive material properties used during end-diastolic state simulations were also used during end-systolic state simulation.

4.2 Materials and Methods

4.2.1 MRI Dataset

The meshes used for active contraction were identical to the mesh sets used at end-diastole simulation. The short axis sets for systolic simulation are the same as the diastolic filling as shown in Figure 3-2. It should be noted here that the MRI data used for the healthy model at end-diastole and active contraction were constructed from the same animal. In addition, the MRI data for the two-week and four-week infarcted rat heart were reconstructed from the same animal.

4.2.2 Geometrical reconstruction

The 3D geometries used to model the active contraction are those that were used at end-diastole. As expected, the dimensions of the heart change considerably at ES. In other words, the wall volumes, endocardial volume, epicardial volume parameters are large compared to parameters at end-diastole phase. The physical dimensions at ES phase are detailed in Table 4-2.

4.2.3 Tissue structure definition and implementation of fibre orientation

The fibre orientation adopted in this study was detailed in section 3.2.4. It was assumed that the fibre angle distribution at end-diastole and end-systole remains the same.

4.2.4 Geometry verification

To simulate passive filling the geometry validation was done by adjusting material constant C such that the LV and RV EDVs correspond with the MRI data. The adjusted material constant was found to be 0.02 MPa. To validate the geometry to simulate active contraction, the isometric tension under maximal activation (T_{max}) was adjusted such that the LV and RV ESVs correspond with MRI data. The value T_{max} used to simulate active contraction is 67.88 kPa. This value is different to the T_{max} used in Guccione *et al.* (1993b) of 135.7 kPa.

4.2.5 Modelling of infarcted myocardium

The infarcted tissue of the heart was modelled as passive material. The active contraction of the infarcted material was switched off completely. The functional border zone was not considered in the current study. In our model, there are two sets of material definition, (1) active contraction was modelled as described in section 4.2.6 and (2) the passive mechanical properties of infarcted myocardium was modelled as described in section 3.2.5.

4.2.6 Constitutive model of active myocardium

To simulate the active contraction of the rat heart, the active stress tensor is added in to the passive strain energy function detailed in section 3.2.5 (Guccione *et al.*, 1995b). The active contraction studies were performed on the LV of a human heart and currently there is no literature on finite element analysis of active contraction on a rat heart model using the Fung orthotropic isotropic model. The results obtained at end-systole are within the range

presented by Guccione *et al.* (1993b). Therefore, the results obtained using these constitutive models for both the diastolic filling and systolic ejection is presented for the infarcted rat models. Furthermore, the constitutive model to be used for active contraction simulation was validated as presented in section 3.6. Definitions for each terms used at ES modelling are defined in the nomenclature.

$$\mathbf{T} = \mathbf{T}^{(a)} + \mathbf{T}^{(p)} \quad (70)$$

The passive and active fibre stresses are given by the following equations (Guccione et al., 1993b).

$$\mathbf{T}^{(p)} = pJ\mathbf{C}^{-1} + 2J^{-2/3}Dev\left(\frac{\partial\bar{W}}{\partial\mathbf{c}}\right) \quad (71)$$

$$\mathbf{T}^{(a)} = \mathbf{T}_o\{t, Ca_o, l, T_{max}\} \quad (72)$$

$$\mathbf{T} = \mathbf{T}_o\mathbf{C}_v \quad (73)$$

$$\mathbf{T}_o = T_{max} \frac{Ca_o^2}{Ca_o^2 + ECa_{50}^2} \mathbf{C}_t \quad (74)$$

$$ECa_{50} = \frac{Ca_{o_{max}}}{\sqrt{\exp[B(l-l_o)-1]}} \quad (75)$$

$$\mathbf{C}_t = \frac{1}{2}(\mathbf{1} - \mathbf{cos}\omega) \quad (76)$$

$$\omega = \begin{cases} \pi \frac{t}{t_o} & \text{when } 0 \leq t < t_o \\ \pi \frac{t-t_o+t_r}{t_r} & \text{when } t_o \leq t < t_o + t_r \\ 0 & \text{when } t_o + t_r \leq t \end{cases} \quad (77)$$

$$t_r = ml + b \quad (78)$$

$$l = l_R \sqrt{2\bar{E}_{FF} + 1} \quad (79)$$

B is regarded as constant, $Ca_{o_{max}}$ is the maximum peak intracellular calcium concentration, l_o is the sarcomere length at which no activation tension develops and l_R is the stress free sarcomere length. ω is the load wave, t_o is time-to-peak tension t_r is a linear function of sarcomere length, t is the time it takes to complete the active contraction phase. Table 4-1 shows the material properties used during the systolic simulation (Guccione *et al.*, 1963b) The T_{max} as presented by Guccione *et al.* (1963b) is 135.7 kPa as compared to the value of 67.88 kPa used in this study. Also, for validation of ES, the T_{max} was reduced until the LV and RV ESVs are equal to the MRI data.

Table 4-1: Parameters used in the active contraction model (Guccione *et al.*, 1963b)

Parameters	Value	Unit
T_{max}	67.88	kPa
Ca_o	4.35	μM
$(Ca_o)_{max}$	4.35	μM
B	4.75	μm^{-1}
l_o	2.04	μm^{-1}
t_o	0.1	Sec
m	1.0489	Sec
b	-1.429	Sec
l_R	1.85	μm

The infarcted region of both the two and four-week heart models are modelled using the Fung constitutive model detailed in section 3.2.5.1. It was assumed that the active contraction in the infarcted area is switched off completely. The functional border zone is not considered in the current study. The material properties on the infarcts are different for the rest of the heart. It was assumed that the material in the infarcted region has stiffer scaling factor C.

4.2.7 Implementation of the active contraction

This section describes a three dimensional constitutive model used for simulating the active myocardium during the contraction phase and its finite element implementation in Abaqus®. The starting point was to give background on the continuum mechanics needed for implementation of the constitutive model. The Fung strain energy function for myocardium is

used as an example. The UMAT subroutine generated is validated using both the analytical and numerical methods.

The present work was motivated by an interest in the development of computational models in modelling active materials. The Fung model was programmed using Fortran 77. In this study, there are two different Fung models used. The coded Fung model is referred as an ORIENT subroutine in Fortran 77. The Abaqus® Fung model is referred to as the in-built Fung model in Abaqus®. The coded Fung model was compared with the Abaqus® Fung model. In order to achieve this, three tests were developed. The uniaxial, eqi-biaxial and shear tests were developed using one hex element. The results are presented in the section below.

Abaqus® provides an application programming interface (API). The API is regarded as an extension of Python®, an object-oriented programming language. This interface assists programming and can be used to create and modify parts, steps, materials and loading conditions. The API or subroutine programming can also be used in the post processing of results and analysis of results. The availability of user subroutines in Abaqus® may assist in the modelling of highly complex behaviour of materials. In Abaqus® user subroutines are programmed in Fortran language. The successful implementation of a UMAT subroutine is achieved by initially developing the proper definition of the constitutive equation (Hibbitt et al., 1997). This task requires the following steps:

- Explicitly define the Cauchy stress for large strain applications;
- Define the stress rate in corotational framework;
- Define the dependence on time (Active contraction);
- Explicitly define the internal state variables; and
- Transform the constitutive rate of equation into and incremental equation using a suitable integration procedure.

4.2.8 Boundary conditions

The endocardial pressures of LV and RV were applied such that the required end-systolic volumes were obtained. The pressures of 14.6 kPa and 2.92 kPa were applied on the LV and RV endocardial walls as shown in Figure 4-1. Systolic simulations were performed using the pressure time relationships shown in Figure 4-2. The end-diastolic pressure in the LV is recorded to be approximately 0.627 kPa. On the LV the pressure increases from an end-diastolic value of 0.627 kPa to a peak pressure of 16.67 kPa in 0.15 seconds. Similarly, in the RV the pressure increases from an end-diastolic value of 0.1254 kPa to a peak pressure of 3.334 kPa in 0.15 seconds. The end systolic pressure is recorded to be approximately 14

kPa at the time of 0.4 seconds on the LV. The time series plot was recorded with an average heart rate of 120 beat/minutes (Guccione et al., 1993a). In this study the end systolic pressure used was 14.6 kPa and 2.92 kPa in the LV and RV, respectively. Figure 4-2 was then implemented in Abaqus® to represent the pressure as a function of time. All simulations were run using Abaqus® version 6-12. The simulation duration was 0.15 seconds at which the full contraction was achieved. The time steps used in solving the equations is 0.01 seconds for contraction model (see Figure 4-2).

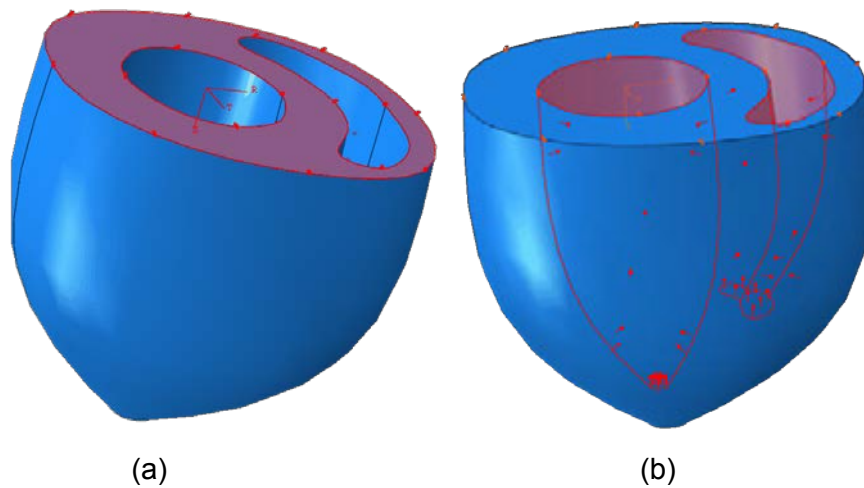


Figure 4-1: Boundary conditions at ES. (a) Basal surface and (b) Endocardial pressure applied on LV and RV.

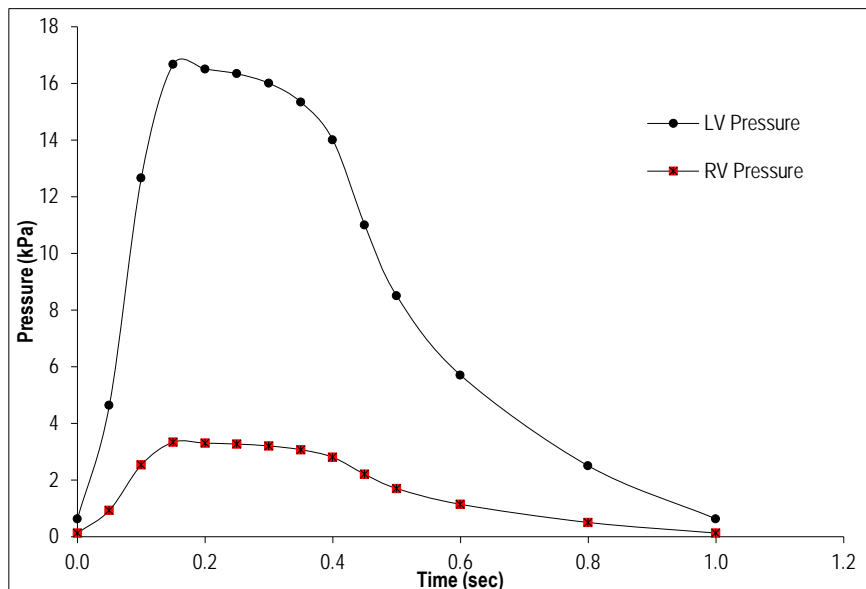


Figure 4-2: The pressure wave form of the left and right ventricle against time (Guccione et al., 1993b)

4.3 Results

4.3.1 Reconstructed geometry

4.3.1.1 3D reconstructed healthy model

The geometrical reconstruction of a 3D model during end-systolic phase was conducted the same way as that which was reported in section 3.2.2.

4.3.1.2 Dimensions of reconstructed healthy model at ES

Table 4-2 shows the overall dimensions of the healthy heart model at end-systole. Parameters used at ES phase are different to those that were used at end-diastole phase as shown in Table 4-1. The number of elements used before and after meshing is equal. The objective of Table 4-2 is to show the dimensions of a healthy model that was reconstructed from the MRI data. The end-systolic dimensions were validated by comparing them with the MRI data of the same heart model. The overall radius of the LV of the healthy model is labelled as g and has a magnitude of 2.784 mm. The distance from the centre of the LV to the epicardium is recorded to be 5.14 mm and is labelled as f. The wall thickness d of the RV has the magnitude of 1.136 mm (see Table 4-2).

Table 4-2: Geometrical dimensions at ES

Parameters	After Meshing (mm)	Before Meshing (mm)
a	12.500	12.500
b	11.254	11.300
c	12.963	12.950
d	1.1363	1.1500
e	5.5835	5.6000
f	5.1440	5.1500
g	2.7840	2.7500
h	3.4585	3.4600
i	2.7675	2.7700
No. of elements	18569	

4.3.1.3 MI model geometry

Figure 4-3 (a) and (b) shows the two-week infarcted rat heart bi-ventricular model reconstructed from the MRI. This model was validated by comparing EDV and ESV of the model and the MRI data. The cream and green colours represent the infarcted region and healthy myocardium, respectively. The infarcted region covers approximately 16% of the LV of the wall volume. It is clear from Figure 4-3 that the infarct in this case is located in the LV only. As shown by different colours the infarct is modelled by changing the scaling factor C . This was achieved by assigning the elements on the infarcted region different material properties.

The infarcted region of the four-week rat heart model is shown in Figure 4-3 (c, d). The cream and green colours indicate the infarcted region and healthy myocardium, respectively. The infarcted region in the four-week model covers approximately 26% of the LV. When comparing it to the two-week infarct model, this model has a higher infarcted area. Again, the infarct is visible on the LV only.

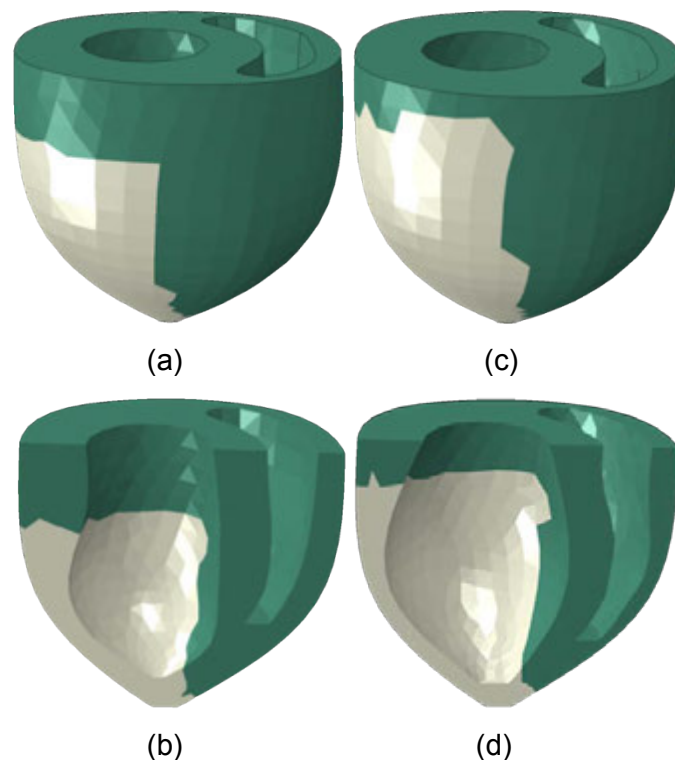


Figure 4-3: (a) Sectional view and (b) 3D model of the two-week infarct model. (c) Sectional view and (d) 3D reconstructed bi-ventricular model of a four-week infarct rat heart model. Green and white colours represent healthy and infarcted tissues, respectively.

4.3.2 Comparison of numerical models and MRI measurements

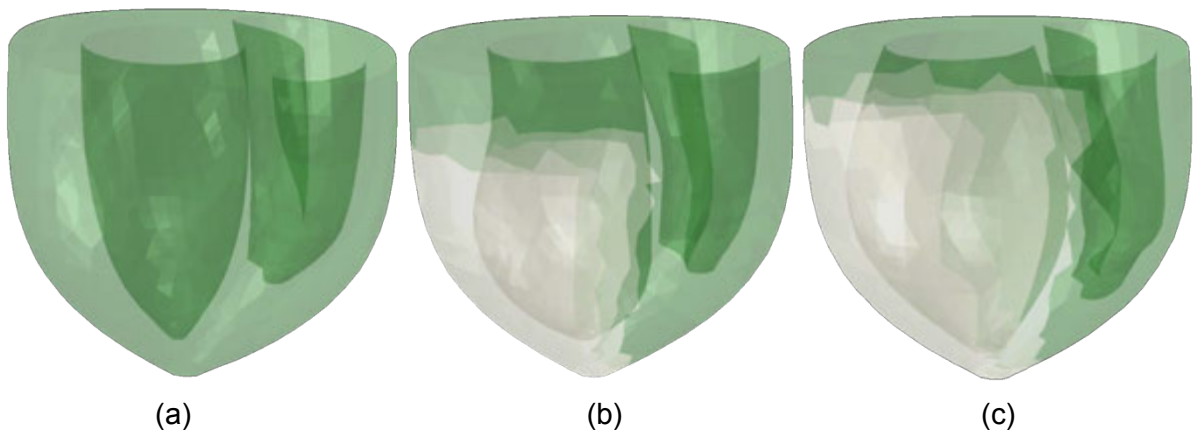


Figure 4-4: Meshed smoothed and calibrated end-systolic 3D rat heart geometries. (a) Healthy model, (b) two-week infarct model, and (c) four-week infarct model. Green and white colours represent healthy and infarcted tissues, respectively.

Figure 4-4 (a-c) shows the healthy two and four-week infarct models during end-diastolic phase. It can be seen from Figure 4-4 (a) that the model shows uniform thickness of the myocardial wall in both LV and RV. Figure 4-4 (b) shows the heart that has an infarct after two-week. During this time, the wall starts thinning due to the infarct. Further infarct is shown in Figure 4-4 (c) after four-week. The LV wall shows further thinning when comparing it with the healthy and two infarcted hearts.

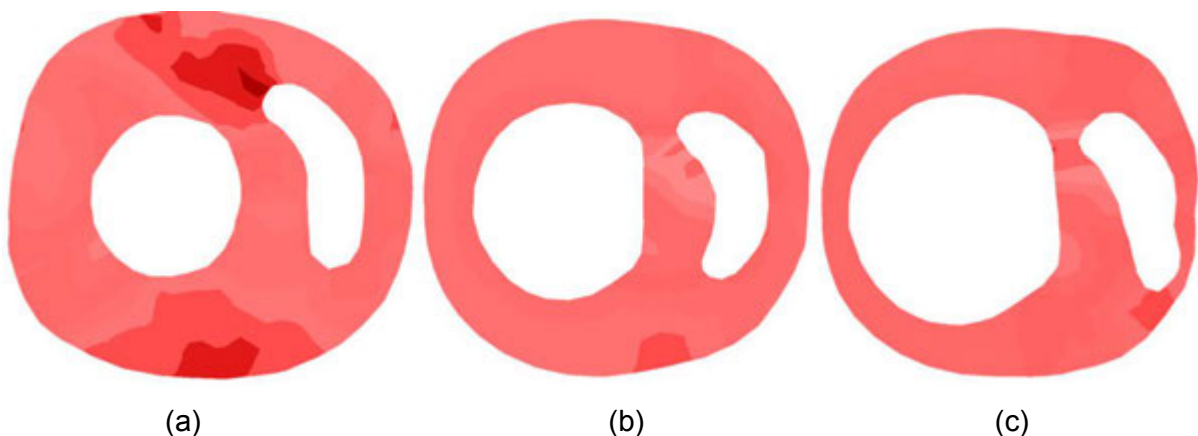


Figure 4-5: Finite element models at end-systole. (a) Healthy model, (b) two-week infarct model, and (c) four-week infarct model (Colour does not represent anything).

At end-systole time point, the MRI data was segmented and compared with the simulated data from Abaqus® using Solid Edge®. The reconstructed 3D rat heart geometries (see Figure 4-4) were calibrated using in vivo MRI data. The left ventricular volumes were

measured using Solid Edge® and compared with *in vivo* MRI data as shown in Table 4-3. The results show that all geometries (healthy, two and four-week infarcted myocardium) measures from Solid Edge® and MRI differed between 0.1 % and 5.2 %. It must be noted that this procedure was done on both diastolic and systolic volumes. This was achieved by measuring the exact inner volume of left ventricle of each geometry. It can be seen from Table 4-3 that the calculated error is 5.2 % in both end-diastolic and end-systolic volume.

After fitting the FE mesh on the contours that were segmented from the MRI data, the EDV and ESV of healthy and infarcted heart models are presented in Table 4-3. The calculated error in cavity volume of the LV at end-diastolic time point of the healthy and infarct models at two and four-week are 1.5 %, 5.1 % and 4.2 %, respectively. Similarly, the error in cavity volume of the LV at end-systolic time point of the healthy and infarct models at two and four-week are 15.1 %, 4.4 % and 7.2 %, respectively.

In Table 4-4, the model right ventricular (RV) volumes for all models are presented. The calculated error in cavity volume of the RV at end-diastolic time point of the healthy and infarct models at two and four-week are 0.75 %, 2.09 % and 1.53 %, respectively. The wall volumes of the healthy and infarct models are 1010.68 mm³, 913.64 mm³ and 848.00 mm³, respectively (see Table 4-5). Table 4-6 and Table 4-7 show the heart epicardial wall area of the healthy and infarct models and cavity area, respectively. For the healthy model, the heart wall area has an error of -0.61 %. The highest error of 5.7 % of the heart wall area was found to be on the two-week infarct model.

Table 4-3: Comparison of LV cavity volumes obtained from reconstructed models and MRI

	Healthy	Two-week infarcted	Four-week infarcted
Model ESV (μL)	73.52	181.23	245.25
MRI ESV (μL)	86.57	189.56	264.23
Error (EDV)%	-1.54	-5.06	-4.24

Table 4-4: Comparison of epicardial volume during ES of RV

Epicardial volume RV	Healthy	Two-week infarcted	Four-week Infarcted
MRI Cavity Volume (μL)	106.35	105.65	106.85
Model Cavity Volume (μL)	110.704	103.268	104.854
Error (%)	-4.09	2.26	1.87

Table 4-5: Comparison of wall volume of the heart during ES

	Healthy	Two-week infarcted	Four-week Infarcted
Model Wall Total Volume (mm ³) (before subtracting the LV and RV volumes)	1194.356	1194.356	1194.356
Model Wall Volume (mm ³)	1010.682	913.638	848.002
MRI Wall Volume (mm ³)	910.55	843.78	927.87
Error (%)	9.907	7.646	-9.418

Table 4-6: Comparison of wall area of the heart during ES

	Healthy	Two-week infarcted	Two-week Infarcted
Model Total Wall Area (mm ²)	584.41	584.41	584.41
Model Wall Area (mm ²)	209.27	184.62	141.23
MRI Wall area (mm ²)	210.55	195.22	145.63
Error (%)	-0.612	-5.742	-3.115

Table 4-7: Comparison of endocardial area of LV and RV during ES

Endocardial area	Healthy	Two-week Infarcted	Four-week Infarcted
LV Endocardial area (mm ²)	191.97	219.24	261.18
RV Endocardial area (mm ²)	183.17	180.55	182.00

4.3.3 Validation of the active contraction code

4.3.3.1 Uniaxial tests

This section presents the results of both the Fung coded and Abaqus® Fung material models. The same one-element model was run and the stress and strain of the same one element were compared between two codes. A cubic element of 20x20 mm was used. The displacement of 10 mm (50 % strain) was applied on the element as shown in Figure 4-6. The boundary conditions of the uniaxial test are shown in Figure 4-6.

As shown in Figure 4-6, one element cube is fixed in four corners to ensure that pure compression and tension is achieved. In order to control the displacement in the z or y or x direction, the displacement of 10 mm was applied instead of force or pressure. The displacement of 10 mm is equivalent to 50 % of the displacement since the element is 20x20

mm in dimension. Table 4-8 shows the material constants used to validate the active contraction model. As shown in Table 4-9, the boundary conditions applied on the uniaxial test of single hex element were applied such that pure tension and compression is achieved.

Table 4-8: Constitutive model parameters for validation of active contraction code (Omens et al., 1993)

Parameter	Constants	Value	Units
Fibre strain coefficient	b_f	9.2	-
Cross-fibre strain coefficient	b_t	3	-
Shear strain coefficient	b_{fs}	3.7	-
Stress scaling factor	C	0.002	MPa

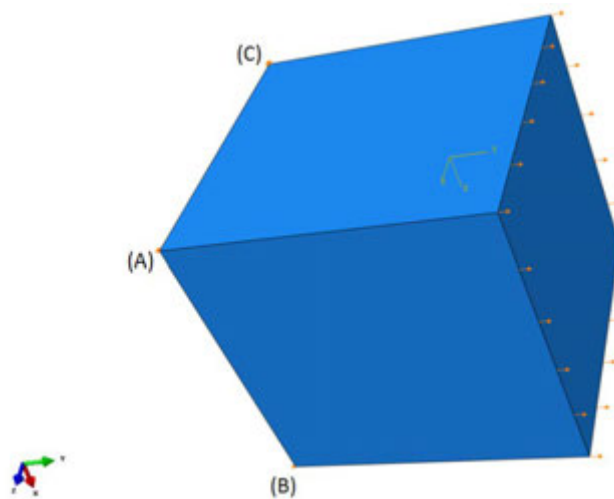


Figure 4-6: Uniaxial test loading and boundary conditions

Table 4-9: Boundary conditions of uniaxial test in single hex element (along x-direction)

Point	x-coordinate	y-coordinate	z-coordinate
(A)	0	free	free
(B)	0	0	free
(C)	0	free	0
(D)	0	0	0

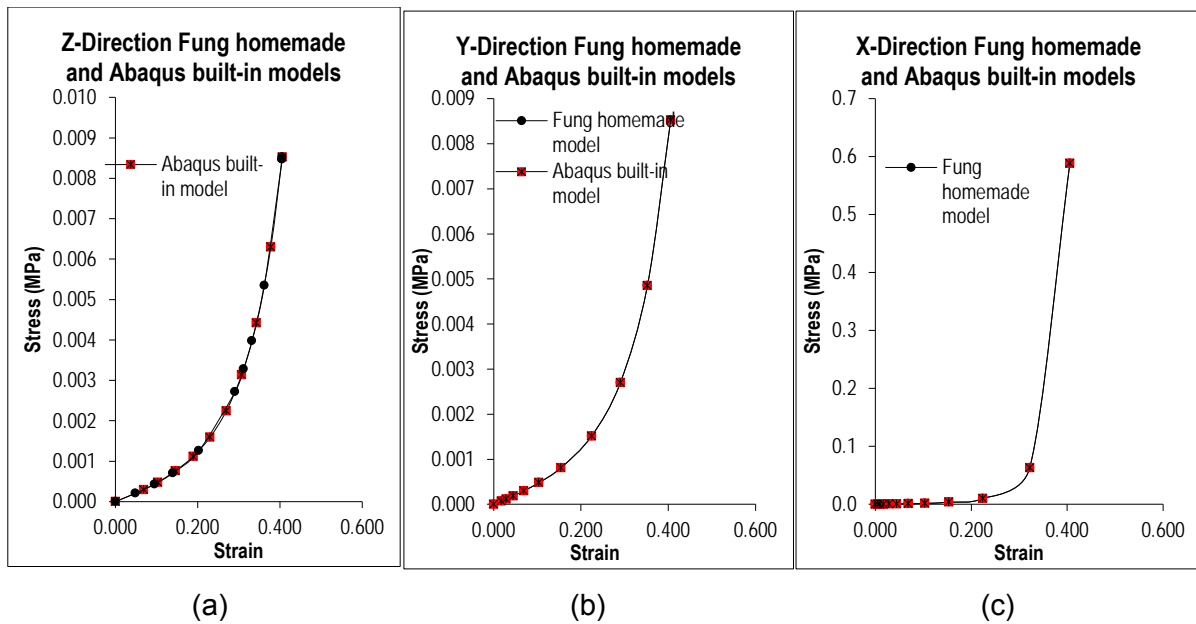


Figure 4-7: Stress vs. strain of uniaxial test in Z, Y and X directions. (a) along Z-direction and (b) along Y– direction and (c) uniaxial test along X– direction

Figure 4-7 shows the principal stresses and strains (S33 and S22) in Z and Y directions for both the Fung coded and Fung Abaqus® models. It can be seen that in this range of stress the hyperelastic behaviour is well exploited as shown in Figure 4-7 (a) and (b). There is a close fit of nearly 95% between the homemade coded model and Abaqus® built-in Fung model. It can be concluded that for tensile and compression tests the homemade coded and Abaqus® built-in models have negligible errors in the Z, Y and X directions.

Figure 4-8 shows the stress and strain in the S11 direction during a stretching in the X direction. When comparing those results with Z and Y directions, it can be concluded that the stress and strain in the Y direction for the coded Fung model is the same as the built-in Abaqus® Fung model. The highest principal stress (S11) in the X direction is 0.65 MPa and the highest principal stress in the Z and Y directions are 0.009 MPa and 0.0085 MPa, respectively. The principal stress in the X direction is higher than the principal stresses in the Z and Y direction by a factor of 72.22 and 76.47 respectively. This is mainly because the load was applied in the X direction and therefore the expectation is that the element will stretch more in this direction. It can be seen that the stress values are constant along the length of the element model. The maximum stress in the X direction where the displacement is applied is approximately 0.65 MPa. When comparing the maximum stress in the Z and Y directions, the maximum stresses are 0.009 MPa and 0.0085 MPa in the Z and Y directions, respectively.

4.3.3.2 Eqi-biaxial tests

The eqi-biaxial test is critical in accessing the accuracy of the coded Fung model. This is mainly because the elements to be used are subjected to the biaxial loading. Therefore it is important to see if the coded Fung model gives the accurate results as compared to the Abaqus® Fung orthotropic model. Figure 4-8 shows the one element model in Abaqus® loadings in both sides of the element model. In this case the element is subjected to displacement of 10 mm in the Y and X directions. The boundary conditions at the nodes are modified to accommodate the biaxial tests. This is because the element constraints are pure tension or compression testing and is not the same as the bi-axial test.

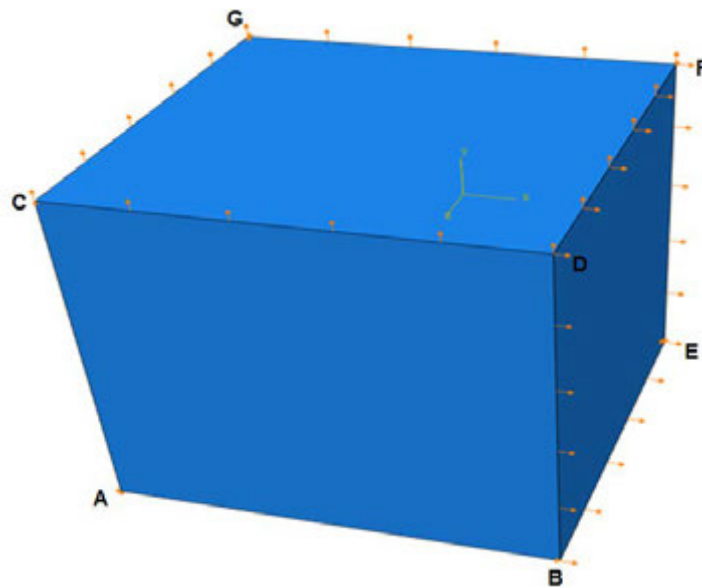


Figure 4-8: Eqi-biaxial test loading and boundary conditions

Table 4-10: Boundary conditions of biaxial test in single hex element (along x-direction)

Point	x-coordinate	y-coordinate	z-coordinate
(A)	0	free	0
(B)	free	free	0
(C)	0	0	0
(D)	0	free	0
(E)	free	0	free
(G)	0	0	free
(H)	0	free	free

It can be seen that the coded Fung and Abaqus® models provide the same stress and strain in 22 directions. This clearly indicates that the coded model is yielding the same results as the built in Abaqus® model.

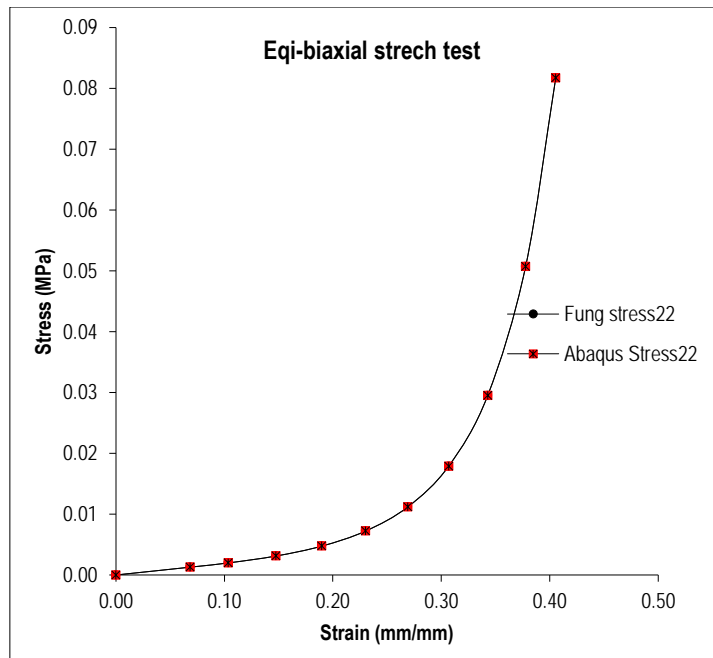


Figure 4-9: Stress vs. strain of uniaxial test along X and Y directions

The validation of passive Fung model coded using Fortran 77 language is performed by comparing the stress and strain in three directions using pure tension test, eqi-biaxial test and shear test. The highest stress in S22 direction for both the coded and Abaqus® modules is shown to be 0.085 MPa in Figure 4-9.

4.3.3.3 Shear tests

The shear test configuration in Abaqus® user inference is shown in Figure 4-10. The constraints in the four positions are modified to accommodate the shear test configuration. To ensure that the twisting mode is achieved, the displacement load of 10 mm was applied in the X direction on the one side of the element model. The consistent stress in the S11 direction during shear test is -0.00527 MPa.

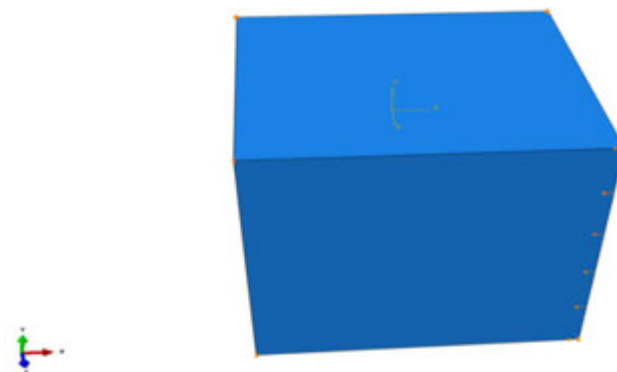


Figure 4-10: Shear test loading and boundary conditions

Table 4-11: Boundary conditions of shear test in single hex element (along x-direction)

Point	x-coordinate	y-coordinate	z-coordinate
(A)	0	0	0
(B)	0	0	0
(C)	0	0	0
(D)	0	0	0
(E)	0	0	free

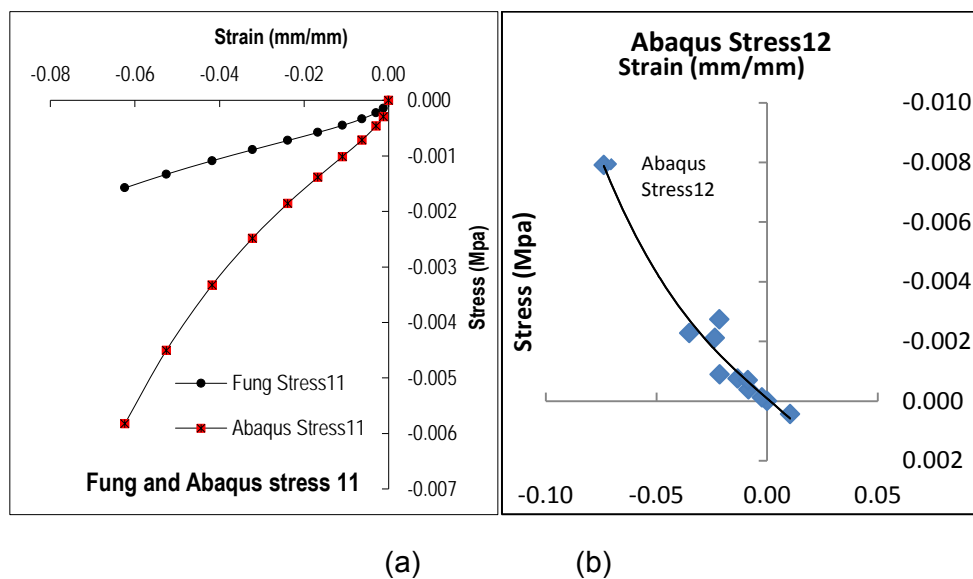


Figure 4-11: Stress vs. strain in the S11 and S12 directions

The maximum stress during shear test in the S11 direction for Abaqus® model is -0.006 MPa while the maximum stress in the S11 direction is -0.002 MPa. The difference in the stress values in the S11 direction might be due to various reasons (See Figure 4-11)

4.3.3.4 Validation of stress on active material

The selected results used to validate the model were modelled with the T_{max} of 0.3714 kPa with the magnitude of 5.891 mm. A magnitude of 5.891 mm was applied in the X direction on the passive material only (See Figure 4-12). It is concluded that the higher T_{max} parameter yields higher stress and the displacement in the U1 direction. The principal stresses are summarised in Figure 4-12.

Table 4-12 shows the stresses in S11, S22 and S33 of active material and passive material, respectively. The error of the stress in S11 direction is calculated to be 6.95%. This error is the smallest error when comparing it with the error calculated in S22 and S33 directions. The active stress values were achieved by running the simulation of one element model using the coded Fung model. As per the definition of the active model, the model must contract without applying any external load on it. On this case, the displacement of the model depends on the magnitude of the T_{max} .

Table 4-12: Validation of active stress model

Stress	Active (kPa)	Passive (kPa)	Error (%)
S11	-26.38	-28.35	-6.95
S22	-16.37	-21.94	-25.39
S33	-16.37	-21.94	-25.39

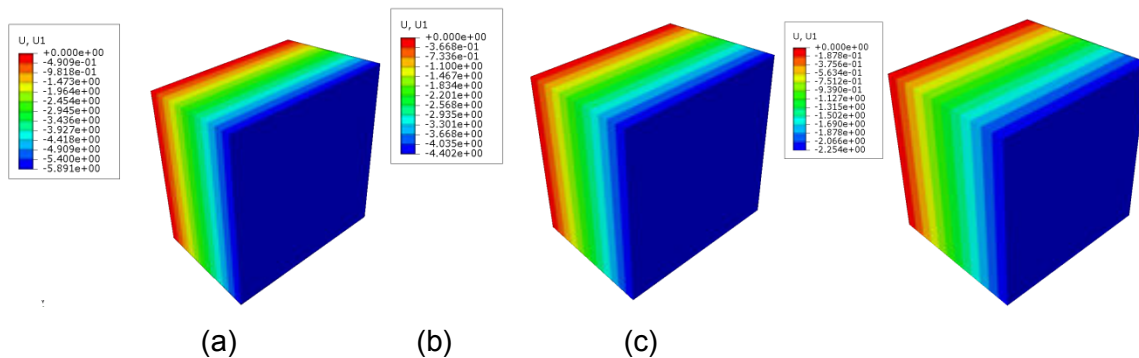


Figure 4-12: Active contraction of one element (a): $T_{max} = 0.3714$ kPa, (b): $T_{max} = 0.2714$ kPa, (c): $T_{max} = 0.1357$ kPa

4.3.3.5 Validation of strains on active material

Figure 4-13 shows the contour plots of the strain during active modelling by varying the T_{max} . It can be seen that the highest T_{max} produced the highest magnitude in the U1 direction. To validate and verify the active model, the U1 of 5.891 mm was applied on the one element model using the passive coded model. The strains in the LE11, LE22 and LE33 of the active and passive models were compared. The results for maximum and minimum strains in LE11, LE22 and LE33 are shown in Table 4-13 and Table 4-14, respectively.

As shown in Table 4-13 and Table 4-14 the maximum strains are shown to have the minimum errors when comparing them with the minimum strains. The error on the maximum strain is 0.62 % while the error of 0.44 % is recorded on the minimum strains in the LE11. The errors of 0.47 % and 0.66 % have been recorded for maximum and minimum strain, respectively along LE22. Along LE33 Table 4-13 and Table 4-14 show the error of 0.47 % and 0.66 % in the maximum and minimum strains, respectively. It is therefore concluded that the active models show that the developed and implemented models are both accurate and reliable and are suitable in the application to study the local cardiac mechanics during systolic phase.

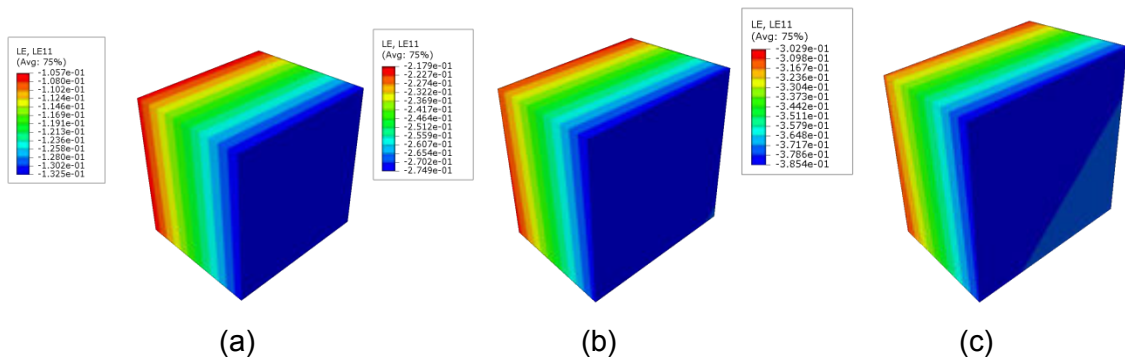


Figure 4-13: Active contraction of one element strain contours (a): $T_{max} = 0.3714$ kPa, (b): $T_{max} = 0.2714$ kPa, (c): $T_{max} = 0.1357$ kPa

Table 4-13: Validation of active maximum strain model

Strains (maximum)	Active Strain	Passive Strain	Error (%)
LE11	-0.3029	-0.3048	0.62
LE22	0.1928	0.1919	-0.47
LE33	0.1928	0.1919	-0.47

Table 4-14: Validation of active minimum strain model

Strains (minimum)	Active Strain	Passive Strain	Error (%)
LE11	-0.3854	-0.3837	-0.44
LE22	0.1514	0.1524	0.66
LE33	0.1514	0.1524	0.66

4.3.4 Ventricular function

Figure 4-14 shows the end-diastolic volume and end-systolic volume of healthy two-week and four-week infarct models, respectively. The ED volume of the healthy model increased from 207 μL to 369 μL on the four-week infarct models (see Figure 4-14 (b)). Figure 4-14 (a) shows the end-diastolic volume of the LV in healthy, two-week and four-week infarct models. The ES volume for the healthy model was predicted to be 73 μL whereas the ES volume of two-week and four-week infarcted hearts was predicted to be 119 μL and 186 μL , respectively.

Figure 4-15 shows the stroke volume calculated using ESV and EDV as shown in Figure 4-15. The SV of healthy, two and four-week infarct models are 134.77 μL , 142.76 μL and 182.91 μL . The ejection fraction for the healthy model was 64.9 %. Figure 4-16 shows that there is a decrease in ejection fraction for two-week and four-week infarct models to 54.6 % and 49.5 %, respectively.

The reduction in ejection fraction on the infarct models is attributed to the increase of collagen and stiffening of the scar tissue. Another reason for the decline in ejection fraction is that the infarcted area is set to behave like a passive material. While the healthy region is contracting due to active forces on the myocardium, the diseased area on the heart does not contract. Figure 4-17 shows the EDPVR and ESPVR of healthy, two-week and four-week infarct models. The slope of the EDPVR is smaller than that of ESPVR.

Figure 4-18 shows the contractility of healthy and infarct models at ES. The healthy model shows high contractility as opposed to infarct models which show the decrease of contractility. The contractility was calculated by measuring the slope of the graph for all models. As shown in Figure 4-18 the contractility at two-week and four-week infarct models was reduced to 0.2634 $\text{kPa}/\mu\text{L}$ and 0.1935 $\text{kPa}/\mu\text{L}$, respectively.

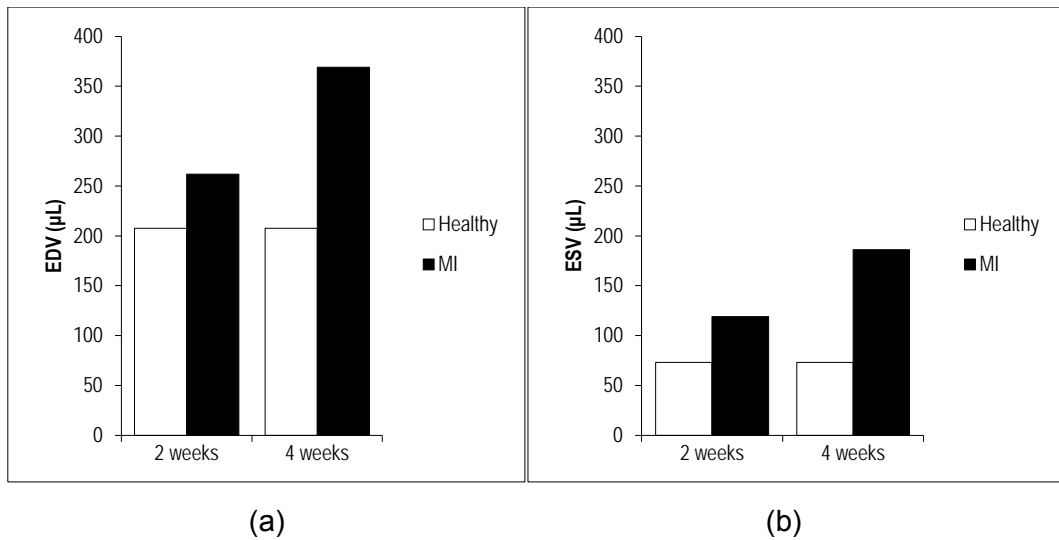


Figure 4-14: EDV and ESV for healthy, two-week infarct and four-week infarct models.

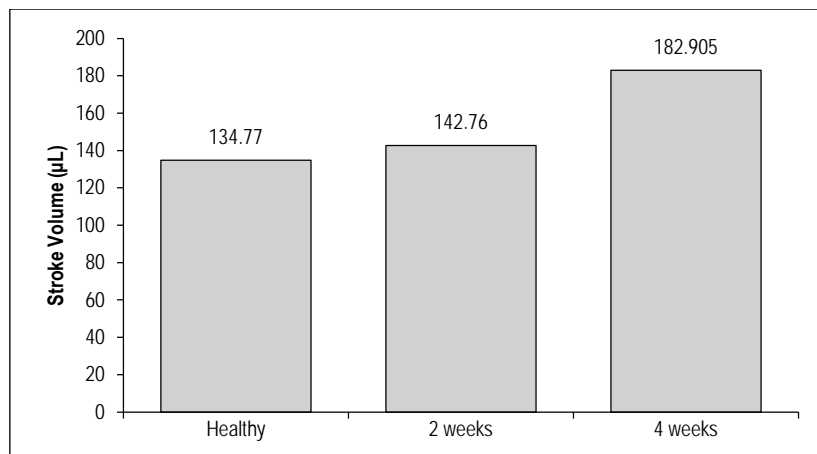


Figure 4-15: Stroke volume for each model.

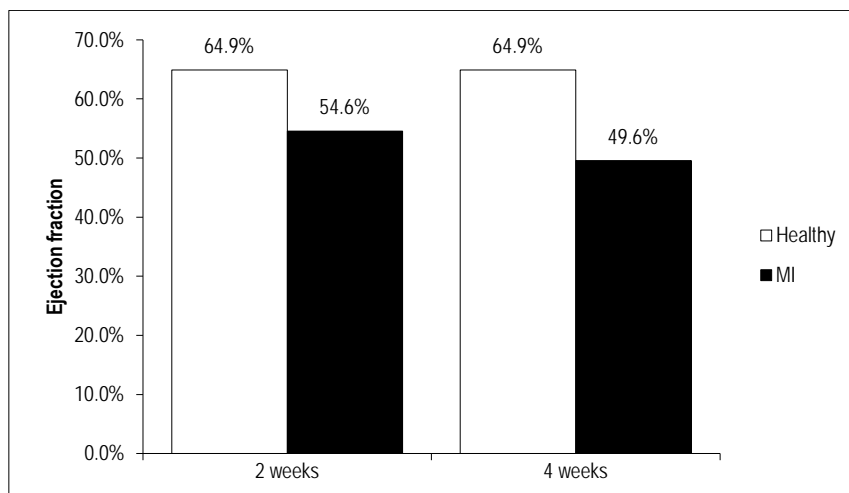


Figure 4-16: Ejection fraction for healthy, two-week and four-week infarct models.

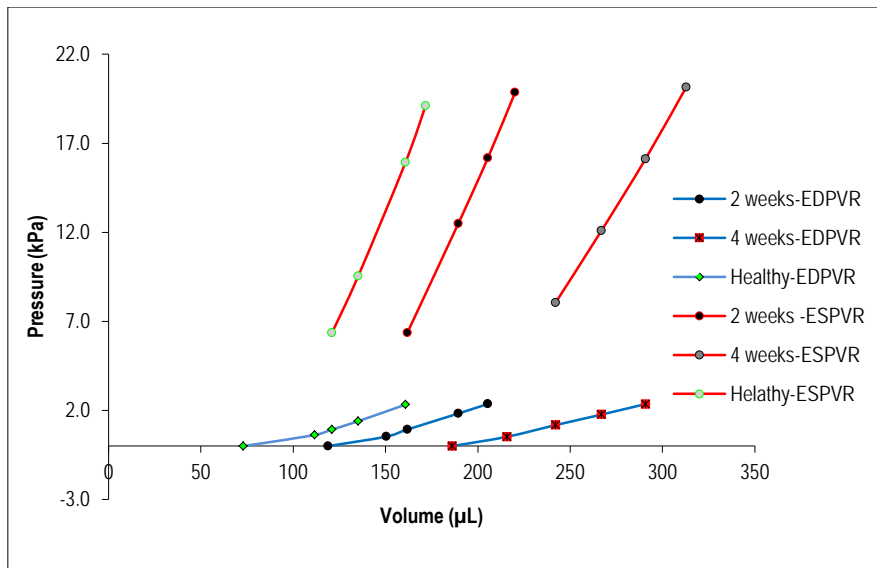


Figure 4-17: The effects of large infarcts on diastolic and systolic (EDPVR and ESPVR) pressure-volume relationship.

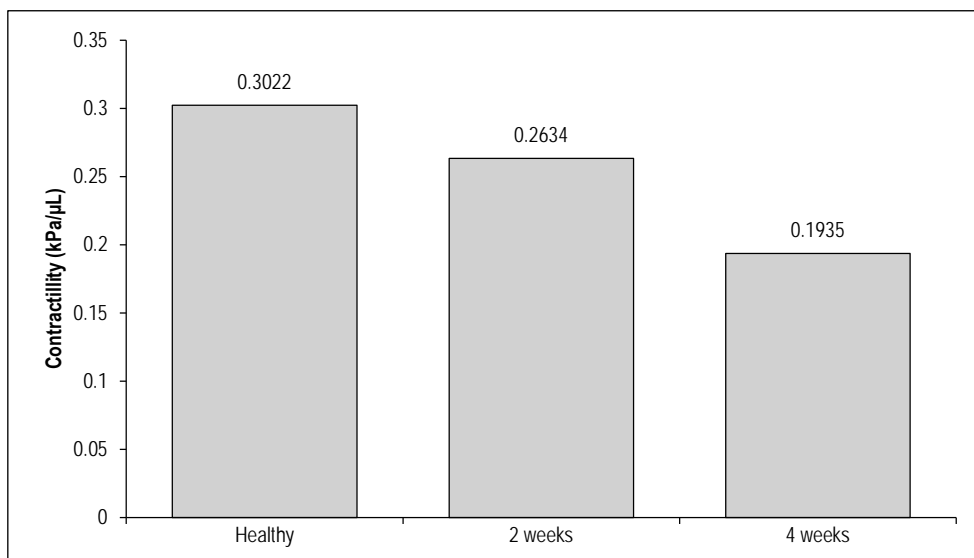


Figure 4-18: Contractility of healthy, two-week and four-week infarct models

4.3.5 End-systolic myocardial mechanics in left and right ventricle

4.3.5.1 Distribution of end-systolic strain in the left and right ventricle

The results presented in this section were obtained using the subroutine developed for simulating the end-systolic state presented in Appendix A. It can be seen that the radial strain is higher at the infarcted regions in both the infarct models. At ES and at end-diastole the contour plots of the Figure 4-19 shows the strain in radial, circumferential and

longitudinal directions in healthy and infarcted hearts after two and four-week, respectively. Figure 4-19 (a)-(c) shows the radial strains in radial direction of the healthy and two infarcted heart models, respectively. The radial strain is lower in the infarcted regions in both infarct models. Furthermore, Figure 4-19 shows the long axis of healthy and infarct models. In Figure 4-20 the infarcted area of the two-week model has a radial strain of -0.04 when compared to the four-week infarct model which has a radial strain of -0.002. However, the infarct model at two-week has low radial strain when comparing it to the four-week infarct model.

The circumferential strains in the four-week infarct model are higher than the radial and longitudinal strains by an average of 30 % and 95 %, respectively. This behaviour could be interpreted to mean that all models have higher strain in the circumferential direction when compared with radial and longitudinal directions. This is contrary because the pressure applied on the model was applied on the endocardial wall. The high strain in the circumferential direction could also be attributed to the fact that the active contraction was assumed to be on the fibre direction only.

The apex region for healthy and infarct models shows high strains in all directions considered. This is normally due to the computational error during simulation. This area is therefore not considered in further processing of the results. As compared to the strain distribution at end-diastole, the longitudinal strains are high at ES by 95 %. It should be noted here that the longitudinal strains at end-diastole and active contraction simulation are minor when compared with radial and circumferential strains.

It can be concluded that the models translate further in the circumferential direction at end-diastole and active contraction simulation. This confirms what was expected because the heart model is constrained in both the circumferential and longitudinal directions at the basal surface. The material properties at the infarcts were modelled with an increased C of 0.02 kPa. The infarcted area modelled at ES is identical with that modelled at end-diastole. The infarcted region has resulted in the increase of strain in radial, circumferential and longitudinal direction during the active contraction phase. This is attributed to the fact that the material in the infarcted regions was increased by tenfold. This has increased the strains but the increase of stress is shown in these regions. Figure 4-19, Figure 4-20 and Figure 4-21 show the strain contour plots of healthy and infarct models along short-axis, long-axis and 3D rat heart model contour plots, respectively. It can be seen that in Figure 4-19 (b) and (c) the infarcted area in the two-week model is less than the infarcted

area in the four-week model. This has an influence in the strain distribution along all three directions (radial, circumferential and longitudinal) because there is a reduction of strain in the infarcted region.

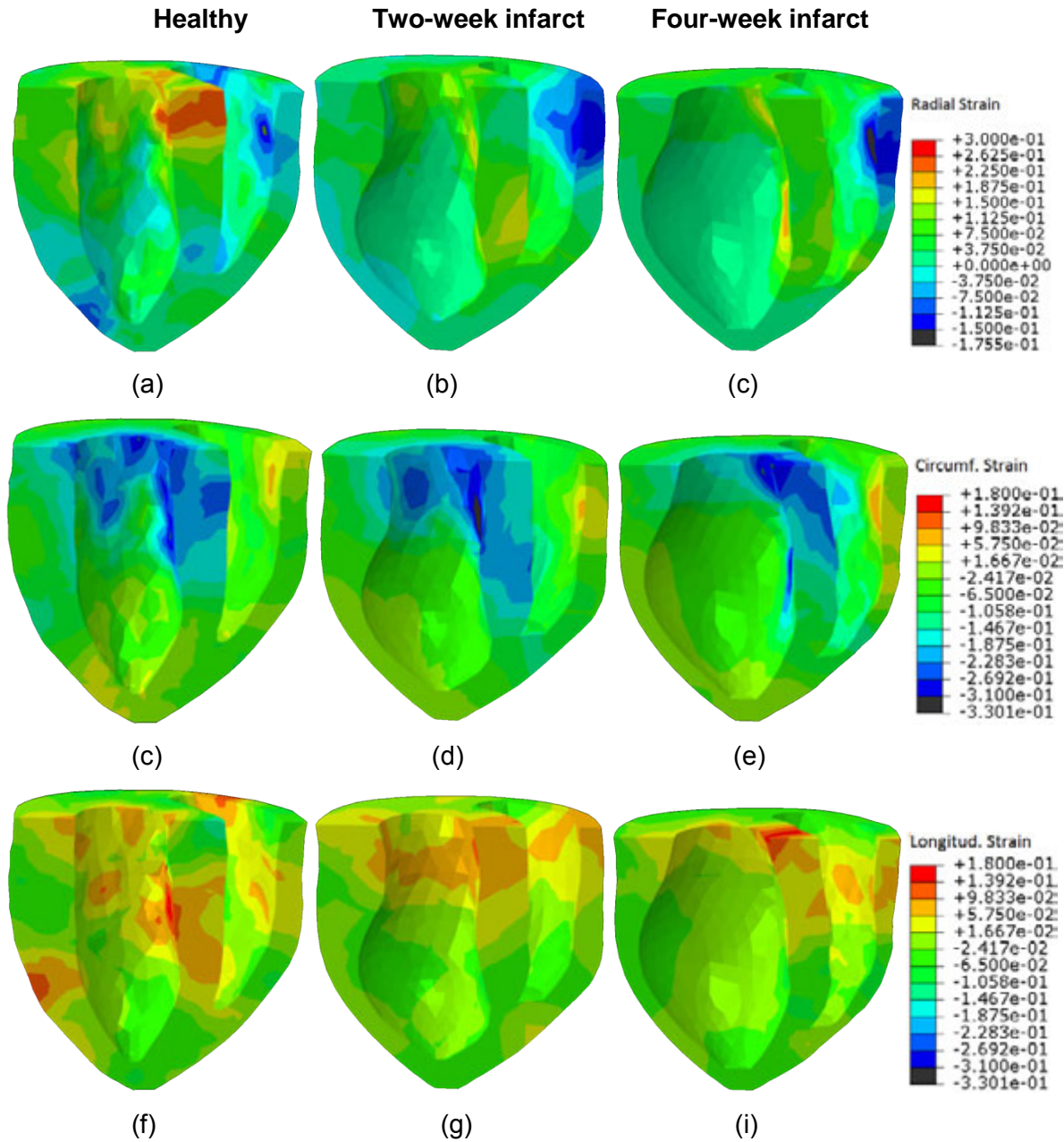


Figure 4-19: Contour plots of end-systolic strains in a central long axis cross-section and endocardium of healthy, two-week and four-week infarct models. (a)-(c): Radial strains. (d)-(f): Circumferential strains. (g)-(i): Longitudinal strains.

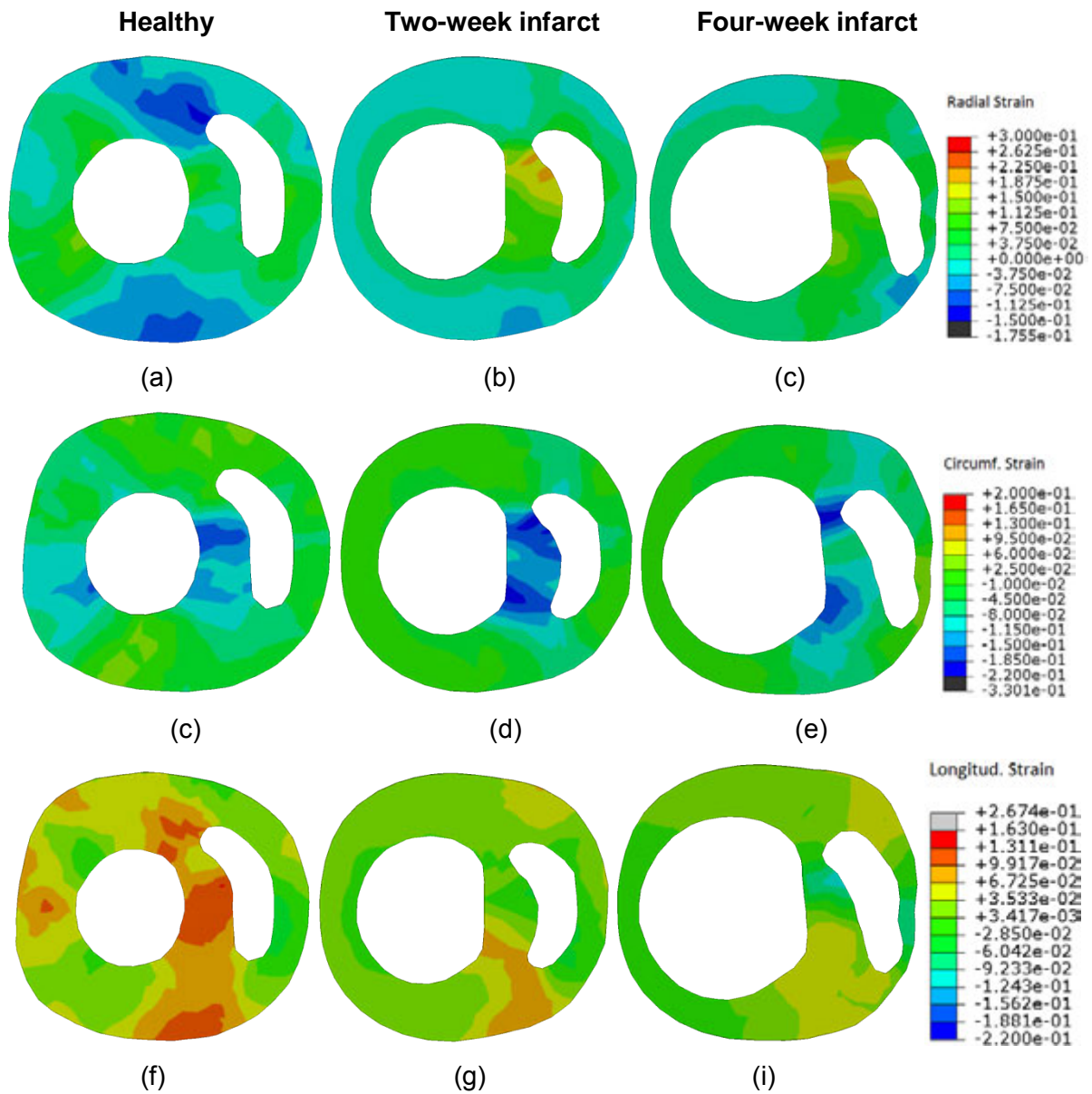


Figure 4-20: Contour plots of end-systolic strains on the short-axis cross-section equidistant between the base and the apex of the healthy, two-week and four-week infarct models. (a)-(c): Radial strains. (d)-(f): Circumferential strains. (g)-(i): Longitudinal strains.

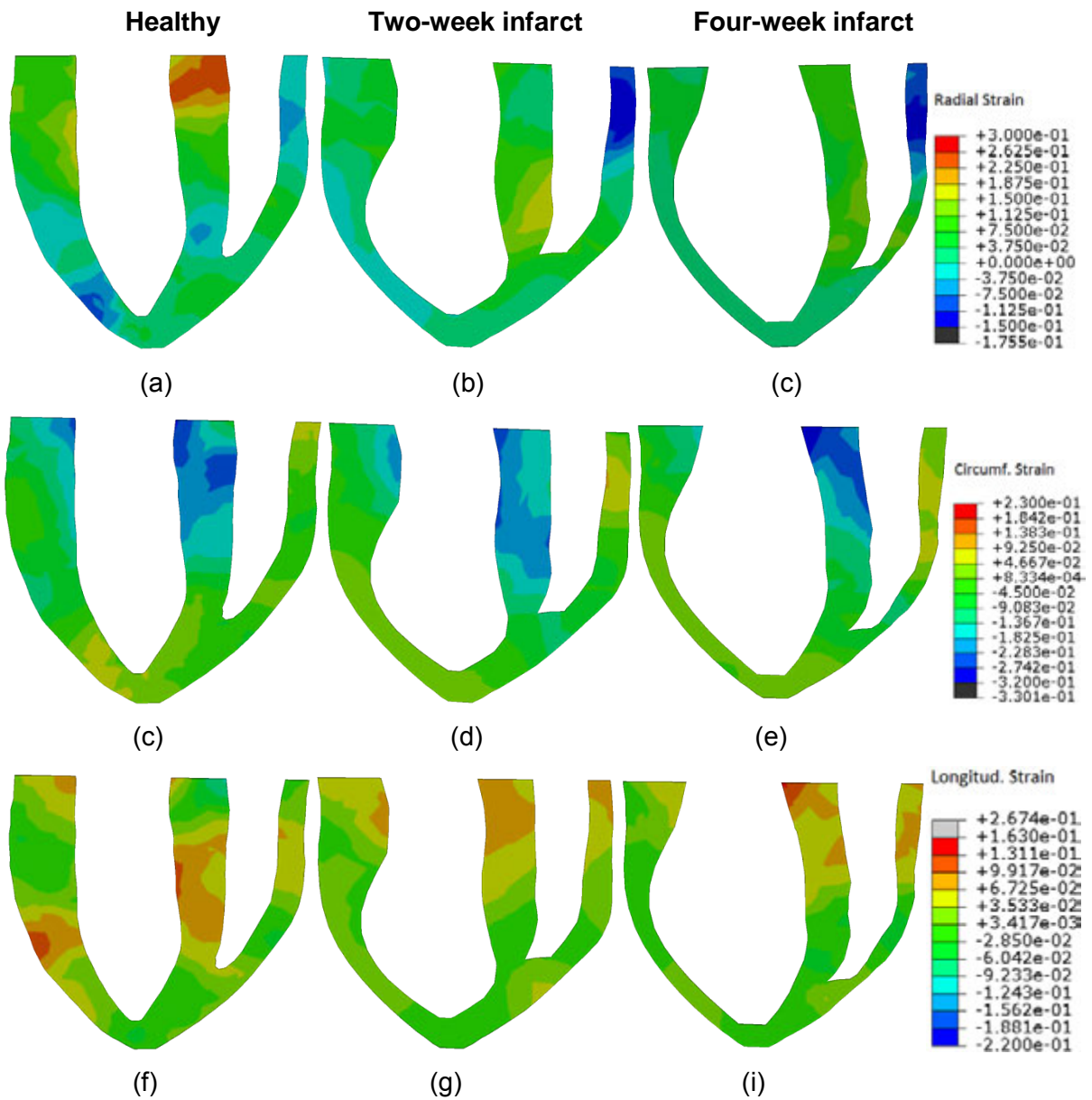


Figure 4-21: Contour plots of end-systolic strains in the central long axis cross section of the healthy, two-week and four-week infarct models. (a)-(c): Radial strains. (d)-(f): Circumferential strains. (g)-(i): Longitudinal strains.

4.3.5.2 End-systolic stress along intramural paths in the left ventricle

Figure 4-22 represents the end-systolic stresses along intramural paths in the LV free wall (i.e. the region affected by the infarct) and the non-infarcted septal wall. The transmural position is expressed by the normalised myocardial thickness. Transmural position and normalised myocardial thickness correspond as follows:

- LV free wall: 0 = epicardium, 0.5 = mid-wall and 1 = endocardium,
- Septal wall: 0 = RV endocardium, 0.5 = mid-wall and 1 = LV endocardium.

The selected paths are C, D, E and F in the LV free wall and I, J, K and L in the septal wall (see Figure 3-13).

Figure 4-22 (a), (d) and (g) indicate that radial stress in all regions in the healthy model are lower than the radial stresses in the infarcted regions. This means that in the infarct, the thinned wall extends more than the thick wall of the healthy model. The regions I, J, K and L exhibit higher radial stresses compared to regions C, D, E and F at ES phase in both the healthy and infarct models. It is important to note that the circumferential stresses at two-week infarct models are higher than the radial and longitudinal stresses by an average of 65% in the same model.

Longitudinal stresses on the healthy model are shown to be more equal to circumferential stresses but higher than stresses in the radial direction. It is to be noted that the contraction is assumed to be in the fibre direction. These patterns exist in both the two and four-week infarct models. The infarcted regions D, E and F in the infarct models show a linear increase of stress from the endocardium to the epicardium across the myocardial wall. This may be attributed to the further thinning of the myocardial wall due to MI progression and remodelling. This behaviour of the stresses across the myocardial wall does not manifest in the non-infarcted regions (I, H, K and L) across the myocardial wall thickness from the endocardium to the epicardium.

Generally, the stresses in the radial, circumferential and longitudinal direction in healthy and infarct models seem to increase linearly from the epicardium to the mid-wall. However, the observation of the stresses behaviour from the mid-wall to the endocardium is different. In this case, the stresses increase sharply from mid-wall to endocardium in healthy and infarct models. This may be attributed to the myofibre orientation across the wall from the epicardium to endocardium. The myofibre orientations are distributed such that it is zero degrees at the mid-wall and -55° at the epicardium and $+55^\circ$ at the endocardium.

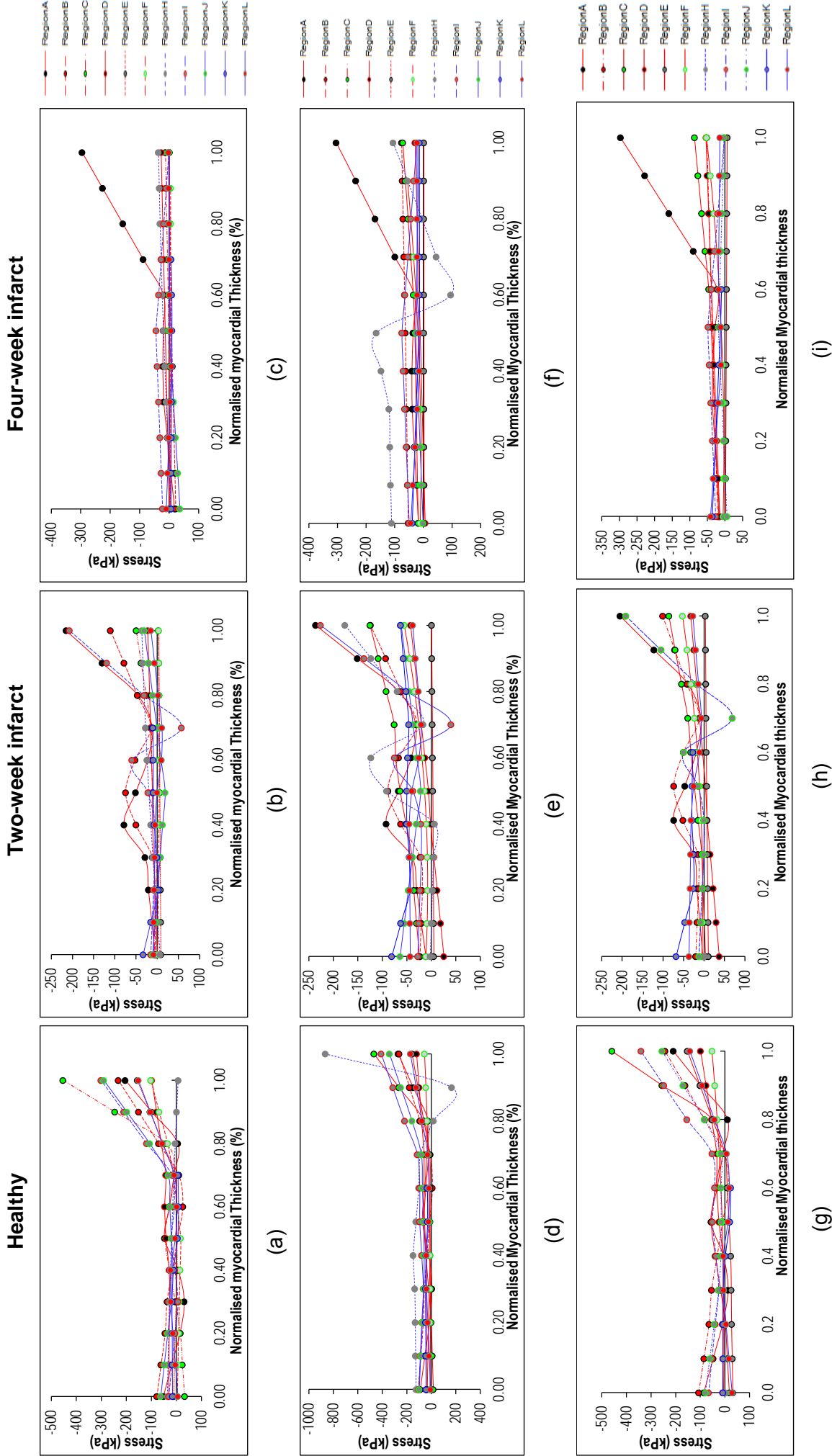


Figure 4-22: Transmural distribution of end-systolic stresses as function of normalised myocardial thickness of LV free wall and septal wall for of healthy, two-week and four-week infarct models. (a)-(c): Radial stresses, (d)-(f): Circumferential stresses, and (g)-(i): Longitudinal stresses. (Paths C, D, E and F: red; paths I, J, K and L: blue.)

4.3.5.3 End-systolic strain along intramural paths in the left ventricle

Figure 4-23 shows the distribution of radial, confereential and longitudinal strains from the epicardial to endocardial wall of the healthy and two and four-week infarct models. Figure 4-23 (a), (d) and (g) show that the radial strains show the widest spread from 0.23 to -0.05 in the radial direction. This is followed by the strains in the circumferential direction as shown in Figure 4-23 (d). The least spreading of the strain has occurred in the longitudinal direction from 0.05 to -0.05. This behaviour is contrary to that of the two-week infarct model as shown in Figure 4-23 (c), (f) and (i). In this model, the shortest spread is shown in Figure 4-23 (e) from -0.05 to -0.15 in the circumferential direction.

From Figure 4-23 (a), (b) and (c), it is observed that the radial strains for the healthy model are lower than in the infarct models at two and four-week. Figure 4-23 (c) shows the radial strains of the infarct model after four-week. In this model, the radial strains in the selection regions are high especially in the region where the infarct is clearly visible. The radial, circumferential and longitudinal strains are low in the C, D, E and F regions. However, the radial, circumferential and longitudinal strains are high at the infarcted regions I, J, K and L as shown in Figure 4-23 (c), (f) and (i).

At ES, the variations of strains in all three directions seem to vary linearly. This is opposite to the observation made from the passive filling modelling results. In active contraction the strain variation is linear and does not shows sign of hyperbolic or parabolic. In passive filling phase the myocardial walls are only moved by the internally applied pressure on the endocardial wall of both the LV and RV. At ES simulation, even though the high pressure of 14.6 kPa is applied on the endocardial walls of LV and RV, the active stress is still generated within the myocardial wall to counter the pressure applied in the endocardial walls.

Figure 4-23 (d)-(f) shows that the highest strains are in the circumferential direction for healthy and infarct models. This means that the movement on the circumferential direction is independent of whether the heart is infarcted or not.

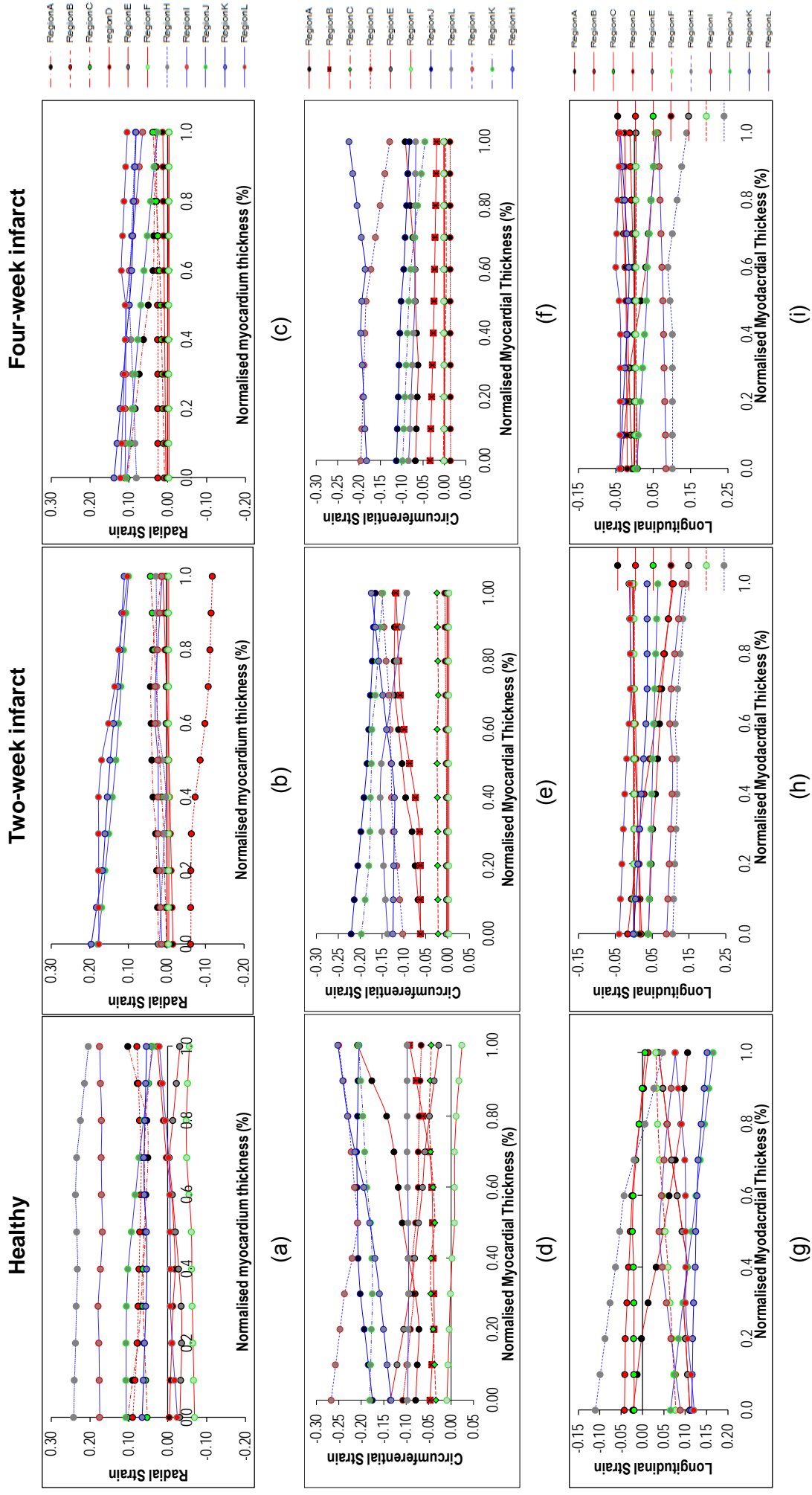


Figure 4-23: Transmural distribution of end-systolic strains as function of normalised myocardial thickness in LV free wall and septal wall for healthy, two-week and four-week infarct models. (a)-(c): Radial stresses, (d)-(f): Circumferential stresses, and (g)-(i): Longitudinal stresses. (Paths C, D, E and F: red; paths I, J, K and L: blue.)

4.3.6 End-systolic myocardial mechanics in the LV infarct region and the non-infarcted septal wall

This section shows the stresses and strains in radial, circumferential and longitudinal directions for healthy two-week and four-week infarct models at ES. The radial, circumferential and longitudinal stresses at epicardial, mid-wall and endocardium at regions C, D, E and F are plotted for comparison purposes. This section allows comparing how stresses and strains behave in different regions of both the healthy and infarct models. In a later section, the average stresses and strains are computed in order to compare the average values of stresses and strains in healthy and infarcted regions. This allows one to gain an understanding of the mechanisms of myocardial infarction in healthy and infarcted myocardium. This understanding is critical in the adoption of MI treatment during these stages.

4.3.6.1 Stress and strain in the left-ventricular infarct region

Figure 4-24 shows the stresses in the radial, circumferential and longitudinal direction for healthy and infarct models at the endocardium, mid-wall and epicardium. Radial stresses are shown in Figure 4-24 (a)-(c) whereas Figure 4-24 (d)-(f) shows the circumferential stresses and Figure 4-24 (g)-(i) shows the longitudinal stresses. Generally, the stresses (radial, circumferential and longitudinal) are highest at the endocardium and lowest at the epicardium. This is attributed to the fact that the internal pressure of 14.6 kPa and 2.92 kPa was applied at LV and RV, respectively in healthy and infarct models.

The infarct model at four-week shows that the radial, circumferential and longitudinal stresses are high compared to those in the healthy and the infarct model at two-week. The highest stresses are in the circumferential direction at four and two-week model after infarction. The healthy model shows the lowest stress values in all directions.

At the epicardium, the radial stresses are low compared to the stress values in the circumferential and longitudinal directions. The highest radial stress recorded is 75 MPa for the four week infarct model. The highest circumferential stress value is 150 MPa in the four-week infarct model at regions D and E. Regions C and F show the lowest values of stress in all direction at the epicardium and the mid-wall positions as shown in Figure 4-24 (c), (f) and (i).

At the endocardium, region C shows the highest stress values in radial, circumferential and longitudinal directions. However, as shown in Figure 4-24 (d) and (g), the circumferential and longitudinal stresses are low in region F. This is not the same for radial stress in the region F. This is expected because region F is near to the apex and it is not expected that it will have deformation as the deformation constraint by the apex. At the mid-wall position, the radial, circumferential and longitudinal stress at region F is low as compared to regions C,D and E for healthy and infarct models at two and four-week.

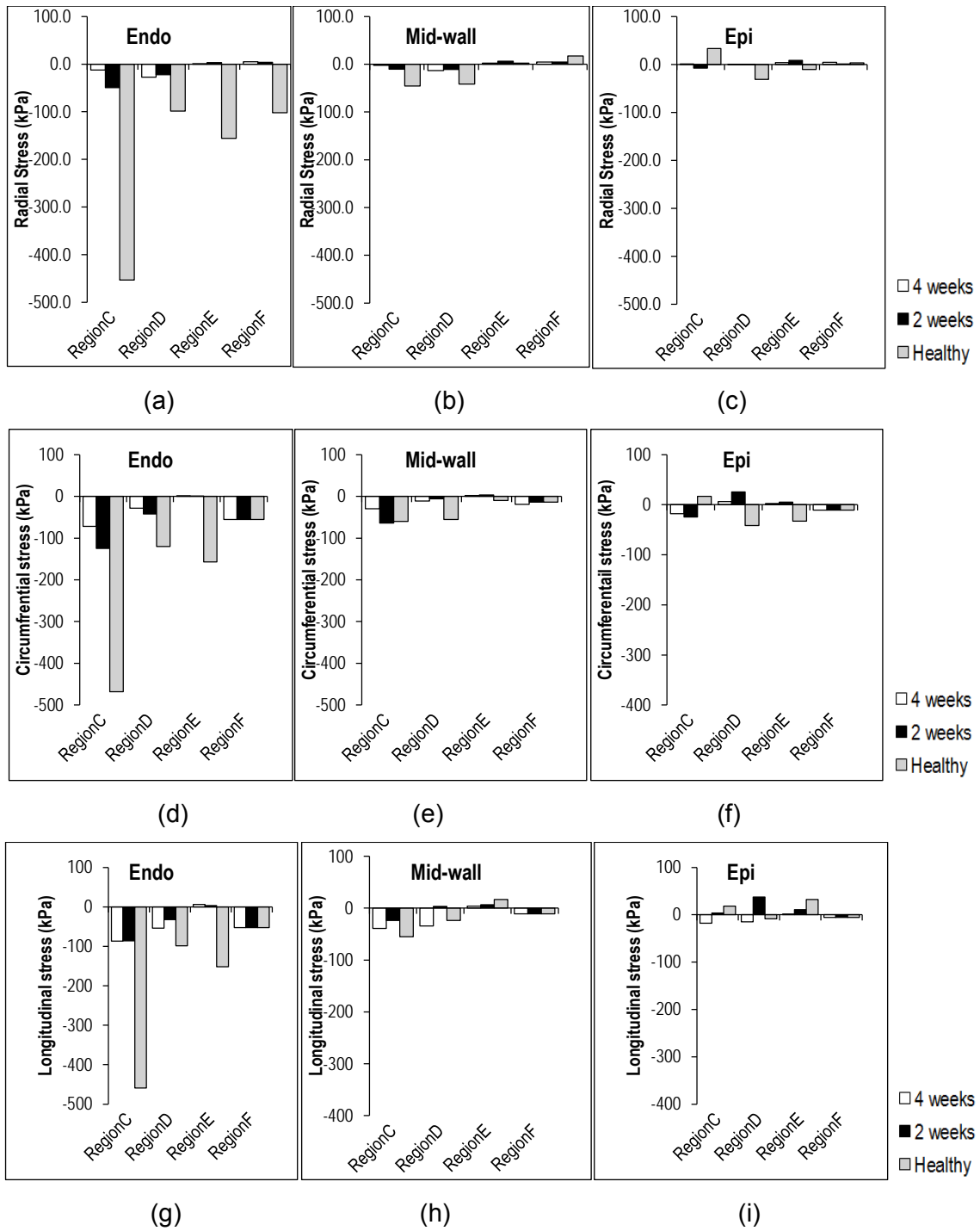


Figure 4-24: Comparison of end-systolic stresses at endocardium, mid-wall and epicardium in regions C, D, E and F of the healthy, two-week and four-week infarct models. (a)-(c): Radial stresses, (d)-(f): Circumferential stresses, and (g)-(i) Longitudinal stresses.

Figure 4-25 shows the strains in radial, circumferential and longitudinal direction at the endocardium, mid-wall and epicardium for healthy and infarct models. Radial strains are shown in Figure 4-25 (a)-(c) whereas circumferential strains are shown in Figure 4-25 (d)-(f), and longitudinal strains are shown in Figure 4-25 (g)-(i).

The strains in all three directions are high in the four-week infarcted heart when compared to two weeks infarcted and healthy heart models. In the four-week infarct model, region C shows the highest strains in radial, circumferential and longitudinal directions. Small strain values are recorded in the epicardium position in all regions C, D, E and F.

The longitudinal strains are shown to be the lowest in all the regions (endocardium, mid-wall and epicardium). This is contrary to the strains in radial and circumferential directions. Circumferential strain shows to be the highest compared to radial and longitudinal strains. The highest strain value is recorded in the circumferential direction at region C as shown in Figure 4-25 (d) for four-week infarct model. Region F shows the lowest strain values in the radial, circumferential and longitudinal directions in the healthy model at the endocardium position. The highest value of strain at region F is recorded to be -0.16 in the four-week infarct model.

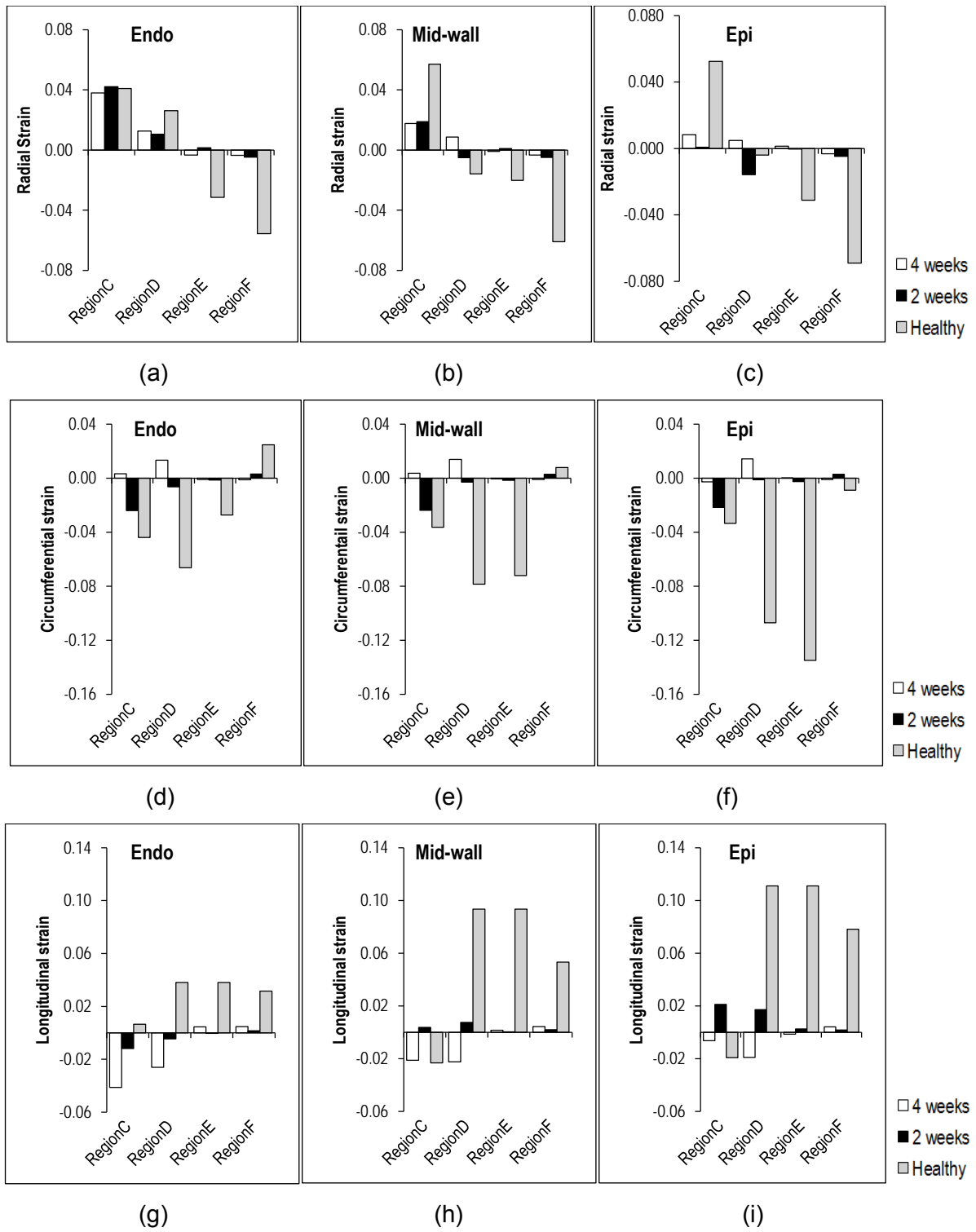


Figure 4-25: Comparison of end-systolic strains at endocardium, mid-wall and epicardium in regions C, D, E and F of the healthy, two-week and four-week infarct models: (a)-(c): Radial strains, (d)-(f): Circumferential strains, and (g)-(i): Longitudinal strains.

4.3.6.2 Stress and strain in the non-infarcted septal wall

Stress in radial, circumferential and longitudinal directions for healthy and infarct models in the I, J, K and L regions are shown in Figure 4-26. The circumferential stress at the endocardium is higher than the circumferential stress in the mid-wall and inner surface of the septal wall (LV). The radial, circumferential and longitudinal stress at the endocardium in the Regions I, J, K and L are higher than the stress in the mid-wall and epicardium. Contrary to the passive filling phase modelling, the higher radial stress is recorded in the two-week infarct model. As shown in Figure 4-26 (a) the radial stress in the regions I, J, K and L are -120 kPa, -90 kPa, 175 kPa, -220 kPa for two-week infarct model at the endocardium, respectively. Moreover, the radial stress in the Regions I, J, K and L are 20kPa, -20kPa, -30 kPa, -35 kPa for two-week infarct model at the mid-wall, respectively. Finally, the radial stress in the regions I, J, K and L are 50 kPa, -20 kPa, 25 kPa, -18 kPa for two-week infarct model at the epicardium, respectively.

When comparing the stress in circumferential and longitudinal direction at ES, it can be seen from Figure 4-26 (d) and (g) that the longitudinal and circumferential stresses have equivalent magnitude. This is contrary to the passive filling because during this phase there is no active force generated by the myocardium. Radial stress in the mid-wall position has the same magnitude when comparing to the stress in the epicardial position as indicated in Figure 4-26 (b) and (c). The observation is the same when looking at the circumferential and longitudinal stresses in the Regions I, J, K and L of the mid-wall and epicardium (see Figure 4-26 (e), (f), (h) and (i)). It is important to note that this observation happens in healthy and infarct models.

I, J, K and L regions are labelled as shown in Figure 4-26 (a) and (b). As shown in Figure 4-26 the Regions I, J, K and L represent the myocardial wall which is between the LV and RV. This tissue wall is subjected to pressure applied on the LV and RV plus the active forces generated at ES. When comparing the circumferential stresses in the I, J, K and L regions, it can be seen that the circumferential stress for four-week infarct model are -295 kPa, -140 kPa, -200 kPa, -250 kPa, respectively at the endocardium. The maximum circumferential stress in the regions is -295 kPa. Consequently, the circumferential stresses for regions I, J, K and L in the four-week infarct model are -130 kPa, -80 kPa, -81 kPa, -85 kPa, respectively at the mid-wall. Consequently, the circumferential stresses for regions I, J, K and L in the four-week infarct model are -110 kPa, -80 kPa, -20 kPa, -30 kPa, respectively at the epicardium.

In Figure 4-26 (d) and (e) it can be seen that in region I, the circumferential stress in Figure 4-26. (d) is higher in the two-week infarct model while in Figure 4-26 (e) the circumferential stress is higher in the four-week infarct model. This trend continues even in Figure 4-26 (f) where circumferential stress at the epicardial position is shown. The circumferential stress at the endocardium in regions I, J, K and L for two-week infarct model are -500 kPa, -270 kPa, -150 kPa, -110 kPa, respectively. Furthermore, the circumferential stress at the mid-wall in Regions I, J, K and L for two-week infarct model are -110 kPa, -60 kPa, -80 kPa, -45 kPa, respectively. Moreover, the circumferential stress at the epicardium in regions I, J, K and L for two-week infarct model are 10 kPa, 75 kPa, -40 kPa, -45 kPa, respectively. As expected the circumferential stress in the endocardial position are higher than mid-wall. The smallest circumferential stresses are found in the epicardial position as shown in Figure 4-26 (f).

Figure 4-26 (g)-(i) shows the stress in the longitudinal direction at ES at the endocardium, mid-wall and epicardium in the regions I, J, K and L. As expected the highest stress in this case are found in the endocardium. The lowest circumferential stresses are found in the epicardium. As shown in Figure 4-26 (g) and (h), the highest longitudinal stresses are found in the two-week infarct model. This is not what was observed at end-diastole phase. The longitudinal stresses at the endocardium for two-week infarct model are -450 kPa, -240 kPa, -120 kPa, -100 kPa in regions I, J, K and L, respectively. In addition, the longitudinal stresses at the mid-wall for two-week infarct model are -100 kPa, -30 kPa, -80 kPa, -60 kPa in regions I, J, K and L, respectively. Furthermore, the longitudinal stresses at the epicardium for two-week infarct model are 15 kPa, -55 kPa, 30 kPa, -45 kPa in regions I, J, K and L, respectively. At the epicardial position, the longitudinal stress in region I is positive which signal that the myocardium is in tension. The observation is different from others in the two-week infarct model where the majority of longitudinal stresses are in compression.

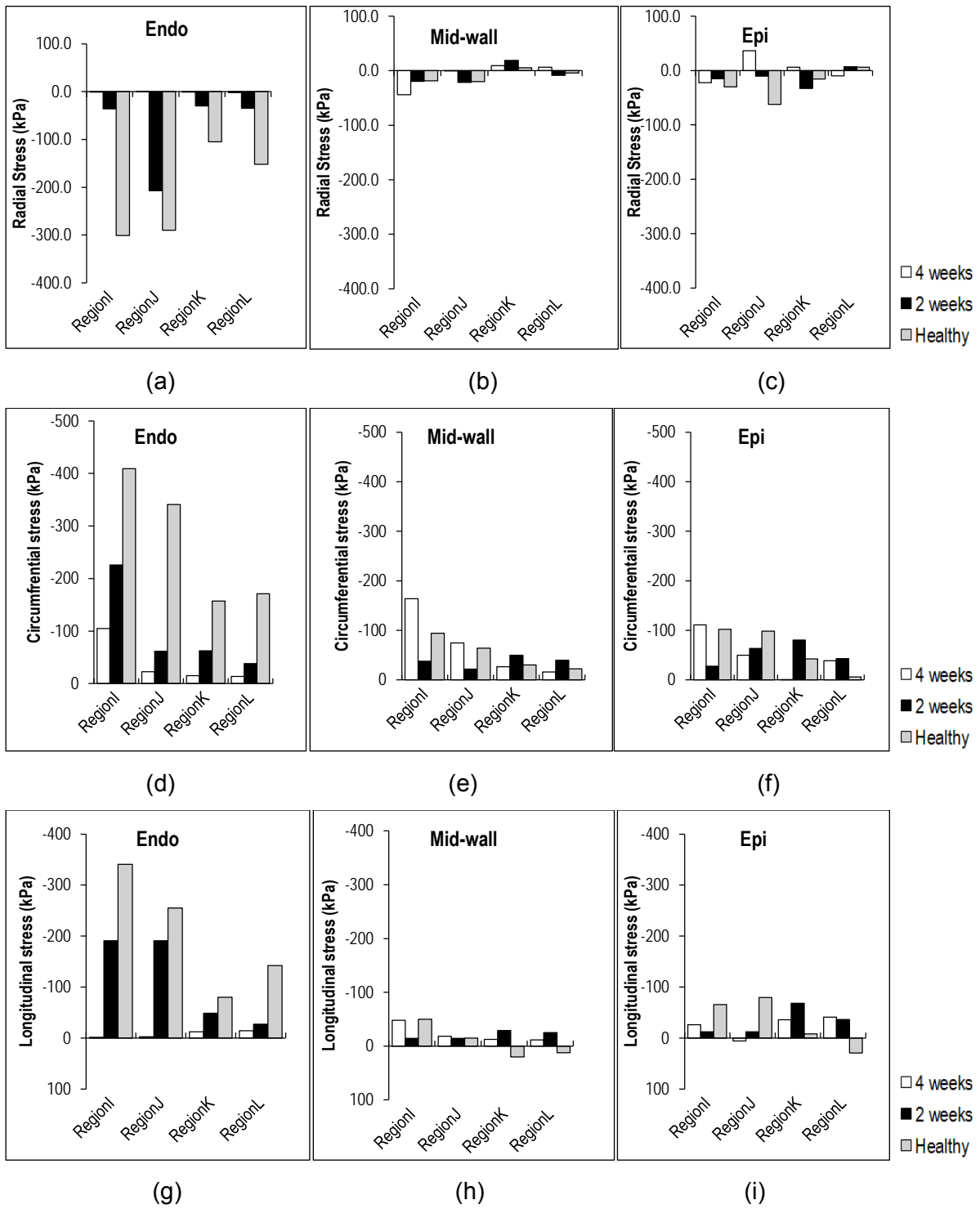


Figure 4-26: Comparison of stresses in Epicardium, Mid-wall and Endocardium at ES in IJKL region. (a), (b) and (c) represents the radial stresses of the healthy, two-week and four-week infarct models, respectively; (d)-(f) represents the circumferential stresses of the healthy, two-week and four-week infarct models, respectively and (g)-(i) represents the longitudinal stresses of the healthy, two-week and four-week infarct models, respectively.

Strains in radial, circumferential and longitudinal directions for healthy and infarct models in the I, J, K and L are shown in Figure 4-27. The observation here is that the radial strains in the endocardium, mid-wall and epicardium have equivalent magnitude as shown in Figure 4-27 (a)-(c). The above described observation holds in circumferential strains as shown in Figure 4-27 (d)-(f). The same applies when looking at the longitudinal strains at the endocardium, mid-wall and epicardium as shown in Figure 4-27 (g)-(i). Even though there is no pressure applied on the epicardium, due to the force generated in the myocardial tissue the epicardium still experiences strain due to active stress. This is different from the passive filling simulation because in this case, there are no active generated forces by the myocardium. When comparing the radial, circumferential and longitudinal strains, it can be seen that the radial strain is higher than the circumferential strain followed by the longitudinal strain. This trend is however similar to that observed at end-diastole phase as shown in Figure 4-27. It is vital to note that the radial stress at the endocardium on the two-week infarct model is higher than the radial stress of the healthy and two-week infarct model as shown in Figure 4-27. This trend is different when looking at the radial strain as shown in Figure 4-27. It can be seen that Figure 4-27 (a) shows that the radial strain of the two-week infarct model in the endocardium is lower than the radial strain of the healthy and four-week infarct model in the endocardium.

The radial strains at the endocardium in the Region I, J, K and L for two-week infarct model as shown in Figure 4-27 (a) are 0.10, 0.14, 0.145, and 0.13, respectively. Furthermore, the radial strains at the mid-wall in the Region I, J, K and L for two-week infarct model as shown in Figure 4-27 (b) are 0.09, 0.14, 0.15, 0.13, respectively. Likewise, the radial strains at the epicardium in the Region I, J, K and L for two-week infarct model as shown in Figure 4-27 (c) are 0.065, 0.14, 0.15, 0.145, respectively. From the information given, it can be concluded that the radial strains in the endocardium, mid-wall and epicardium for the two-week infarct model are evenly distributed. The highest radial strains are produced by the four-week infarct models at Region I as shown in Figure 4-27 (a), (b) and (c). The radial strains on the endocardium of the four-week infarct model in the Regions I, J, K and L at ES phase are 0.26, 0.15, 0.10, and 0.04, respectively as shown in Figure 4-27 (a). Likewise, the radial strains on the mid-wall of the four-week infarct model in the Regions I, J, K and L at ES phase are 0.23, 0.14, 0.10, 0.05, respectively as shown in Figure 4-27 (b). Equally, the radial strains on the epicardium of the four-week infarct model in the Regions I, J, K and L at ES phase are 0.19, 0.12, 0.09 and 0.06, respectively as shown in Figure 4-27 (c). To note here is that the radial strains are all positive in the endocardium, mid-wall and epicardium. This

means that the radial strains are all in tension. However, Figure 4-27 (a), (b) and (c) shows that the radial stresses are all negative which signals that the myocardial tissue is in compression.

Figure 4-27 (d)-(f) shows the circumferential strains in the endocardium, mid-wall and epicardium on the regions I, J, K and L. It can be seen that the highest strain in the circumferential direction is observed at the endocardium followed by the mid-wall. The lowest circumferential strains are observed in the epicardium on the four-week infarct model. In the endocardial position, the circumferential strain of the four-week infarct model in the regions I, J, K and L at ES phase are -0.27, -0.10, 0.01 and 0.05, respectively. Also, in the mid-wall position, the circumferential strain of the four-week infarct model in the Regions I, J, K and L at ES phase are -0.26, -0.11, -0.04 and -0.08, respectively. Equally, in the epicardial position, the circumferential strain of the four-week infarct model in the Regions I, J, K and L at ES phase are -0.26, -0.07, -0.09 and -0.06, respectively.

Figure 4-27 (g)-(i) shows the longitudinal strains on the healthy and infarct models in the regions I, J, K and L at ES at endocardium, mid-wall and epicardium. The longitudinal strains in all regions (I, J, K and L) at endocardium, mid-wall and epicardium are found to be lower than the radial and circumferential strains. In this region, the mixer of negative and positive longitudinal strains in various regions is observed. This is opposite to the circumferential strains where every strain was negative. As shown in Figure 4-27 (g),(h) and (i) the positive longitudinal strains are observed in the endocardium, mid-wall and epicardium at Region I. Looking at Region I, the longitudinal strain at the endocardium in region I for four-week infarct model is 0.015. On the mid-wall and epicardium the longitudinal strains at region I are 0.03 and 0.06, respectively. In region L, the longitudinal strains in the endocardium, mid-wall and epicardium are shown to be positive and hence in tension for healthy model. Again, in region L, the longitudinal strain is positive only at the endocardial and mid-wall positions. The highest longitudinal strain is found in region K at the endocardium. However, at the mid-wall position the highest longitudinal strain is found to be in region J for four-week model. The observation is the same in the epicardial position where the highest longitudinal strain is found in region J.

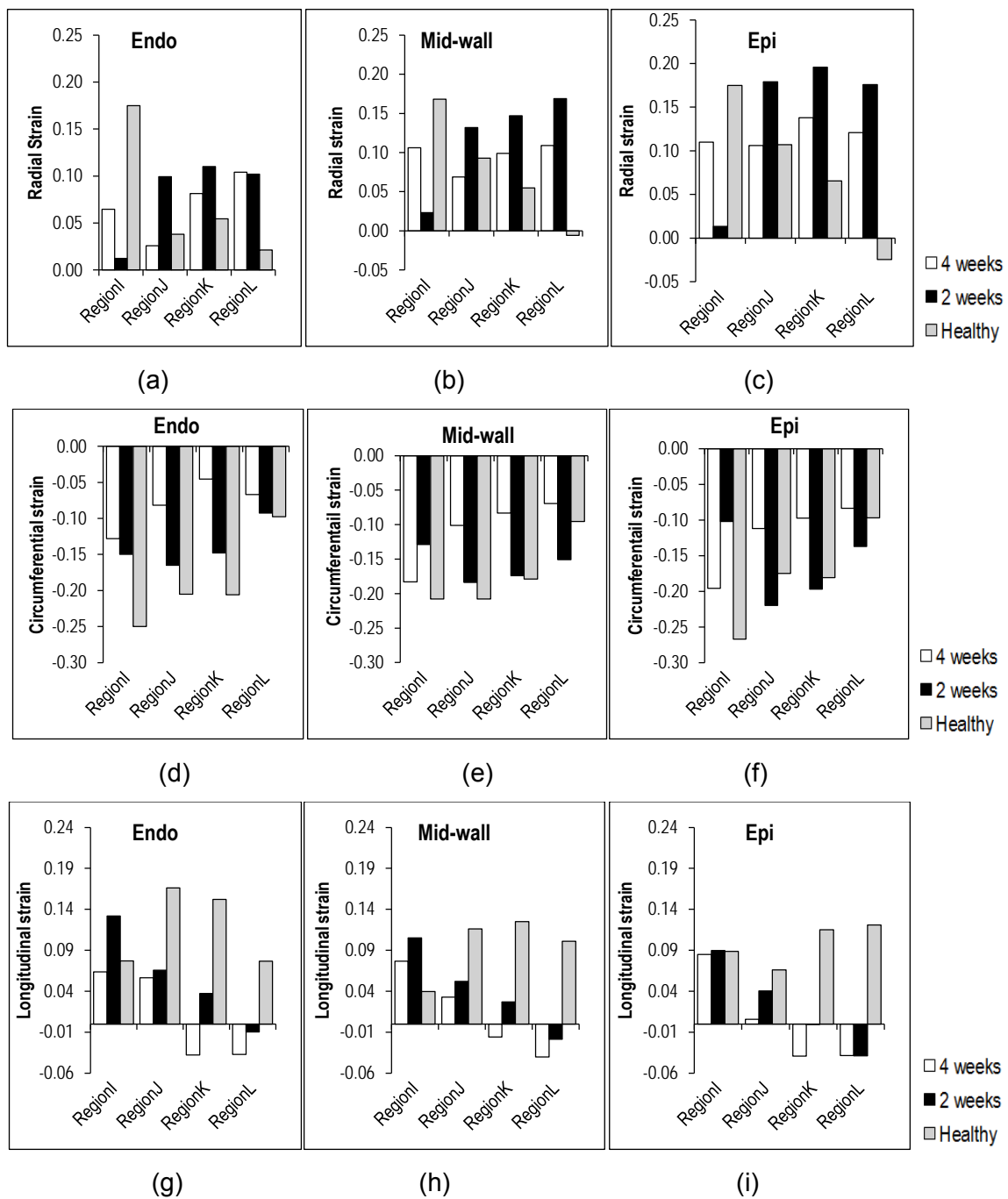


Figure 4-27: Comparison of strains in Epicardium, Mid-wall and Endocardium at ES in IJKL region. (a), (b) and (c) represents the radial stresses of the healthy, two-week and four-week infarct models respectively; (d)-(f) represents the circumferential stresses of the healthy, two-week and four-week, infarct models, respectively and (g)-(i) represents the longitudinal stresses of the healthy, two-week and four-week infarct models, respectively.

4.3.6.3 Comparison of end-systolic stress and strain in infarct region and septal region

Figure 4-28 (a)-(f) shows the systolic stresses in radial, circumferential and longitudinal direction in the selected regions C, D, E and F and I, J, K and L. The C, D, E and F paths are located where the tissue infarct is present. Consequently, the I, J, K and L is located where there is no tissue infarct, but these paths are the wall which separate the LV and RV. As shown in Figure 4-28 (a), (b) and (c), the radial, circumferential and longitudinal stresses at the endocardium position are -202.32 kPa, -200.05 kPa and -190.48 kPa, respectively for healthy model. In the same way, the radial, circumferential and longitudinal stresses at the mid-wall are -17.00 kPa, -38.81 kPa and -18.31 kPa, respectively. The radial stress in the mid-wall is lower than in the circumferential and longitudinal directions by 52.35% and 7.10%, respectively. Similarly, Figure 4-28 (a), (b) and (c) for healthy model at the epicardium, shows that the radial, circumferential and longitudinal stresses are -1.25 kPa, -17.17 kPa and 9.15 kPa, respectively. Nonetheless, the trend resembles that which was observed at end-diastole modelling, including that the magnitudes of the stresses in all directions are much high than the latter.

Generally, the radial, circumferential and longitudinal stresses for two and four-week infarct models are lower than that of the healthy model. For example, as shown in Figure 4- (a)-(c) at the endocardium, the radial stress of the healthy model is 92.1 % and 95.8 % higher when compared to two and four-week infarct models. In the two-week infarct model at the endocardium, the radial, circumferential and longitudinal stresses are -16.13 kPa, -55.46 kPa and -41.77 kPa, respectively. When comparing two-week infarct model to the healthy model, it has been observed that the radial, circumferential and longitudinal stresses at the mid-wall are higher than the stresses at the epicardium position. This observation is different from that which was observed at end-diastole modelling results. For example, for two-week infarct model, the circumferential stress at the mid-wall is -49.24 kPa while the stress is -36.20 kPa at the epicardium position. Similarly as shown in Figure 4-28 (c), the longitudinal stress at the mid-wall position is -14.06 kPa and -36.10 kPa at the epicardium position.

Figure 4-28 (a), (b) and (c) show the low distribution of stresses in radial, circumferential and longitudinal directions for four-week infarcted heart model as compared to healthy and two-week infarct models. The low stress distribution might be due to the further thinning of the wall in the infarcted regions C, D, E and F. Again, the low stress value in the infarcted region is observed due to the fact that the infarcted tissue was modelled as passive material. The circumferential and longitudinal stresses for four-week infarct model at the endocardium are -38.49 kPa and -46.66 kPa, respectively. At the mid-wall and epicardium positions the

circumferential and longitudinal stresses for four-week model are -14.4 kPa, -20.10 kPa and -4.997 kPa, -9.011 kPa, respectively. This means that the radial, circumferential and longitudinal stresses at all positions (endocardium, mid-wall and epicardium) are low than those presented in healthy and two-week infarct model. In conclusion, it was expected that the four-week infarct model will present the lowest stress magnitudes in radial, circumferential and longitudinal directions because of the passive material behaviour imposed on the infarcted tissue.

Generally, the I, J, K and L paths show the average of high stresses compared to the C, D, E and F regions. For example, the average radial stress in the C, D, E and F paths is -202.32 kPa and -212.00 kPa in the I, J, K and L paths. This is mainly because the I, J, K and L regions are subjected to pressure in both the endocardium and epicardium positions because of the position of the wall region. Another reason why this is so, could be that the I, J, K and L paths are characterised by healthy tissue which is modelled by active constitutive law whereas the C, D, E and F paths is modelled as passive material. Ideally, the stresses in radial, circumferential and longitudinal directions should be equal because in this region there are no infarction, wall thinning and dilation. However, this is not observed mainly because the stresses in all these directions does not only depend on the geometry of the I, J, K and L paths but also on the geometry of the whole heart model and material properties applied on the model. It is important to note that, the general trend of magnitude of radial, circumferential and longitudinal stresses in healthy and infarcted heart models is maintained as compared to the C, D, E and F paths.

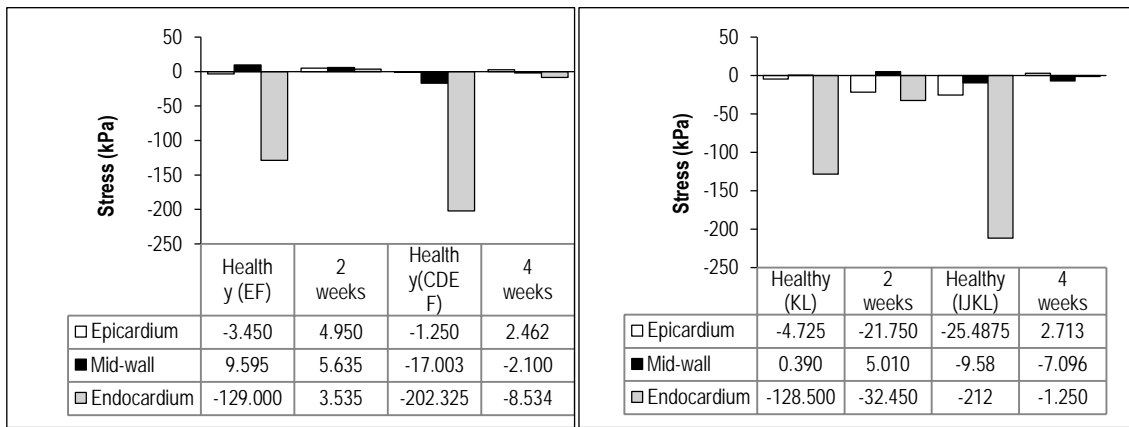
In the I, J, K and L regions, the average radial stresses are -212.00 kPa, -77.02 kPa and -1.250 kPa at the endocardium position for healthy, two-week and four-week infarct models, respectively (Figure 4-28 (d), (e) and (f)). Average radial and circumferential stresses of the healthy model at the mid-wall position show the magnitude of -9.58 kPa and -52.75 kPa, respectively. In these positions, the stresses at the mid-wall position are higher than that in the epicardium position for healthy model. Average longitudinal stress for healthy model, shows the stress of -31.04 kPa at the epicardium position and -8.28 kPa at the mid-wall position. This shows that the magnitude of the longitudinal stress at epicardial position is greater than stress at the mid-wall position by 73.6 %. It is important to note that similar observation was made in the C, D, E and F paths.

At two-week infarct model, the radial stress at the endocardium is -77.02 kPa compared to -97.00 kPa in the circumferential direction. In the same model, the longitudinal stress is

recorded to be -114.48 kPa. This means that the circumferential stress for two-week model is higher than the radial and longitudinal stress at the endocardium position. For two-week heart model, the highest stress magnitude is recorded at the endocardium position, followed by the mid-wall position and the lowest stress magnitude is recorded at the epicardium position. At the mid-wall the radial, circumferential and longitudinal stresses are -7.75 kPa, -37.20 MPa and -20.83 kPa, respectively. Consequently, at the epicardium position, the radial, circumferential and longitudinal stresses are -12.84 kPa, -53.68 kPa and -32.40 kPa, respectively.

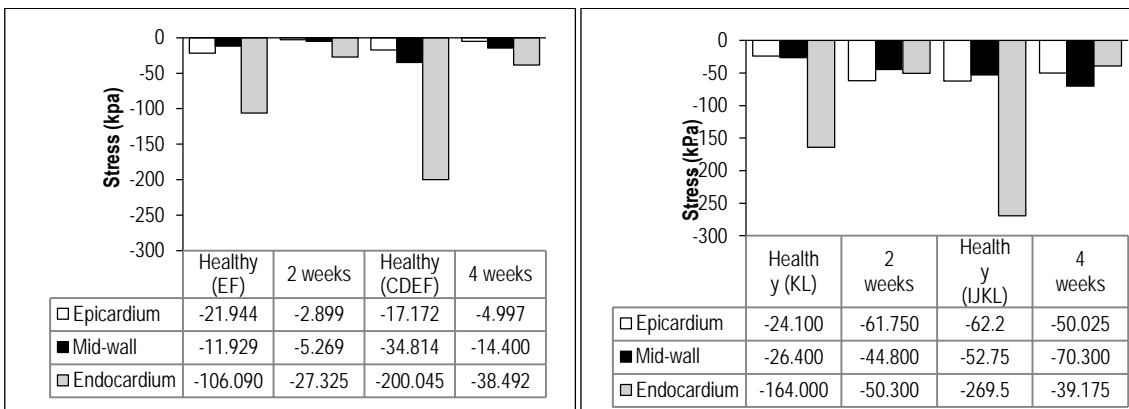
At the I, J, K and L paths for four-week infarcted heart model, the radial stress at the endocardium is -1.25 kPa. On mid-wall and epicardium positions the radial stresses are -7.096 kPa and 2.713 kPa, respectively. The circumferential stresses at the endocardium position are the highest stress magnitude of -39.18kPa. Consequently, the longitudinal stress at the endocardium position is showing the magnitude of -7.663 kPa. As compared to the healthy and two-week infarct models, the stress distribution in the I, J, K and L are higher. This is the same stress distribution as compared to the C, D, E and F paths.

The radial, circumferential and longitudinal stresses at the mid-wall position for four-week infarct model are -7.096kPa, -70.30 kPa and -22.63 kPa, respectively. It can be seen that the circumferential stress for four-week model remains higher when comparing to radial and longitudinal stress. Moreover, the radial, circumferential and longitudinal stresses at the epicardium position for four-week infarct model are 2.713 kPa, -50.025 kPa and -23.343 kPa, respectively. This shows that the average stresses at four-week infarct models in the I, J, K and L paths are higher than those presented by the healthy and two-week infarct models. Again, it can be concluded that the infarcts mainly shown in the C, D, E and F regions have an influence in the stress distribution in the I, J, K and L.



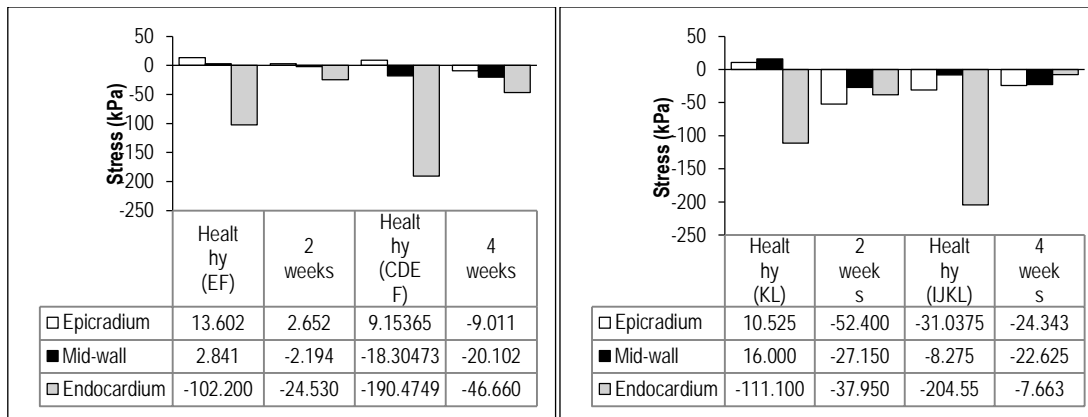
(a)

(d)



(b)

(e)



(c)

(f)

Figure 4-28: End-systolic stress for healthy, two-week and four-week infarct models. Average radial (a), circumferential (b) and longitudinal (c) stress at paths C, D, E and F. Average radial (d), circumferential (e) and longitudinal (f) stress at paths I, J, K and L.

Figure 4-29 (a)-(f) show the radial, circumferential and longitudinal strains in the C, D, E and F paths and I, J, K and L paths in the endocardium, mid-wall and epicardium positions. The healthy model shows the lowest strains in the radial, circumferential and longitudinal directions at endocardium, mid-wall and epicardium positions. This is what was expected because the healthy model has thick and proper thickness and as such will have little movement in all directions as compared to the infarct models. However, in the two-week infarct model, the radial, circumferential and longitudinal strains are higher than those presented in healthy model in all positions (endocardium, mid-wall and epicardium). The highest radial, circumferential and longitudinal strains are shown in the four-week infarct model. This is according to what was expected because the four-week infarct model, has the thinnest wall thickness in the infarcted region due to the remodelling of the heart wall and pressure applied in the endocardium.

In the C, D, E and F paths, the radial strains in the healthy model are lower than circumferential and longitudinal strains at the endocardium by 81.7% and 81.4%, respectively. The radial, circumferential and longitudinal strains for healthy model at endocardium position are -0.005, -0.028 and 0.029, respectively. Moreover, the radial, circumferential and longitudinal strains at mid-wall position for the healthy model are -0.010, -0.045 and 0.054, respectively. Consequently, the radial, circumferential and longitudinal strains at epicardial position for the healthy model are -0.013, -0.071 and -0.070, respectively. Following the observation recorded in the healthy model, the highest recorded strains in the C, D, E and F regions are in the circumferential direction followed by the longitudinal direction. The lowest recorded strains in the healthy model are in the radial direction. The lowest recorded strain in the radial direction is observed because the infarct models are mostly restricted to have some movement due to passive material behaviour imposed.

The radial strains in the two-week infarct models at the endocardium, mid-wall and epicardium are 0.012, 0.002 and -0.005, respectively. Additionally, the average circumferential strains in the two-week infarct models at the endocardium, mid-wall and epicardium are -0.007, -0.006 and -0.006, respectively. Similarly, the longitudinal strains in the two-week infarct models at the endocardium, mid-wall and epicardium -0.004, 0.003 and 0.011, respectively. The radial strains for two-week infarct models at endocardium, mid-wall and epicardium positions are lower than circumferential and longitudinal strains in the same positions. The radial strain at endocardium in the two-week infarct model is doubled than that of the healthy model. This means that the regions C, D, E and F has moved by half in

the endocardium of the two infarct model as compared to healthy model has moved more than double in the radial direction. The same applies when comparing the strains of the two-week infarct model with the healthy model in the circumferential and longitudinal directions. In Figure 4-29 (c), the longitudinal strain for two-week infarct model are -0.004, 0.003 and 0.011 in the endocardium, mid-wall and epicardium positions.

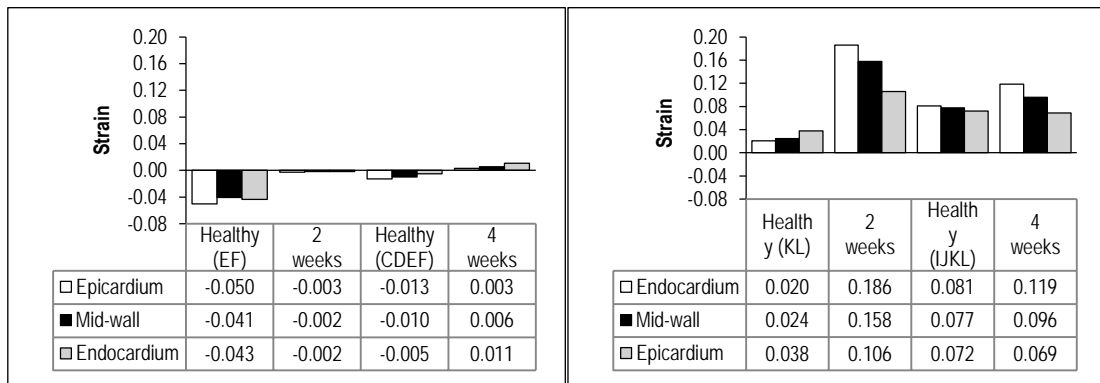
The four-week infarct model has lowest strains in the radial, circumferential and the longitudinal directions when comparing to healthy and two-week infarct models. This behaviour is attributed to the fact that the infarct tissue becomes stiff and passive in its behaviour. The radial strain in the endocardium position for four-week infarct model has the strain magnitude of 0.011. On the mid-wall and epicardium, the radial strains for four week infarct model are 0.006 and 0.003, respectively. The circumferential strains on the endocardium, mid-wall and epicardium positions are 0.004, 0.004 and 0.003, respectively in the four-week infarct model. Similarly, the longitudinal strains on the endocardium, mid-wall and epicardium positions are -0.015, -0.009 and -0.006, respectively in the four-week infarcted. It is clear that the average strain (radial, circumferential and longitudinal) in the epicardium, mid-wall and endocardium in healthy model is higher than that of the infarct models.

Figure 4-29 (d)-(f) show the magnitude of strains in three positions (endocardium, mid-wall and epicardium) in the radial, circumferential and longitudinal directions. The strains in this region are expected to be higher than those in the C, D, E and F regions because the wall is subjected to the pressure in both ends and the wall is thicker than the C, D, E and F wall. Generally, the radial strains in endocardium, mid-wall and epicardium positions are higher than circumferential and longitudinal strains in the same positions for all the models (healthy and infarct models). Consequently, the longitudinal strains in the endocardium, mid-wall and epicardium are lower than circumferential strain in healthy and infarct models.

The radial strain in the I, J, K and L paths for healthy model has the magnitude of 0.081, 0.077 and 0.072 in the endocardium, mid-wall and the epicardium positions. On the same healthy model, the circumferential strains in the I, J, K and L paths for healthy model has the magnitude of -0.190, -0.173 and -0.180 in the endocardium, mid-wall and the epicardium positions. The longitudinal strain in the I, J, K and L paths for healthy model has the magnitude of 0.118, 0.095 and 0.098 in the endocardium, mid-wall and the epicardium positions. Therefore, as expected, the radial strain in the healthy model is higher than the circumferential and longitudinal in the endocardium, mid-wall and epicardium positions.

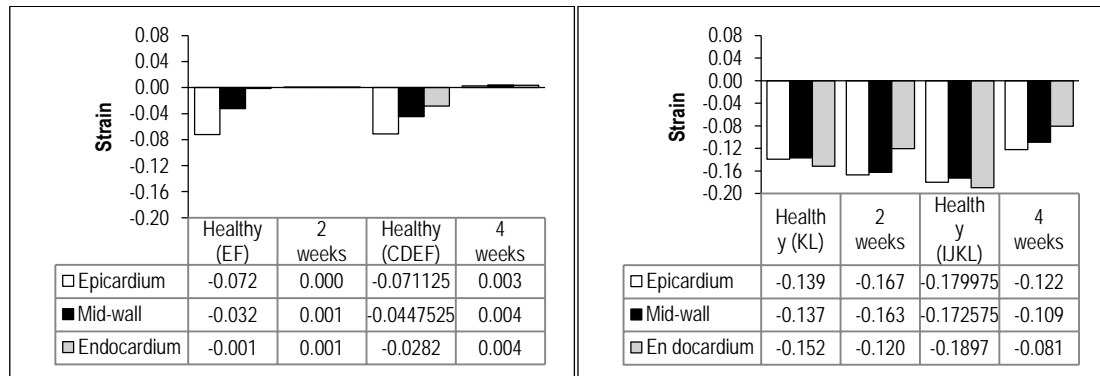
The radial strains of the healthy model are lower than the radial strain in the two-week infarct model. However, in the I, J, K and L paths, the circumferential strains (two-week infarct model) in the endocardium, mid-wall and epicardium position is lower than the circumferential strain in the healthy model. For two-week infarct model, the radial strain in the endocardium, mid-wall and epicardium are 0.141, 0.118 and 0.162, respectively. The circumferential strains in the endocardium, mid-wall and epicardium are -0.139, -0.160 and -0.164, respectively. Similarly, the longitudinal strain in the endocardium, mid-wall and epicardium are 0.056, 0.041 and 0.023, respectively.

The radial strains in the four-week infarct model at endocardium, mid-wall and epicardium position are 0.119, 0.096 and 0.069, respectively. The radial strains in the four-week infarct models at endocardium, mid-wall and epicardium are higher than radial strains in the two-week infarcted and healthy models. Similarly, the circumferential strains in the four-week infarct model at endocardium, mid-wall and epicardium position are -0.081, -0.109 and -0.122, respectively. Moreover, the longitudinal strains in the four-week infarct model at endocardium, mid-wall and epicardium position are 0.011, 0.013 and 0.003, respectively. At four-week infarct model, the radial strain is 50 % more than the circumferential strain at the endocardium, mid-wall and epicardium positions. The similar trend prevails in the mid-wall and epicardium positions. The longitudinal strain in the endocardium position is 38 times in the circumferential strains while the circumferential strain at the endocardium is approximately 0.5 times the radial strain in the same position. The trend is the same in the mid-wall and epicardium positions for radial, circumferential and longitudinal direction.



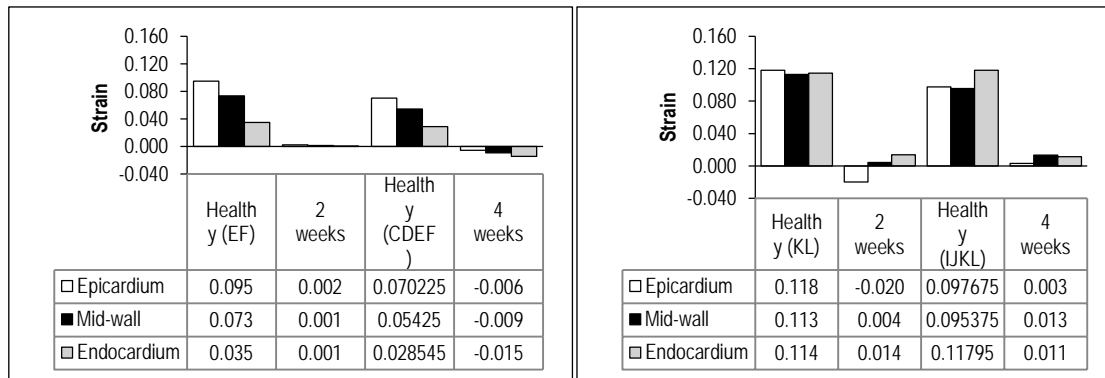
(a)

(d)



(b)

(e)



(c)

(f)

Figure 4-29: End-systolic strain for healthy, two-week and four-week infarct models. Average radial (a), circumferential (b) and longitudinal (c) strain at paths C, D, E and F. Average radial (d), circumferential (e) and longitudinal (f) strain at paths I, J, K and L.

5 Discussion

5.1 Overall Discussion

This study investigated the effects of remodelling in the infarcted rat heart using the FEM at two time points (two and four-week) after MI. The biventricular geometry of a rat heart was reconstructed from short-axis MRI and the infarcts were modelled by changing the material constitutive parameters in the infarcted region. As a result, three models of a rat heart were developed, namely that of a healthy heart, of a heart with a LV infarct two-week after infarct induction, and of the same infarcted heart four-week after infarction. These models were used to study the effect of myocardial infarction and post-infarct remodelling on the functioning of the left ventricle and the cardiac, i.e. myocardial, mechanics in the rat heart.

A number of animal models to study cardiac mechanics have been proposed (Guccione et al., 1995a, Janz and Grimm, 1972, McCulloch et al., 1992, Mojsejenko et al., 2014, Omens et al., 1993, Pao et al., 1974, Ratcliffe et al., 1998). The importance of these previous studies was to utilise animal models in an attempt to understand various heart diseases including MI. It is evident that knowledge of cardiac and cardiovascular physiology was generally obtained and gathered through the use of animals (Gilson and Kraitchman, 2007, Nahrendorf et al., 2003, Nahrendorf et al., 2001, Rehwald et al., 1997). The use of big animals like dogs for cardiovascular research has declined recently due to the cost associated with the large animal model. Rat models have been developed extensively to study heart failure, aging and post infarct remodelling.

The cavity pressures and the volumes of the cavity play an important role in understanding the cardiac performance of the heart. In the current study the regional mechanics of the myocardium were used to understand the underlying mechanisms of the myocardium by utilising the biventricular rat heart models. The research study conducted was based on the MRI images obtained using a 3D MRI machine. The geometries captured by MRI were used to create 3D models. These models were validated and verified by measuring the mass of the heart (model), the end-systolic and end-diastolic volumes of the LV and RV. The volumes of these 3D models were measured and compared with those of the MRI. The images obtained from MRI contain three time points, one the healthy (control) model, two the two-week infarcted and three the four-week rat heart models.

To understand the myocardial behaviour of the heart, it is critical to understand the stresses and strains. Therefore, the radial, circumferential and longitudinal strains and stresses were

all analysed for both healthy and infarcted tissues. This was achieved by comparing stresses and strains during both filling and contraction ejection. The main aim was to observe if the effect of post-infarct remodelling has any adverse effect on the functional parameters of the heart. This finding has serious implications on the treatment of the infarcted hearts and the understanding of the mechanisms of cardiac mechanics. To achieve this understanding the stresses and strains were recorded at various regions across the myocardium thickness. The advantage of capturing the stresses and strains in this way is that one is able to capture the behaviour of both the healthy and infarcted tissue. This is critical in terms of understanding the mechanism of infarcted hearts. In this study the wall thinning of the myocardium played an important role in understanding the cardiac mechanics of the infarcts. Therefore, during 3D reconstruction of the geometries the wall thinning was observed with interest. In order to quantify the experimentally measured strain and stress data, the mathematical models are used here to predict the stress and strain across the wall thickness of the healthy and infarcted tissue.

In order to simulate the passive filling, the inner pressure of 4.8 kPa and 1.2 kPa was applied in LV and RV, respectively in all models. The passive modelling was achieved by using the Fung constitutive model (Guccione et al., 1995b). To simulate the active contraction, the endocardial pressure of 14.6 kPa and 2.9 kPa was applied in LV and RV, respectively in healthy and infarcted rat heart models. The active simulation was achieved by combining the passive and active models. The infarcted areas were modelled as the passive materials but with stiffer material properties. In active and passive models the stresses and strains together with the measurements of volumes were measured and presented.

In this study the active contraction model presented by Guccione et al., (1993a) and Guccione et al., (1993c) was used to study the effects of infarction on the bi-ventricular models. This was achieved by studying the distributions of stresses and strains on infarcted regions during systolic phase. In order to obtain the accurate finite element analysis, the following complex features are to be taken into consideration, namely: (i) large deformations; (ii) transmural muscle fibre orientation; and (iii) non-linear anisotropic material properties.

The constitutive parameters used in this study are higher than those used in Omens *et al.* (1993). The differences may be attributed to the fact that the geometrical models reported in Guccione *et al.* (1995a) and Omens *et al.* (1993) are not exactly the same as those presented in this study. The stress scaling factor was increased from 1.1 kPa to 2kPa such that the difference between the EDV of the model and EDV of the MRI is minimised. This

optimization was manually performed in such a way that the ESV of the model after applying the inner pressure is equal or close to the EDV of the MRI measured values. Therefore, the constitutive parameters were optimised and adjusted accordingly to ensure that the ES geometry of the reconstructed model is equal to EDV of the MRI data after applying the inner pressure. This was achieved by assuming the inner pressure applied is the same as found in the literature. It should be noted that the boundary conditions also play a role in how the ESV and EDV increases.

The active contraction model was implemented such that it has two forcing functions, (1) the forcing function C_t and (2) internal myocardial wall pressure (also previously defined as endocardial pressure). In order to simulate the endocardial pressures at end-systole, the pressures of 14.6 kPa and 2.9 kPa were applied on LV and RV. The pressure applied on the endocardial surface is a function of time. The stresses and strains data were taken at time 0.4 seconds. The time 0.4 seconds, represents the point at which end-diastolic occurs. During active simulation, the models actively contracted against the applied endocardial pressure as shown in Figure 4-2 applied on the endocardial surfaces of LV and RV. Figure 4-2 shows the time course of the internal pressure applied to the endocardial surfaces of the RV and LV. Transversely the isotropic model for rat heart was presented by Omens *et al.* (1993). In this study, the researchers studied the behaviour of resting rat myocardium using the Fung model. The results of this study, especially stress and strains of the healthy myocardium during diastolic filling, match the results presented by (Omens *et al.*, 1993).

As tabulated in Table 4-1, peak intracellular calcium concentration was 4.35 μM . In this study, the elastance model was used, where the C_v is set to unity. This means that the force-velocity relation was excluded in the model.

5.2 Development of FEM

5.2.1 Geometrical reconstruction of healthy and infarct models

The MRI data used during this study was first reported in Saleh *et al.* (2012). The Allegra MRI 3T scanner with a small animal coil and gradient-echo sequence was used to record the long-term ventricular remodelling Saleh *et al.* (2012). The MRI parameters used for acquiring the data are as follows: field of view (FOV) = 60 mm, matrix size = 256 \times 256, in-plane resolution 234 μm , slice thickness 1.0 mm, TR 7.7ms, TE 3.5ms, flip angle 25° to 40°, and 3 signal averages. For the four-week scan, FOV and matrix size were increased to 75mm and

320 × 320, respectively (Saleh et al., 2012, Saleh, 2012). The data received from the MRI scanner was of high quality such that the papillary muscles in the ventricles were visible. As compared to most studies in the area of cardiac biomechanics, the papillary muscles in this study were disregarded (Guccione *et al.*, 1995a; Klepach et al., 2012; Kortsmmit *et al.*, 2012; Miller *et al.*, 2013; Omens *et al.*, 2013; Wenk *et al.*, 2005). Therefore, all papillary muscles were discarded in order to achieve this.

The MRI was smoothed to allow the alignment of data (long-axis) longitudinal direction (z). This was done in such a way that the cavity volumes and the mass of the myocardium were not tampered with or affected. The smoothing was achieved by manually moving the short-axis data of the LV and RV. Furthermore, the data smoothing was performed by Solid Edge® 3D modelling software. Segment® software was used to manually segment the epicardial and endocardial contours of LV and RV. The 3D model segmented from Segment® software was then used to create the 3D model in Solid Edge®. The Egis model was then imported into Abaqus® to be meshed. In this study, the 3D rat heart geometry was meshed with tetrahedral elements quadratic constant pressure C5H10D with a total of 32221 elements and 6540 nodes.

5.2.2 Boundary and loading conditions

Boundary conditions are critical in obtaining the accurate simulation results. In modelling the biventricular models of the heart, it is critical that the real conditions are emulated. The boundary conditions are applied on the basal surface of the RV and LV to imitate the properties of valves and annuli. Various researchers who performed a biventricular model simulation have used different boundary conditions (Ratcliffe et al., 1998, Guccione et al., 1995a, Kortsmmit et al., 2012, Kortsmmit et al., 2013, Wang et al., 2013, Wenk et al., 2013a). The boundary conditions of the heart were set such that the displacements of the nodes are restricted in the circumferential-radial plane. This means that only the longitudinal displacements are allowed to move (Wenk *et al.*, 2013a). In other work, the longitudinal displacement of the base is set to zero. Consequently, the circumferential displacement of epicardial wall is set to zero. In this case the ventricular wall is set free including the apex. In other research work, the nodes at the apex are constrained to move along the long axis and the basal axis is constrained in all directions (Ratcliffe *et al.*, 1998a). Consequently, the displacement of the epicardial-basal edge was constrained fully. The remainder of the nodes were allowed to move in the radial direction (Wenk et al., 2013a). The boundary conditions presented by Wenk *et al.* (2013) have come close to the boundary conditions used for this study except that in this study the nodes at the base including the endocardial and epicardial

edge at the base were fully constrained in the longitudinal and circumferential directions but free to move in the radial direction. On the contrary Wenk *et al.* (2005) has constrained nodes only at the epicardial basal edge. In this study the boundary conditions were set such that the real conditions are emulated. The nodes at the basal surface are fixed in transitional radial and circumferential directions. The rest of the model was left free to move in both the transitional and rotational directions.

The EDPVR was mimicked by applying a pressure with a linear increase from 0-4.8 kPa on the LV and 0.98 kPa on the RV. In the literature, there are different values of EDP reported for rat models ranging from EDP of 0.4 kPa to 7 kPa (Dobner *et al.*, 2009, Fletcher *et al.*, 1981, Landa *et al.*, 2008, Pacher *et al.*, 2004, Prunier *et al.*, 2002, Raya *et al.*, 1988). Variations of these values are mainly attributed to the difficulty of measuring pressure in such a small rat heart and the accuracy of the equipment used in these experiments. The pressures applied at the endocardial surfaces of the LV and RV were higher than the pressure reported of 1.33 kPa (Pacher *et al.*, 2004). Even though the value of EDP (4.8 kPa) used in this study is higher than reported research papers in some instances (Fletcher *et al.*, 1981; Prunier *et al.*, 2002; Raya *et al.*, 1988), it is still acceptable because it falls within the maximum reported EDP value of 7kPa. In this study, the EDP (of LV and RV) was determined mainly by matching the EDV of MRI data and retaining the stability of the model. The linear variation of pressure during passive filling is regarded as unphysiologic; however, this method has been used by others to mimic the passive filling phase of the heart models (Kerckhoffs *et al.*, 2007; Kortsmid *et al.*, 2012; Kortsmid *et al.*, 2013; Miller *et al.*, 2013; Walker *et al.*, 2008; Wenk *et al.*, 2013a). The linear pressure increment method used in this study is validated in the above mentioned studies. The EDP of 4.8 kPa was applied in healthy and infarct heart models. Even though in reality, the EDP could slightly decrease or increase after infarction, the literature is not conclusive (Kerckhoffs *et al.*, 2007; Kortsmid *et al.*, 2012; Kortsmid *et al.*, 2013; Miller *et al.*, 2013; Walker *et al.*, 2008; Wenk *et al.*, 2013a).

To mimic the ESPVR, the time varying pressure was applied on the endocardial surfaces of RV and LV as 14.6 kPa and 2.9 kPa, respectively (Pacher *et al.*, 2004). The ESP on the RV during active contraction was rarely reported in the literature. Therefore the value of ESP applied in the RV was obtained and estimated by the rule which states that the RVESP is nearly 20% of the LVESP. The ESPVR was mimicked by applying a time varying pressure shown in Figure 4-2. The same pressure waveform was applied on the endocardial of LV and RV in all models. The end-systolic volume was then read at the end-systolic time of 0.4 seconds. In other studies, the active contraction volume was modelled by holding the peak

pressure constant (Kortsmit et al., 2012, Miller et al., 2013). The transmural stresses and strains were determined using the end-systolic and end-diastolic configurations. In this study, it was assumed that there are no external loadings on the heart model. Naturally, this is not true as the heart is situated near other organs.

5.2.3 Constitutive law and the active stress model

The myocardium of a heart portrays highly complex features such as non-linear anisotropic material properties, fibre orientation variation across the myocardium, large deformation and residual stresses. To achieve the accuracy of material behaviour of these conditions, finite element analysis needs to be used. The transmural variation of stresses and strains plays an important role in selecting the appropriate constitutive model suitable for passive filling and active contraction simulation. To achieve the desired results of the study, the rat heart was modelled as nearly incompressible. The general purpose finite element analysis Abaqus® was selected. Based on biaxial testing results, it has been showing that the myocardium behaves more like anisotropic material with high stiffness in the fibre direction. The constitutive material parameters used in this study were presented, tested and validated in previous studies (Omens et al., 1993). Active contraction of healthy heart has been presented by various authors but very limited studies have presented the active contraction simulation of the infarcted heart models (Vetter and McCulloch, 2000, Wang et al., 2010b, Wang et al., 2010a, Whiteley et al., 2007).

The combination of passive stress tensor component and the active fibre directional component was used to model the active contraction of the rat heart. Accordingly, the active directional component was described to depend on various factors including: the maximum peak intracellular calcium concentration, the stress free sarcomere length, the peak isometric tension-sarcomere length relation and the sarcomere length at which no tension is developed (Guccione et al., 1993a). In Abaqus®, it is possible to assign different material properties in the same model. This was achieved by assigning the elements in the infarcted region, the passive material components (Abaqus® built-in Fung model) and the rest of the myocardium was assigned the active contraction model.

A transversely isotropic material model was used to model the behaviour of the passive and active tissue. This was achieved by implementing the passive and active models using the ORIENT subroutine in Abaqus®. In order to simulate the tissue as transversely isotropic material model, constitutive parameters including fibre strain, shear strain, and cross-fibre coefficients need to be defined. In this study the parameters used to model the healthy and

infarcted tissues were based on the study presented in (Omens et al., 1993). The parameters selected were based on the arrested rat heart during passive filling.

The heart is regarded as a muscle with both connective tissue and cells which are bounded by liquid filled extracellular space. Incompressible models usually are problematic and demand more time to converge. Therefore, in the current study the myocardium is modelled as near incompressible by defining the bulk modulus D of the material. D was assigned a value of $1E-06$ during passive filling and active contraction simulation. This value has allowed the modelling of a tissue material as approximately incompressible. Most studies have modelled the tissue as a quasi-compressible material (Doll *et al.*, 2000; Kortsmid *et al.*, 2012; Kortsmid *et al.*, 2013; Miller *et al.*, 2013).

5.2.4 Developing the infarct models

In the bi-ventricular rat heart model, the infarction occurred in the LV. Therefore, the LV was modelled with the passive behaviour and the active behaviour during active ejection phase. The RV was also modelled similarly to the LV. The rat heart model was modelled at two time posts after the infarction: two-week after infarction and four-week after infarction. In the two-week infarct model, the infarcts had accounted for approximately 16% of the LV. For the four-week infarct model, the infarcts accounted for approximately 26% of the LV. The infarct in the two-week infarct model was labelled regions E and F. Similarly, the four-week infarct model transmural paths were labelled regions C, D, E and F.

For both the two-week and four-week infarct models, the infarct was assumed to have increased the stiffness by tenfold compared to that of the healthy tissue, similar to that seen in recent studies by Lee *et al.* (2014a) and Mojsejenko *et al.* (2014) and previous studies by Lee *et al.* (2013); Wenk *et al.* (2005); and Wenk *et al.* (2010) for various animal models. By conducting biaxial testing in sheep and pig hearts, it was shown that in both cases the stiffness of the infarcted tissue is greater than the healthy tissue. The increase of stress scaling factor (C) catered for the formation of scar in the infarct region.

In this study, the fibre orientation in the scar tissue (infarct) was left the same as that of the healthy tissue. There is little evidence in the literature on how collagen fibre direction changes due to MI. Like those who argue to the contrary, a study by (Holmes et al., 1997) in pig model concluded that during passive inflation of isolated, arrested hearts, the infarcted tissue revealed circumferential strain is significantly less compared to radial and longitudinal strains; on the contrary, longitudinal and radial strains remain the same when compared with

healthy models. Furthermore, (Rouillard and Holmes, 2012) confirmed that in rat heart, there is less strain in circumferential direction compared to radial and longitudinal directions in the infarcted tissue of the heart after three weeks MI. The tests on collagen fibre orientation in the infarct are conclusive on pig and sheep heart models changes considerably. This implies that the isotropic material properties were assigned in the infarct region with equal stiffness in the fibre and cross-fibre directions.

5.3 Validation of the Models

5.3.1 Implementation of active contraction code

The coding of UMAT subroutine for hyperelastic material behaviour remained a challenge as manual coding was required. The hyperelastic materials have underlying anisotropic fibres which must be represented in strain energy function. The hand coding of a UMAT subroutine remains a tedious job as a lot of debugging needs to be done with no guarantee of success. The manual coding of a Fung model implementation was attempted by Sun *et al.* (2005). One may appreciate that this involves a high level of work and the accuracy maybe compromised.

The automatic generation of a UMAT subroutine is the best option as presented by Young *et al.* (2010). The automatic generation of the UMAT subroutine used in this study was adopted from Young *et al.* (2010). Mathematica® was used to automate the UMAT coding for the Fung model. The main function of the Mathematica® was to solve the partial differential equations to give a ready-made solved equation based on given pseudoelastic strain energy function. In Abaqus® the UHYPER, UANISTROHYPER_STRAIN and UNISOHYPER_INV subroutines are available for modelling hyperelastic material. These subroutines are easily available and do not require intensive work as compared to a UMAT subroutine. The challenge with the latter is that does not offer the user the opportunity to access the Cauchy stress tensor. In order to model the active contraction of the heart, the access to the Cauchy stress tensor is vital because there is a need to add the active stress on the passive stress. Therefore, the only way to model active filling in Abaqus® is to give the user access to the Cauchy stress tensor. The success of working the UMAT subroutine depends on the accurate definition of the Cauchy stress tensor, the corotational tensor of elasticity and the specific strain energy (Abaqus, 2010).

5.3.2 Validation of the developed passive and active models

The strain energy function used to model the tissue material was first developed by Fung (1984). The active contraction was modelled by adding the active stress in the direction of the fibre. The ED, LV and RV volumes were validated by measuring the ED volumes of the RV and LV of the models as presented in Table 3-4, Table 3-8 and Table 3-9. The MRI was assumed to be an accurate measurement. The error was minimised to ensure that the volumes measured on the reconstructed 3D models are similar to those of the MRI. During passive filling, the internal pressure of different magnitudes was applied together with the constitutive parameters until the end-systolic volume of the model based on MRI data is reached. Once the end-diastolic volume is accurate, the model was then recreated using Solid Edge® software to create the IGES file for remeshing into Abaqus®. In conclusion, the passive and active models were validated by measuring both the RV and LV volumes of the 3D reconstructed models against the MRI data.

5.4 Comparison of Healthy and Infarcted Cases

The performance of the heart is normally determined by firstly considering the pressure-volume relationships including the functional parameters and secondly, analysing the myocardial deformation. The myocardial mechanics include the determination of transmural stress and strain in healthy and infarcted tissues. In this section, the effect of infarct sizes on functional parameters and wall mechanics is compared and discussed. The results indicate that stress and strains distribution at healthy and infarcted regions are different.

5.4.1 Cardiac functional parameters

The functional parameters used to evaluate the heart functioning are ejection fraction (EF), stroke volume (SV) and contractility. The parameters in this study are compared to other experimental studies that are available in the literature. These quantities were computed by measuring and comparing the state of the mesh from the beginning of simulation to the end of simulation time.

The EF for healthy rat heart models varies from 45 % to 79 % (Carapella et al., 2014, Daire et al., 2008, Liu et al., 2006, Ruetten et al., 2005, Saleh et al., 2012, Yoon et al., 2009, Wang et al., 2009, Wise et al., 1998). The variation of EF in healthy rat heart is attributed to many factors including the age, size and type of the rat, natural variability in material properties of the myocardium, the type of anaesthesia used during experimentation, etc. This variation does not only apply to the same animal model but across different animal species. It is

important to note that the regional contractile function in the normal rat heart was measured using cardiac cine and tagged cardiovascular magnetic resonance (CMR). In this study, the EF was found to be 74.2 ± 4.4 %. The EF ($=SV/EDV$) for the healthy rat heart model in this study was determined to be 62 %. The EF determined and presented by this study is similar to the EF of 61% presented by (Wise et al., 1998). It is important to note that the EF of the healthy model presented in this study falls within the value that is reported in the provided literature (Carapella et al., 2014, Ruetten et al., 2005, Saleh et al., 2012, Yoon et al., 2009, Wang et al., 2009). The MRI measured EF was based on the rat heart when the rat was subjected to anaesthesia. The anaesthesia has the tendency to lower the contractility of the heart (Tsamis and Stergiopoulos, 2009). The EF calculated for the four-week infarct model was reduced to 49 %. EF is reported to decrease as a function of infarct size. The higher the infarct size the lower the EF (Gaudron et al., 1993, Kostuk et al., 1973, Pfeffer et al., 1988, Pfeffer and Braunwald, 1990, Pfeffer et al., 1991, Pfeffer, 1995). As shown in the literature, the reduction of EF at the four-week model was expected since this model has large infarct region which has the ability to significantly reduce the contractility. The infarct models have shown the reduction of EF to 55% and 49% for the two-week and four-week infarct models, respectively. The infarct stretching occurs due to degradation of intermyocyte collagen struts by serine proteases and activation of matrix metalloproteinases which is released from neutrophils (Cleutjens et al., 1995a, Cleutjens et al., 1995b). This infarct stretching is the main cause of wall thinning and ventricular dilation which increase the diastolic and systolic wall stresses. The decrease in EF after MI is associated with considerable structural and functional alterations including the decrease in contractility, the increase in SV and the increase in EDV and ESV. The SV ($=EDV-ESV$) was found to be increasing from 135 μ L for the healthy case to 143 μ L and 183 μ L for the two-week and four-week infarct models, respectively. This increase of SV is in line with literature and is mainly attributed to the wall thinning and ventricular dilation (Cleutjens et al., 1995a, Cleutjens et al., 1995b). The relationship between the ejection fraction and myocardial strain using a simple left ventricle FE heart model was established (Maclver et al., 2015).

The LVEDV (left ventricle end-diastolic volume) increased from 208 μ L of the healthy model to 262 μ L and 369 μ L of two-week and four-week infarcted heart models, respectively. To model the structural changes of the infarcted tissue, the stress scaling factor has been changed. At four-week there is severe wall thinning and dyskinesia in the infarcted area. The collagen scarring after four-week infarct was evident (Saleh et al., 2012). It is understood that transformation of fibroblasts to myofibroblasts are responsible for the formation of collagen (Dai et al., 2005, Jugdutt, 2003b, Jugdutt, 2003a, Villarreal et al., 1991). The

decrease in wall thickness at the infarcted region is attributed to the necrosis of myocytes. The wall thinning in the infarcted regions caused the increase in EDV and ESV in the two-week and four-week infarct models. There was a significant movement in the infarcted region which contributed to the increase of EDV and ESV in all models. The reduction of strain and increase of stress in the two-week model is smaller than that of the four-week model because the infarcted region in the four-week model is larger than that of the two-week infarcts. There is considerable volume dilation on the two and four-week infarcted heart models. This observation is consistent with what has been reported in the literature (Epstein et al., 2002, Gilson et al., 2004). At four-week there was enlargement of EDV and ESV in the myocardium compared to the healthy model.

The ESPVR for each model was used to calculate the contractility during the active contraction phase. The healthy model has the highest contractility of 0.3 kPa/ μ L. The two-week and four-week infarct models have experienced a reduction in contractility of 0.2 kPa/ μ L and 0.1 kPa/ μ L, respectively. The four-week model has the lowest contractility because it has the largest infarcted area. The infarct area is modelled as the passive material and has no contraction attributed to it. It is critical to note that the myocardium in the LV for the healthy model has the ability to contract because all materials are modelled as healthy.

5.4.2 Myocardial stress and strain

The Cauchy stress tensor represents the true stress of the model. Therefore, the Cauchy stress tensor was used to measure how myocardium reacts under certain applied pressure. The Green-Lagrangian strain tensor was used to compare the strain on the model because it is useful when the structure exhibits high deformation. The expected strains in soft tissue mechanics can be as high as 40 % of the original deformed shape. The average stresses and strains are to be compared in (i) regions C, D, E and F in the LV wall that are exposed to infarction and (ii) regions I, J, K and L in the septal wall. It should be noted that for the two-week infarct model, only the paths E and F are in the infarcted region whereas the paths C and D are located in non-infarcted myocardium. As such, only paths E and F are considered for the two-week infarct model and correspondingly in the healthy control case. For the four-week infarct model, all four paths C, D, E and F are located in the infarcted region. Consequently, separate average healthy control data are provided for the two-week infarct (from path E and F) and the four-week infarct (from paths C, D, E and F). In the following sections, the graphs for the LV free wall region present four cases, data from the E-F region for the two-week infarct and the corresponding region of the healthy case, and data from the

I-J-K-L region for the four-week infarct and from the healthy case. For the septal wall region that is non-infarcted in all models, the four septal paths I, J, K, and L were considered for all models to provide data from the same region in all models for comparison purpose. The graphs for the septal region as such comprise three cases only, i.e. healthy, two week infarct and four-week infarct. Please note that strain and stress always refers to average values unless stated otherwise.

5.4.2.1 Strain in the healthy and infarct models during passive filling

Figure 5-1 shows the average radial, circumferential and longitudinal strains in the healthy, two-week and four-week infarct models along the paths C, D, E and F and I, J, K and L, respectively. The C, D, E and F (free wall) paths are in the infarcted region (see notes above) while the paths I, J, K and L are in the non-infarcted septal wall.

As shown in Figure 5-1 (a), in the free wall, the radial, circumferential and longitudinal strains of the healthy models are higher than those of the two-week and four-week infarct models. The radial strain in the two-week and four-week infarct model is 83.6 % and 76.1 % lower, respectively, than the radial strain in the healthy models. The circumferential strain in the two-week and four-week infarct model is 69.5 % and 66.7 % lower, respectively, than circumferential strain in the healthy models. In longitudinal direction, the strain in the two-week and four-week infarct model is 45.9 % and 95.2 % lower, respectively, than the strain in the healthy case. In the radial direction, the strain in the four-week infarct model was found to be 85.0 % higher compared to the two-week infarct model. In the circumferential direction, the strain in the four-week infarct model was found not to have changed compared to the two-week infarct model. In the longitudinal direction, the strain in the two-week infarct model was found to be 90.0 % higher compared to the four-week infarct model (see Table 5-1).

The maximum decrease of strain in two-week infarct model is found to be in the radial direction. Furthermore, the maximum decrease of strain in four-week infarct model is found to be in the longitudinal direction. The strain in the radial direction for four-week infarct model was found to be higher than that of the two-week infarct model. The finding is based on the fact that the four-week infarct model has a larger infarct size compared to the two-week infarct model whereas the infarct stiffness in both models was the same ($C = \text{constant}$). As the infarcted tissue stiffens compared to the healthy tissue, the strain in all directions decreased. This is mainly attributed to the fact that after infarction, the collagen substance expands quickly and infarct stiffness is generally associates with collagen content. The

healing infarct soon enters a stage where new collagen deposition is the essential determinant of structural and mechanical changes. The stage after two-week infarction is characterized as starting when the quantity of fibroblasts and extent of new collagen start to increment speedily in the healing infarct more or less 5 days after dead tissue in the rat and consummation when collagen amassing moderates and mechanical properties decouple from collagen content. In rats, the collagen substance starts ascending on day 4 or 5 and keeps on increasing for no less than 3 weeks. The mean introduction of the collagen fibres fluctuates with complexity underneath the epicardium in a pattern comparable to that for healthy muscle fibres excluding that the transmural range of mean angles is reduced. The accessible evidence recommends that during this stage infarct stiffness peaks and the recuperating infarct acquire a particular anisotropy. Due to lack of available data in the literature regarding the stiffness factor for rat, the infarct stiffness of both the two-week and four-week model were modelled using the same magnitude.

As shown in Figure 5-1 (a), the strain in the healthy regions E and F and C, D, E and F have different stress values. It was further observed that in the radial direction, the strain in the C, D, E and F region is 21.3 % higher than the E and F region in the healthy model. Similarly, it was observed that in the longitudinal direction, the strain in the C, D, E and F region is 11.9 % higher than the E and F region in the healthy model. In the contrary, the circumferential strain in the E and F region is 8.6 % higher than the C, D, E and F region.

Figure 5-1 (b) shows the strains in the radial, circumferential and longitudinal direction in the septal wall (I, J, K and L paths) for healthy, two-week and four-week infarct models. It is important to recall that the septal wall region is non-infarcted in all three models. The radial strain in the two-week and four-week infarct model is 41.7 % and 83.3 % higher than radial strain in the healthy models, respectively. The circumferential strain in the two-week and four-week infarct model is 62.5 % and 100.0 % higher than circumferential strain in the healthy models, respectively. The longitudinal strain in the two-week and four-week infarct model is 25.0 % and 50.0 % higher than longitudinal strain in the healthy models, respectively. In the radial direction, the strain in the four-week infarct model was found to be 29.4 % higher compared to the two-week infarct model. In the circumferential direction, the strain in the four-week infarct model was found to be 23.1 % higher compared to the two-week infarct model. In the longitudinal direction, the strain in the four-week infarct model was found to be 20.0 % higher compared to the two-week infarct model.

The presented results show that the infarct and its size has major influence on the strain in the septal wall. The infarct in the LV free wall induces increased, i.e. hyper-physiological, strains in the non-infarcted septal wall. When comparing the infarcted models to the healthy model, it was found that in the two-week infarct model the strain has risen by to 41.7 % in the radial direction. In the four-week infarct model with a larger infarct size, the strain has even risen by to 83.3 % compared to the healthy case in the radial direction.

It is worth emphasising that bi-ventricular finite element models were utilised in this study. The septal wall is pressurised from both sides, i.e. the LV side and the RV side. The pressure applied at the LV side is much higher than that applied on the RV side. Due to the geometry of the bi-ventricular model, as the free wall is forced to have minimal strain due to stiffening of the scar tissue on the wall, this myocardial energy needs to be accommodated by the septal wall. This means that as the free wall stiffens due to scarring with increase in collagen content after infarction and the LV cavity pressure is assumed to remain the same, the septal wall will compensate and absorb some of the pressure load and associated energy. This explains higher strain in all directions in the two-week and four-week infarct models compared to the healthy case. These findings have practical implications as when the free wall in the infarct region may trigger adverse remodelling of the heart.

The minimum increase of strain in two-week infarct model is found in the longitudinal direction. In addition, the minimum increase of strain in four-week infarct model is found to be in the longitudinal direction. Similarly, the maximum increase of strain in two-week infarct model is found to be in the circumferential direction. Furthermore, the maximum increase of strain in four-week infarct model is found to be in the circumferential direction (See Table 5-1).

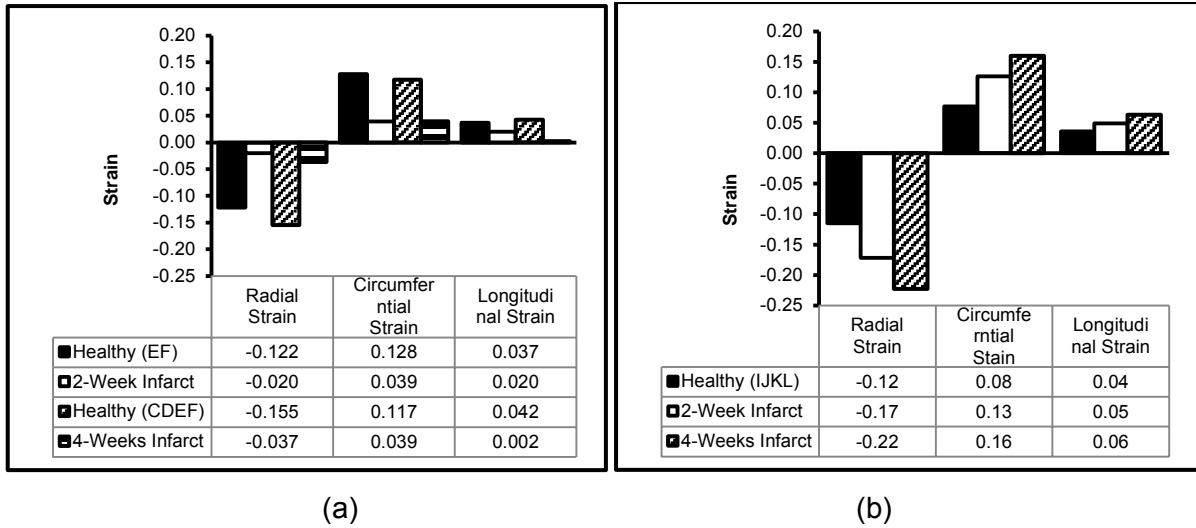


Figure 5-1: Average radial, circumferential and longitudinal strains during passive filling simulation in (a) free wall paths C, D, E and F and (b) septal wall paths I, J, K and L.

Table 5-1: Difference of average strain in the LV free wall (infarct region) for different models at end-diastole

	Radial Strain	Circumferential Strain	Longitudinal Strain
Two-Week Infarct versus Healthy	-83.6 %	-69.5 %	-45.9 %
Four-Week Infarct versus Healthy	-76.1 %	-67.7 %	-95.2 %
Four-Week Infarct versus Two-Week Infarct	85.0 %	0.0 %	-90.0 %

Table 5-2: Difference of average strain in the septal wall for different models at end-diastole

	Radial Strain	Circumferential Strain	Longitudinal Strain
Two-Week Infarct versus Healthy	41.7 %	62.5 %	25.0 %
Four-Week Infarct versus Healthy	83.3 %	100.0 %	50.0 %
Four-Week Infarct versus Two-Week Infarct	29.4 %	23.1 %	20.0 %

5.4.2.2 Stress in the healthy and infarct models during passive filling

Figure 5-2 shows the average radial, circumferential and longitudinal stresses in the healthy, two-week infarcted and four-week infarcted heart models along the paths C, D, E and F and I, J, K and L. The C, D, E and F (free wall) paths are in the infarcted region (see notes above) while paths I, J, K and L are in the non-infarcted septal wall.

In the LV free wall region (see Figure 5-2 (a)), the stress is, for all cases studied, considerably higher in the circumferential direction compared to the radial and longitudinal directions. The positive values of the stress indicates extension in the circumferential and longitudinal direction, whereas the negative, i.e. compressive, stress in radial direction is associated with wall thinning during filling (as indicated by the compressive radial strains in Figure 5-2 a). The average radial stress in the two-week infarct model is 178.4 % higher than the healthy model. The average radial stress in the four-week infarct model is 58.2 % higher than the healthy model. The average radial stress in the four-week infarct model is 51.3 % higher than the two-week infarct model.

The circumferential stress in the two-week and four-week infarct model is 74.2 % and 91.1 % higher than for the healthy model, respectively. The circumferential stress in the four-week infarct model is 15.9 % higher than the two-week infarct model. The longitudinal stress in the two-week and four-week infarct was predicted to be 7.7 % and 11.4 % higher than the stress in the healthy model, respectively. In the longitudinal direction, the stress in the four-week model is found to be 49.6 % higher than in the two-week model.

It was observed that the stress in the healthy regions E and F (as reference for the two-week infarct) and C, D, E and F (as reference for the four-week infarct) have different stress values. The radial stress in the healthy (EF) region is 62.4 % higher than the healthy (CDEF) region. Contrary to the radial direction, in the circumferential direction, the stress in the healthy (EF) region is 5.6 % higher than the healthy (CDEF) region. In addition, the longitudinal stress in the healthy (EF) region is 44.7 % higher than the healthy (CDEF) region.

Figure 5-2 (b) shows the stress in the radial, circumferential and longitudinal direction in the septal wall (I, J, K and L paths) for healthy, two and four-week infarct models. It is important to recall that the septal wall region is non-infarcted, i.e. healthy, in all three models.

As observed in the free wall, the stresses are: (i) positive associated with extension in circumferential and longitudinal direction compared to negative stresses in radial direction caused by thinning of the septal wall during filling, and (ii) of substantially larger magnitude in the circumferential direction compared to the radial and longitudinal directions.

Related to the higher strain magnitudes observed in the two-week and four-week infarct models compared to the healthy heart, the stress magnitudes are higher in the infarcted hearts compared to the healthy heart. Similarly, higher stress magnitudes are observed in the four-week infarcted heart compared to the two-week infarcted heart.

The radial stress in the two-week and four-week infarct model is 64.9% and 52.3 % higher than in the healthy model, respectively. In circumferential direction, the stress in the two-week and four-week infarct model is 94.8 % and 188.6 % higher than in the respective healthy model, and the stress in longitudinal direction of the two-week and four-week infarct model is 16.7 % and 287.0 % higher than in the respective healthy model.

Comparing the infarct models, the circumferential and longitudinal stress was found to be 48.1 % and 231.5 % higher in the four-week infarct model than in two-week infarct model, whereas the radial stress was 7.6 % lower in in the four-week infarct case compared to two-week infarct case.

Similar to the indications for strain (Figure 5-2 b), it has been found that the size of the infarct in the LV free wall has a definite influence on the stress in the septal wall (during passive

filling). Whereas both infarcts cause elevated stresses in the non-infarcted septal wall, the increase in stress beyond the level found in the healthy heart was generally larger for the larger four-week infarct compared to the smaller two-week infarct.

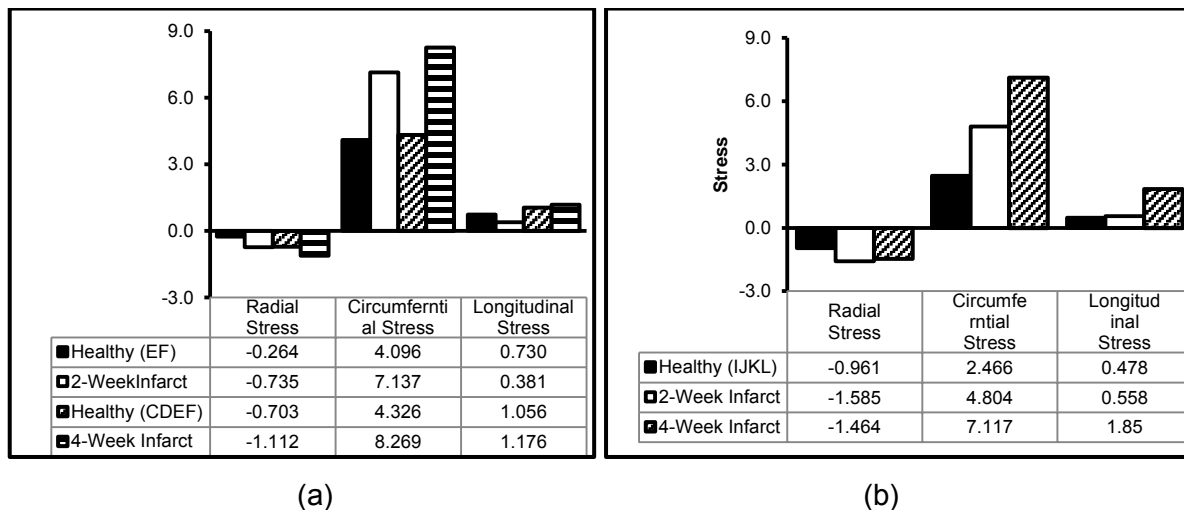


Figure 5-2: Average radial, circumferential and longitudinal stresses at end-diastole along (a) paths C, D, E and F in the free wall infarct region and (b) paths I, J, K and L in the septal wall.

Table 5-3: Difference of average stress in the free wall (Infarct region) for different models at end-diastole

	Radial Stress	Circumferential Stress	Longitudinal Stress
Two-Week Infarct versus Healthy	178.4 %	74.2 %	7.7 %
Four-Week Infarct versus Healthy	58.2 %	91.1 %	11.4 %
Four-Week Infarct versus Two-Week Infarct	51.3 %	15.9 %	49.6 %

Table 5-4: Difference of average stress in the septal wall for different models at end-diastole

	Radial Stress	Circumferential Stress	Longitudinal Stress
Two-Week Infarct versus Healthy	64.9 %	94.8 %	16.7 %
Four-Week Infarct versus Healthy	52.3 %	188.6 %	287.0 %
Four-Week Infarct versus Two-Week Infarct	7.6 %	48.1 %	231.5 %

5.4.2.3 Strain in healthy and infarct models during active contraction

Figure 5-3 shows the average radial, circumferential and longitudinal strains in the healthy, two and four-week infarcted heart models in the paths C, D, E and F and I, J, K and L,

respectively. The C, D, E and F (free wall) paths are in the region of the infarct (see notes above) whereas paths I, J, K and L are in the non-infarcted septal wall.

Generally, it was observed that the average strains (radial, circumferential and longitudinal) in the free wall (C, D, E and F regions) have lower magnitude compared to the septal wall (I, J, K and L regions). The average strain magnitudes are largest in circumferential direction followed by the longitudinal and the radial direction in the free wall, whereas in the septal wall strains in radial direction are larger than in longitudinal direction magnitude.

In the LV free wall region of the infarct (Figure 5-3 a), the radial strain in the two-week and four-week infarct is 80.0 % and 92.3 % lower, respectively, than the strain in the healthy heart. The circumferential strain in the two-week and four-week infarct is 97.1 % and 93.3 % lower than in the healthy case. The longitudinal strain in the two-week and four-week infarct cases is 87.2 % and 83.9 % lower than in the healthy model, respectively. When compared to the two-week infarct, the strain in the four-week infarct model was found to be 150.0 %, 133.3 % and 200.0 % higher in the radial, circumferential and longitudinal direction, respectively. The large relative differences in strain of the two infarct cases should be seen in context of the small absolute values of the strain.

The positive radial strain in the healthy cases indicates an increase in myocardial thickness associated with contractile deformation of the LV in circumferential and longitudinal direction expected due to active contraction and indicated by the negative strain values. However, the radial strains in both the two-week and four-week infarcted models have been found to be negative, although of marginal magnitude, related to slight wall thinning. This is due to the loss of active contractility that the infarcted area, with the small strain magnitudes in radial direction agree with similar low strain magnitudes in circumferential and longitudinal direction – effectively indicating small deformations in the infarcts in all direction compared to the same region on the healthy heart.

The strain in the healthy regions E and F and C, D, E and F have different stress values. It was further observed that in the radial direction, the strain in the C, D, E and F region is 550.0 % higher than the E and F region in the healthy model. Similarly, it was observed that in the longitudinal direction, the strain in the C, D, E and F region is 135.9 % higher than the E and F region in the healthy model. In the contrary, the circumferential strain in the C, D, E and F region is 1.96 % lower than the E and F region in the healthy model.

Figure 5-3 (b) shows the strain in the radial, circumferential and longitudinal direction in the non-infarcted septal wall (I, J, K and L paths) for healthy, two-week and four-week infarct cases. The radial strain in the two-week and four-week infarct model is 17.1 % and 19.8 % lower than in the healthy model, respectively. The circumferential stress in the two-week and four-week model is 24.3 % and 30.7 % lower than circumferential strain in the healthy models, respectively. The longitudinal strain in the two-week and four-week model is 35.1 % and 45.5 % lower than longitudinal strain in the healthy models, respectively. Contrary to the free wall, the strain in the septal wall of the four-week infarct case is lower than in the two-week infarct case in all three directions, namely by 3.3 %, 8.4 % and 16.0 % in radial, circumferential and longitudinal direction.

The presence of an infarct, and its size, in the free wall affects the strain in the septal wall at end-systole similarly to what was observed at end-diastole. The free wall infarct leads to increased septal strain values in the infarct cases compared to the healthy case, and for the larger free wall infarct (four-week) compared to the smaller infarct (two-week). For example, at end-diastole (Figure 5-3 b) the circumferential septal strain increases from healthy case to two-week infarct case and further in the four-week infarct case. At end-systole, the same is observed although the circumferential strain is negative in all three cases (Figure 5-3 b) – the compressive strain values decrease from healthy case to two-week infarct case and four-week infarct case. The same is observed for the longitudinal direction, and the radial direction appropriately for the opposite change in sign of the strains between end-diastole and end-systole.

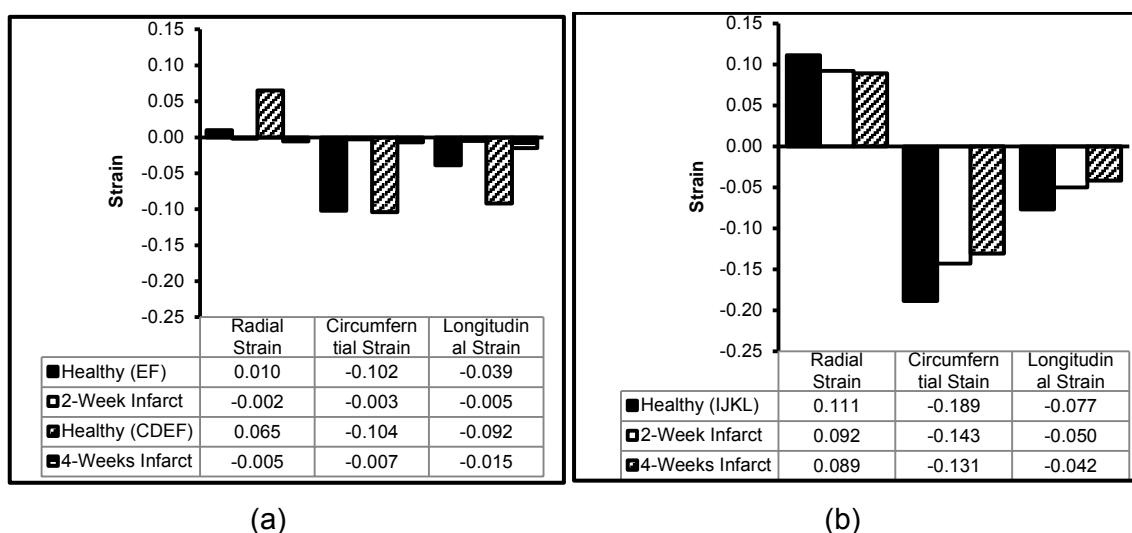


Figure 5-3: Average radial, circumferential and longitudinal strains during active contraction simulation along (a) paths C, D, E and F in the free wall and (b) paths I, J, K and L in the septal wall.

Table 5-5: Difference of average strain in the LV free wall (infarct region) for different models at end-systole

	Radial Strain	Circumferential Strain	Longitudinal Strain
Two-Week Infarct versus Healthy	-80.0 %	-97.1 %	-87.2 %
Four-Week Infarct versus Healthy	-92.3 %	-93.3 %	-83.7 %
Four-Week Infarct versus Two-Week Infarct	150.0 %	133.3 %	200.0 %

Table 5-6: Difference of average strain in the septal wall for different models at end-systole

	Radial Strain	Circumferential Strain	Longitudinal Strain
Two-Week Infarct versus Healthy	-17.1 %	-24.3 %	-35.1 %
Four-Week Infarct versus Healthy	-19.8 %	-30.7 %	-45.5 %
Four-Week Infarct versus Two-Week Infarct	-3.3 %	-8.4 %	-16.0 %

5.4.2.4 Stress in healthy and infarct models during active contraction

Figure 5-4 shows the average stresses in the radial, circumferential and longitudinal directions for healthy, two-week infarct and four-week infarct models in the LV free wall (paths C, D, E and F) and the septal wall (paths I, J, K and L).

In general, absolute stress values are highest in circumferential direction followed by longitudinal and radial directions - for all models both free wall and septal wall region.

In the LV free wall (Figure 5-4 a), the radial stress in the two-week and four week infarct is 60.0 % and 98.7 % lower in magnitude, respectively, and of opposite sign than the stress in the healthy model. In the absence of contractility, the radial strain becomes negative indicating wall thinning similarly to the radial strain in the end-diastolic infarcts (Figure 5-4 a). In circumferential direction, the stress in the two-week and four week infarct case is 83.9 % and 45.3 % lower than the stress in the healthy model, respectively. The longitudinal stress in the two-week and four-week infarct case is 56.0 % and 58.0 % lower than the stress in the healthy model, respectively. The radial, circumferential and longitudinal stress in the four-week infarct model is 96.7 % lower, 219.3 % higher and 45.3 % lower than the respective stress in the two-week infarct model.

In the non-infarcted septal wall region (Figure 5-4 b), the radial stress in the two-week and four-week infarct model is 66.1 % and 81.6 % lower than in the healthy models, respectively. The circumferential stress in the two-week and four-week infarct model is 63.9 % and 68.1 % lower, respectively, than the circumferential stress in the healthy models. The longitudinal stress in the two-week and four-week infarct model is 61.9 % and 72.6 % lower than in the healthy case, respectively. The stress in four-week infarct model is 45.7 %, 11.8 % and 28.1 % lower than in the two-week infarct model for radial, circumferential and longitudinal direction, respectively.

In this study, the three dimensional models of the rat, healthy and infarcted at two and four-week, and transmural muscle fibre distribution are used to compute the global strain and stress to assess transmural distributions of the stress and strains in radial, circumferential and longitudinal directions. The results presented here show that there is a significant variation in a transmural distribution. The radial, circumferential and longitudinal stresses in the healthy model (free wall) of -40.95 kPa, -46.65 kPa and -28.59 kPa, respectively, are in good agreement with the fibre stresses of between 30-43 kPa as presented by Guccione et al. (1995c) for the dog heart. The substantial differences in stress in the septal wall of the healthy heart and the infarct cases confirm the substantial effect of the LV free wall infarcts in remote regions.

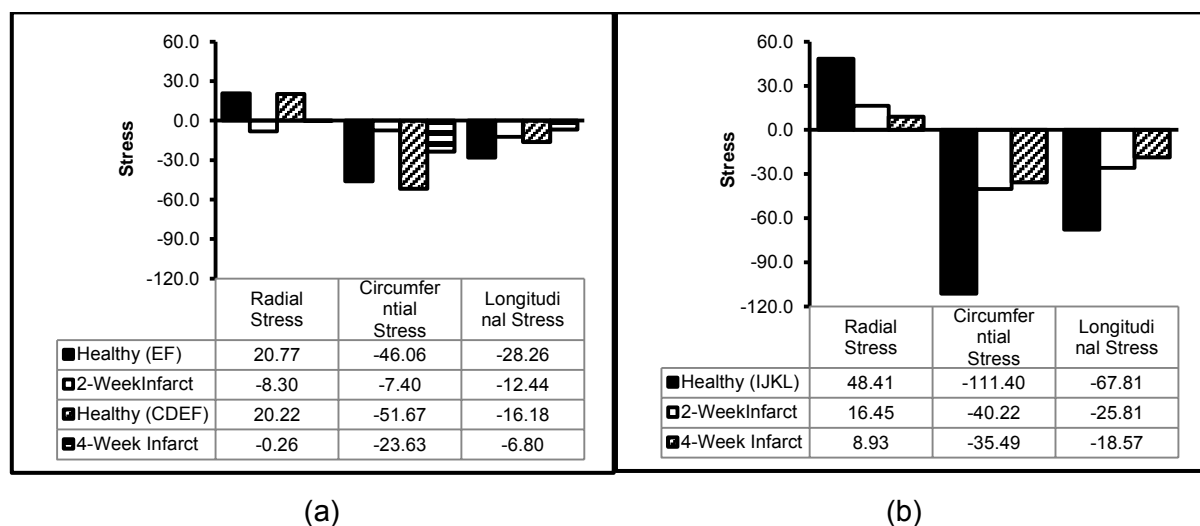


Figure 5-4: Average stresses during active contraction along (a) paths at C, D, E and F in the free wall and (b) paths I, J, K and L in the septal wall.

Table 5-7: Difference of average stress in the LV free wall (infarct region) for different models at end-systole

	Radial Stress	Circumferential Stress	Longitudinal Stress
Two-Week Infarct versus Healthy	-60.0 %	-83.9 %	-56.0 %
Four-Week Infarct versus Healthy	-98.7 %	-54.3 %	-58.0 %
Four-Week Infarct versus Two-Week Infarct	-96.7 %	-219.3 %	-45.3 %

Table 5-8: Difference of average stress in the LV septal wall for different models at end-systole

	Radial Stress	Circumferential Stress	Longitudinal Stress
Two-Week Infarct versus Healthy	-66.6 %	-63.9 %	61.9 %
Four-Week Infarct versus Healthy	-81.6 %	-68.1 %	-72.6 %
Four-Week Infarct versus Two-Week Infarct	-45.7 %	-11.8 %	-28.1 %

5.4.3 Review of strains and stress in the septal wall in conjunction with LV dimensions of healthy and infarcted cases

Many studies including the present have investigated the changes in wall mechanics of the LV infarct region associated with various stages of myocardial infarction, infarct healing and post-infarct ventricular remodelling.

The current study has however also assessed in detail the changes in wall mechanics of the septal wall in presence of an infarct in the LV free wall. As pointed out before, the septal wall is not exposed to infarct injury and healing but remains healthy and functional, i.e. contractile while the LV infarct region and LV undergoes the stages of infarct healing and ventricular remodelling.

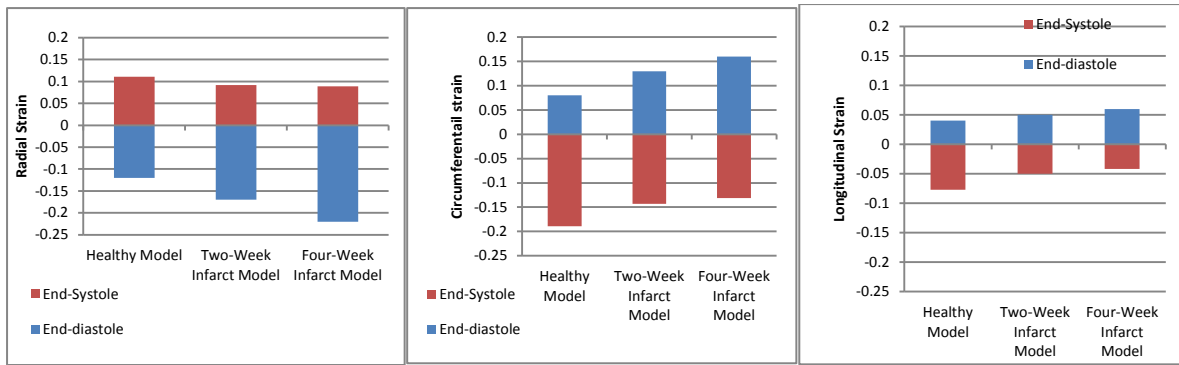
As described in previous sections, substantial changes in strains and stresses have been observed in the septal wall between the healthy heart and the infarcted cases. In general, ED strain and stress increased in the presence of the LV infarct in all directions whereas ES strain and stress decreased in all directions in the infarct models compared to the healthy case (Table 5-9). The observed changes of strain and stress at both the ED and the ES time point results in the non-physiological adaptation of the ranges that septal strain and stress undergo in a cardiac cycle due to the LV infarct, illustrated in Figure 5-5 and Figure 5-6. The changes in the strain range are moderate and vary between an increase of 34% in radial

direction and a decrease of 14% in longitudinal direction. The range of the septal wall stress is however affected more substantially and reduced between 60% and 80% - with larger reductions being associated with the larger 4w infarct.

The non-physiological mechanics of the non-infarcted septal wall in a heart with an LV infarct may well contribute to the adverse post-infarct processes at multiple levels and during various stage of infarct healing and remodelling of the LV. Adverse effects could include local reduction of contractile efficiency of the cardiac muscle in the septal wall contributing to the functional impairment of the LV, and potentially the RV, and mitigating therapeutic efforts focussing on infarct region in the LV free wall.

Table 5-9. Infarct sizes, LV volumes and functional parameters, as well as ED and ES values and ranges of strains and stresses in septal wall for healthy, 2-week infarct and 4-week infarct cases and comparison between cases

	Healthy	2w infarct	4w infarct	2w vs H (%)	4w vs H (%)	4w vs 2w (%)
Infarct size (%)	n/a	16.2	30.3	n/a	n/a	87.0
LV EDV (μL)	207.5	261.7	369.7	26.1	78.2	41.3
LV ESV (μL)	73.0	118.9	186.2	62.9	155.1	56.6
LV SV (μL)	134.4	142.8	183.5	6.3	36.5	28.5
LV EF (%)	64.8	54.6	49.6	-15.8	-23.4	-9.0
ED Strain radial	-0.120	-0.170	-0.220	41.7	83.3	29.4
ES Strain radial	0.111	0.092	0.089	-17.1	-19.8	-3.3
ED-ES Strain range radial	0.231	0.262	0.309	13.4	33.8	17.9
ED Strain circum	0.080	0.130	0.160	62.5	100.0	23.1
ES Strain circum	-0.189	-0.143	-0.131	-24.3	-30.7	-8.4
ED-ES Strain range circum	0.269	0.273	0.291	1.5	8.2	6.6
ED Strain longit	0.040	0.050	0.060	25.0	50.0	20.0
ES Strain longit	-0.077	-0.050	-0.042	-35.1	-45.5	-16.0
ED-ES Strain range longit	0.117	0.100	0.102	-14.5	-12.8	2.0
ED Stress radial (kPa)	-0.96	-1.59	-1.46	64.9	52.3	-7.6
ES Stress radial (kPa)	48.4	16.5	8.9	-66.0	-81.6	-45.7
ED-ES Stress range radial (kPa)	49.4	18.0	10.4	-63.6	-78.9	-42.2
ED Stress circum (kPa)	2.47	4.80	7.12	94.8	188.6	48.1
ES Stress circum (kPa)	-111.4	-40.2	-35.5	-63.9	-68.1	-11.8
ED-ES Stress range circum (kPa)	113.9	45.0	42.6	-60.5	-62.6	-5.3
ED Stress longit (kPa)	0.48	0.56	1.85	16.7	287.0	231.5
ES Stress longit (kPa)	-67.8	-25.8	-18.6	-61.9	-72.6	-28.1
ED-ES Stress range longit (kPa)	68.3	26.4	20.4	-61.3	-70.1	-22.7

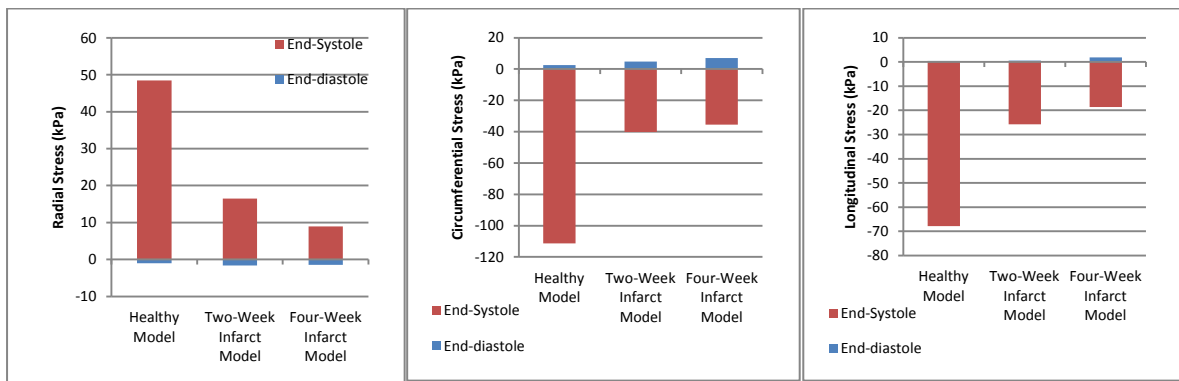


(a)

(b)

(c)

Figure 5-5: Strain range in the septal wall in (a) radial, (b) circumferential and (c) longitudinal direction.



(a)

(b)

(c)

Figure 5-6: Stress range in the septal wall in (a) radial, (b) circumferential and (c) longitudinal direction.

6 Conclusions and Recommendations

6.1 Review of Aims and Outcomes of the Research

The aim of this study was to use a biomechanical model to study the cardiac mechanics of the remodelling rat heart after myocardial infarction. The specific aims in order to achieve the overall aim were as follows:

- (a) Create and segment a 3D rat heart healthy biventricular model and models at two time points after myocardial infarction are created based on the MRI data. To achieve the accurate finite element models, the validation and verification of the 3D geometries are performed such that the accurate EDV, ESV and wall volume is achieved. The realistic geometries are segmented based on the MRI data of the rat heart at two time points after infarction.
- (b) Use the segmented geometries to study the cardiac mechanics of the remodelling rat heart of the healthy models. The accurate fibre orientation in the heart remains the vital part in studying the cardiac mechanics as fibre plays a vital role in the beating of the heart. This is ensuring that the infarct models at two-week and four-week are compared with the healthy model.
- (c) Develop the Fung model suitable to study the cardiac mechanics of remodelling rat heart at end-systole. Currently Abaqus® has implemented the Fung constitutive model which is only suitable for passive simulation.
- (d) Study the cardiac mechanics of the infarcted regions in the rat heart. The functional parameters of the heart namely, ejection fraction, stroke volume and the contractility are then determined based on the geometries of the rat heart.

In this work, the anatomically realistic model of the rat biventricular model that employs a structure-based constitutive Fung model and a rule-based cardiac fibre distribution was developed. The model uses the Fung orthotropic model assuming that the myocardium is incompressible due to its high water content. This model was then used to simulate the diastolic and systolic mechanics of the healthy and infarcted hearts at two time points (two-week and four-week after myocardial infarction). The left and right ventricular myocardium were treated as an inhomogeneous, thick-walled, nonlinearly elastic, incompressible material, following the modelling framework of the Fung Model (Ateshian and Costa, 2009, Sun and Sacks, 2005), which takes into account the fibre-reinforced microstructure of ventricular myocardium. In addition, the end-diastolic and end-systolic pressure–volume relationship of the model prediction agrees well with published *ex vivo* rat heart

measurements. The changes in the fibre angle distribution change the distributions of stress and strain dramatically. This highlights the importance of using realistic fibre structures.

The transmural distributions of the stress and strain of the healthy model were compared with results in infarcted regions at different time points (two and four-week infarcted). Large differences were found in the stress and strain predictions generated at different regions especially in the infarcted regions at end-diastole and end-systole. In addition, although similar trends can be identified, these results are also different from published results from animal LV models. This highlights the significance of bi-ventricular models and accurate fibre orientation during simulation especially at end-systole. Modelling of ESPVR and EDPVR to simulate diastolic and systolic state, respectively, is significant in studying the functional performance of the healthy and diseased hearts. Functional parameters of the rat heart were determined based on the geometries of the healthy and infarcted rat heart models. The comparison of stress and strain in radial, circumferential and longitudinal directions was used to assess differences in the healthy and the infarcted hearts at end-diastole and end-systole.

Following this study, future study could continue developing the clinical data by firstly improving on the heart model. By using FE models, progress has been made in understanding the ventricular mechanics of the heart at end-diastole and end-systole time points. The biventricular FE models of a heart give an overview and understanding of cardiac mechanics of both LV and RV. In addition, the FE models provide computational tools to study the effect of the infarcted area size of myocardium and thereby implement the right procedure for MI patients' management. Better understanding of MI mechanisms gained from this study may lead to better understanding of MI therapies.

This study has further assisted in the development of computational tools for the study of cardiac mechanics involved in the progression of myocardial infarction. In addition, the contribution of this study could be seen in accelerating the translation of myocardial infarction therapy concepts into clinical application. Moreover, a reduction in the use of research animals in pre-clinical research on MI and CVD therapies could be achieved by studying the effect of MI on the global functioning of the heart using FE models.

6.2 Novel Aspects of the Presented Study

The generation of 3D rat heart models is critical in finite element analysis. In this study, the 3D model geometries of the remodelling rat heart were generated from cardiac MRI data

obtained from the same animal at different time points after infarction. This has assisted in acquiring the real geometries of the infarcted rat hearts. The wall thinning plays a critical role in the global functions of the heart. In our models, the real geometries were used in simulating and understanding the mechanisms of the cardiac mechanics during myocardial infarction.

A Fung-based material model was developed with the inclusion of the active stress components. The model was implemented in Abaqus® software with the active contraction UMAT subroutine being coded in Fortran 77. This enabled cardiac mechanical simulations with fully developed active contraction.

The fibre orientation in the rat heart plays a vital role during active ejection and passive filling phases. The accurate representation of fibre orientation in the myocardium required the use of a subroutine called ORIENT. The fibre orientation was not modelled physically. In our study, the fibre orientation was modelled accurately in the LV reflecting the exact fibre arrangement in the epicardium, mid-wall and endocardium.

The general purpose finite element software Abaqus® was used to study the biomechanical analysis of remodelling of rat heart after myocardial infarction. The stress and strain results obtained using the general purpose finite element software is in agreement with results obtained using the specialised finite element analysis for biomechanical simulation. We were therefore, able to prove that the general purpose software could be used in understanding the complex nonlinear behaviour of remodelling of rat heart.

The behaviour of remodelling rat heart was achieved with great accuracy. This study demonstrated, through finite element analyses, how functional parameters of the heart change at various stages after myocardial infarction. The global parameters of the remodelling rat heart including ejection fraction, stroke volume and contractility were accurately determined at each infarction stage using the biomechanical models. This has contributed greatly to the body of knowledge because the understanding of infarcted heart could be drawn from the biomechanical model as compared to *in-vivo* studies.

Substantial changes in strains and stresses have been observed in the septal wall between the healthy heart and the infarcted cases. In general, ED strain and stress increased in the presence of the LV infarct in all directions whereas ES strain and stress decreased in all directions in the infarct models compared to the healthy case. The observed changes of

strain and stress at both the ED and the ES time point results in the non-physiological adaptation of the ranges that septal strain and stress undergo in a cardiac cycle due to the LV infarct. The non-physiological mechanics of the non-infarcted septal wall in a heart with an LV infarct may well contribute to the adverse post-infarct processes at multiple levels and during various stage of infarct healing and remodelling of the LV.

6.3 Recommendations for Further Work

To achieve the specific aims of the research, this model for healthy and infarcted hearts can be considered accurate and acceptable. In performing a simulation, there is a need to balance the accuracy and reliability of the results. Therefore, sometimes there is a need to trade-off in accuracy or reliability of the model simulation results. In this study, the complex simulation of healthy and infarcted hearts at end-diastole and active contraction was achieved. The finite element analysis performed in this study provides the information required in studying the cardiac mechanics of remodelling the rat heart after myocardial infarction. In this model, certain assumptions were made and the removal of these assumptions could improve the accuracy of the results. Many possibilities for further work have been identified during the work of this thesis. The recommended aspects for future work include the following: Determination of contribution of the infarct in the septal strain and stress, residual stress during segmentation; fibre orientation in the infarcted heart; the effect of blood perfusion; and the development of specific fibre orientation.

6.3.1 Determination of contribution of the infarct in the septal strain and stress

Further research beyond the current study and scope of the doctoral thesis is required / will contribute to a more detailed understanding of contributions of non-physiological mechanics of the septal wall. Of particular interest and a possible first target is to identify the concurrent roles of changing mechanics of the infarct region in the free LV wall on the one hand and the ventricular remodelling and dilation on the other hand – such as an increase in circumferential strain caused by a dilated ventricle. The best way to achieve this and determine their contribution would be to run simulations with 2w and 4w infarct geometries with dilated LV but without an infarct, i.e the LV is healthy. These simulations would indicate the increased septal wall strain due to dilated LV. The difference in septal strain and stress to the 2w and 4w infarct models would be the contribution of the infarct.

6.3.2 Residual stress in reconstructed geometric configuration

We assume the reference configuration, which is derived from imaging data obtained at end-diastole, to be a stress-free configuration. In the presence of *external* pressure loads, this configuration would not actually be stress-free in a real heart. The presence of the residual stresses in the myocardium was proved by observing movement of the heart after the remaining (residual) stresses were relieved Omens *et al.*, 1990; Omens *et al.*, 1998; Rodriguez *et al.*, 1993; Zamir *et al.*, 2004. The observations from these authors have far reaching implications on the mathematical models where the configuration is assumed to be stress free. Some authors have argued that the residual stress and strain are more uniform during the passive filling phase, whereas others have urged that these residual stresses are minimal at the end-systole phase due to high stress generated by the active forces within the myocardium. The impact of initial strains and residual stresses on the mechanical behaviour of the LV in diastole must be addressed in future work. During segmentation, the model was assumed to be at a stress free state. In conclusion, there is a need to look at how residual stress and strain at a particular point of interest during segmentation can be taken into account.

6.3.3 Fibre orientation in the infarcted region

The fibre structure is also rule-based, and may not reflect the fibre structure of the particular rat LV and RV used to construct the geometrical model. The myofibre plays an important role during passing, filling and active contraction. As such, the exact myofibre orientation based on a specific model may improve the results. In this study, the fibre orientation in the infarcted region was assumed to be the same as in the healthy tissue. This happens mainly due to lack of information on a specific model. Myofibre orientation plays an important role in the understanding of cardiac mechanics. Without a proper and detailed myofibre orientation of the specific object, the details of the mechanics may be lost. In future, there is a need to look in detail at the myofibre orientation in the infarcted regions as this could influence the results of the myocardial mechanics in those regions.

6.3.4 The effect of blood perfusion

The effect of blood perfusion was not taken into account in this study. The flow of blood in heart vessels also plays an important role on the global functioning of the heart. The inclusion of this process in the rat heart model could change the mechanism of heart function on the healthy and infarcted hearts.

6.3.5 Development of specific fibre structure

Further work is required to develop patient-specific fibre structure estimated from *in-vivo* DTMR datasets, to evaluate the impact of initial strains and residual stresses, and to account for fluid–structure interaction. It is clear that closely matched experimental data are needed for more in-depth LV modelling. Fibre orientation is critical in the movement of the heart during the filling and active contraction phases. In our model, the fibre orientation used is not for the specific model.

6.3.6 Modelling of functional border zone

The border zone between the infarct and the healthy area was not considered in this study. The non-ischemic infarct border zone is responsible for the depression of wall thickening and systolic shortening (Homans et al., 1985, Jackson et al., 2002, Jackson et al., 2003). The improvement of contraction in the border zone of the infarct is said to have the ability to improve the global ejection capability of the infarcted heart (Zhang et al., 2012). The understanding of perfused infarct border zone mechanics may lead to the improvement of LV pump function. The contractility in the border zone is not homogenous. This means that the FE models must be defined such that this limitation is reduced.

6.3.7 Boundary conditions

The LV and RV pressures applied on the model were investigated from the literature. The mimicked endocardial pressures used in the current study could be less accurate since the individual models have their own endocardial pressures. Therefore, the precise measurements of end-systolic and end-diastolic pressures of LV and RV could improve the accuracy of the model.

6.3.8 Structure and Fluid interaction

The current model treats the LV and RV as a hyperelastic structure, without accounting for fluid–structure interactions, and the boundary conditions are therefore necessarily simplified. In applying the boundary conditions applied on the models, the assumption made was that the heart is free of contact from other organs surrounding it. This may pose a limitation and compromise on the accuracy of the results because in reality this is not the case.

6.3.9 Possible dyssynchrony of the ventricles due to the infarct

Possible dyssynchrony of the ventricles due to the infarct is not considered in this study. This could have a possible influence on simulation results as the implemented model which assumes uniform contraction. In future studies, there is a need to look at the possible influence of dyssynchrony of the ventricles due to the infarct.

References

- ABAQUS (2010) User Subroutine Reference Manual.
- ABDESSALEM, K. B., MANSOURI, S., SALAH, R. B. & ABDESSALEM, S. B. (2010a) New technique of flow rate and pressure separation within the arterial system: Part I. *Computer Methods in Biomechanics and Biomedical Engineering*, 13, 9 - 10.
- ABDESSALEM, K. B., MANSOURI, S., SALAH, R. B. & ABDESSALEM, S. B. (2010b) New technique of flow rate and pressure separation within the arterial system: Part II. *Computer Methods in Biomechanics and Biomedical Engineering*, 13, 11 - 12.
- AHN, B. & KIM, J. (2010) Measurement and characterization of soft tissue behavior with surface deformation and force response under large deformations. *Medical Image Analysis*, 14, 138-148.
- AIKAWA, Y., ROHDE, L., PLEHN, J., GREAVES, S. C., MENAPACE, F., ARNOLD, J. M. O., ROULEAU, J.-L., PFEFFER, M. A., LEE, R. T. & SOLOMON, S. D. (2001) Regional wall stress predicts ventricular remodeling after anteroseptal myocardial infarction in the Healing and Early Afterload Reducing Trial (HEART): An echocardiography-based structural analysis. *American Heart Journal*, 141, 234-242.
- ATESHIAN, G. A. & COSTA, K. D. (2009) A frame-invariant formulation of Fung elasticity. *Journal of Biomechanics*, 42, 781-785.
- AYACHE, N., DELINGETTE, H., SERMESANT, M., BISHOP, M., HALES, P., PLANK, G., GAVAGHAN, D., SCHEIDER, J. R. & GRAU, V. (2009) Comparison of Rule-Based and DTMRI-Derived Fibre Architecture in a Whole Rat Ventricular Computational Model. *Functional Imaging and Modeling of the Heart*. Springer Berlin Heidelberg.
- BELLE, V. R., KAHLER, E., WALLER, C., ROMMEL, E., VOLL, S., HILLER, K. H., BAUER, W. R. & HAASE, A. (1998) In Vivo quantitative mapping of cardiac perfusion in rats using a noninvasive MR spin-labeling method. *Journal of Magnetic Resonance Imaging*, 8, 1240-1245.
- BERR, S. S., ROY, R. J., FRENCH, B. A., YANG, Z., GILSON, W., KRAMER, C. M. & EPSTEIN, F. H. (2005) Black blood gradient echo cine magnetic resonance imaging of the mouse heart. *Magnetic resonance in medicine*, 53, 1074-1079.
- BETTENDORFF-BAKMAN, D. E., SCHMID, P., LUNKENHEIMER, P. P. & NIEDERER, P. (2006) A finite element study relating to the rapid filling phase of the human ventricles. *Journal of Theoretical Biology*, 238, 303-316.
- BETTENDORFF-BAKMAN, D. E., SCHMID, P., LUNKENHEIMER, P. P. & NIEDERER, P. (2008) Diastolic ventricular aspiration: A mechanism supporting the rapid filling phase of the human ventricles. *Journal of Theoretical Biology*, 250, 581-592.

- BEYAR, R. & SIDEMAN, S. (1984a) A computer study of the left ventricular performance based on fiber structure, sarcomere dynamics, and transmural electrical propagation velocity. *Circulation Research*, 55, 358-375.
- BEYAR, R. & SIDEMAN, S. (1984b) A computer study of the left ventricular performance based on fiber structure, sarcomere dynamics, and transmural electrical propagation velocity. *Circ Res*, 55, 358 - 375.
- BILSTON, L. E. (2002) The effect of perfusion on soft tissue mechanical properties: a computational model. *Computer Methods in Biomechanics & Biomedical Engineering*, 5, 283-290.
- BOGAERT, J., MAES, A., VAN DE WERF, F., BOSMANS, H., HERREGODS, M.-C., NUYTS, J., DESMET, W., MORTELMANS, L., MARCHAL, G. & RADEMAKERS, F. E. (1999) Functional Recovery of Subepicardial Myocardial Tissue in Transmural Myocardial Infarction After Successful Reperfusion An Important Contribution to the Improvement of Regional and Global Left Ventricular Function. *Circulation*, 99, 36-43.
- BONET, J. (1997) *Nonlinear continuum mechanics for finite element analysis*, Cambridge university press.
- BOVENDEERD, P. H. M., KROON, W. & DELHAAS, T. (2009) Determinants of left ventricular shear strain. *American Journal of Physiology - Heart and Circulatory Physiology*, 297, H1058-H1068.
- BOVENDEERD, P. H. M., RIJCKEN, J., VAN CAMPEN, D. H., SCHOOF, A. J. G., NICOLAY, K. & ARTS, T. (2002) Optimization of left ventricular muscle fiber orientation. *IUTAM Symposium on Synthesis in Bio Solid Mechanics*. Springer.
- BRADSHAW, D., GROENEWALD, P., LAUBSCHER, R., NANNAN, N., NOJILANA, B., NORMAN, R., PIETERSE, D., SCHNEIDER, M., BOURNE, D. E. & TIMAIUS, I. M. (2003) Initial burden of disease estimates for South Africa, 2000: original article. *South African Medical Journal*, 93, p. 682-688.
- BRAU, A., HEDLUND, L. W. & JOHNSON, G. A. (2004) Cine magnetic resonance microscopy of the rat heart using cardiorespiratory synchronous projection reconstruction. *Journal of Magnetic Resonance Imaging*, 20, 31-38.
- BUCHOLZ, E., GHAGHADA, K., QI, Y., MUKUNDAN, S. & JOHNSON, G. A. (2008) Four dimensional MR microscopy of the mouse heart using radial acquisition and liposomal gadolinium contrast agent. *Magnetic resonance in medicine*, 60, 111-118.
- CAO, J., AKKERMAN, R., BOISSE, P., CHEN, J., CHENG, H. S., DE GRAAF, E. F., GORCZYCA, J. L., HARRISON, P., HIVET, G., LAUNAY, J., LEE, W., LIU, L., LOMOV, S. V., LONG, A., DE LUYCKER, E., MORESTIN, F., PADVOISKIS, J., PENG, X. Q., SHERWOOD, J., STOILOVA, T., TAO, X. M., VERPOEST, I.,

- WILLEMS, A., WIGGERS, J., YU, T. X. & ZHU, B. (2008) Characterization of mechanical behavior of woven fabrics: Experimental methods and benchmark results. *Composites Part A: Applied Science and Manufacturing*, 39, 1037-1053.
- CARAPPELLA, V., BORDAS, R., PATHMANATHAN, P., LOHEZIC, M., SCHNEIDER, J. E., KOHL, P., BURRAGE, K. & GRAU, V. (2014) Quantitative Study of the Effect of Tissue Microstructure on Contraction in a Computational Model of Rat Left Ventricle. *PLoS ONE*, 9, e92792.
- CARR, C. A., STUCKEY, D. J., TATTON, L., TYLER, D. J., HALE, S. J. M., SWEENEY, D., SCHNEIDER, J. R. E., MARTIN-RENDON, E., RADDI, G. K. & HARDING, S. E. (2008) Bone marrow-derived stromal cells home to and remain in the infarcted rat heart but fail to improve function: an in vivo cine-MRI study. *American Journal of Physiology-Heart and Circulatory Physiology*, 295, H533-H542.
- CHEN, B. T., YORDANOV, A. T. & JOHNSON, G. A. (2005a) Ventilation synchronous magnetic resonance microscopy of pulmonary structure and ventilation in mice. *Magnetic resonance in medicine*, 53, 69-75.
- CHEN, J. (2005) Characterization of myocardial fiber and sheet structure in normal and post-infarct rat hearts with diffusion tensor MRI. *ProQuest Dissertations and Theses*. Ann Arbor, Washington University.
- CHEN, J., LIU, W., ZHANG, H., LACY, L., YANG, X., SONG, S.-K., WICKLINE, S. A. & YU, X. (2005b) Regional ventricular wall thickening reflects changes in cardiac fiber and sheet structure during contraction: quantification with diffusion tensor MRI. *American Journal of Physiology - Heart and Circulatory Physiology*, 289, H1898-H1907.
- CHEN, J., SONG, S.-K., LIU, W., MCLEAN, M., ALLEN, J. S., TAN, J., WICKLINE, S. A. & YU, X. (2003a) Remodeling of cardiac fiber structure after infarction in rats quantified with diffusion tensor MRI. *American Journal of Physiology-Heart and Circulatory Physiology*, 285, H946-H954.
- CHEN, J., SONG, S.-K., LIU, W., MCLEAN, M. & ET AL. (2003b) Remodeling of cardiac fiber structure after infarction in rats quantified with diffusion tensor MRI. *American Journal of Physiology*, 54, H946-H954.
- CLEUTJENS, J. P., VERLUYTEN, M. J., SMITHS, J. F. & DAEMEN, M. J. (1995a) Collagen remodeling after myocardial infarction in the rat heart. *Am J Pathol*, 147, 325-38.
- CLEUTJENS, J. P. M., KANDALA, J. C., GUARDA, E., GUNTAKA, R. V. & WEBER, K. T. (1995b) Regulation of collagen degradation in the rat myocardium after infarction. *Journal of Molecular and Cellular Cardiology*, 27, 1281-1292.

- COSTA, K. D., HOLMES, J. W. & MCCULLOCH, A. D. (2001) Modelling cardiac mechanical properties in three dimensions. *Royal Society of London Philosophical Transactions Series A*, 359, 1233-1250.
- CRISFIELD, M. A. (1997) *Non-linear finite element analysis of solids and structures: Advanced topics*, John Wiley & Sons, Inc.
- CROWLEY, J. (1997) A quantitative description of dynamic left ventricular geometry in anaesthetized rats using magnetic resonance imaging. *Experimental Physiology*, 82, 887-904.
- DAI, W., WOLD, L. E., DOW, J. S. & KLONER, R. A. (2005) Thickening of the infarcted wall by collagen injection improves left ventricular function in rats: a novel approach to preserve cardiac function after myocardial infarction. *J Am Coll Cardiol*, 46, 714-9.
- DAIRE, J.-L., JACOB, J.-P., HYACINTHE, J.-N., CROISILLE, P., MONTET-ABOU, K., RICHTER, S., BOTSIKAS, D., LEPETIT-COIFFE, M., MOREL, D. & VALLEE, J.-P. (2008) Cine and tagged cardiovascular magnetic resonance imaging in normal rat at 1.5 T: a rest and stress study. *Journal of Cardiovascular Magnetic Resonance*, 10, 48.
- DANG, A. B., GUCCIONE, J. M., MISHHELL, J. M., ZHANG, P., WALLACE, A. W., GORMAN, R. C., GORMAN, J. H., 3RD & RATCLIFFE, M. B. (2005) Akinetic myocardial infarcts must contain contracting myocytes: finite-element model study. *Am J Physiol Heart Circ Physiol*, 288, H1844-50.
- DE BAKER, J. M. T., CORONEL, R., TASSERON, S., WILDE, A. A. M., OPTHOF, T., JANSE, M. J., VAN CAPELLE, F. J. L., BECKER, A. E. & JAMBROES, G. (1990) Ventricular tachyrdia in the infarcted, Langendorff-perfused human heart: Role of the arrangement of surviving cardiac fibers. *Journal of the American College of Cardiology*, 15, 1594-1607.
- DE BAKKER, J. M., VAN CAPELLE, F. J., JANSE, M. J., WILDE, A. A., CORONEL, R., BECKER, A. E., DINGEMANS, K. P., VAN HEMEL, N. M. & HAUER, R. N. (1988) Reentry as a cause of ventricular tachycardia in patients with chronic ischemic heart disease: electrophysiologic and anatomic correlation. *Circulation*, 77, 589-606.
- DELHAAS, T., KROON, W., DECALUWE, W., RUBBENS, M., BOVENDEERD, P. & ARTS, T. (2008) Structure and torsion of the normal and situs inversus totalis cardiac left ventricle. I. Experimental data in humans. *Am J Physiol Heart Circ Physiol*, 295, H197-201.
- DOBNER, S., BEZUIDENHOUT, D., GOVENDER, P., ZILLA, P. & DAVIES, N. (2009) A Synthetic Non-degradable Polyethylene Glycol Hydrogel Retards Adverse Post-infarct Left Ventricular Remodeling. *Journal of Cardiac Failure*, 15, 629-636.

- DORRI, F., NIEDERER, P. F. & LUNKENHEIMER, P. P. (2006) A finite element model of the human left ventricular systole. *Computer Methods in Biomechanics and Biomedical Engineering*, 9, 319 - 341.
- DRIEHUYS, B., NOULS, J., BADEA, A., BUCHOLZ, E., GHAGHADA, K., PETIET, A. & HEDLUND, L. W. (2008) Small animal imaging with magnetic resonance microscopy. *ILAR journal*, 49, 35-53.
- EPSTEIN, F. H., YANG, Z., GILSON, W. D., BERR, S. S., KRAMER, C. M. & FRENCH, B. A. (2002) MR tagging early after myocardial infarction in mice demonstrates contractile dysfunction in adjacent and remote regions. *Magnetic Resonance in Medicine*, 48, 399-403.
- FLETCHER, P. J., PFEFFER, J. M., PFEFFER, M. A. & BRAUNWALD, E. (1981) Left ventricular diastolic pressure-volume relations in rats with healed myocardial infarction. Effects on systolic function. *Circulation Research*, 49, 618-626.
- FOGEL, M. A. (2000) Assessment of Cardiac Function by Magnetic Resonance Imaging. *Pediatric Cardiology*, 21, 59-69.
- FRANK, O. (1899) Die Grundform des arteriellen Pulses erste Abhandlung: Mathematische Analyse. *Z Biol*, 37, 483-526.
- FUNG, Y. C. (1984) Structure and stress-strain relationship of soft tissues. *American Zoologist*, 24, 13-22.
- GARDNER, P. I., URSELL, P. C., FENOGLIO, J. J. & WIT, A. L. (1985) Electrophysiologic and anatomic basis for fractionated electrograms recorded from healed myocardial infarcts. *Circulation*, 72, 596-611.
- GAUDRON, P., EILLES, C., KUGLER, I. & ERTL, G. (1993) Progressive left ventricular dysfunction and remodeling after myocardial infarction. Potential mechanisms and early predictors. *Circulation*, 87, 755-763.
- GILSON, W. D. & KRAITCHMAN, D. L. (2007) Cardiac magnetic resonance imaging in small rodents using clinical 1.5 T and 3.0 T scanners. *Methods (Amsterdam)*, 43, 35-45.
- GILSON, W. D., YANG, Z., FRENCH, B. A. & EPSTEIN, F. H. (2004) Complementary displacement encoded MRI for contrast enhanced infarct detection and quantification of myocardial function in mice. *Magnetic Resonance in Medicine*, 51, 744-752.
- GÖKTEPE, S., ACHARYA, S. N. S., WONG, J. & KUHL, E. (2011) Computational modeling of passive myocardium. *International Journal for Numerical Methods in Biomedical Engineering*, 27, 1-12.
- GRANZIER, H. L. & IRVING, T. C. (1995) Passive tension in cardiac muscle: contribution of collagen, titin, microtubules, and intermediate filaments. *Biophys J*, 68, 1027-44.

- GUCCIONE, J. M., COSTA, K. D. & MCCULLOCH, A. D. (1995a) Finite element stress analysis of left ventricular mechanics in the beating dog heart. *J Biomech*, 28, 1167-77.
- GUCCIONE, J. M., COSTA, K. D. & MCCULLOCH, A. D. (1995b) Finite element stress analysis of left ventricular mechanics in the beating dog heart. *Journal of Biomechanics*, 28, 1167-1177.
- GUCCIONE, J. M. & MCCULLOCH, A. D. (1993) Mechanics of active contraction in cardiac muscle: Part I-Constitutive relations for fiber stress that describe deactivation. *J Biomech Eng*, 115, 72-81.
- GUCCIONE, J. M., MOONLY, S. M., MOUSTAKIDIS, P., COSTA, K. D., MOULTON, M. J., RATCLIFFE, M. B. & PASQUE, M. K. (2001) Mechanism underlying mechanical dysfunction in the border zone of left ventricular aneurysm: a finite element model study. *The Annals of Thoracic Surgery*, 71, 654-662.
- GUCCIONE, J. M., WALDMAN, L. K. & MCCULLOCH, A. D. (1993a) Mechanics of active contraction in cardiac muscle: Part II - Cylindrical models of the systolic left ventricle. *Journal of biomechanical engineering*, 115, 82-90.
- GUCCIONE, J. M., WALDMAN, L. K. & MCCULLOCH, A. D. (1993b) Mechanics of active contraction in cardiac muscle: Part II—Cylindrical models of the systolic left ventricle. *Journal of biomechanical engineering*, 115, 82-90.
- HEALY, L. J., JIANG, Y. & HSU, E. W. (2011) Quantitative comparison of myocardial fiber structure between mice, rabbit, and sheep using diffusion tensor cardiovascular magnetic resonance. *Journal of Cardiovascular Magnetic Resonance*, 13, 74.
- HEATLIE, G. J. & POINTON, K. (2004) Cardiac magnetic resonance imaging. *Postgraduate Medical Journal*, 80, 19-22.
- HEIBERG, E., SJOGREN, J., UGANDER, M., CARLSSON, M., ENGBLOM, H. & ARHEDEN, H. K. (2010) Design and validation of Segment-freely available software for cardiovascular image analysis. *BMC medical imaging*, 10, 1.
- HIBBITT, KARLSSON & SORENSEN (1997) *ABAQUS: Theory Manual*, Hibbitt, Karlsson and Sorensen.
- HIGUCHI, T., ANTON, M., DUMLER, K., SEIDL, S., PELISEK, J., SARASTE, A., WELLING, A., HOFMANN, F., OOSTENDORP, R. A. J. & GANSBACHER, B. (2009) Combined reporter gene PET and iron oxide MRI for monitoring survival and localization of transplanted cells in the rat heart. *Journal of Nuclear Medicine*, 50, 1088-1094.
- HOLMES, J. W., BORG, T. K. & COVELL, J. W. (2005) Structure and mechanics of healing myocardial infarcts. *Annu Rev Biomed Eng*, 7, 223-53.

- HOLMES, J. W., NUNEZ, J. A. & COVELL, J. W. (1997) Functional implications of myocardial scar structure. *American Journal of Physiology-Heart and Circulatory Physiology*, 41, H2123.
- HOLZAPFEL, G. A. & OGDEN, R. W. (Eds.) (2009a) *Biomechanical modelling at the molecular, cellular and tissue levels*, Wien, Springer.
- HOLZAPFEL, G. A. & OGDEN, R. W. (2009b) Constitutive modelling of passive myocardium: a structurally based framework for material characterization. *Philosophical Transactions of the Royal Society A: Mathematical, Physical and Engineering Sciences*, 367, 3445-3475.
- HOMANS, D. C., ASINGER, R., ELSPERGER, K. J., ERLIEN, D., SUBLETT, E., MIKELL, F. & BACHE, R. J. (1985) Regional function and perfusion at the lateral border of ischemic myocardium. *Circulation*, 71, 1038-1047.
- HU, T. & DESAI, J. P. (2004) Characterization of soft-tissue material properties: large deformation analysis. *Medical Simulation*. Springer.
- HU, Z., METAXAS, D. & AXEL, L. (2005) Computational modeling and simulation of heart ventricular mechanics with tagged MRI. *Proceedings of the 2005 ACM symposium on Solid and physical modeling*. Cambridge, Massachusetts, ACM.
- JACKSON, B. M., GORMAN, J. H., 3RD, SALGO, I. S., MOAINIE, S. L., PLAPPERT, T., ST JOHN-SUTTON, M., EDMUNDS, L. H., JR. & GORMAN, R. C. (2003) Border zone geometry increases wall stress after myocardial infarction: contrast echocardiographic assessment. *Am J Physiol Heart Circ Physiol*, 284, H475-9.
- JACKSON, B. M., GORMAN, J. H., MOAINIE, S. L., GUY, T. S., NARULA, N., NARULA, J., JOHN-SUTTON, M. G. S., EDMUNDS, L. H. & GORMAN, R. C. (2002) Extension of borderzone myocardium in postinfarction dilated cardiomyopathy. *Journal of the American College of Cardiology*, 40, 1160-1167.
- JANZ, R. F. & GRIMM, A. F. (1972) Finite-Element Model for the Mechanical Behavior of the Left Ventricle: PREDICTION OF DEFORMATION IN THE POTASSIUM-ARRESTED RAT HEART. *Circulation Research*, 30, 244-252.
- JUGDUTT, B. I. (2003a) Remodeling of the myocardium and potential targets in the collagen degradation and synthesis pathways. *Curr Drug Targets Cardiovasc Haematol Disord*, 3, 1-30.
- JUGDUTT, B. I. (2003b) Ventricular remodeling after infarction and the extracellular collagen matrix: when is enough enough? *Circulation*, 108, 1395-403.
- KATZ, A. M. (2010) *Physiology of the heart*, Philadelphia, PA, Wolters Kluwer Health/Lippincott Williams & Wilkins Health.

- KERCKHOFFS, R. C. P. (2003) Depolarization wave and mechanics in the paced heart. *Department of Biomedical Engineering*. Eindhoven, Eindhoven University of Technology.
- KERCKHOFFS, R. C. P., HEALY, S. N., USYK, T. P. & MCCULLOCH, A. D. (2006) Computational methods for cardiac electromechanics. *Proceedings of the IEEE*, 94, 769-783.
- KLEPACH, D., LEE, L. C., WENK, J. F., RATCLIFFE, M. B., ZOHDI, T. I., NAVIA, J. L., KASSAB, G. S., KUHL, E. & GUCCIONE, J. M. (2012) Growth and remodeling of the left ventricle: A case study of myocardial infarction and surgical ventricular restoration. *Mechanics research communications*, 42, 134-141.
- KORTSMIT, J., DAVIES, N. H., MILLER, R., MACADANGDANG, J. R., ZILLA, P. & FRANZ, T. (2013) The effect of hydrogel injection on cardiac function and myocardial mechanics in a computational post-infarction model. *Comput Methods Biomech Biomed Engin*. 2012 Mar 22.
- KORTSMIT, J., DAVIES, N. H., MILLER, R., ZILLA, P. & FRANZ, T. (2012) A COMPUTATIONAL STUDY OF THE EFFECT OF A LAYERED HYDROGEL INJECTATE ON CARDIAC FUNCTION AND MYOCARDIAL MECHANICS IN AN INFARCTED HEART. *Journal of Biomechanics*, 45, Supplement 1, S131.
- KOSTUK, W. J., KAZAMIAS, T. M., GANDER, M. P., SIMON, A. L. & ROSS, J. (1973) Left Ventricular Size after Acute Myocardial Infarction Serial Changes and their Prognostic Significance. *Circulation*, 47, 1174-1179.
- KROON, W., DELHAAS, T., BOVENDEERD, P. & ARTS, T. (2008) Structure and torsion in the normal and situs inversus totalis cardiac left ventricle. II. Modeling cardiac adaptation to mechanical load. *Am J Physiol Heart Circ Physiol*, 295, H202-210.
- LANDA, N., MILLER, L., FEINBERG, M. S., HOLBOVA, R., SHACHAR, M., FREEMAN, I., COHEN, S. & LEOR, J. (2008) Effect of injectable alginate implant on cardiac remodeling and function after recent and old infarcts in rat. *Circulation*, 117, 1388-96.
- LEE, L. C., GENET, M., ACEVEDO-BOLTON, G., ORDOVAS, K., GUCCIONE, J. M. & KUHL, E. (2014a) A computational model that predicts reverse growth in response to mechanical unloading. *Biomechanics and modeling in mechanobiology*, 1-13.
- LEE, L. C., GENET, M., DANG, A. B., GE, L., GUCCIONE, J. M. & RATCLIFFE, M. B. (2014b) Applications of Computational Modeling in Cardiac Surgery. *Journal of Cardiac Surgery*, 29, 293-302.
- LEE, L. C., WALL, S. T., GENET, M., HINSON, A. & GUCCIONE, J. M. (2014c) Bioinjection treatment: Effects of post-injection residual stress on left ventricular wall stress. *Journal of Biomechanics*.

- LEE, L. C., WALL, S. T., KLEPACH, D., GE, L., ZHANG, Z., LEE, R. J., HINSON, A., GORMAN III, J. H., GORMAN, R. C. & GUCCIONE, J. M. (2014d) Algisyl-LVRA with coronary artery bypass grafting reduces left ventricular wall stress and improves function in the failing human heart. *International journal of cardiology*, 168, 2022-2028.
- LEE, L. C., WENK, J. F., ZHONG, L., KLEPACH, D., ZHANG, Z., GE, L., RATCLIFFE, M. B., ZOHDİ, T. I., HSU, E. & NAVIA, J. L. (2013) Analysis of patient-specific surgical ventricular restoration: importance of an ellipsoidal left ventricular geometry for diastolic and systolic function. *Journal of Applied Physiology*, 115, 136-144.
- LEGRICE, I. J., SMAILL, B. H., CHAI, L. Z., EDGAR, S. G., GAVIN, J. B. & HUNTER, P. J. (1995a) Laminar structure of the heart: ventricular myocyte arrangement and connective tissue architecture in the dog. *American Journal of Physiology-Heart and Circulatory Physiology*, 269, H571-H582.
- LEGRICE, I. J., SMAILL, B. H., CHAI, L. Z., EDGAR, S. G., GAVIN, J. B. & HUNTER, P. J. (1995b) Laminar structure of the heart: ventricular myocyte arrangement and connective tissue architecture in the dog. *American Journal of Physiology-Heart and Circulatory Physiology*, 38, H571.
- LITTLE, R. C. (1981) *Physiology of the Heart and Circulation*.
- LIU, W., ASHFORD, M., CHEN, J., WATKINS, M., WILLIAMS, T., WICKLINE, S. & YU, X. (2006) MR tagging demonstrates quantitative differences in regional ventricular wall motion in mice, rats, and men. *American Journal of Physiology - Heart and Circulatory Physiology*, 291, H2515 - 2521.
- LIU, Y., KERDOK, A. E. & HOWE, R. D. (2004) A nonlinear finite element model of soft tissue indentation. *Medical Simulation*. Springer.
- LUKE, R. A. & SAFFITZ, J. E. (1991) Remodeling of ventricular conduction pathways in healed canine infarct border zones. *Journal of Clinical Investigation*, 87, 1594.
- MAÑÁ, W., BADEA, C. T., WHEELER, C. T., HEDLUND, L. W. & JOHNSON, G. A. (2005) Effects of breathing and cardiac motion on spatial resolution in the microscopic imaging of rodents. *Magnetic resonance in medicine*, 53, 858-865.
- MACIVER, D. H., ADENIRAN, I. & ZHANG, H. (2015) Left ventricular ejection fraction is determined by both global myocardial strain and wall thickness. *IJC Heart & Vasculature*.
- MARSDEN, S. S. A. J. E., WIGGINS, L. S. S., GLASS, L., KOHN, R. V. & SASTRY, S. S. (1993) *Interdisciplinary Applied Mathematics*.

- MCCULLOCH, A. & MAZHARI, R. (2001) Regional myocardial mechanics: Integrative computational models of flow-function relations. *Journal of Nuclear Cardiology*, 8, 506-519.
- MCCULLOCH, A., WALDMAN, L., ROGERS, J. & GUCCIONE, J. (1992) Large-scale finite element analysis of the beating heart. *Critical Reviews in Biomedical Engineering*, 20, 427-449.
- MCPHERSON, D. D., SKORTON, D. J., KODIYALAM, S., PETREE, L., NOEL, M. P., KIESO, R., KERBER, R. E., COLLINS, S. M. & CHANDRAN, K. B. (1987) Finite element analysis of myocardial diastolic function using three-dimensional echocardiographic reconstructions: application of a new method for study of acute ischemia in dogs. *Circulation Research*, 60, 674-682.
- MEKKAOUI, C., HUANG, S., CHEN, H. H., DAI, G., REESE, T. G., KOSTIS, W. J., THIAGALINGAM, A., MAUROVICH-HORVAT, P., RUSKIN, J. N., HOFFMANN, U., JACKOWSKI, M. P. & SOSNOVIK, D. E. (2012) Fiber architecture in remodeled myocardium revealed with a quantitative diffusion CMR tractography framework and histological validation. *Journal of Cardiovascular Magnetic Resonance*, 14, 70.
- MILLER, R., DAVIES, N. H., KORTSMIT, J., ZILLA, P. & FRANZ, T. (2013) Outcomes of myocardial infarction hydrogel injection therapy in the human left ventricle dependent on injectate distribution. *International Journal for Numerical Methods in Biomedical Engineering*, 29, 870-884.
- MOJSEJENKO, D., MCGARVEY, J., DORSEY, S., GORMAN, J., III, BURDICK, J., PILLA, J., GORMAN, R. & WENK, J. (2014) Estimating passive mechanical properties in a myocardial infarction using MRI and finite element simulations. *Biomechanics and Modeling in Mechanobiology*, 1-15.
- MONROE, R. G. & FRENCH, G. N. (1961) Left ventricular pressure-volume relationships and myocardial oxygen consumption in the isolated heart. *Circulation Research*, 9, 362-373.
- MONTET-ABOU, K., DAIRE, J. L., IVANCEVIC, M. K., HYACINTHE, J. N., NGUYEN, D., JORGE-COSTA, M., MOREL, D. R. & VALLEE, J. P. (2006) Optimization of cardiac cine in the rat on a clinical 1.5-T MR system. *Magnetic Resonance Materials in Physics, Biology and Medicine*, 19, 144-151.
- MOUSTAKIDIS, P., MANIAR, H. S., CUPPS, B. P., ABSI, T., ZHENG, J., GUCCIONE, J. M., SUNDT, T. M. & PASQUE, M. K. (2002) Altered left ventricular geometry changes the border zone temporal distribution of stress in an experimental model of left ventricular aneurysm: A finite element model study. *Circulation*, 106, 1-168-175.

- NAHRENDORF, M., HILLER, K. H., HU, K., ERTL, G., HAASE, A. & BAUER, W. R. (2003) Cardiac magnetic resonance imaging in small animal models of human heart failure. *Medical Image Analysis*, 7, 369-375.
- NAHRENDORF, M., WIESMANN, F., HILLER, K. H., HU, K., WALLER, C., RUFF, J., LANZ, T. E., NEUBAUER, S., HAASE, A., ERTL, G. & BAUER, W. R. (2001) Serial cine-magnetic resonance imaging of left ventricular remodeling after myocardial infarction in rats. *Journal of Magnetic Resonance Imaging*, 14, 547 - 555.
- NAPADOW, V. J., CHEN, Q., MAI, V., SO, P. T. C. & GILBERT, R. J. (2001) Quantitative Analysis of Three-Dimensional-Resolved Fiber Architecture in Heterogeneous Skeletal Muscle Tissue Using NMR and Optical Imaging Methods. *Biophys. J.*, 80, 2968-2975.
- NARDINOCCHI, P., TERESI, L. & VARANO, V. (2010) Myocardial Contractions and the Ventricular Pressure--Volume Relationship. *arXiv preprint arXiv:1005.5292*.
- NASH, M. & HUNTER, P. (2000) Computational Mechanics of the Heart. *Journal of Elasticity*, 61, 113-141.
- NGUYEN, B.-K., MALTAIS, S., PERRAULT, L. P., TANGUAY, J.-F., TARDIF, J.-C., STEVENS, L.-M., BORIE, M., HAREL, F., MANSOUR, S. & NOISEUX, N. (2010) Improved Function and Myocardial Repair of Infarcted Heart by Intracoronary Injection of Mesenchymal Stem Cell-Derived Growth Factors. *Journal of Cardiovascular Translational Research*, 3, 547-558.
- NIELSEN, B. F., CAI, X., SUNDNES, J. & TVEITO, A. (2009) Towards a computational method for imaging the extracellular potassium concentration during regional ischemia. *Mathematical Biosciences*, 220, 118-130.
- NUCIFORA, G., DELGADO, V., BERTINI, M., MARSAN, N. A., VAN DE VEIRE, N. R., NG, A. C. T., SIEBELINK, H.-M. J., SCHALIJ, M. J., HOLMAN, E. R., SENGUPTA, P. P. & BAX, J. J. (2010) Left Ventricular Muscle and Fluid Mechanics in Acute Myocardial Infarction. *American Journal of Cardiology*, 106, 1404-1409.
- OHNISHI, S., YANAGAWA, B., TANAKA, K., MIYAHARA, Y., OBATA, H., KATAOKA, M., KODAMA, M., ISHIBASHI-UEDA, H., KANGAWA, K. & KITAMURA, S. (2007) Transplantation of mesenchymal stem cells attenuates myocardial injury and dysfunction in a rat model of acute myocarditis. *Journal of molecular and cellular cardiology*, 42, 88-97.
- OLIVETTI, G., CAPASSO, J. M., SONNENBLICK, E. H. & ANVERSA, P. (1990) Side-to-side slippage of myocytes participates in ventricular wall remodeling acutely after myocardial infarction in rats. *Circulation Research*, 67, 23-34.

- OMENS, J. H., MACKENNA, D. A. & MCCULLOCH, A. D. (1993) Measurement of strain and analysis of stress in resting rat left ventricular myocardium. *Journal of Biomechanics*, 26, 665-676.
- OPIE, L. H. (2004) *Heart physiology: from cell to circulation*, Lippincott Williams & Wilkins.
- PACHER, P. L., MABLEY, J. G., LIAUDET, L., EVGENOV, O. V., MARTON, A., HASKA, G., KOLLAI, M. R. & SZABA, C. (2004) Left ventricular pressure-volume relationship in a rat model of advanced aging-associated heart failure. *American Journal of Physiology-Heart and Circulatory Physiology*, 287, H2132-H2137.
- PAO, Y. C. & RITMAN, E. L. (1998) Comparative Characterization of the Infarcted and Reperfused Ventricular Wall Muscles by Finite Element Analysis and a Myocardial Muscle-Blood Composite Model. *Computers and Biomedical Research*, 31, 18-31.
- PAO, Y. C., RITMAN, E. L. & WOOD, E. H. (1974) Finite-element analysis of left ventricular myocardial stresses. *Journal of Biomechanics*, 7, 469-477.
- PFEFFER, J. M., PFEFFER, M. A., FLETCHER, P. J. & BRAUNWALD, E. (1991) Progressive ventricular remodeling in rat with myocardial infarction. *American Journal of Physiology*, 260, H1406-14.
- PFEFFER, M. A. & BRAUNWALD, E. (1990) Ventricular remodeling after myocardial infarction. Experimental observations and clinical implications. *Circulation*, 81, 1161-72.
- PFEFFER, M. A., LAMAS, G. A., VAUGHAN, D. E., PARISI, A. F. & BRAUNWALD, E. (1988) Effect of captopril on progressive ventricular dilatation after anterior myocardial infarction. *New England Journal of Medicine*, 319, 80-86.
- PFEFFER, M. D. P. D. M. A. (1995) Left ventricular remodeling after acute myocardial infarction. *Annual Review of Medicine*, 46, 455-466.
- PRUNIER, F., GAERTNER, R., LOUEDEC, L., MICHEL, J.-B., MERCADIER, J.-J. & ESCOUBET, B. (2002) Doppler echocardiographic estimation of left ventricular end-diastolic pressure after MI in rats. *American Journal of Physiology-Heart and Circulatory Physiology*, 283, H346-H352.
- RABBEN, S. I., IRGENS, F. & ANGELSEN, B. (1999) Equations for estimating muscle fiber stress in the left ventricular wall. *Heart and Vessels*, 14, 189-196.
- RATCLIFFE, M. B., HONG, J., SALAHIEH, A., RUCH, S. & WALLACE, A. W. (1998) The effect of ventricular volume reduction surgery in the dilated, poorly contractile left ventricle: a simple finite element analysis. *J Thorac Cardiovasc Surg*, 116, 566-77.
- RAYA, T. E., GAY, R. G., LANCASTER, L., AGUIRRE, M., MOFFETT, C. & GOLDMAN, S. (1988) Serial changes in left ventricular relaxation and chamber stiffness after large myocardial infarction in rats. *Circulation*, 77, 1424-1431.

- REESE, S., BÖL, M. & CHRIST, D. (2010) Finite element-based multi-phase modelling of shape memory polymer stents. *Computer Methods in Applied Mechanics and Engineering*, 199, 1276-1286.
- REESE, T. G., WEISSKOFF, R. M., SMITH, R. N., ROSEN, B. R., DINSMORE, R. E. & WEDEEN, V. J. (1995) Imaging myocardial fiber architecture in vivo with magnetic resonance. *Magnetic resonance in medicine*, 34, 786-791.
- REHWALD, W. G., REEDER, S. B., MCVEIGH, E. R. & JUDD, R. M. (1997) Techniques for high-speed cardiac magnetic resonance imaging in rats and rabbits. *Magnetic Resonance in Medicine*, 37, 124-130.
- RIJCKEN, J., BOVENDEERD, P. H., SCHOOF, A. J., VAN CAMPEN, D. H. & ARTS, T. (1999) Optimization of cardiac fiber orientation for homogeneous fiber strain during ejection. *Ann Biomed Eng*, 27, 289-97.
- ROUILLARD, A. D. & HOLMES, J. W. (2012) Mechanical regulation of fibroblast migration and collagen remodelling in healing myocardial infarcts. *The Journal of physiology*, 590, 4585-4602.
- RUDIN, M., PEDERSEN, B., UMEMURA, K. & ZIERHUT, W. (1991) Determination of rat heart morphology and function in vivo in two models of cardiac hypertrophy by means of magnetic resonance imaging. *Basic research in cardiology*, 86, 165-174.
- RUETTEN, H., GEHRING, D., HISS, K., SCHINDLER, U., GERL, M., BUSCH, A. E. & SCHAEFER, S. (2005) Effects of combined inhibition of the Na and H⁺ exchanger and angiotensin converting enzyme in rats with congestive heart failure after myocardial infarction. *British Journal of Pharmacology*, 146, 723-731.
- SALEH, M. G. (2012) Methods and adaptations required to perform small-animal MRI scanning using a large bore clinical MRI. University of Cape Town.
- SALEH, M. G., SHARP, S.-K., ALKATHAFI, A., SPOTTISWOODE, B. S., ANDRE, J. W. V. D. K., DAVIES, N. H., FRANZ, T. & MEINTJES, E. M. (2012) Long-Term Left Ventricular Remodelling in Rat Model of Nonreperfused Myocardial Infarction: Sequential MR Imaging Using a 3T Clinical Scanner. *Journal of Biomedicine and Biotechnology*, 10 pages.
- SAVADJIEV, P., STRIJKERS, G. J., BAKERMANS, A. J., PIUZE, E., ZUCKER, S. W. & SIDDIQI, K. (2012a) Heart wall myofibers are arranged in minimal surfaces to optimize organ function. *Proceedings of the National Academy of Sciences of the United States of America*, 109, 9248.
- SAVADJIEV, P., STRIJKERS, G. J., BAKERMANS, A. J., PIUZE, E., ZUCKER, S. W. & SIDDIQI, K. (2012b) Heart wall myofibers are arranged in minimal surfaces to

- optimize organ function. *Proceedings of the National Academy of Sciences*, 109, 9248-9253.
- SAVADJIEV, P., ZUCKER, S. W. & SIDDIQI, K. (2007) On the Differential Geometry of 3D Flow Patterns: Generalized Helicoids and Diffusion MRI Analysis. *Computer Vision, 2007. ICCV 2007. IEEE 11th International Conference on*.
- SCHMID, H., H. (2006) Myocardial Material Parameter Estimation-A Comparative Study for Simple Shear. *Journal of biomechanical engineering*, 128, 742.
- SCHMID, H., WANG, Y. K., ASHTON, J., EHRET, A. E., KRITTIAN, S. B. S., NASH, M. P. & HUNTER, P. J. (2009) Myocardial material parameter estimation: a comparison of invariant based orthotropic constitutive equations. *Computer Methods in Biomechanics and Biomedical Engineering*, 12, 283 - 295.
- SCOLLAN, D. F., HOLMES, A., WINSLOW, R. & FORDER, J. (1998) Histological validation of myocardial microstructure obtained from diffusion tensor magnetic resonance imaging. *Am J Physiol*, 275, H2308-18.
- SHAO, Y., CHERRY, S. R., FARAHANI, K., SLATES, R., SILVERMAN, R. W., MEADORS, K., BOWERY, A., SIEGEL, S., MARSDEN, P. K. & GARLICK, P. B. (1997) Development of a PET detector system compatible with MRI/NMR systems. *Nuclear Science, IEEE Transactions on*, 44, 1167-1171.
- SLAWSON, S. E., ROMAN, B. B., WILLIAMS, D. S. & KORETSKY, A. P. (1998) Cardiac MRI of the normal and hypertrophied mouse heart. *Magnetic resonance in medicine*, 39, 980-987.
- SLIWA, K., WILKINSON, D., HANSEN, C., NTYINTYANE, L., TIBAZARWA, K., BECKER, A. & STEWART, S. (2008) Spectrum of heart disease and risk factors in a black urban population in South Africa (the Heart of Soweto Study): a cohort study. *The Lancet*, 371, 915-922.
- SOSNOVIK, D. E., WANG, R., DAI, G., REESE, T. G. & WEDEEN, V. J. (2009) Diffusion MR tractography of the heart. *Journal of Cardiovascular Magnetic Resonance*, 11, 1-15.
- STERGIOPULOS, N., WESTERHOF, B. E. & WESTERHOF, N. (1999) Total arterial inertance as the fourth element of the windkessel model. *Am J Physiol*, 276, H81-8.
- STEVENS, C. & HUNTER, P. J. (2003) Sarcomere length changes in a 3D mathematical model of the pig ventricles. *Prog Biophys Mol Biol*, 82, 229-41.
- STEYN, K., FOURIE, J. & BRADSHAW, D. (1992) The impact of chronic diseases of lifestyle and their major risk factors on mortality in South Africa. *South African medical journal= Suid-Afrikaanse tydskrif vir geneeskunde*, 82, 227-231.

- STEYN, K., KAZENELLENBOGEN, J. M., LOMBARD, C. J. & BOURNE, L. T. (1997) Urbanization and the risk for chronic diseases of lifestyle in the black population of the Cape Peninsula, South Africa. *Journal of Cardiovascular Risk*, 4, 135-142.
- STEYN, K., SLIWA, K., HAWKEN, S., COMMERFORD, P., ONEN, C., DAMASCENO, A., OUNPUU, S., YUSUF, S. & FOR THE INTERHEART INVESTIGATORS IN AFRICA (2005) Risk Factors Associated With Myocardial Infarction in Africa: The INTERHEART Africa Study. *Circulation*, 112, 3554-3561.
- STREETER, D. D., JR. & HANNA, W. T. (1973a) Engineering mechanics for successive states in canine left ventricular myocardium. I. Cavity and wall geometry. *Circ Res*, 33, 639-55.
- STREETER, D. D., JR. & HANNA, W. T. (1973b) Engineering mechanics for successive states in canine left ventricular myocardium. II. Fiber angle and sarcomere length. *Circ Res*, 33, 656-64.
- STREETER, D. D., SPOTNITZ, H. M., PATEL, D. P., ROSS, J. & SONNENBLICK, E. H. (1969) Fiber Orientation in the Canine Left Ventricle during Diastole and Systole. *Circulation Research*, 24, 339-347.
- STRIJKERS, G. J., BOUTS, A., BLANKESTEIJN, W. M., PEETERS, T. H. J. M., VILANOVA, A., VAN PROOIJEN, M. C., SANDERS, H. M. H. F., HEIJMAN, E. & NICOLAY, K. (2009) Diffusion tensor imaging of left ventricular remodeling in response to myocardial infarction in the mouse. *NMR in Biomedicine*, 22, 182-190.
- STUCKEY, D. J., CARR, C. A., TYLER, D. J. & CLARKE, K. (2008) Cine-MRI versus two-dimensional echocardiography to measure in vivo left ventricular function in rat heart. *NMR in Biomedicine*, 21, 765-772.
- SUH, J. K., SPILKER, R. L. & HOLMES, M. H. (1991) A penalty finite element analysis for nonlinear mechanics of biphasic hydrated soft tissue under large deformation. *International journal for numerical methods in engineering*, 32, 1411-1439.
- SUN, W. & SACKS, M. S. (2005) Finite element implementation of a generalized Fung-elastic constitutive model for planar soft tissues. *Biomechanics and Modeling in Mechanobiology*, 4, 190-199.
- TSAMIS, A. & STERGIOPULOS, N. (2009) Arterial remodeling in response to increased blood flow using a constituent-based model. *Journal of Biomechanics*, 42, 531-536.
- URSELL, P. C., GARDNER, P. I., ALBALA, A., FENOGLIO, J. J. & WIT, A. L. (1985) Structural and electrophysiological changes in the epicardial border zone of canine myocardial infarcts during infarct healing. *Circulation Research*, 56, 436-451.

- USYK, T. P., LEGRICE, I. J. & MCCULLOCH, A. D. (2002) Computational model of three-dimensional cardiac electromechanics. *Computing and Visualization in Science*, 4, 249-257.
- USYK, T. P., OMENS, J. H. & MCCULLOCH, A. D. (2001) Regional septal dysfunction in a three-dimensional computational model of focal myofiber disarray. *Am J Physiol Heart Circ Physiol*, 281, H506-514.
- VETTER, F. J. & MCCULLOCH, A. D. (1998) Three-dimensional analysis of regional cardiac function: a model of rabbit ventricular anatomy. *Prog Biophys Mol Biol*, 69, 157-83.
- VETTER, F. J. & MCCULLOCH, A. D. (2000) Three-dimensional stress and strain in passive rabbit left ventricle: a model study. *Ann Biomed Eng*, 28, 781-92.
- VILLARREAL, F. J., LEW, W. Y., WALDMAN, L. K. & COVELL, J. W. (1991) Transmural myocardial deformation in the ischemic canine left ventricle. *Circ Res*, 68, 368-81.
- WALKER, J. C., GUCCIONE, J. M., JIANG, Y., ZHANG, P., WALLACE, A. W., HSU, E. W. & RATCLIFFE, M. B. (2005a) Helical myofiber orientation after myocardial infarction and left ventricular surgical restoration in sheep. *The Journal of thoracic and cardiovascular surgery*, 129, 382-390.
- WALKER, J. C., RATCLIFFE, M. B., ZHANG, P., WALLACE, A. W., FATA, B., HSU, E. W., SALONER, D. & GUCCIONE, J. M. (2005b) MRI-based finite-element analysis of left ventricular aneurysm. *Am J Physiol Heart Circ Physiol*, 289, H692-700.
- WALKER, J. C., RATCLIFFE, M. B., ZHANG, P., WALLACE, A. W., HSU, E. W., SALONER, D. A. & GUCCIONE, J. M. (2008) Magnetic resonance imaging-based finite element stress analysis after linear repair of left ventricular aneurysm. *The Journal of Thoracic and Cardiovascular Surgery*, 135, 1094-1102.e2.
- WALL, S. T., WALKER, J. C., HEALY, K. E., RATCLIFFE, M. B. & GUCCIONE, J. M. (2006) Theoretical impact of the injection of material into the myocardium - A finite element model simulation. *Circulation*, 114, 2627-2635.
- WANG, H., ZHANG, X., LI, Y., MA, Y., ZHANG, Y., LIU, Z., ZHOU, J., LIN, Q., WANG, Y., DUAN, C. & WANG, C. (2010a) Improved myocardial performance in infarcted rat heart by co-injection of basic fibroblast growth factor with temperature-responsive Chitosan hydrogel. *Journal of Heart and Lung Transplantation*, 29, 881-887.
- WANG, H. M., GAO, H., LUO, X. Y., BERRY, C., GRIFFITH, B. E., OGDEN, R. W. & WANG, T. J. (2013) Structure-based finite strain modelling of the human left ventricle in diastole. *International journal for numerical methods in biomedical engineering*, 29, 83-103.
- WANG, H. M., LUO, X. Y., GAO, H., OGDEN, R. W., GRIFFITH, B. E., BERRY, C. & WANG, T. J. (2014) A modified Holzapfel-Ogden law for a residually stressed finite

- strain model of the human left ventricle in diastole. *Biomechanics and modeling in mechanobiology*, 13, 99-113.
- WANG, V. Y., LAM, H. I., ENNIS, D. B., COWAN, B. R., YOUNG, A. A. & NASH, M. P. (2009) Modelling passive diastolic mechanics with quantitative MRI of cardiac structure and function. *Medical Image Analysis*, 13, 773-784.
- WANG, V. Y., LAM, H. I., ENNIS, D. B., COWAN, B. R., YOUNG, A. A. & NASH, M. P. (2010b) Cardiac active contraction parameters estimated from magnetic resonance imaging. *Statistical Atlases and Computational Models of the Heart*. Springer.
- WATANABE, H., SUGIURA, S., KAFUKU, H. & HISADA, T. (2004) Multiphysics Simulation of Left Ventricular Filling Dynamics Using Fluid-Structure Interaction Finite Element Method. *Biophys. J.*, 87, 2074-2085.
- WENK, J. F., GE, L., ZHANG, Z., MOJSEJENKO, D., POTTER, D. D., TSENG, E. E., GUCCIONE, J. M. & RATCLIFFE, M. B. Biventricular Finite Element Modeling of the Acorn CorCap Cardiac Support Device on a Failing Heart. *The Annals of Thoracic Surgery*, 95, 2022-2027.
- WENK, J. F., GE, L., ZHANG, Z., MOJSEJENKO, D., POTTER, D. D., TSENG, E. E., GUCCIONE, J. M. & RATCLIFFE, M. B. (2013a) Biventricular Finite Element Modeling of the Acorn CorCap Cardiac Support Device on a Failing Heart. *The Annals of Thoracic Surgery*, 95, 2022-2027.
- WENK, J. F., GE, L., ZHANG, Z., SOLEIMANI, M., POTTER, D. D., WALLACE, A. W., TSENG, E., RATCLIFFE, M. B. & GUCCIONE, J. M. A coupled biventricular finite element and lumped-parameter circulatory system model of heart failure. *Computer methods in biomechanics and biomedical engineering*, 16, 807-818.
- WENK, J. F., GE, L., ZHANG, Z., SOLEIMANI, M., POTTER, D. D., WALLACE, A. W., TSENG, E., RATCLIFFE, M. B. & GUCCIONE, J. M. (2013b) A coupled biventricular finite element and lumped-parameter circulatory system model of heart failure. *Computer methods in biomechanics and biomedical engineering*, 16, 807-818.
- WENK, J. F., KLEPACH, D., LEE, L. C., ZHANG, Z., GE, L., TSENG, E. E., MARTIN, A., KOZERKE, S., GORMAN III, J. H. & GORMAN, R. C. (2011a) First evidence of depressed contractility in the border zone of a human myocardial infarction. *The Annals of thoracic surgery*, 93, 1188-1193.
- WENK, J. F., SUN, K., ZHANG, Z., SOLEIMANI, M., GE, L., SALONER, D., WALLACE, A. W., RATCLIFFE, M. B. & GUCCIONE, J. M. (2011b) Regional left ventricular myocardial contractility and stress in a finite element model of posterobasal myocardial infarction. *Journal of biomechanical engineering*, 133, 044501.

- WHITELEY, J. P., BISHOP, M. J. & GAVAGHAN, D. J. (2007) Soft tissue modelling of cardiac fibres for use in coupled mechano-electric simulations. *Bulletin of Mathematical Biology*, 69, 2199-2225.
- WICKLINE, S. A., VERDONK, E. D., WONG, A. K., SHEPARD, R. K. & MILLER, J. G. (1992) Structural remodeling of human myocardial tissue after infarction. Quantification with ultrasonic backscatter. *Circulation*, 85, 259-268.
- WILLIAMS, D. S., GRANDIS, D. J., ZHANG, W. & KORETSKY, A. P. (1993) Magnetic resonance imaging of perfusion in the isolated rat heart using spin inversion of arterial water. *Magnetic resonance in medicine*, 30, 361-365.
- WISE, R. G., HUANG, C. L.-H., AL-SHAFEI, A. I. M., CARPENTER, T. A. & HALL, L. D. (1999) Geometrical models of left ventricular contraction from MRI of the normal and spontaneously hypertensive rat heart. *Physics in Medicine and Biology*, 2657.
- WISE, R. G., HUANG, C. L. H., GRESHAM, G. A., AL-SHAFEI, A. I. M., CARPENTER, T. A. & HALL, L. D. (1998) Magnetic resonance imaging analysis of left ventricular function in normal and spontaneously hypertensive rats. *Journal of Physiology (Cambridge)*, 513, 873-887.
- WONG, J. & KUHL, E. (2014) Generating fibre orientation maps in human heart models using Poisson interpolation. *Computer Methods in Biomechanics and Biomedical Engineering*, 17, 1217-1226.
- WU, M.-T., TSENG, W.-Y. I., SU, M.-Y. M., LIU, C.-P., CHIOU, K.-R., WEDEEN, V. J., REESE, T. G. & YANG, C.-F. (2006) Diffusion Tensor Magnetic Resonance Imaging Mapping the Fiber Architecture Remodeling in Human Myocardium After Infarction Correlation With Viability and Wall Motion. *Circulation*, 114, 1036-1045.
- YOON, S. J., FANG, Y. H., LIM, C. H., KIM, B. S., SON, H. S., PARK, Y. & SUN, K. (2009) Regeneration of ischemic heart using hyaluronic acid-based injectable hydrogel. *Journal of Biomedical Materials Research Part B: Applied Biomaterials*, 91B, 163-171.
- YOUNG, J. (2010) Techniques for extended modeling of cardiac morphogenesis in the embryonic chick. *Doctoral Thesis, University of Rochester*.
- YOUNG, J. M., YAO, J., RAMASUBRAMANIAN, A., TABER, L. A. & PERUCCHIO, R. (2010) Automatic Generation of User Material Subroutines for Biomechanical Growth Analysis. *Journal of Biomechanical Engineering*, 132, 104505.
- ZHANG, H. Z., KIM, M. H., LIM, J. H. & BAE, H. R. (2013) Time-dependent expression patterns of cardiac aquaporins following myocardial infarction. *J Korean Med Sci*. 2013 Mar;28(3):402-8. doi: 10.3346/jkms.2013.28.3.402. Epub 2013 Mar 4.

- ZHANG, Z., SUN, K., SALONER, D., WALLACE, A. W., GE, L., BAKER, A., GUCCIONE, J. M. & RATCLIFFE, M. B. (2012) The benefit of enhanced contractility in the infarct borderzone: A virtual experiment. *Frontiers in Physiology*, 3.
- ZIMMERMAN, S. D., CRISCIONE, J. & COVELL, J. W. (2004) Remodeling in myocardium adjacent to an infarction in the pig left ventricle. *American Journal of Physiology - Heart and Circulatory Physiology*, 287, H2697-H2704.
- ZIMMERMANN, W.-H., MELNYCHENKO, I., WASMEIER, G., DIDI, M., NAITO, H., NIXDORFF, U., HESS, A., BUDINSKY, L., BRUNE, K. & MICHAELIS, B. (2006) Engineered heart tissue grafts improve systolic and diastolic function in infarcted rat hearts. *Nature medicine*, 12, 452-458.

Appendix A – UMAT subroutine

This user material (UMAT) subroutine is generated by Mathematica® (Young, 2010) and (Young et al., 2010) and used for simulating active contraction phase of healthy and infarcted rat heart model. The coding is attached to the thesis pdf file.

Appendix B – ORIENT Subroutine

The aim of this subroutine is to assign myofibre orientation to cardiac geometry. The coding is attached to the thesis pdf file.